PhD Thesis

Detailed modelling of biomass steam gasification in a dual fluidized bed gasifier with temperature variation

Supervisors:

1. Prof. Franco Rispoli
2. Hermann Hofbauer

Department of of Astronautical, Electrical and Energy Engineering (DIAEE), Sapienza University of Rome

December 2020

Arash Aghaalikhani

A thesis submitted for the degree of Doctor of Philosophy Sapienza University of Rome

1. Abstract

Biomass gasification is a very efficient process to produce clean energy in the form of green hydrogen, synthetic natural gas (methane) and liquid chemicals. The products of biomass gasification process can be employed for energy production in a more efficient way.

The modelling of biomass gasification enables the optimization of the process designs, but it is a challenge due to its high complexity. In most cases this process is treated with a black box approach where the sub-processes are neglected and only changes between the input and output are assessed. Here a model for prediction of the performance of a 100-kW dual bed fluidized biomass gasifier is derived and implemented. Detailed pyrolysis modelling is properly addressed, and this is believed to be a key factor of this approach and enables more accurate results. The proposed model and its basic assumptions were extensively validated on a range of operating temperature by conducting experiments using softwood pellets as fuel and fresh olivine sand as bed material.

To achieve the objective, experimental tests have been conducted and theoretical models have been developed. The results provide understanding of the conversion processes occurring in the different parts of the gasifier enabling optimization of the system under different conditions. The main achievements are summarized in the following:

- The fluid dynamics of the system, i.e. the distribution of gas and solids in different parts of the gasifier, the mixing of fuel with bed particles and the operational range at which the gasifier can be safely operated are calculated and validated against the experimental measurements.
- The main fuel conversion processes (devolatilization and char gasification) were studied thoroughly. The former through the literature and the latter by the experiments conducted in a thermogravimetric analyzer (TGA).
- Water gas shift reaction as the main and most important homogenous reaction in the process of biomass steam gasification has been investigated experimentally to obtain the proper kinetic parameters.
- A reactor model of the DFB gasifier system of TUW was developed using the findings from the experimental studies conducted previously, supported by additional data from literature. Simulations were performed to obtain the main outputs of the biomass

gasification process and the results have been validated with the experimental measurements.

The overall conclusion of this work is that the proposed model for the DFB gasifier is an interesting method to simulate the thermochemical conversion of biomass in the gasifier and this technology is very suitable for electricity production from biomass and waste. Further research on tar conversion processes is necessary as well as testing the flexibility of the model against various bed materials.

2. Introduction

The global energy scenario is showing a constant growth in demand, a phenomenon naturally linked to important issues such as the emission of greenhouse gases and the economic and environmental sustainability of our energy production systems. For these reasons, sustainable energy technologies, renewable energy sources and scientific research focused on the evolution of these techniques are becoming increasingly important.

One of the most widespread and easily available renewable energy sources is biomass: mainly agricultural crop residues and vegetable waste. In addition to the direct energy uses of biomass, such as combustion, there are a series of treatments and conversion methods that make it possible to obtain a more valuable fuel from the raw material. Within this study, gasification will be considered, a process that allows the generation of a synthesis gas mainly composed of H_2, CO, CO_2 and CH_4 from different types of biomass. Thermochemical conversion of biomass is a poly-generation process that can lead to production of heat, electricity, synthetic gas and synthetic chemicals such as methanol, Fischer-Tropsch diesel, gasoline and kerosene. The concept of polygeneration is shown in the Figure 1.

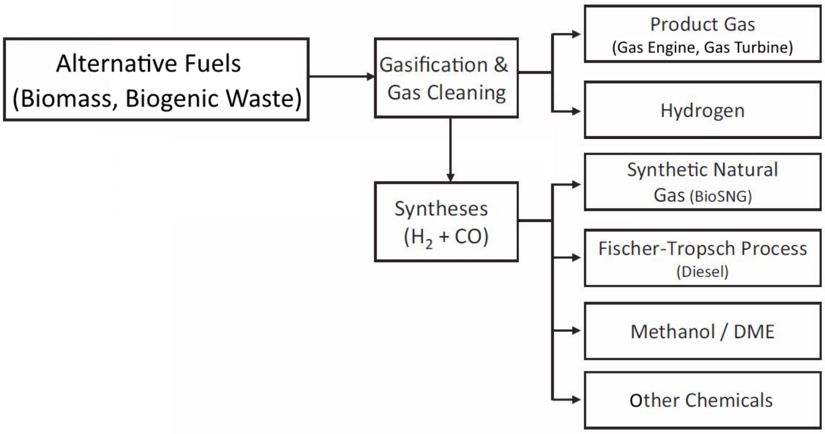

Figure 1: Polygeneration Concept[1]

In this work I focused on the circulating fluidized bed (CFB) gasifier of Technical University of Vienna (TUW) whose goal is to produce syngas from the gasification of biomass, with a series of syngas cleaning. For the different uses that can be made of the syngas produced by gasification it is often necessary to remove the main pollutants: the TAR. These are condensable hydrocarbons produced form gasification process which impose obstacle for the use of syngas in devices such as combustion engines and turbines. This problem becomes even

---

[1] Koppatz et al., 2011, p. 470

more relevant for the project that has been analyzed since the final product of gasification and post-treatments is intended for the supply of a fuel cell, a device that requires a very high purity of the supply gas. The tar content in the producer gas from gasification process in the CFB gasifier of TUW is further reduced in-situ with the circulation of bed material with catalytic activity.

In this study the behavior of CFB gasifier of TUW will be studied with olivine sand as bed material and softwood as fuel, in a wide range of operational temperature.

1.1 Definition of biomass

Biomass is defined in national legislation as the biodegradable fraction of products, waste and residues of biological origin from agriculture (including plant and animal substances), forestry and related industries, including fishing and aquaculture, mowing and pruning from public and private green areas, as well as the biodegradable part of industrial and urban waste. The term biomass includes a large quantity of extremely heterogeneous materials, in general this term means everything that has an organic, vegetable or animal matrix, which can be exploited for energy purposes.

Biomass is considered a renewable energy source since, if properly used, the rate of use does not exceed the regeneration capacity of plant formations. However, fossil substances and their derivatives are not to be considered biomass, because the regeneration time of these substances is far greater than the time of use.

Biomass represents a sophisticated form of solar energy storage: thanks to the photosynthesis process, plants can convert radiant energy into chemical energy and store it in the form of chains of carbon, oxygen and hydrogen.

It is therefore possible to derive energy from biomass through direct uses, such as combustion, or after transformation into solid, liquid or gaseous fuels that are then defined as biofuels.

Despite the direct combustion of biomass or that of the fuels it produces carbon dioxide, biomass is considered neutral for the purpose of increasing CO_2 emissions: the quantity of CO_2 thus generated is equal to that absorbed during its growth.

1.1.1 Classification of biomass

Biomasses for energy use, both directly and indirectly, can be divided into two categories: residual and non-residual. Non residual biomasses are grown specifically for energy purposes and can be divided into three types:

- Carbohydrate crops, with a high sugar content;

- Oil crops, characterized by a high content of usable vegetable oil directly or transformed into biodiesel;
- Lignocellulosic biomass crops, characterized by a high quantity of dry matter can be used in different types of conversion (combustion, gasification, pyrolysis ...)

The residual biomass, generally consisting of waste material coming from different activities, can thus be classified according to the category of origin:

- Agricultural: crop residues from agricultural activities and from dedicated crops of lignocellulosic species, oil plants for the extraction of oils and transformation into biodiesel, alcohol-producing plants for the production of bioethanol;
- Forest and agroforestry: forestry or agroforestry residues, use of coppice woods, etc;
- Zootechnical: zootechnical wastewater for biogas production;
- Industrial: residues from the wood and paper industries, as well as residues of the agri-food industry;
- Urban waste: residues from public green maintenance operations and the organic fraction of solid urban waste.

1.1.2 Characterization of biomass

The properties that best describes various types of biomass are humidity, chemical composition in, ash content and calorific value.

Since lignocellulosic biomass is the one that is of interest in the present work, the characteristic properties of softwood and hardwood are shown in the Table 1:

Table 1: Fuel properties and elementary composition of wooden biomass[2]

Property	Unit	Softwood pellets	Hardwood chips
Proximate Analysis			
Water content	wt-%	6.1	5.7
Residual char	wt-%$_{db}$	13.5	16.0
Volatile matter	wt-%$_{db}$	86.5	84.0
Lower heating value (dry)	MJ/kg$_{db}$	18.8	18.2
Lower heating value (moist)	MJ/kg	17.5	17.0
Ultimate analysis			
Ash content	wt-%$_{db}$	0.3	1.0
C, carbon	wt-%$_{db}$	50.2	48.8
H, hydrogen	wt-%$_{db}$	6.0	5.9
O, oxygen [a]	wt-%$_{db}$	43.4	44.1
N, nitrogen	wt-%$_{db}$	0.05	0.15
S, sulphur	wt-%$_{db}$	0.005	0.02
Cl, chlorine	wt-%$_{db}$	0.003	0.003

---

[2] Schmid et al., 2012, pp. 208-209

The heating value represents the heat that a unit of fuel at Standard or Normal conditions can produce by burning completely in the air; this parameter can refer to the weight or volume of fuel.

The higher heating value (HHV) is the quantity of heat that is made available due to the complete combustion at constant pressure of the unit mass of the fuel, when the products of combustion are brought back to the initial temperature of the fuel and of the oxidizer.

In most cases (apart from condensing boilers, condensation cogeneration engines, etc.), the combustion products are not returned to the initial temperature of the fuel and the oxidizer, so that the heat associated with condensation is mainly lost due to water vapor produced by combustion. Normally, not only is it difficult to reduce the temperature of the combustion products below the condensation point but the heat at that temperature is also unusable, therefore we consider the lower heating value (LHV) where the water remains in the vapor phase. The overall amount of heat made available is therefore smaller.

Heating value can also be calculated based on the elemental composition of the biomass using the famous equation of Boie:

$$HHV=34.8\ C + 93.9\ H + 10.5\ S + 6.3\ N - 10.8\ O$$

This equation shows a maximum error of 4% to compare with experimental results.

Below is a summary table of the heating values of the main fuels in common use:

Table 2 Heating values of common fuels

Fuel	LHV [kJ/kg]	Density [kg/NL]
Dry wood	18600	0.4000
Coal	31395	1.3000
Char	34032	2.2670
Crude oil	41860	0.8500
Gasoline	42697	0.8600
Benzine	43953	0.7400
Liquid LPG	46046	0.5100
LPG gas	46046	0.0019
Liquid methane	48179	0.4256
Methane gas	48179	0.0007
Liquid hydrogen	120667	0.0710
Hydrogen gas	120667	0.0001

Each type of biomass is composed of some water, commonly called humidity or moisture content, and a part of dry substance. Humidity tends to bring itself into balance with the environment, so its content can change radically; for this reason, the properties of the biomass tend to be expressed on the dry (without ash) basis, rather than on the sample as it is which includes humidity.

The humidity contained intrinsically in the biomass disadvantages the combustion as it reduces the quantity of combustible substance and causes the waste of part of the heat developed to obtain complete drying. Generally, the humidity negatively influences the heating value, the performances in the system, the transport and drying costs. The maximum concentration of water that allows the use of biomass as a fuel is around 30-40%. Beyond this limit, the heat required for the evaporation of the water is greater than the intrinsic energy of the fuel: in these cases, the combustion would not be sustained if it did not supply energy from the outside.

The composition and humidity are fundamental characteristics to define the most suitable type of treatment for each type of biomass; to this end, the parameters described are then evaluated using the humidity rate and the C / N ratio, carbon content on nitrogen content in the biomass composition.

1.2 Conversion processes

Biomass conversion processes can be divided into two categories: thermochemical and biochemical processes. The thermochemical conversion processes are based on the action of heat that allows the chemical reactions necessary to transform matter into energy; biochemical conversion processes allow to obtain energy through chemical reactions due to the presence of enzymes, fungi and other microorganisms that are formed in the biomass maintained under particular conditions.

As already mentioned, the parameters that determine the choice of the type of process to be adopted for the treatment of a type of biomass are the C / N ratio and humidity. In particular, for biomasses with C / N values> 30 and a humidity rate lower than 30% the most suitable process is the thermochemical one; in this case the heating value of the biomass that is influenced by its humidity takes on great importance. For this reason, if you choose to treat biomass with thermochemical processes, it is necessary to provide a preliminary drying phase.

1.2.1 Thermochemical processes

As already illustrated, the thermochemical conversion processes are based on the action of heat that allows the chemical reactions necessary to transform into energy, and can be used for cellulose and wood products and residues in which the C / N ratio has values higher than 30 and the moisture content does not exceed 30%. An illustrative graph of the biomass gasification steps is shown in the Figure 2:

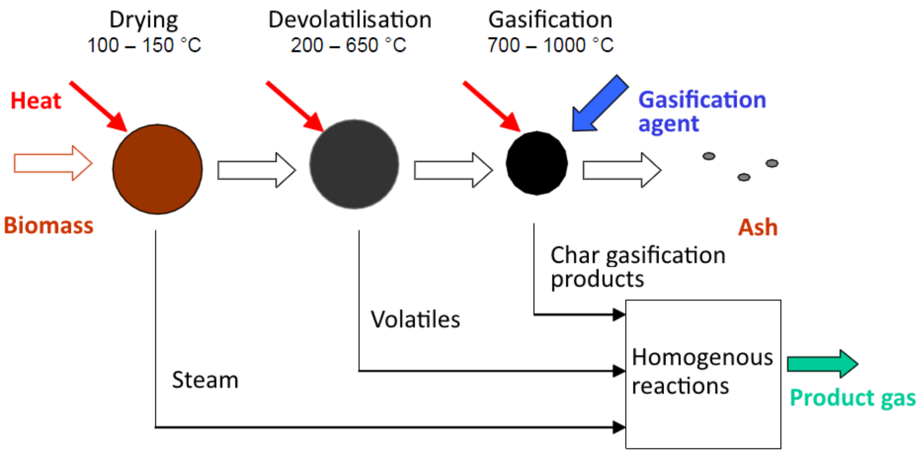

Figure 2: Process during gasification of a single particle3

The most suitable biomasses to undergo thermochemical conversion processes are:

- Wood and all its derivatives (sawdust, shavings, etc.)
- Ligno-cellulosic crop by-products (cereal straw, pruning residues, etc.)
- Processing waste (husks, chaff, shells, hazels, etc.)

The main thermochemical processes are combustion, gasification, pyrolysis and carbonization (torrefaction). Except combustion, the other processes are highly endothermic. One main difference in these processes are the amount of oxidizing agent provided. In absence of oxidizing agent, the process is called pyrolysis. With stoichiometric or higher value of oxygen provided, it’s combustion. Torrefaction and gasification lye in between. These phases of the thermochemical conversion are shown in the Figure 3:

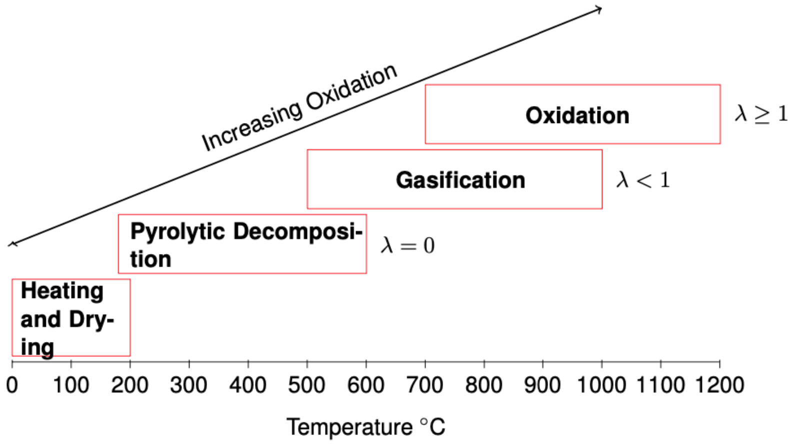

Figure 3 Phases of thermochemical conversion

---

[3] Kaltschmitt et al., 2016, pp. 668

The most important reactions happening during processes of gasification and combustion are listed in the Table 3 below, and the thermochemical conversions will be described in the following.

Table 3: Important reactions of gasification and combustion[4,5]

Name of reaction		Enthalpy	
Heterogeneous reactions (gas-solid)			
Oxidation of carbon	$C + O_2 \rightarrow CO_2$	Highly exothermic	*Eq. 2.1*
Partial oxidation of carbon	$C + \frac{1}{2}\,O_2 \rightarrow CO$	Exothermic	*Eq. 2.2*
Heterogeneous water-gas reaction	$C + H_2O \rightarrow CO + H_2$	Endothermic	*Eq. 2.3*
Boudouard reaction	$C + CO_2 \rightarrow 2\,CO$	Endothermic	*Eq. 2.4*
Hydrogenation of carbon	$C + 2\,H_2 \rightarrow CH_4$	Slightly exothermic	*Eq. 2.5*
Generalised steam gasification of solid fuel (bulk reaction)	$C_xH_yO_z + (x-z)H_2O \rightarrow x\,CO + \left(x - z + \frac{y}{2}\right) H_2$	Endothermic	*Eq. 2.6*
Homogeneous reactions (gas-gas)			
Oxidation of hydrogen	$2\,H_2 + O_2 \rightarrow 2\,H_2O$	Highly exothermic	*Eq. 2.7*
Water-gas shift	$CO + H_2O \leftrightarrow CO_2 + H_2$	Slightly exothermic	*Eq. 2.8*
Methanation	$CO + 3\,H_2 \leftrightarrow CH_4 + H_2O$	Exothermic	*Eq. 2.9*
Generalised steam reforming of hydrocarbons	$C_xH_y + x\,H_2O \rightarrow x\,CO + \left(x + \frac{y}{2}\right) H_2$	Endothermic	*Eq. 2.10*
Generalised dry reforming of hydrocarbons	$C_xH_y + x\,CO_2 \rightarrow 2x\,CO + \frac{y}{2}\,H_2$	Endothermic	*Eq. 2.11*

Combustion

It is the simplest thermochemical process and consists in the complete oxidation of the fuel by the oxidizer; the reaction produces mainly H_2O and CO_2 products and and is highly exothermic. Usually the combustion is carried out inside furnaces, devices that allow the exchange of heat between the combustion fumes and a process fluid, for example water. Biomass combustion takes place in four phases:

- Heating and drying (up to 200 ° C);
- Pyrolysis (225 ° C ÷ 500 ° C): leads to the formation of gases, tar and carbon compounds in almost pure state;
- Gas phase (500 ° C ÷ 750 ° C): burns previously formed gases;
- Oxidation reaction of carbon.

---

[4] Schmid, 2014, p. 60

[5] Kaltschmitt et al., 2016, pp. 669

The furnaces used for combustion can be of different types: rotary drum oven, controlled air, grid and fluid bed.

Torrefaction

It is a pretreatment of the plant material which consists in the thermochemical conversion of the biomass in order to improve its characteristics through the transformation of the molecules of wood products into coal type; this process takes place in the presence of heat which allows the elimination of water and volatile substances from the biomass.

Pyrolysis

It is a process that takes place at high temperatures, between 400 and 800 ° C, in complete absence or with very small quantities of oxidizing agents. Under these conditions the biomass is thermochemically degraded giving rise to gaseous, liquid and solid products and their yields are depending on the methods used (fast, slow or conventional pyrolysis) and the parameters of the reaction.

Gasification

Solid, liquid and gaseous pyrolysis products are forced to further reactions by increasing the heat level. Gasification is a highly endothermic reaction which requires heat to proceed. The required heat can be either provided internally (autothermal) with oxidizing part of the products, or externally (allo-thermal) where the heat is generated in another reactor and transported for the gasification to occur.

The process gives a gaseous fuel, called producer gas (PG), as a product. The PG is mainly composed of H_2, CO, CO_2, CH_4 and H_2O accompanied by ash and hydrocarbons in the form of tars. The composition of the generated PG varies greatly depending on the type of gasifier, the type of gasification, the biomass used and the operating temperatures.

In case of autothermal gasification, an oxidizing agent is needed which can be either pure oxygen or air. Pure oxygen has a drawback of high cost but offers a producer gas free of nitrogen with high heating value. Air on the other hand is a free oxidizing agent but due to its high content of nitrogen, delivers a producer gas diluted with N_2 and therefore offers lowers heating value.

The types of gasification are summarized:

- Gasification in air: treating the biomass with a quantity of sub-stoichiometric air produces a syngas with low heating value mainly composed of H_2, CO and CO_2 and very diluted in inert N_2. This type of gas can be used in boilers and internal combustion engines.
- Oxygen gasification: using reduced quantities of pure oxygen, in sub-stoichiometric proportions, gasification produces a syngas with a high heating value.
- Steam gasification: not being diluted in inert nitrogen, the syngas produced by this gasification has a higher heating value than the one generated in the process in the air. But in this process, the heat must be generated externally and transported to the gasification reactor.

Here gasification process will be described in more details. This is the process that generates the syngas object of our study inside the fluidized bed reactor.

Gasification of biomass produces a gaseous fuel; this type of process has a series of advantages such as the practicality of generating a gaseous fuel rich in H_2 and/or CH_4 from solid material with low energy density. Furthermore, the raw material for gasification is generally waste material from vegetation so it is advantageous to exploit waste from agricultural production and other sectors. The technology of the gasification process is now consolidated as known and perfected over the years even if it is still evolving. As we will see later in the chapter, the gasification has several products among which, in addition to the syngas, there are tar: these are heavy hydrocarbons that form in the process of biomass devolatilization. The presence of these compounds constitutes a disadvantage because they are pollutants of the syngas and must be converted or removed and disposed of, even though they contain a notable share of energy.

Gasification occurs at high temperatures means either the heat must be provided or in the presence of an oxidizing agent which can be air or oxygen and can be also mixed with steam and/or carbon dioxide. The reaction that describes the steam gasification process for a biomass with a generic composition is the following:

$CH_{\alpha}O_{\beta}+H_2O \rightarrow x_1C+x_2H_2+x_3CO+x_4H_2O+x_5CO_2+x_6CH_4+x_7CH_xO_y$

The process takes place in four main phases:

Drying: occurs between 100 and 150 ° C, it is the phase in which the humidity contained in the biomass evaporates. The steam produced will be useful for subsequent gasification reaction;

Pyrolysis: occurs between 200 and 650 ° C, in this phase the biomass thermochemically decomposes to smaller and less complex molecules giving rise to gas, tar (heavy condensable hydrocarbons) and char (solid carbon residue); the process can take place both in total absence and in the presence of limited quantities of an oxidizing agent. The composition and the fraction of the reaction products depend on different conditions, such as the composition and size of the parent fuel, the heating rate and the peak temperature reached, as well as the residence time of the particle in the reaction phase;

Reduction gasification processes: between 650 and 1000 °C, it is the phase in which the pyrolysis products react giving rise to the final products; gasification occurs through a series of endothermic and exothermic reactions (overall endothermic) supported by the heat produced by the combustion of the char, tar and/or part of the producer gas. The composition of the syngas produced through the reactions strongly depends on the operating parameters such as the pressure and temperature inside the reactor, as well as on the particular gasifying agent chosen;

Oxidation processes: between 700 and 1200 ° C, in this phase the combustion of the char with heat generation takes place.

The main chemical reactions that take place during the gasification process have been already reported in the Table 3.

These reactions can be classified into two groups of heterogenous and homogenous reactions. Heterogenous reactions occur between the solid residual part of the biomass, namely char and other gases:

- Steam gasification of char:

$C+H_2O \rightarrow CO+H_2 \quad \Delta H^{850^\circ C}=135.8\ kJ/mol \quad \Delta G^{850^\circ C}=-25\ kJ/mol$

It is the reaction that solid residual carbon of the biomass after devolatilization process reacts with steam to produce combustible gases of CO and H_2. This is an endothermic reaction and is favored at low pressures and at high temperatures.

- Reaction of Boudouard:

$C+CO_2 \rightarrow 2CO \quad \Delta H^{850^\circ C}=170\ kJ/mol \quad \Delta G^{850^\circ C}=-26\ kJ/mol$

The carbon dioxide in the reactor reacts with the char to produce carbon monoxide; this reaction is favored at high temperatures and low pressures and has a very low kinetics and is also highly endothermic.

- Methanation reaction:

$C+2H_2 \rightarrow CH_4 \quad \Delta H^{850^\circ C}=-91\ kJ/mol \quad \Delta G^{850^\circ C}=33\ kJ/mol$

It is the exothermic reaction of methane formation which can be accelerated by nickel-based catalysts at high temperatures and pressures. The reaction is favored at low temperatures and high pressures, in fact in the gasification process the inverse reaction of methane decomposition prevails.

Char can also react with oxygen to produce either carbon monoxide or carbon dioxide, but since the focus of this work is on steam gasification of biomass, they are avoided here.

In the Figure 4, equilibrium constant of the mentioned heterogenous reactions are reported:

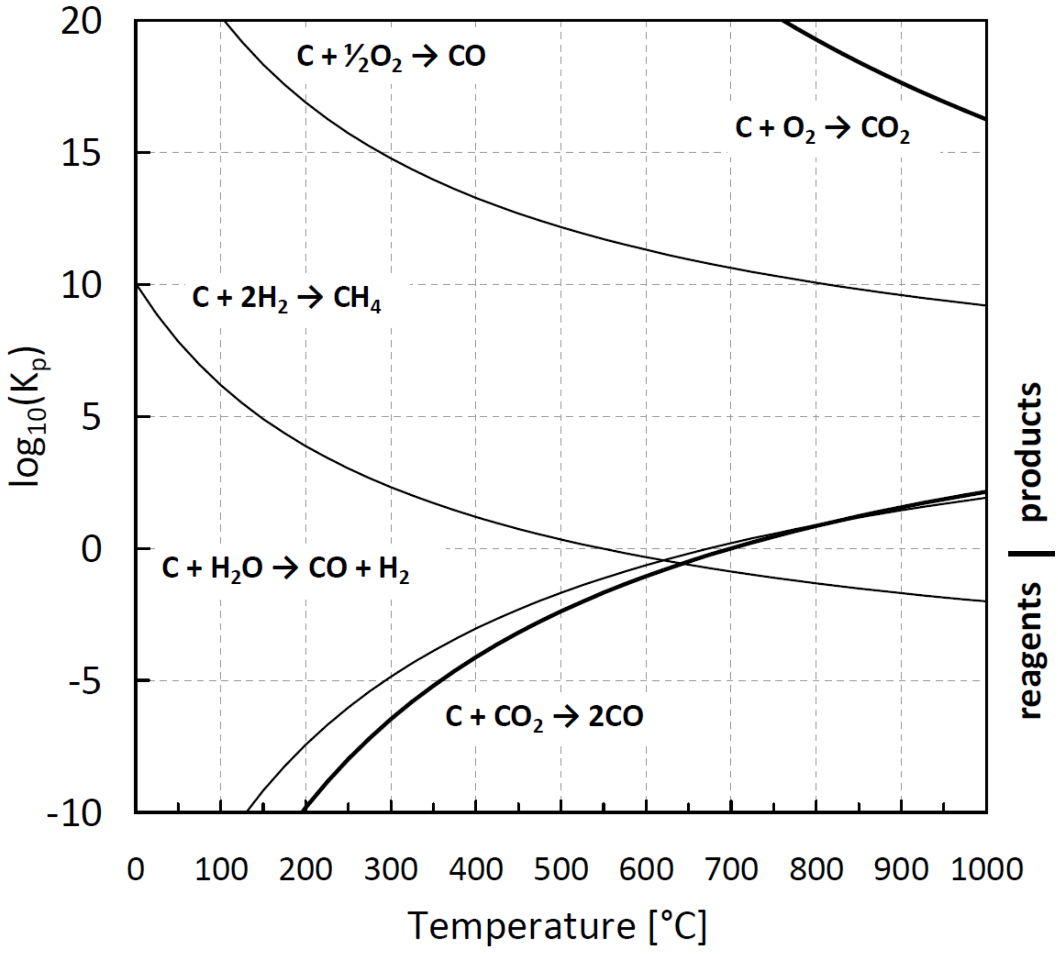

Figure 4 Equilibrium constant of heterogenous reactions occurring during gasification process

Important homogenous reactions in the process of gasification are methane steam reforming, water gas shift reaction, and reforming the tar vapors with steam.

- Water gas shift (WGS) reaction:

$CO+H_2O\leftrightarrow CO_2+H_2$ $\Delta H^{850^\circ C}$=-34 kJ/mol $\Delta G^{850^\circ C}$=0.9 kJ/mol

The water gas shift reaction is one of the most important in the process of hydrogen production by gasification, since it allows to strongly modify the composition of the outgoing syngas. Carbon monoxide can in fact react with steam in a slightly exothermic way to form hydrogen and carbon dioxide. This reaction is thermodynamically unfavorable at high temperatures due to its exothermicity.

- Reaction of methane steam reforming:

$CH_4+H_2O \leftrightarrow CO+3H_2$ $\Delta H^{850^\circ C}$=226 kJ/mol $\Delta G^{850^\circ C}$=-58 kJ/mol

It is a strongly endothermic reaction, favored in fact at high temperatures and low pressures. In the gasification process it is an important reaction for the production of a H_2-rich syngas.

The methane reforming reaction is greatly influenced, in addition to the temperature, by the steam to biomass ratio. Furthermore, methane can also be reformed by CO_2.

In the Figure 5, equilibrium constant of the main possible homogenous reactions in the process of gasification including reactions with oxygen are reported:

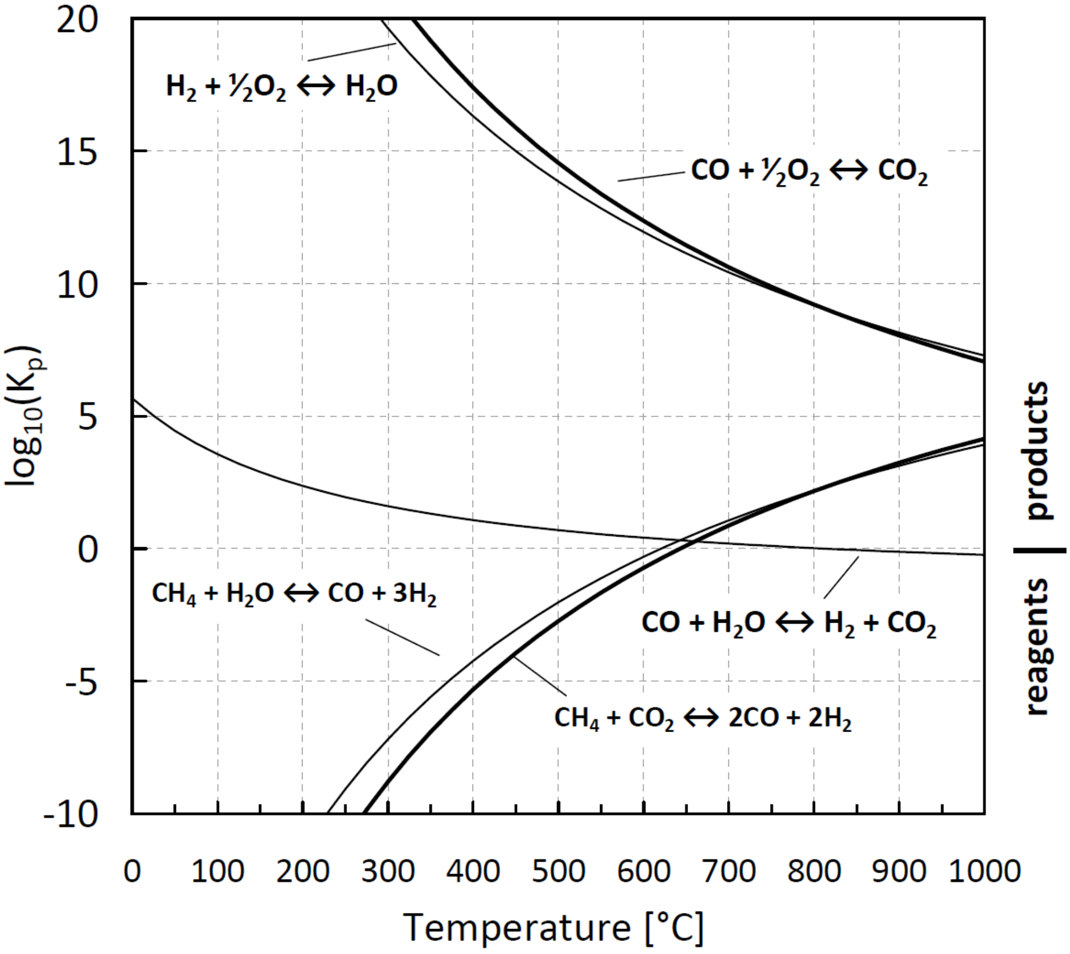

Figure 5 Equilibrium constant of homogenous reactions occurring during gasification process

- Steam reforming reaction of the tar:

$C_mH_nO_p+H_2O+heat \rightarrow CO+H_2$

The TARs are hydrocarbons of high molecular weight, therefore they too, in the presence of steam, react to produce carbon monoxide and hydrogen in quantities that depend on the particular reacting chemical species. Steam reforming of tar and steam methane reforming, these are very slow reactions that require the use of catalysts to shift the balance towards the generation of products.

1.3 Gasification technologies

The gasification process can take place in different types of reactors that differ in configuration and operation. There are three main categories of gasification reactors: fixed-bed, fluid-bed and entrained flow reactors; this subdivision is based on the greater or lesser movement of the material inside the reactor. The Figure 6 shows the configurations of the main categories of gasification reactors:

- Fixed bed gasifiers:
    - Updraft
    - Downdraft
- Fluidized bed gasifiers:
    - Bubbling fluidized bed (BFB)
    - Circulating fluidized bed (CFB)
    - Dual fluidized bed (DFB)
- Other types:
    - Entrained flow

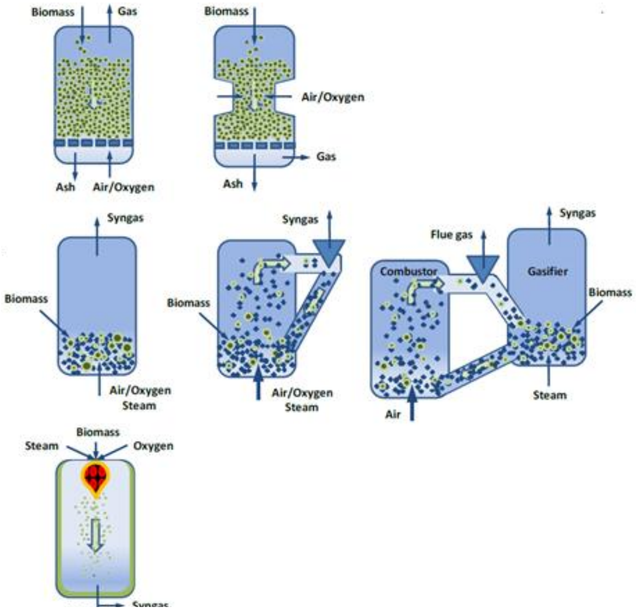

Figure 6 Different types of gasifiers

Fixed bed gasifiers

Fixed bed gasification reactors are characterized by the stationary nature of the internal material; they consist of a grid in the lower part on which the biomass is put and the oxidizing agent passes; the grill also serves for the discharge of the ashes. This type of gasifier works at temperatures between 800 and 1300 °C and with powers generally lower than megawatt scale. Fixed bed gasifiers are divided into two configurations:
updraft (countercurrent) and downdraft.

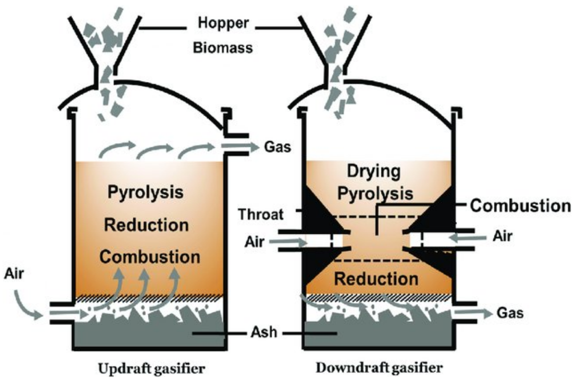

Figure 7 Fixed bed gasifiers updraft and downdraft

In the Figure 7 we can observe the differences between the two categories of gasifiers: in the updraft configuration the biomass enters from the upper part of the reactor while the oxidizing agent enters from below. The gasification phases take place along the height of the reactor, establishing a profile of increasing temperatures from the top to the bottom of the reactor; in the lower part the char combustion takes place which provides the heat necessary for endothermic reactions. The combustion gases then react with the pyrolysis products in the gasification zone to give rise to the syngas; the latter moving upwards pyrolysis and dries the biomass to finally exit the upper part of the gasifier.

This configuration has a series of advantages: the constructive simplicity of the gasifier, the high residence time of the biomass inside the reactor which therefore involve a higher conversion rate, the contextual exploitation of the heat of the syngas itself which comes out of the reactor at low temperatures and the possibility of using biomass with high moisture content. Given these advantageous features, this type of reactor also has some negative aspects: it is necessary to use air as an oxidizing agent, consequently the product syngas has a low LHV (5 MJ / Nm^3); moreover, in this type of reactor, the production of tar that comes out together with the gas flow is very high.

The other type of configuration is the downdraft, in which the flows of gas and biomass are in aligned and both move towards the bottom of the reactor. In the central part of the reactor there is a narrowing zone at which the oxidizing agent that gives rise to combustion enters; in the lower part instead the reduction reactions take place and therefore the formation of the syngas. The heat generated in the oxidation phase is supplied both to the pyrolysis area, located above, and to the lower reduction area. Therefore, a high temperature zone is created which facilitates the cracking of tar produced by pyrolysis. These reactions greatly reduce the tar content in the syngas which, unlike the updraft configuration, is very low in output. However, the gas leaves the reactor at high temperature and therefore its heat is not efficiently exploited for endothermic reactions and for the drying of biomass; for this reason, in this type of reactor it is necessary to use biomass with reduced moisture content. Furthermore, the conversion of the carbon is low and there are high amounts of particulate in the outgoing gas.

Fluidized bed gasifiers

In this type of gasifier, the main characteristic is the presence of a solid granular material moved by a current of gas; the system thus generated has characteristics similar to those of a liquid and, therefore, allows a good mixing. For these reasons this system has the ability to standardize temperatures and concentrations within the reactor, a characteristic that involves a high reaction speed and therefore consistent conversion values.

Fluidized bed gasifiers therefore exploit these characteristics to increase the efficiency of gasification; the biomass, reduced to a maximum size of 20 mm, is then mixed with the material making up the bed, generally inert such as sand, olivine or dolomite with a diameter of 0.5 ÷ 1 mm. The inert bed is then fluidized by the flow of oxidizing agent or by pressurized steam. In this type of reactor the necessary heat is provided by the combustion of the char that is recirculated in the reactor; the pyrolysis phase occurs very quickly and is immediately followed by the gasification phase; operating temperatures are between 750 and 900 ° C. Fluidized bed gasifiers therefore have many features that enhance their performance; however the presence of TAR is higher than the downdraft configuration, for this reason it is necessary to have technologies for removing or converting TAR downstream of the reactor. As will be analyzed below, ceramic catalytic filters are a very efficient method for this purpose.

In the bubbling fluidized bed configuration (BFB) the speed of the gasification agents is such as to avoid the entrainment of particles outside the reactor. In this configuration two zones can be distinguished: at the bottom there is a dense bed, and at the top a diluted area called freeboard. Inside the bed, bubbles of the reaction gas are generated, which on the surface guarantee a continuous mixing of the solid phase.

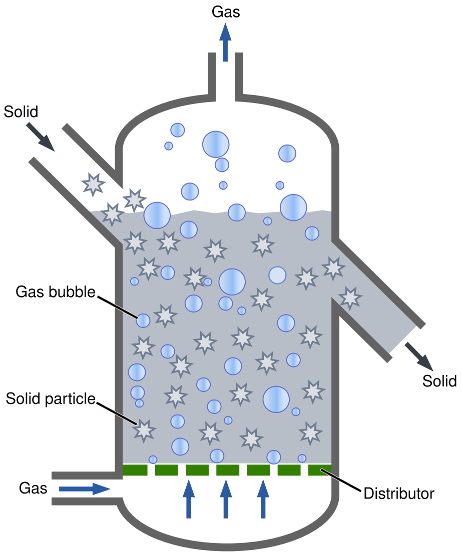

Figure 8 Bubbling fluidized bed gasifier (BFB)

The advantages presented by this configuration are many: the excellent temperature control, the high stability of the composition of the produced syngas and the almost total conversion of the carbon, up to 95%. The geometry of this type of reactor is very compact and also allows the addition of hot conditioning systems in the upper part of the reactor. However, there is a high presence of particulate in the gas which therefore necessarily involves conditioning treatments of the outgoing syngas.

Another type of configuration is the recirculating fluidized bed (CFB); in this gasifier the speed of the gasification agent is such as to drag particles out of the reactor, the outgoing gas flow is then filtered by a cyclone and the separated material is then reinserted in the lower part of the bed. The recirculation of material thus established allows to fluidize the entire reactor and therefore obtain temperatures up to 1200 ° C. A configuration is shown in the Figure 9 below:

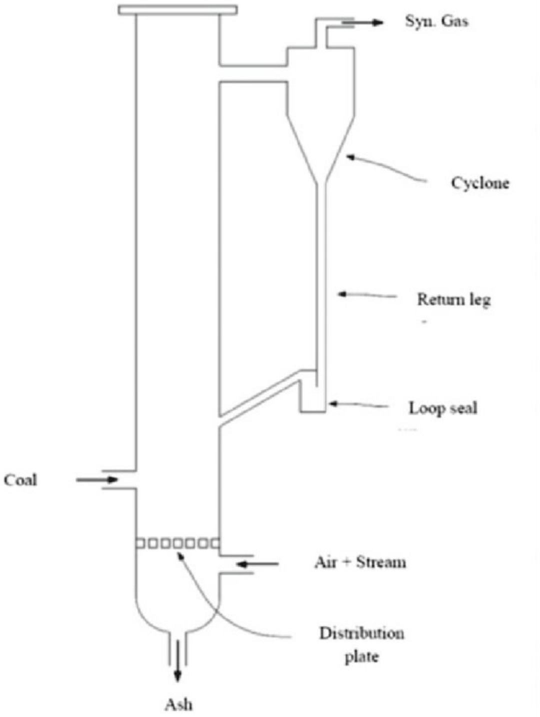

Figure 9 Circulating fluidized bed gasifier

However, a greater height of the reactor is necessary to guarantee the same residence time of the biomass despite the higher speed of the fluid. Further difficulties are encountered with regard to the biomass that must be introduced into the reactor with a very small size, furthermore there may be problems linked to the agglomeration of the ashes due to high operating temperatures.

A particular configuration of gasifiers is that with a double fluidized bed, this includes two chambers: one for gasification and the other for combustion. In the gasification chamber, biomass and steam are inserted, while in the combustion chamber, air or alternatively pure oxygen is inserted. The two reactors are connected to generate a recirculation of char and bed material; in this way the char feeds the combustion and the recirculation of the material involves a mixing such as to provide the necessary heat in the gasifier for endothermic reactions. Figure 10 shows a schematic view of such gasifiers:

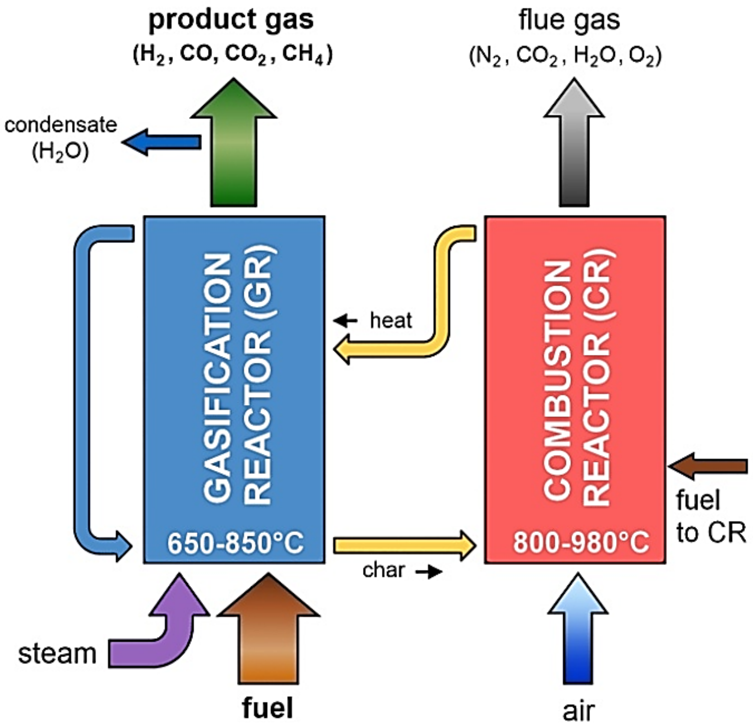

Figure 10 Dual Fluidized bed gasifier

To ensure high biomass residence times, the gasifier uses a reactor with a hot-bed configuration with temperatures around 850 ° C. For the combustor, on the other hand, given the high kinetics of the reactions, a circulating fluid-bed reactor with temperatures around 950 ° C can be used. In this dual reactor configuration, very high efficiency values can be achieved and a syngas can be generated with the highest heating value among all configurations, such as 11 MJ / Nm^3.

In dual fluidized bed gasifiers, combustion and gasification reactors can have different fluidization regimes. Usually the combustion reactor is in fast circulating bed and since the bed is pushed towards the upper part of the reactor, a cyclone is installed to separate the dust contained in the gas. A portion of the combustor bed, which is located at temperatures close to the combustion one, enters the gasification chamber and transfers the heat to the fluidized bed. The syngas thus produced and extracted from the upper part of the gasification reactor.

An example of this type of reactor, called fast external fluidized bed, is present at the 8 MW plant in Gussing (Austria); the external circulation reactor is used here in a cogeneration plant for the combined production of electricity and heat with an overall efficiency of 81%.

The schematic view and the concept of the Gussing plant are shown in the Figure 11:

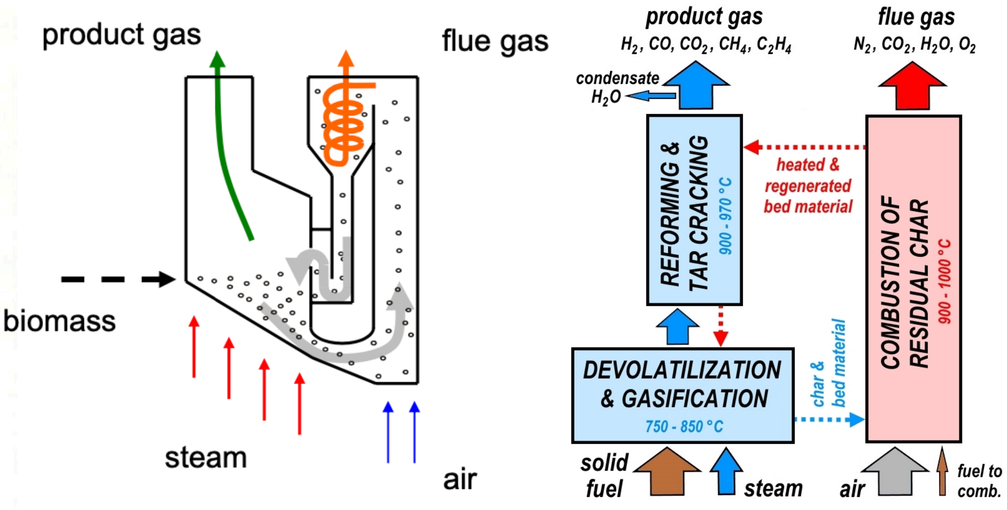

Figure 11 Circulating fluidized bed gasifier with external circulation (Gussing, Austria)

Entrained Flow Gasifiers

Entrained flow gasifiers use pure oxygen or superheated steam and biomass with a very small size, between 50 and 100 mm. The biomass is being inserted in co-current with the gasification agents. The main feature of this type of reactor is to work at very high temperatures, even above 1220 ° C with the advantage of obtaining a syngas with almost zero tar content. However the disadvantage of working at these high temperatures is to have the ashes in the liquid state and therefore difficult to remove. This configuration also involves the output of the syngas at a very high temperature with which it would be preferable to carry out a thermal recovery, a procedure that however involves system complications.

Comparison of the various types of gasifiers

On the basis of the use of the syngas produced by the gasification, the choice of the technology to be adopted may fall on the different categories of gasifiers explained earlier, each of which presents pros and cons which can lead to the evaluation of the best solution. The following table shows the various advantages and disadvantages for the fixed-bed and fluid-bed categories; for the double fluid bed category the characteristics are similar to those described for the fluidized bed.

Table 4 comparison between fixed bed and fluidized bed gasifiers

Type of reactor	Fixed bed		Fluid bed
	(-) limited scale-up	(-) difficult scale-up	(+) scale-up feasible
Technology	(-) limited heat exchange		(+) good heat exchange
	(-) uneven temperature distribution; possibility of hotspot		(+) good temperature distribution; no hotspot

	(-) possible melting of the ashes (-) low specific capacity		(+) good solid-gas contact (+) high specific capacity
	(-) long warm-up time at start-up		(+) easy startup and shutdown; very fast heating
Fuel supply	(+) possibility of using large particles (<100 mm)		(-) biomass particle of limited size (<50 mm)
	(+) possibility of using raw materials with high ash content		(+) tolerance to large variations in fuel quality
	(-) needs uniform sized pellets		(+) possible variations in the size
Gas cleaning	(+) low dust content	(+) low tar content	(-) high dust content
	(-) high tar content	(-) high tar content	(+) medium tar content

From the characteristics shown in the table it is therefore possible to deduce the ranges of applicability and potential of the various technologies: based on the excellent qualities of heat exchange, temperature distribution and specific capacity, fluidized bed systems can be used for larger sizes. Fixed bed systems, on the other hand, have the quality of being simpler and more manageable, and are more suitable in situations where biomass cannot be treated at the entrance. A classification based on the thermal power of the various gasifiers is shown in the Figure 12:

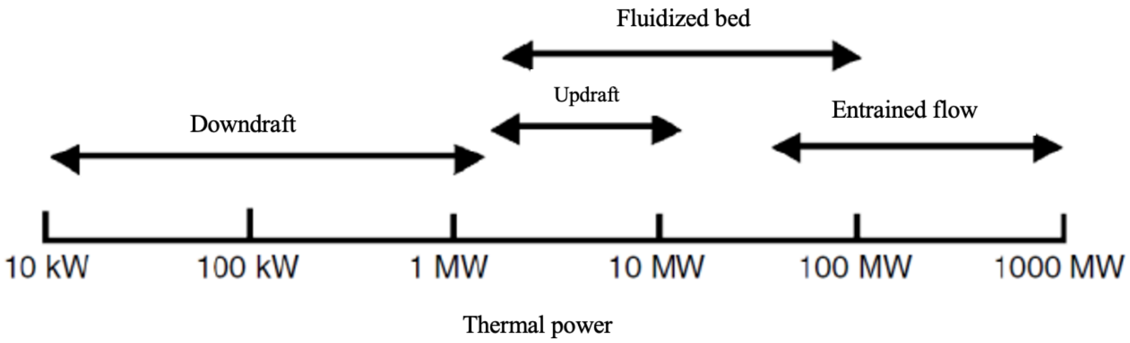

Figure 12 Range of applicability of the different gasification technologies

A summary chart of tar production based on the gasification technology used is also reported in the Table 5.

Table 5 TAR content for different gasification technologies

Type of gasifier	Average concentration of tar in product gas (g/Nm^3)	TAR content (% of the biomass's weight)
Fixed bed downdraft	<1	<2
Fluidized bed	10	1-5
Fixed bed updraft	50	10-20
Entrained flow	Negligible	Negligible

As can be seen from the table, downdraft and entrained flow fixed bed technologies are the most advantageous regarding the reduced tar content in the producer gas. The updraft fixed bed gasifiers on the other hand have a very high tar production and are therefore not advisable from this point of view. As far as fluidized bed technology is concerned, the tar content is slightly higher than that of the downdraft technology, but still acceptable for applications with power above megawatt.

Gasification products

The main products of the gasification process are permanent gases, tar, char and ash. Combustible permanent gases are the desired products therefore the rest of the products must be either reformed or removed from the gas stream. The ashes are the simplest residue of gasification to remove; for the removal of tar and particulate, mechanical and chemical treatments are required. In the following paragraphs, all the gasification products and methods for removing unwanted components will be further discussed.

Gas producer or syngas

Gas producer or syngas is the main product of gasification, it is a synthesis gas mostly composed of H_2, CO, CO_2, CH_4 and H_2O. Its calorific value varies according to the method of gasification and to the type of gasification agent; the range between which varies is between 4 and 13 MJ / Nm^3. The following table shows indicative values of syngas composition based on the gasifying agent.

Table 6 product gas composition based on gasification agent

Gasification agent	Temperature ˚C	H_2%	CO%	CO_2%	CH_4%	N_2%	H_2O%
Air	780-830	5-16	10-22	9-19	2-6	42-62	11-34
Steam	750-850	38-56	17-32	13-17	7-12	0	52-60
Steam+O_2	785-850	14-32	43-52	14-36	6-8	0	38-61

The Table 6 shows that the composition of the product gas varies consistently with the type of gasifying agent used. In particular the production of hydrogen and that of methane are maximized using steam as a gasifying agent. Furthermore, in the case of gasification with steam and with steam and oxygen the percentage of N_2 is equal to zero, this allows the formation of a producer gas less diluted in inert gas and therefore characterized by a greater heating value.

Char

The char is a solid residue of the gasification that composed mainly of carbon (85-95%) and ash, volatile hydrocarbons, hydrogen and oxygen. Due to its composition the char is characterized by a rather high LHV, of around 32 MJ / kg. The char coming from the gasification of different types of biomass has heterogeneous porosity characteristics which therefore differentiate the behavior and reactivity of this gasification product. The main reactions in which the char takes part inside the gasifier are the following:

$Char+O_2 \rightarrow CO_2+CO$

$Char+H_2O \rightarrow H_2+CO$

$Char+CO_2 \rightarrow 2CO$

The reactions described are fundamental to provide the heat necessary for the gasification processes of the syngas components.

TAR

The term tar indicates the heavy condensable hydrocarbons produced by pyrolysis and gasification reactions. Tar is one of the major unwanted products of gasification; it is considered a pollutant since it is present in the gaseous state syngas but at low temperatures it condenses to a very viscous liquid state which can therefore create problems of clogging of the components downstream of the gasifier. In fact, for the use of product gas in internal combustion engines or turbines, the tar must necessarily be eliminated.

The definition of tar provided by the International Energy Agency (IEA) includes in this category all the hydrocarbons with greater molecular weight than benzene. The tar are generated by the depolymerization of the biomass components: cellulose, hemicellulose and lignin. Based on their formation, the tar are divided into primary, secondary and tertiary tar.

- *Primary TARs*: they are generated at temperatures between 20 and 500 ° C from the direct decomposition of hemicellulose, cellulose and lignin. This process generates the "wood-oil" which consists of oxygenated compounds and organic condensable primary molecules, such as acids, sugars, alcohols, ketones, aldehydes, phenols and furans.
- *Secondary TAR*: they are generated at temperatures above 500 ° C from a recombination of primary TARs which at these temperatures reorganize themselves into heavier molecules such as phenols, alkenes and ethylene hydrocarbons.
- *Tertiary TARs*: at temperatures above 500 ° C the primary TARs disappear and tertiaries are formed, divided into alkyl compounds (methyl-naphthalene, toluene and idene) and polycyclic aromatic hydrocarbons (PAH) (benzene, naphthalene, acenaphthylene, anthracene and pyrene).

Furthermore, the TAR can be divided into five different classes based on their chemical-physical properties of solubility and condensability.

The following graph in the Figure 13 shows, as described above, the formation of the different TAR categories as the temperature changes.

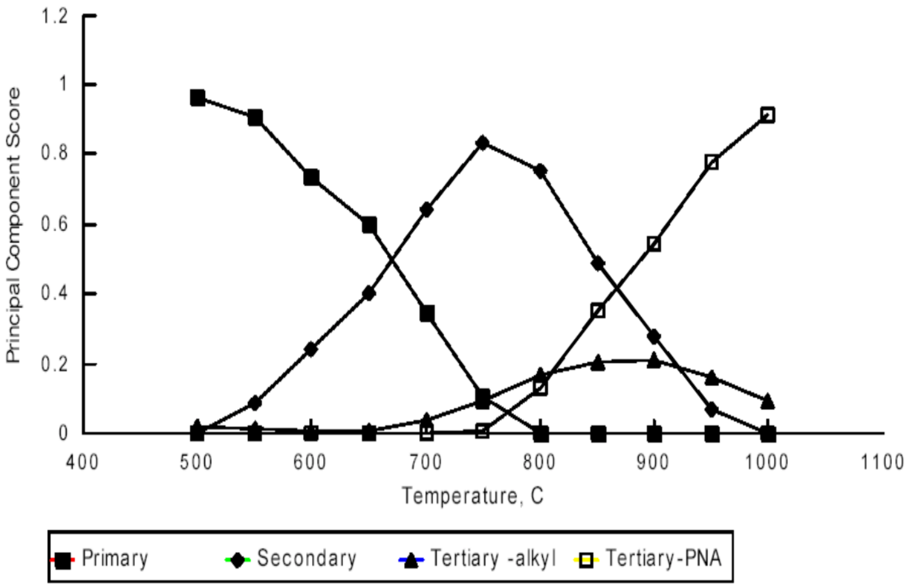

Figure 13 Formation of different TAR classes according to temperature (Ahrenfeldt, Henriksen, Gøbel, & Fjellerup, 2005a)

As can be seen from the graph, for temperatures lower than 700 ° C, the primary TARs generate the secondary TARs, in fact their trends are opposite. At higher temperatures the disappearance of the primary TARs and the formation of the tertiary ones is noted.

From the biomass gasification processes it is found that the tar that are mostly formed, and that therefore remain in the syngas, are benzene, toluene and hydrocarbons with 1 aromatic ring, phenols and, to a lesser extent, naphthalene. In generally negligible proportions, 3 and 4 aromatic ring hydrocarbons are also formed.

The problems caused by these compounds are therefore of various nature: on a technical level a syngas containing tar is unusable in engines or turbines due to the condensation and clogging problems mentioned above; moreover the health problems related to these compounds that possess toxic and cancerous properties and resist in the environment for very long times before degrading are not negligible.

For this series of reasons, the problem of the presence of tar is very important and their removal becomes a necessary.

Particulate

Particulate matter is another unwanted product of gasification, it is in the form of a black powder and consists of an agglomeration of carbon particles and fly ash which is carried by the gas flow and taken outside the reactor. The diameter of these particles varies between a few hundred micrometers and a few micrometers. The production of particulate matter depends on the different types of gasifier, in any case it can reach concentrations that seriously compromise the operation of internal combustion engines and turbines. For these reasons it is necessary to have components downstream of the gasifier suitable for removing the particulates, for this purpose the ceramic filters and the cyclone are in fact provided, thanks to which the particulate is effectively separated from the syngas.

Ashes

The heavy ashes represent the solid residue of the gasification and combustion reactions of the char. The extent of their presence and their composition mainly depend on the type of biomass used. Unlike the volatile ashes that are dragged out of the reactor together with the gas stream, the heavy ashes accumulate. The phenomenon of ash fusion may occur for certain types of biomass and operating temperatures: in these cases the problem is the agglomeration and sintering of the ashes which, by depositing on the bottom of the reactor, can cause blockages at the passage of the gasification agents and altering the fluidization of the bed.

In the next chapter, the fluid dynamic of the gasifiers will be discussed.

3. Fluid-dynamics of CFB gasifier of TUW

Introduction

The term circulating fluidized bed (CFB) has been common since 1970s, although the technology has been originated in 1940s for catalytic processes (Squires, 1994) and later in 1960s has been used for gas-solid processes (REH L, 1971).

In this concept, particles entrained at a considerable flux from a tall main reactor or "riser" and will be separated via cyclones or gravity separator from the carrying fluid and will be returned to the riser forming a recirculation loop. In the CFB concept developed at TUW (Johannes Christian Schmid, 2016), the particles go through the second reactor (Gasification Reactor – GR) to provide the necessary heat for the overall endothermic reactions that are occurring there. The thermal capacity of the CFB gasifier of TUW is 100 kW. The riser works as a combustion reactor and is abbreviated as CR throughout this work.

In order to understand the conversion of fuels in the CFB gasifier of Vienna, represented in the Figure 14 (present at TUW laboratory), and to select the proper operating conditions, the flows of gas and solids in the system need to be characterized. Four main aspects need to be studied:

- Characterization of the bed material particles
- Minimum fluidization velocity
- Fluidization velocity and gas flow rates
- Distribution of solids along the system

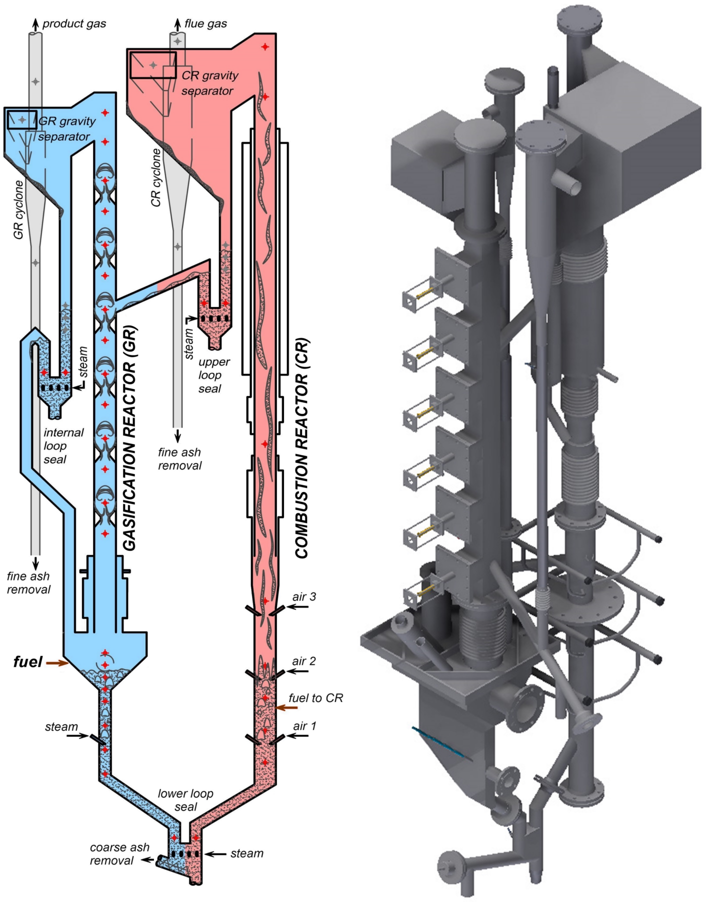

Figure 14 Reactor system of the novel 100 kW gasification facility of TUW

The minimum fluidization velocity is a basic parameter that needs to be determined in order to study the fluid-dynamics, determining the range of gas velocities to be employed in the gasification and combustion reactor. The bed porosity is directly related to the bubble fraction (in bubbling bed regime), which is important for the mixing in the gas phase and thus for the rates of both gas-gas and gas-solid reactions. The bed porosity is also directly related to the fraction of the bed volume occupied by the solids, which means that if the bed porosity is known, the mass of solids in the bed can be calculated or vice-versa.

Expected outcomes of this chapter: calculation of the minimum fluidization velocity U_{mf} and superficial velocity at operational condition U_g (U_s), steam/air input at operational condition Q_{gas}, axial voidage in the CFB ε, particle distribution in the CFB, gas residence time in/out of the bed τ, char residence time and pressure drop ΔP.

Gasification reactor

The gasification reactor (the left-hand side of the reactor as shown in the Figure 14), works in bubbling bed regime to provide a uniform temperature across the bed and give a higher temperature for the biomass to go through various steps of gasification (drying, devolatilization, gasification). The fluidization agent used in the GR is steam, in order to have a N_2-free syngas with high heating value. The steam, besides fluidizing the bed, participate in various reactions:

Char gasification with steam: $C+H_2O \rightarrow CO+H_2$, which produce combustibles;

Water gas shift reaction (WGSR): $CO+H_2O \rightarrow H_2+CO_2$, which turns CO (low heating value) to H_2 (high heating value) gas;

and reform the tar: tar+$H_2O \rightarrow$lighter tars+$H_2O+CO_2+CO+CH_4$.

In order to set the operational condition of the GR for bubbling bed regime, first one needs to characterize the solid particles that are used as bed material.

Particle characterization

In order to set the operational condition, the first step is characterizing the solid materials that are being used. Individual particles can be determined by their size d, a factor that takes their shape into account φ, and their density ρ_P. But in a real system, one must deal with a cluster of particles, therefore more parameters have to be considered. In a cluster, particles don't have the same size and shape, therefore a distribution of the particle sizes must be quantified (d_i,x_i) with a range of particle diameters and the mass fraction associated to each diameter. In a volume containing the solid particles, there's a void space between the layers of the particles over each other and can represented with the porosity ε as the ratio between void volume to the total volume. And finally, the bulk density of the particles ρ_b which due to the void space is always lower than the individual particle density.

To describe the size of the particle, its diameter is used. In practice, for all technically interesting solids, it is necessary to define the particles whose shape deviates from a sphere, therefore an equivalent diameter must be defined. There are a variety of definitions, of which the four most important are given here (Table 7).

Table 7 Equivalent diameter of particles

Symbol	Description	Explanation
d_p	Sieve diameter	Lateral length of the square through which the particle passes
d_v	Volume diameter	Diameter of a sphere with the same volume as the particle
d_s	Surface diameter	Diameter of a sphere with the same surface as the particle
d_{sv}	Surface/Volume diameter	Diameter of a sphere with the same surface / volume ratio as

To determine the particle size, a sieve analysis is usually carried out to determine the equivalent diameter d_p (Sieve diameter). However, the equivalent diameter that is mainly used in the formulas, is d_{sv} (surface/volume diameter). Although there is no general relation between d_{sv} and d_p but for particles which do not deviate too much from the spherical shape, d_{sv} can be approximated by d_p multiplying per shape factor.

Equation 1 $d_{sv} \approx \phi . d_p$

The shape factors for selected technically interesting materials can be found in the literature (Yang, 2007) it assumes the value 1 for spheres, for all other particle shapes it lies between $0 < \varphi < 1$. The olivine sand's shape is very close the shape factor considered for it is approximately 0.9.

As mentioned before, the technically used solid particles are not mono diameters but they have more or less broad distribution of sizes. Assuming that a particle cluster has the number N_1 of spherical particles of size d_1, N_2 of size d_2, etc., then the surface / volume-related average diameter is given by the definition equation as follows:

Equation 2 $d_{pm} = \frac{1}{\sum \frac{x_i}{d_{pi}}}$

Equation 2 for d_{pm} is valid for arbitrary particle forms, so the shape factor φ must also be taken into account in the determination of the d_{sv} for the bulk according to the equations.

In the experiments examined in this study, the solid material that is used in the gasifier is olivine sand and the sieving method and the equations x-y are used to define the equivalent diameter. The characteristic of the olivine is reported in the Table 8:

Table 8 Composition of Olivine sand

parameter	unit	value
MgO	wt.-%	48 - 50
SiO_2	wt.-%	39 – 42
Fe_2O_3	wt.-%	8.0 – 10.5
Al_2O_3+Cr_2O_3+Mg_3O_4	wt.-%	0.7 – 0.9
CaO	wt.-%	< 0.4
NiO	wt.-%	< 0.1
$CaCO_3$	wt.-%	< 0.1
trace elements	wt.-%	< 0.1
hardness	Mohs	6 – 7
particles density	kg/m³	≈ 2850

The olivine sand has been sieved twice with the samples of 330 and 345 grams and for every sieve aperture, the mass fraction has been measured. The Equation 2 is used to calculate the equivalent sieve diameter. With applying the shape factor of "0.9", finally the surface to volume diameter is calculated. The results are shown in the Figure 15 and Figure 16:

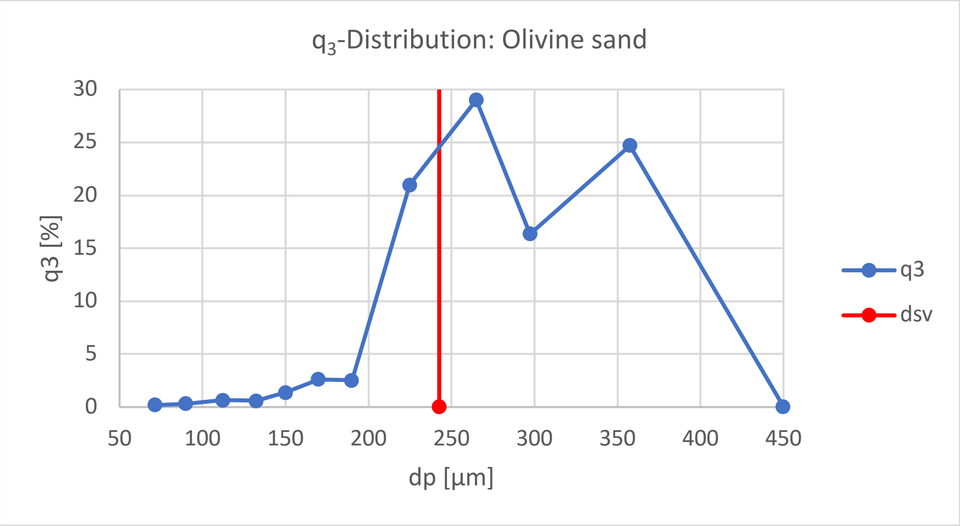

Figure 15 Olivine sand particle size distribution

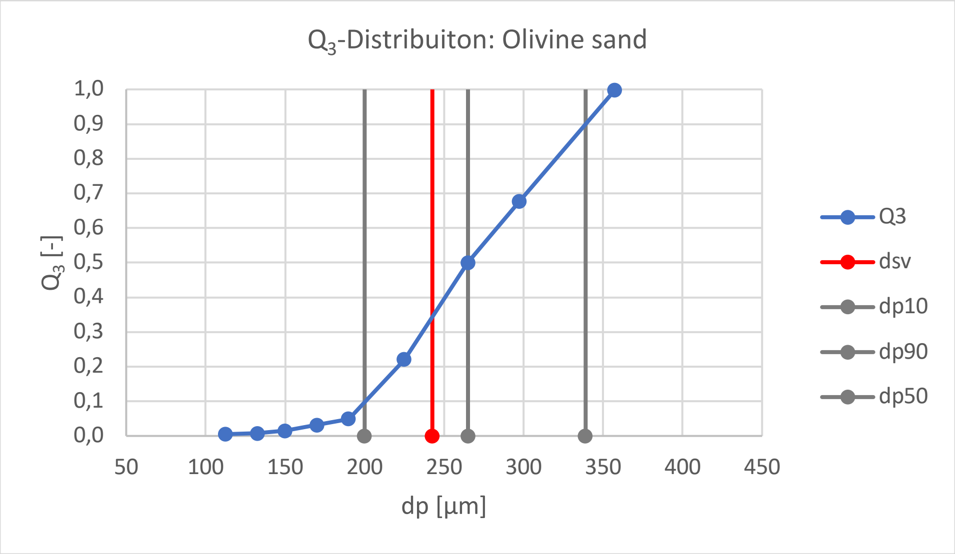

Figure 16 Olivine sand particle size distribution – cumulative

Bed porosity

The next factor to be determined in the fluidized bed reactor is porosity ε, defined as the void volume to the total volume of the reactor's bed. Writing it in the symbols results to Equation 3:

Equation 3 $\varepsilon = \frac{V_B - V_P}{V_B} = 1 - \frac{V_P}{V_B} = 1 - \frac{M}{\rho_P . V_B}$

Where M is the mass of the total particles, ρ_P is the particle density, and V_B is the total bed volume. The bulk density can be determined by dividing the total mass of the particles to the total bed volume and for olivine sand particles is around 1500 kg/m^3 which is almost half of its individual particle density.

Knowing the bulk and particle density of the olivine, the porosity of the fixed bed can be obtained:

$$\varepsilon = 1 - \frac{\rho_b}{\rho_P} = 1 - {}^{1500}\!/_{2850} \approx 0.47$$

The fixed bed porosity is determined at the initial state where the reactor is not in operation yet. Later on, the porosity will be calculated in the beginning of the fluidization regime and in the operational mode. But before that the minimum fluidization velocity must be calculated.

Minimum fluidization velocity

In a reactor filled with solid particles, when a gas or a mixture of gases are introduced from the bottom, the stream of gas will have a pressure drop over the bed height when is passing through it. With increasing the superficial velocity of the gas (volume flow rate of the gas per cross sectional area of the bed= m^3.s^{-1}/m^2), the pressure drop in the bed increases, until it reaches a point where the resistance force of the gas flow to the bulk material is equal to the weight of the sum of the individual particles minus their buoyancy (Shao, Gu, Zhong, & Yu, 2019). At this point, the fixed bed turns into the fluidized bed state.

A large number of authors have proposed different correlations for calculation of pressure drop in the fixed bed. Here the Ergun's equation is used as a reliable method:

Equation 4 $\frac{\Delta p}{H} = 150.\frac{(1-\varepsilon)^2}{\varepsilon^3}\frac{\mu.U}{d_{sv}^2} + 1.75.\frac{1-\varepsilon}{\varepsilon^3}\frac{\rho_g U^2}{d_{sv}}$

Where μ is the dynamic viscosity of the flow.

At the point of fluidization, the force equilibrium can be represented as follows:

Equation 5 $\Delta p.A = A.H_{mf}.(1-\varepsilon_{mf}).(\rho_p - \rho_g).g$

Where H_{mf} and ε_{mf} are the bed height and porosity at the fluidization point. A is the cross-sectional area of the fluidized bed and g is the gravitational constant.

This formula demonstrates the fundamental of the fluidization state, where the pressure drop is independent of the flow velocity. It means the pressure drop remains constant in the fluidization regime until the terminal velocity where the particles will be elutriated.

So, the minimum fluidization velocity is the limiting speed between the fixed bed and the fluidized bed. This limit is determined by means of the pressure profiles in the fixed bed and fluidized bed experimentally or using the equations.

At the minimum fluidization velocity, all the particles are essentially supported by the gas stream. The pressure drop through the bed is then equal to the bed weight divided by the cross-sectional area of the bed, $\Delta p = \frac{M.g}{A}$. Further increases in gas velocity will usually not cause further increases in pressure drop. In actual practice, however, pressure drop at minimum fluidization velocity is actually less then $\frac{M.g}{A}$ because a small percentage of the bed particles is supported by the wall owing to the less than perfect design of the gas distributor, to the finite dimension of the containing vessel, and to the possibility of channeling (Mehta & Hawley, 1969).

At the point of minimum fluidization, the voidage of the bed corresponds to the loosest packing of a packed bed. The loosest mode of packing for uniform spheres is cubic, $\varepsilon_{mf} = \frac{6-\pi}{6} = 0.476$. Noting that this value is slightly higher than the fixed bed voidage of olivine sand that was previously calculated.

An equation for the minimum fluidization velocity can be derived from the equations of the pressure drop in the fixed bed Equation 4 and in the fluidized bed Equation 5, because the pressure at the fluidization point must correspond to that in the fully formed fluidized bed. By putting the equations together and rearranging them:

Equation 6 $$\frac{\rho_g.d_{sv}^3.(\rho_P-\rho_g).g}{\mu^2} = \frac{150.(1-\varepsilon_{mf})}{\varepsilon_{mf}^3}.\frac{\rho_g.d_{sv}.U_{mf}}{\mu} + \frac{1.75}{\varepsilon_{mf}^3}.\frac{\rho_g^2.d_{sv}^2.U_{mf}^2}{\mu^2}$$

The term on the left represents the Archimedes number and on the right the Reynolds number is included. Therefore, many authors use the following relation to determine the minimum fluidization velocity:

Equation 7 $Ar = C1.Re_{mf} + C2.Re_{mf}^2$

For calculating the U_{mf}, equations like Equation 7 are inconvenient since they represent a quadratic term. Therefore, values for ε_{mf} are usually determined on the basis of experimental results and then the square equation for U_{mf} is solved. When ε_{mf} is unknown, to calculate the U_{mf}, C_1 and C_2 need to be determined. In this study the ε_{mf} is assumed to be equal to the voidage of the loosest packing of a packed bed.

Different empirical values of C_1 and C_2 have been proposed in literature (Wen & Yu, 1966); Chitester et al., 1984). Some of them are summarized in (Tannous et al., 1994). Most of these correlations have been obtained for Geldart type A and B particles, although some studies have also included Geldart type D particles (Tannous et al., 1994; Babu et al., 1978; Nakamura et al., 1985; Chyang and Huang, 1988). Different values of U_{mf} are calculated and compared based on the proposed correlations. It was found that for olivine sand the correlations proposed by (Chitester et al., 1984), C1=33.7 and C2=0.048, gave the best agreement, while for the Softwood Pellet char particles studied the best prediction was obtained using correlations proposed by (Chyang and Huang, 1988), C_1=33.3 and C_2=0.033.

The following equation to calculate U_{mf} is valid for the entire Re-number range from 0.001 to 4000 and has proved itself in practice for a wide variety of materials and particle size distribution. C_1, C_2 are obtained from (Chitester et al., 1984):

Equation 8 $$U_{mf} = \frac{\mu}{\rho_g . d_{sv}} \left[\sqrt{{C_1}^2 + C_2 . Ar} - C_1 \right]$$

In order to calculate the Archimedes number for the gasifier, d_{sv} and particle density are already known, but the dynamic viscosity and density of the fluidization agent must be obtained. In the gasification reactor, the fluidization agent is only steam. From the thermodynamic tables of steam[6], dynamic viscosity as a function of temperature is obtained. Since the typical range of gasification temperature is 600 to 1000 ˚C and the gasifier under discussion (TUW) works at atmospheric pressure, therefore only the related values are considered. The results are shown in the Figure 17:

---

[6] DOI: 10.1615/AtoZ.s.steam_tables

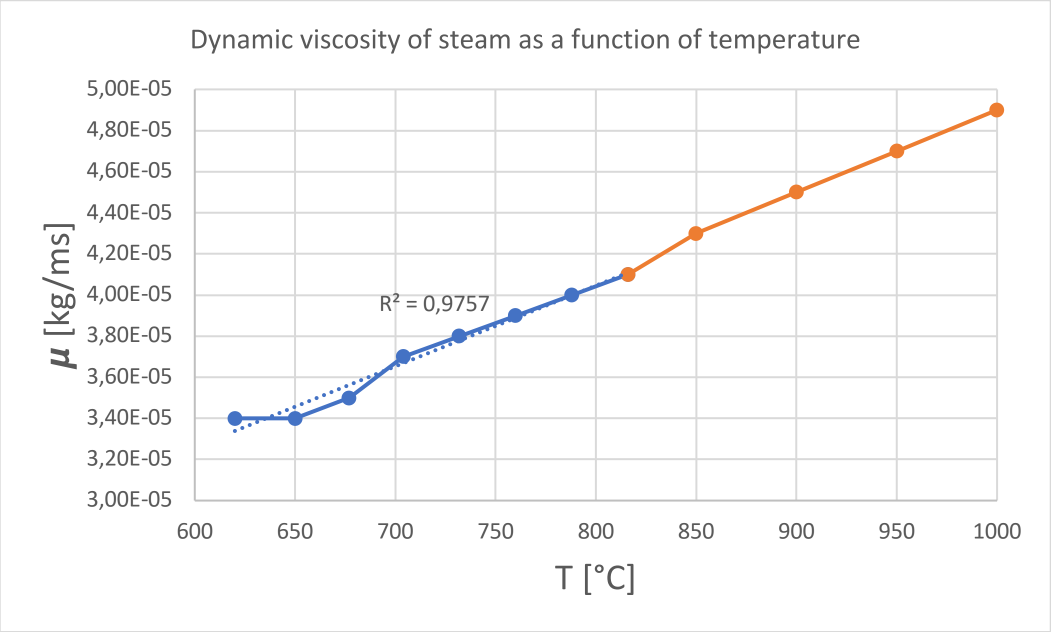

Figure 17 Dynamic viscosity of steam in atmospheric pressure as a function of temperature

The data available in the reference was up to 816 ˚C. The correlation between dynamic viscosity and temperature showed a fairly linear dependency (correlation factor R^2=0.975). Therefore, for higher temperatures, the values of dynamic viscosity were extrapolated and is shown with orange color in the Figure 17.

$$\mu_{steam}(T) * 10^6 = 0.04T + 9 \qquad [\text{kg.m}^{-1}.\text{s}^{-1}]$$

The obtained correlation can be used in the development of a simulation modeling of steam gasification reactor at atmospheric pressure. The temperature is expressed in centigrade; it's considered at atmosphere pressure and is valid in the range of 600 to 1000 ˚C.

The last parameter needed for calculation of Archimedes number is the gas density. The density of steam as a function of temperature at atmospheric pressure is obtained from the data available at thermodynamic tables[7] and the results are shown in the Figure 18:

---

[7] DOI: 10.1615/AtoZ.s.steam_tables

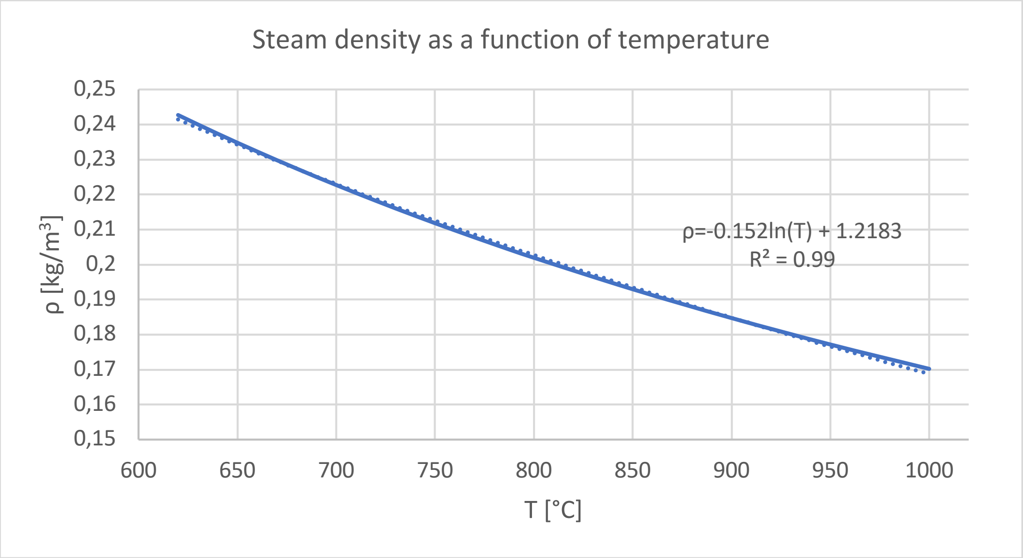

Figure 18 Steam density in higher temperature and atmospheric pressure

Again, a very clear correlation can be observed between the hot steam density and temperature in atmospheric condition. The following equation can be derived to be implemented in the model:

$$\rho_{steam}(T) = -0.152\ln(T) + 1.2183 \qquad [\mathrm{kg.m^{-3}}]$$

In the above correlation, the temperature is expressed in centigrade, it's considered at atmosphere pressure and is valid only in the range of 600-1000 ˚C.

Both density and dynamic viscosity in the equation of Archimedes number are temperature dependent. Therefore, Archimedes number will be also calculated as a function of temperature and the effect of temperature will be discussed in the outcome of Archimedes number.

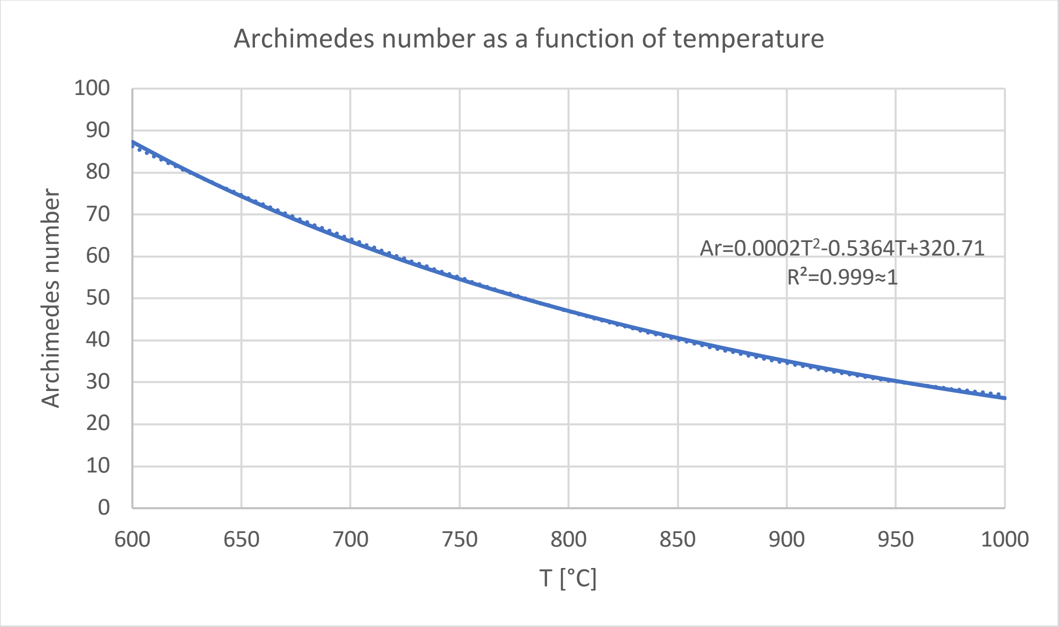

Figure 19 Archimedes number for olivine sand with d_{sv}≈250 µm, with steam as fluidization agent at atmospheric pressure

As can be seen in the Figure 19, also the Archimedes number varies with temperature, and its dependency on temperature shows a very strong correlation with the temperature in the certain set condition (P=atmospheric, Olivine sand d_{sv}≈250µm, steam as fluidization agent).

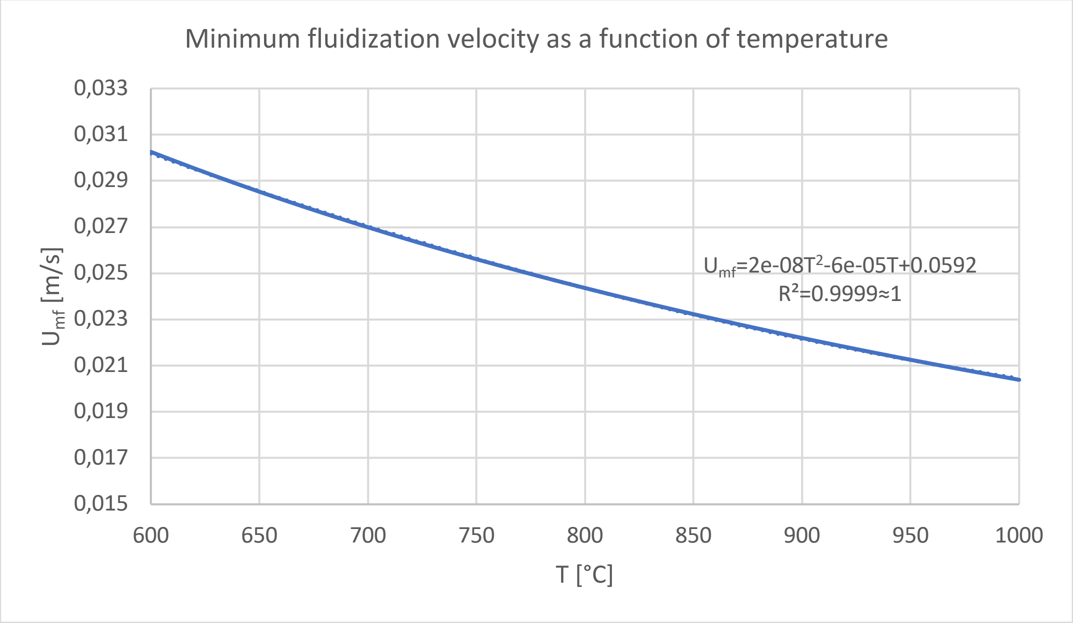

Figure 20 Minimum fluidization velocity in the GR as a function of temperature

Gas superficial velocity in the GR on one hand indicates the fluidization regime, and on the other hand it's influenced by the steam to biomass ratio and the geometry of the CFB. In order to set the gas superficial velocity in the GR, first we discuss the steam to biomass ratio "StB", and then we investigate whether the value obtained for U_s based on StB correspond to our desired bubbling regime or not.

Steam to Biomass ratio

In the literature (Hofbauer & Rauch, 2002), the ratio of steam to biomass "StB" is suggested to be 0.5 to 1.5 as optimal condition for industrial applications. In order to set the steam input to the CFB gasifier, first need to define the biomass input flowrate. The CFB gasifier of TUW has 100 kW thermal capacity, therefore, for gasifying a woody biomass (softwood pellets) as used in this work, the feeding rate will be calculated based on the heating value of the biomass and the thermal capacity of the plant.

Heating value of the biomass can be determined whether experimentally by calorific bombs or using Boe's equation based on the ultimate analysis of the biomass.

The ultimate and proximate analysis of the softwood pellets are shown in the Table 9:

Table 9 Ultimate and proximate analysis of softwood pellets

			Dry	Wet
water content	Water Content	[mass%]	-	7,2
ash content	ASH	[mass%]	0,2	0,2
carbon	C	[mass%]	50,7	47
hydrogen	H	[mass%]	5,9	5,5
oxygen	O	[mass%]	43	
nitrogen	N	[mass%]	0,2	0,2
sulfur	S	[mass%]	0	0
chlorine	Cl	[mass%]	0	0
volatiles	VM	[mass%]	85,4	79,3
fixed carbon	FC	[mass%]	14,4	
Higher Heating Value	HHV	[KJ/Kg]	20248	18784
Lower Heating Value	LHV	[KJ/Kg]	18943	17397

Here the lower and higher heating values are already measured experimentally, but we still can compare the results to the Boie's equation:

LHV_{daf}=34.8C+93.9H+10.5S+6.3N-10.8O [MJ/kg]=18.54 MJ/kg

Relative error between experimental results of LHV and Boie's equation results 2.13%.

Subsequently, the dry ash-free biomass feeding rate can be calculated relating to the thermal capacity of the CFB gasifier:

$$\dot{M}_{biomass,daf} = \frac{P_{thermal}}{LHV_{Biomass,daf}} = \frac{100\ [\frac{kJ}{s}]}{18943\ [\frac{kJ}{kg}]} = 18.95\ [\frac{kg}{h}]$$

Applying the water content and inorganic fraction of the biomass, the feeding rate of the biomass as it's received can be obtained:

$$\dot{M}_{biomass,wet} = \frac{\dot{M}_{biomass,daf}}{(1 - water\ content - ash)} \approx 20.4\ [\frac{kg}{h}]$$

With a lower heating value of 18.94 MJ/kg, results to a feeding rate of 20.4 kg/h wet-basis and 18.95 kg/h dry ash-free basis (7.2% humidity and 0.2% ash). Steam to biomass ratio here is set to be 0.72 when only the steam as fluidization agent is considered to contribute to this ratio. Adding the released moisture content from the wet biomass to the equation, the StB ratio increase to 0.8 and we call it StB*.

Equation 9 StB*=Steam to Biomass ratio (S/R): $\frac{S}{B} = \frac{\dot{m}_{steam}+\dot{m}_{moisture\ in\ biomass}}{\dot{m}_{dry\ biomass}}$

The total steam required to maintain the StB*=0.8 is 13.7 kg/h. The steam is injected in various parts of the system. In the lower loop seal (LLS), which half of it contributes to the GR and the other half fluidize the bed material towards the CR; the main fluidization agent is inserted to the lower gasification part (LGR); and there's steam input to help the circulation of the bed material between the CR and GR in the upper loop seal (ULS); and finally the steam to fluidize the particles that are elutriated from the GR, captured by the cyclone and are putting back to the GR with the internal loop seal (ILS). Although, only the steam input at the LGR and half of the steam input at LLS contributes to the bubbling bed in the GR, the other steam inputs can contribute to the Steam to Biomass ratio, nevertheless.

Besides the steam from the moisture content of the biomass, more steam will be released (pyrolytic water) during the devolatilization of biomass, hence, the StB value will be even slightly higher in the operational condition.

Terminal velocity

In order to determine the terminal velocity as a limiting point for the superficial velocity in the gasification reactor for the bubbling bed fluidization regime, the fundamental of the calculations are explained briefly. Furthermore, terminal velocity will be calculated for the riser as well, but this time as a lower limiting point.

The calculation can begin with a simple force equilibrium being applied on a single spherical particle.

Considering a free-falling individual particle with a projected area diameter d_k in an infinite fluid, the gravity, buoyancy and drag forces are acting on the particle to determine its motion. The force balance on the particle is as follows:

Equation 10 Force of gravity (F_G) – Buoyancy force (F_A) – Resistance/drag force (F_W) = Acceleration force

When the particle has reached its terminal velocity, the acceleration force will be zero. The following relation is then obtained for the free-fall velocity (terminal velocity):

Equation 11 $U_t = \sqrt{\frac{4}{3}\cdot\frac{\rho_p-\rho_g}{\rho_g}\cdot\frac{d_k \cdot g}{C_W}}$

Where the d_k is the diameter of the sphere, ρ_g and ρ_p are the gas and particle density respectively, C_W is the drag coefficient for a single spherical particle, and finally A_p is the projection area of the particle perpendicular to the flow ($d_k^2\pi/4$).

This method can be applied by determining the drag coefficient with correlating it to the Reynolds number, but the results are not satisfactory for non-spherical particles. Although the shape factor φ is not capable of describing the effects occurring, it is nevertheless used by most authors (Pettyjohn and Christiansen, 1948) In the laminar region, the Equation 12 and Equation 13 are suggested:

Equation 12 $U_t = K_1 . \frac{(\rho_p-\rho_g).g.d_k^2}{18.\mu}$

Equation 13 $K_1 = 0.843. log\frac{\phi}{0.065}$

The results are shown in the Figure 21:

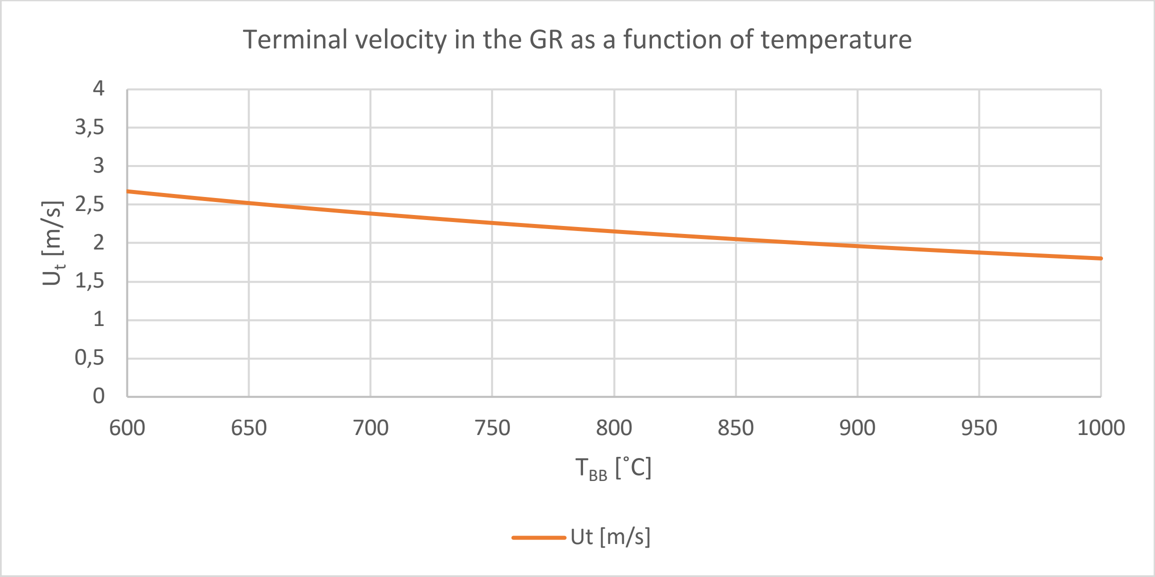

Figure 21 Terminal velocity of the bed material particles according to (Pettyjohn and Christansen, 1948)

It can be noted the terminal velocity decreases by increasing the temperature. It can be attributed to the fact that the dynamic viscosity of steam increases with temperature which can lead to lower terminal velocity of the particles.

Superficial velocity in the GR and fluidization state

In the case of gas / solid fluidized beds, different flow states can occur which depend essentially on the properties of the particles and the gas as well as gas velocity. The fluidization states of the DFB of Vienna is bubbling bed in the gasification reactor to provide a long residence time for biomass to devolatilize and gasify and fast fluid bed in the combustion reactor to provide a high particle flux to maintain the heat in the gasification reactor. Therefore, the operational condition for must be set to satisfy these conditions.

Steam in the GR on one hand works as the fluidization agent, on the other hand indicates the steam to biomass ratio. The steam to biomass ratio has been already set to StB*=0.8 as an optimal value for industrial application of biomass steam gasification. As explained in the previous section, the steam is inserted in the GR in various points (LLS, LGR, ULS, ILS). Although the steam input on mass basis is constant for the experiments, the gas density changes with temperature and subsequently the superficial velocity. The total steam input has been already calculated based on the softwood pellets as fuel and the thermal capacity of the plant, resulting to 13.7 kg/h. Few considerations must take into account in order to calculate the steam input at loop seals and lower gasification part of the system. First of all, the superficial gas velocity in one side of the lower loop seal ($0.5U_{g,LLS}$) must be equal to the superficial velocity of the lower gasification part ($U_{g,LGR}$) in order to maintain the gas superficial velocity in the GR's bed. It's because half the steam input at LLS goes through the CR to fluidize the bed material and unconverted char particles towards the CR. That means:

$$\frac{1}{2}U_{g,LLS} = U_{g,LGR} \rightarrow \frac{1}{2}\frac{\dot{Q}_{steam,LLS}}{A_{LLS}} = \frac{\dot{Q}_{steam,LGR}}{A_{LGR}} = \frac{1}{2}\frac{\frac{\dot{M}_{steam,LLS}}{\rho_{steam}}}{A_{LLS}} = \frac{\frac{\dot{M}_{steam,LGR}}{\rho_{steam}}}{A_{LGR}}$$

Where Q˚ represents the volumetric flowrate of the steam and M˚ is the mass flow rate. Since the temperature at LLS and LGR is almost equal, the density terms can cancel each other out.

At upper loop seal (ULS), since the pipe diameter is the same as the LLS and particle size distribution is the same in those parts, we can conclude:

$$\dot{M}_{steam,LLS} = \dot{M}_{steam,ULS}$$

Noting that, also at ULS, only half part is contributing to the GR and the other half enters the CR.

As for the internal loop seal (ILS), where the fine particles elutriated from the freeboard of the GR, are captured by the cyclone and are transporting back to the GR, the particle are much finer here, therefore, the steam input is considered to be only a third of the steam input at LLS and ULS:

$$\dot{M}_{steam,ILS} = 1/3\dot{M}_{steam,LLS}$$

The total steam for the bubbling bed therefore is:

$$\dot{M}_{steam,BB} = \dot{M}_{steam,LGR} + 1/2\dot{M}_{steam,LLS}$$

The total steam input is already calculated from the steam to biomass ratio:

$$StB^{*} = \frac{\dot{M}_{steam,GR} + \dot{M}_{steam,moisture\ content\ of\ biomass}}{\dot{M}_{dry\ ash-free\ biomass}}$$

The summary of steam inputs is reported in the Table 10:

Table 10 Steam flowrates to the various part of the CFB gasifier

M˚steam to	M˚steam to	M˚steam to	M˚steam to	M˚steam to	M˚total steam to GR
[kg/h]	[kg/h]	[kg/h]	[kg/h]	[kg/h]	[kg/h]
10,68	2,26	2,26	0,75	11,81	13,69

The steam inputs on mass basis are constant for all gasification temperatures, but the change in the steam density results to different volumetric flowrate and hence the change in the superficial gas velocity. The superficial velocity of steam for the range of 600 to 1000 ˚C temperature in the GR is reported in the Figure 22 for various parts of the GR:

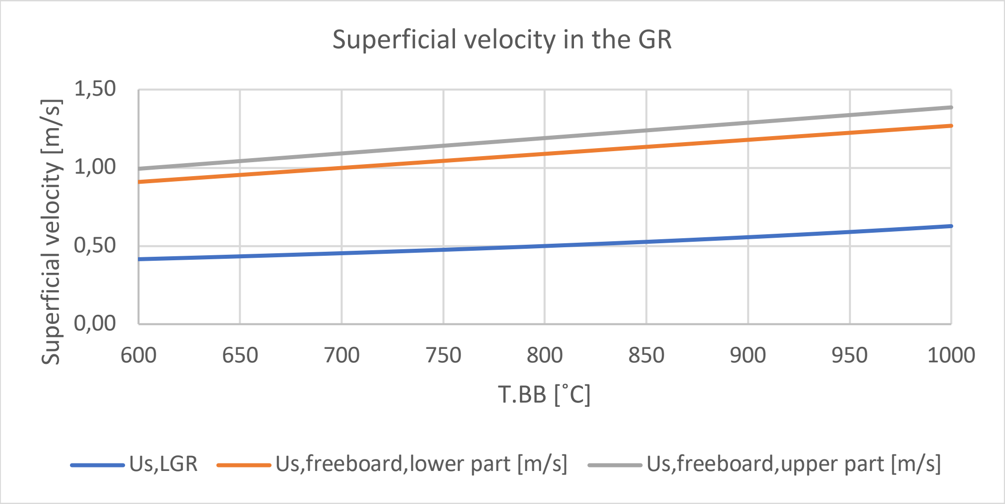

Figure 22 Superficial velocity of steam in various part of the CFB's gasification reactor

The ratio between superficial gas velocity and the minimum fluidization velocity corresponding to the same temperature is reported in the Figure 23:

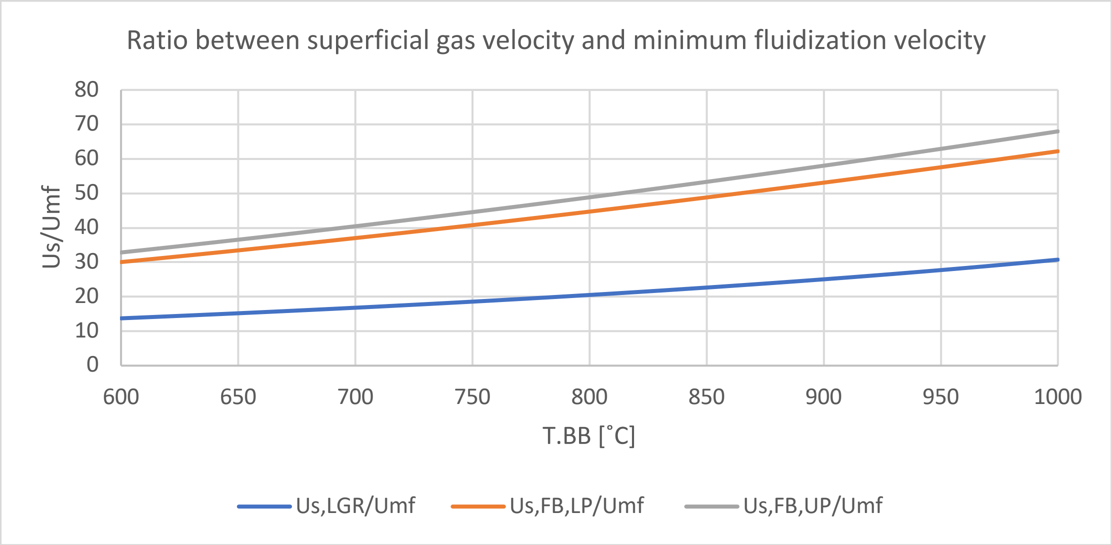

Figure 23 Superficial velocity to the minimum fluidization velocity as a function of temperature

In order to assess the fluidization state based on the superficial velocity and particle characterization, there are different state diagrams where one can look to define the fluidization states. The general state diagram according to Grace (after J. Schmid) is used in this work for such assessment. This diagram is shown in the Figure 24:

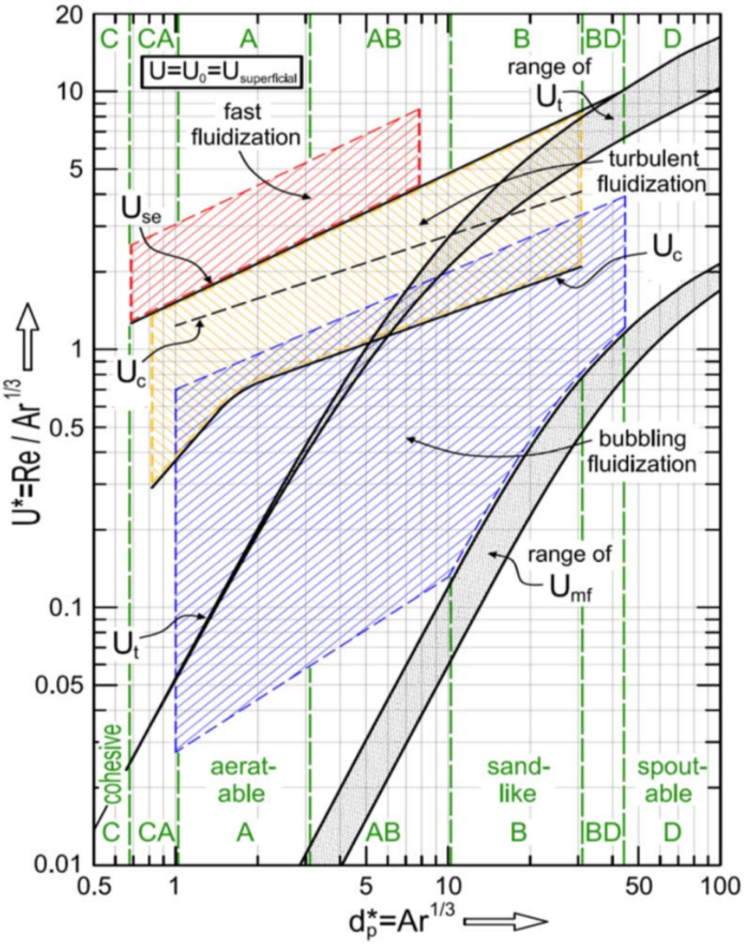

Figure 24 General state diagram according to Grace (after J. Schmid)

This state diagram is divided in different regions according to 1. Fluidization states, 2. Geldart classification of the particles.

A classification of the bulk materials (powders) with regard to their fluidizability was made by Geldart (Geldart, 1973), based on the particle diameters and the density difference between particles and fluid. It is found that the individual types of bulk material can be classified by applying the two mentioned quantities. Geldart divides the powders into four groups (A – D).

According to this classification, olivine sands enter in the Geldart's group B, and softwood pellet and its derived char enters the Geldart's group D.

In Group B particles, the interparticle forces are negligible. The formation of bubbles begins when the minimum fluidization point is reached, and the bed expansion is not homogeneous here. The dominant phenomenon is the formation of bubbles which cause a good intermixing of solids. This group has the greatest practical importance in fluidized bed technology.

The general state diagram in the Figure 24 has two a-dimensional axes. On horizontal axis, d_p^* is a non-dimensional value and is the cube root of Archimedes number which can be derived easily from previous calculations. On the vertical axis, there is U^*, which is a function of both Reynold number and Archimedes number. Archimedes number is already calculated for each temperature, but the Reynold number ($Re = \frac{U.d_p.\rho_g}{\mu}$) is correlated to the superficial velocity. To stay in the bubbling fluidization regime, as can be seen in the Figure 24, the superficial velocity must be higher than U_{mf} as long as we don't reach the U_c (starting of the turbulent zone) and U_t (terminal velocity). Superficial velocity of the steam in the gasification reactor, on one hand, indicates the fluidization regime, and on the other hand, is an indication of steam to biomass ratio. In the operation mode, the superficial velocity is always higher than U_{mf} (usually 4 to 40 times higher) and it must remain lower than the terminal velocity. The superficial velocity of the gasification reactor and its rapport to the U_{mf} is set by the steam to biomass ratio StB*=0.8 and based on that, the fluidization regime is assessed.

Steam, besides fluidizing the bed material, help to fluidize the bed material as well. Therefore, it's worth to look at the fluidization state of the mixture of bed material and biomass at the operational condition.

Softwood pellets (SWP) as they are received, have a length varying in the range of 1 to 3 cm and have diameter of 6 mm. The particle size of the SWP char is very similar to that of the original SWP particles (Gómez-Barea et al. 2010). Both SWP and SWP char are Geldart group D particles, whereas the olivine sand belongs to Geldart group B particles (Geldart, 1973).

The gas velocity necessary for complete fluidization, U_{cf} of the mixture of bed material and SWP particles, depends on the fraction of SWP in the bed and is substantially lower than the theoretical U_{mf} of SWP, in agreement with literature (Noda et al., 1986; Teplitskii et al., 2010). U_{cf} can be calculated using a "mixture density", ρ_m, and a "mixture diameter", d_m, to calculate the Archimedes number (Formisani, 1991). ρ_m and d_m are calculated according to Equation 14 and Equation 15 respectively:

Equation 14
$$\rho_m = \frac{1}{\frac{x_{SWP}}{\rho_{SWP}} + \frac{x_{olivine}}{\rho_{olivine}}}$$

Equation 15
$$d_m = \frac{\frac{1}{\rho_m}}{\frac{x_{SWP}}{d_{SWP}\rho_{SWP}} + \frac{x_{olivine}}{d_{olivine}\rho_{olivine}}}$$

Where X_{SWP} is the fraction of SWP in the mixture. In this study it is assumed that $x_{SWP} << x_{olivine}$, therefore, for simplification, the mixture values are assumed to be equal to the olivine sand values. But nevertheless, the fluidization state for the SWP and its derived char is assessed. To backup this assumption a simple verification has been made. The biomass id being fed continuously to the CFB gasifier with roughly 20 kg/h and the amount of bed material in the system can vary between 70 to 100 kg. According to various correlations in the literature, the devolatilization of woody biomass in high temperature with equivalent diameter of 8 mm is around 30 seconds. The source of these correlations and results are shown in the Table 11:

Table 11 Devolatilization time of different biomass particles under fluidized bed conditions (diameter: d0 [mm], bed temperature: T[K])

REFERENCE	CONDITIONS	DEVOLATILIZATION TIME (S)	T (S)
DE DIEGO ET AL. (2002)	Pine wood, 5 – 32 mm 850°C	$1.03d_0^{1.6}$	28,69
DI BLASI AND BRANCA (2003)	Beech wood, 2 – 10 mm 534 – 834°C	$0.8\exp(1525/T)d_0^{1.2}$	37,72
RAPAGNA AND DI CELSO (2008)	Wood, 5 – 25 mm 700 – 900°C	$2.514d_0^{0.94\exp(352/T)}$	36,46
SREEKANTH AND KOLAR (2010)	Wood,10–30mm 750 – 950°C	$62d_0^{1.6}T^{-0.564}$	32,88
SUDHAKAR AND KOLAR (2011)	Wood,10–25mm 750 – 950°C	$18d_0^{1.548}T^{-0.389}$	29,29
GASTON ET AL. (2011)	White oak, 6 – 25 mm 500 – 900°C	$\exp(1013.2/T^{1.076})d_0^{1.414}$	32,12

In this circumstance, the $X_{SWP} \approx 0.0023 \ll X_{olivine} \approx 0.9977$ and the above-mentioned assumption is valid.

Assuming U_s corresponding to StB*=0.8, we can verify our fluidization regime over our range of temperature variation according to the state diagram for both olivine sand as bed material and softwood pellets as the fuel.

In order to assess the fluidization state, the a-dimensional values of $d_p^* = Ar^{1/3}$ and $U^* = Re/d_p^*$ must be obtained for both olivine sand and SWP. The fed SWP to the system has a diameter of 6 mm and a height in range of 1 to 3 cm. The density is around 640 kg/m^3. The volume to surface diameter d_{sv} is calculated $d_{sv} = 6V_p/O_p \approx 8$mm. Archimedes number and subsequently non-dimensional values based on the U_s is calculated and reported in the Figure 25 and Figure 26 for olivine sand and softwood pellet respectively:

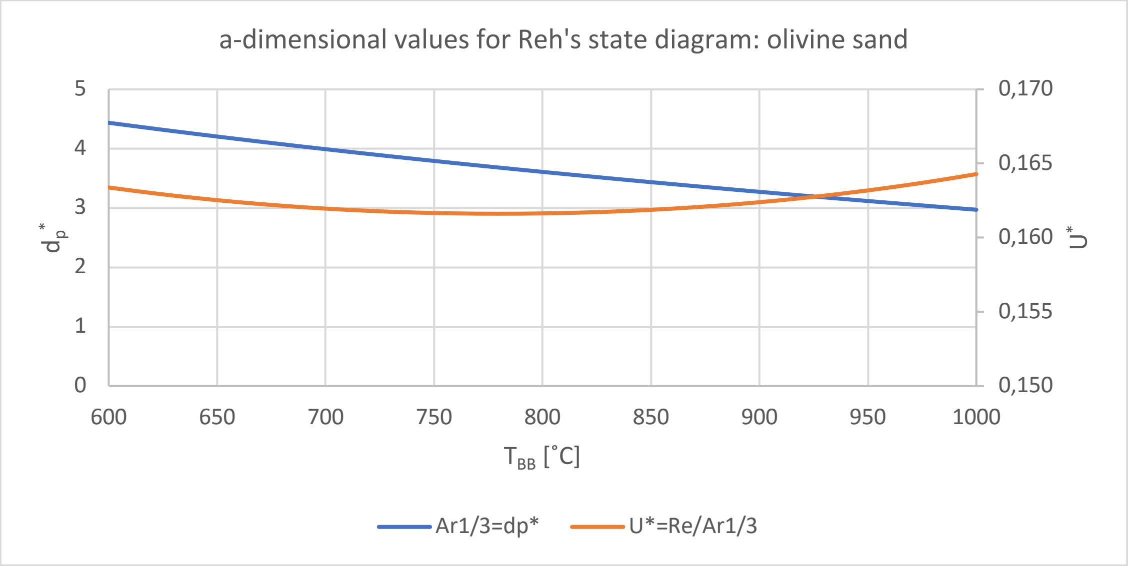

Figure 25 a-dimensional values for Reh's state diagram: Olivine sand

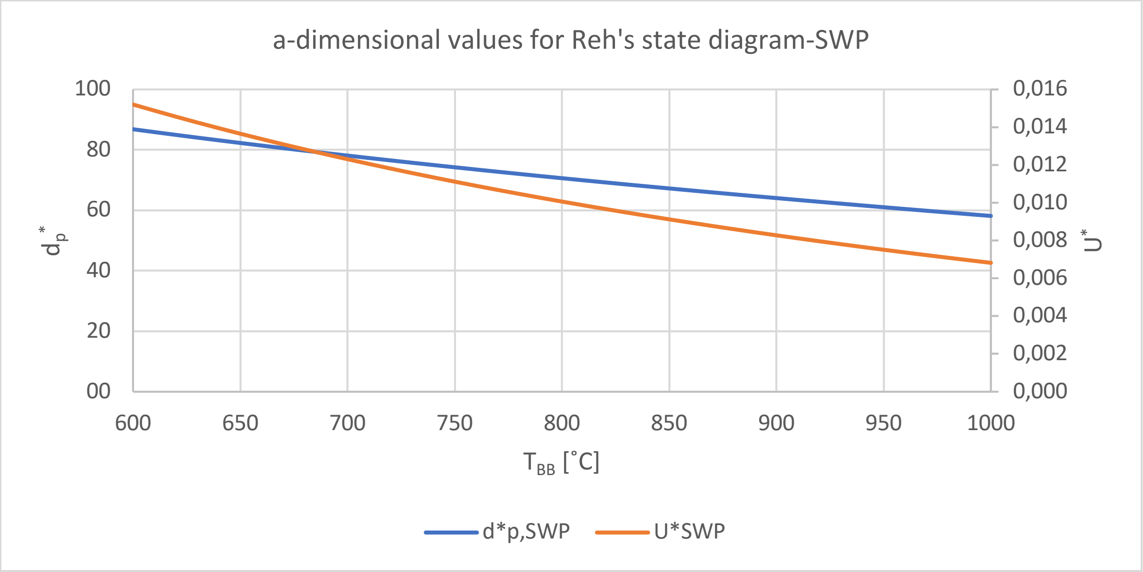

Figure 26 a-dimensional values for Reh's state diagram: Softwood pellets

These values are investigated on the Reh's state diagram to identify the corresponding fluidization regime and it's shown in the Figure 27:

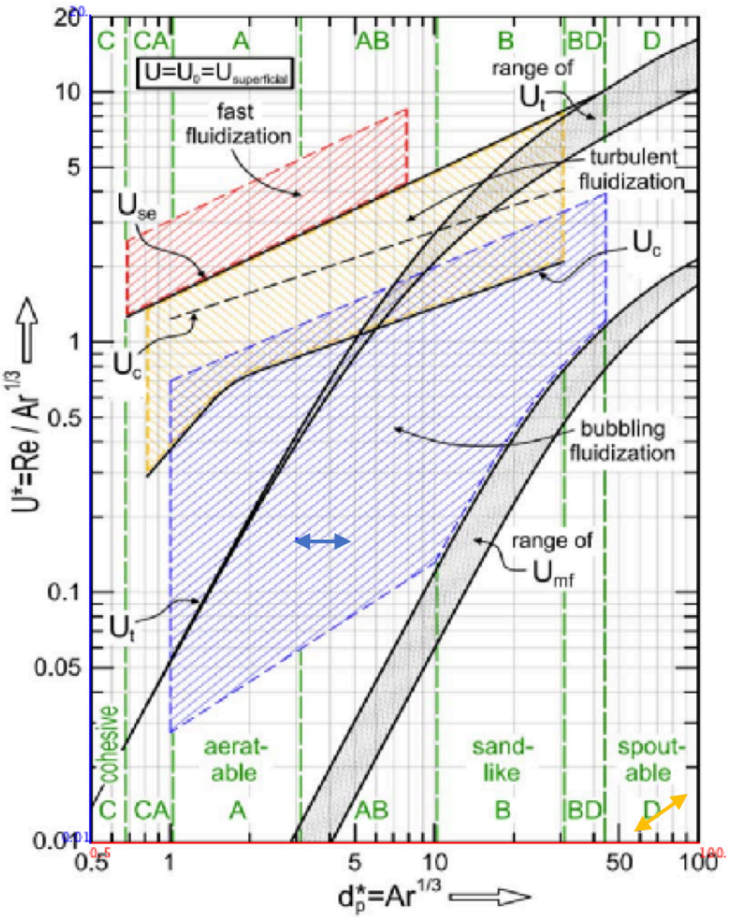

Figure 27 Fluidization regime of Olivine sand and Softwood pellets in the operational condition of CFB gasifier on Reh's state diagram

It can be seen from the diagram that, the fluidization regime for olivine sand will be in bubbling bed (blue line), with higher temperatures resulting to behavior of particles closer to Geldart A type.

And as for the SWP, it can be noted that as expected the range of d^*_p coincide with the Geldart D group on the Reh state diagram (yellow line), and the U^* values are in a range far from fluidization. That means that they can easily mix with the bed material without being carried away, until after they are fully devolatilized, start to gasify and they shrink down to very fine particles (ash content).

To ensure that U_s is lower than U_t for avoiding elutriation in the GR, a comparison has been made between superficial and terminal velocity in the GR and shown in the Figure 28:

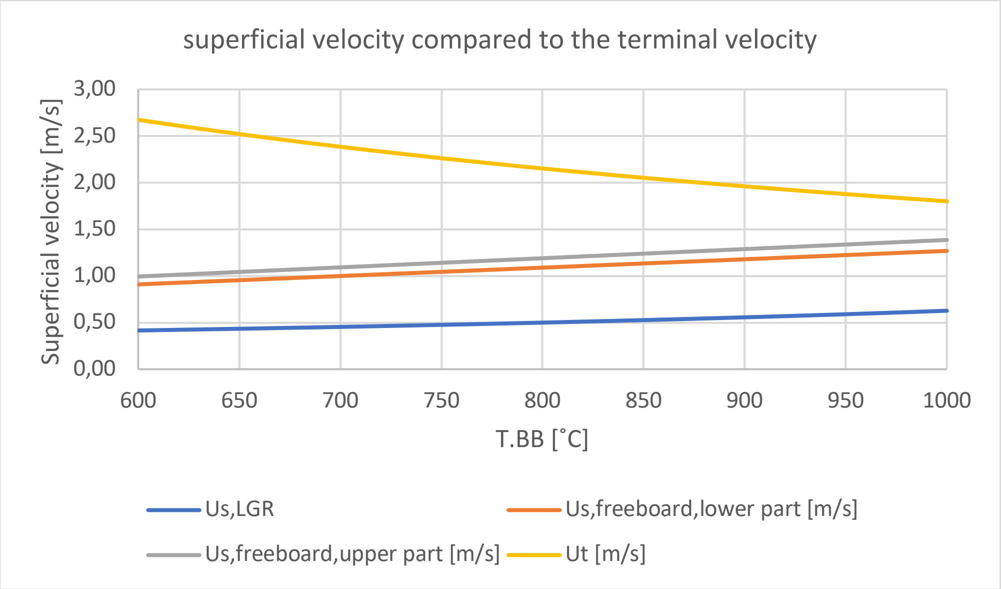

Figure 28 A comparison between superficial velocity and terminal velocity in the gasification reactor

It can be observed from the Figure 28, that even in the upper part of the freeboard, at highest temperature, where the superficial velocity is the highest, it's still lower than terminal velocity. It still doesn't mean that no elutriation can occur, since the particle diameter dsv used in the calculation is reprehensive of the bed material as a whole, with its particle size distribution. Therefore, finer particles which contains a very small fraction of bed material, still can be elutriated. For that reason, a cyclone and a gravity separator are installed at top of the GR to capture these fine particles and put them back to the system via inner loop seal (ILS). Besides the fine particles in the bed material, also some bigger particles can turn into finer particles through fragmentation and abrasion and be easier carried away with the fluidization gas.

In the Figure 28, superficial velocity in the GR is calculated for the lower loop seal, lower gasification part, freeboard before inserting the steam from upper loop seal and beyond that. The trapezoidal section and the rectangular part above it is not taken into account. In these parts, the cross-sectional area increases and hence, the superficial velocity decreases. Therefore, instead of risking getting close to the terminal velocity, there's a chance to reach the lower limit of bubbling bed fluidization. The latter will be investigated for the minimum and maximum bubbling bed temperature, 600 and 1000 ˚C respectively.

In the Figure 29, the cross-sectional area of the GR is reported as a function of the height of the GR:

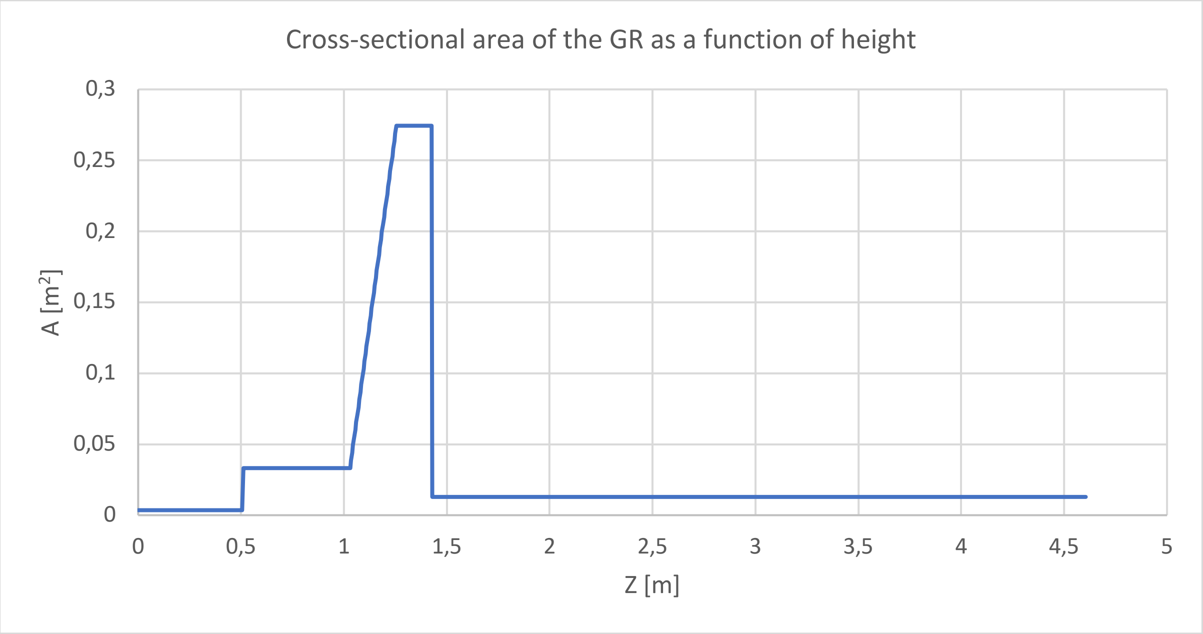

Figure 29 Cross-sectional area of the GR as a function of height

With changing (increasing) of cross-sectional area in the trapezoidal section and eventually staying constant at its maximum value in the rectangular section, the superficial gas velocity decreases. In order to assess whether the superficial velocity reaches the threshold of the minimum fluidization velocity or not, two cases as two extremes of the temperature range is examined and reported in the Figure 30 and Figure 31:

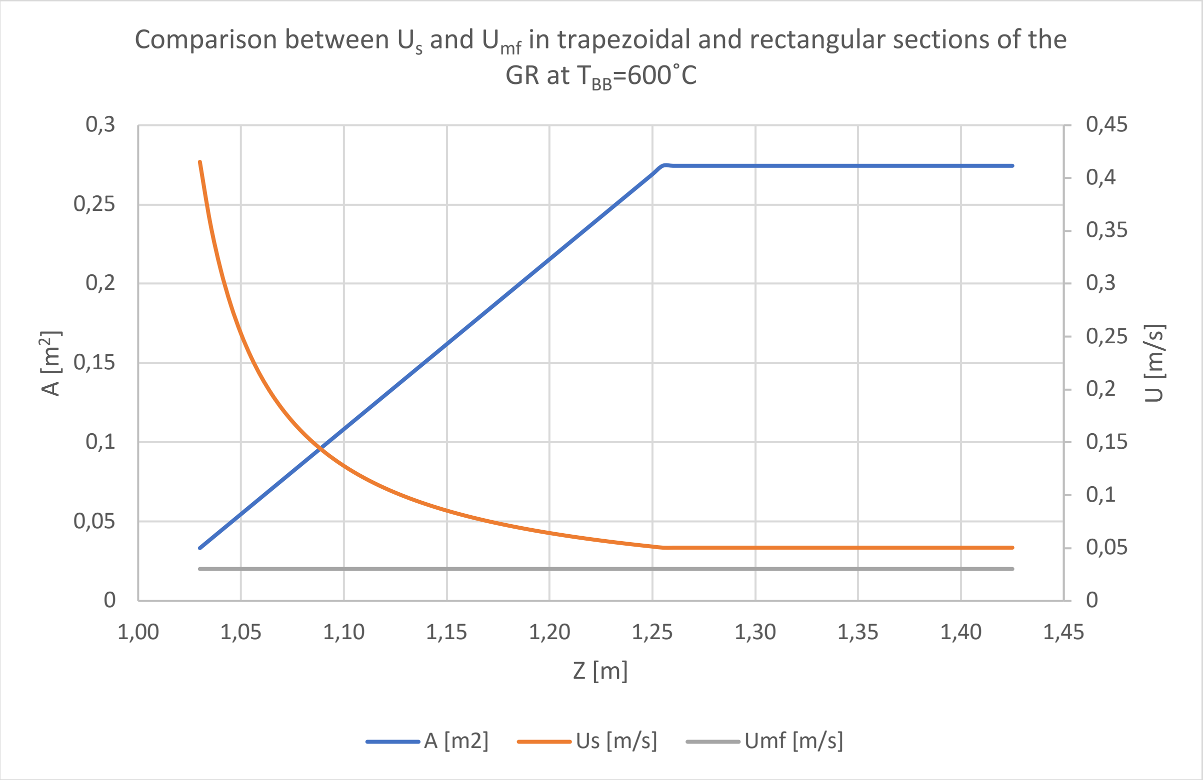

Figure 30 Comparison between superficial velocity and the minimum fluidization velocity in the trapezoidal and rectangular section of the GR at bubbling bed temperature of 600˚C

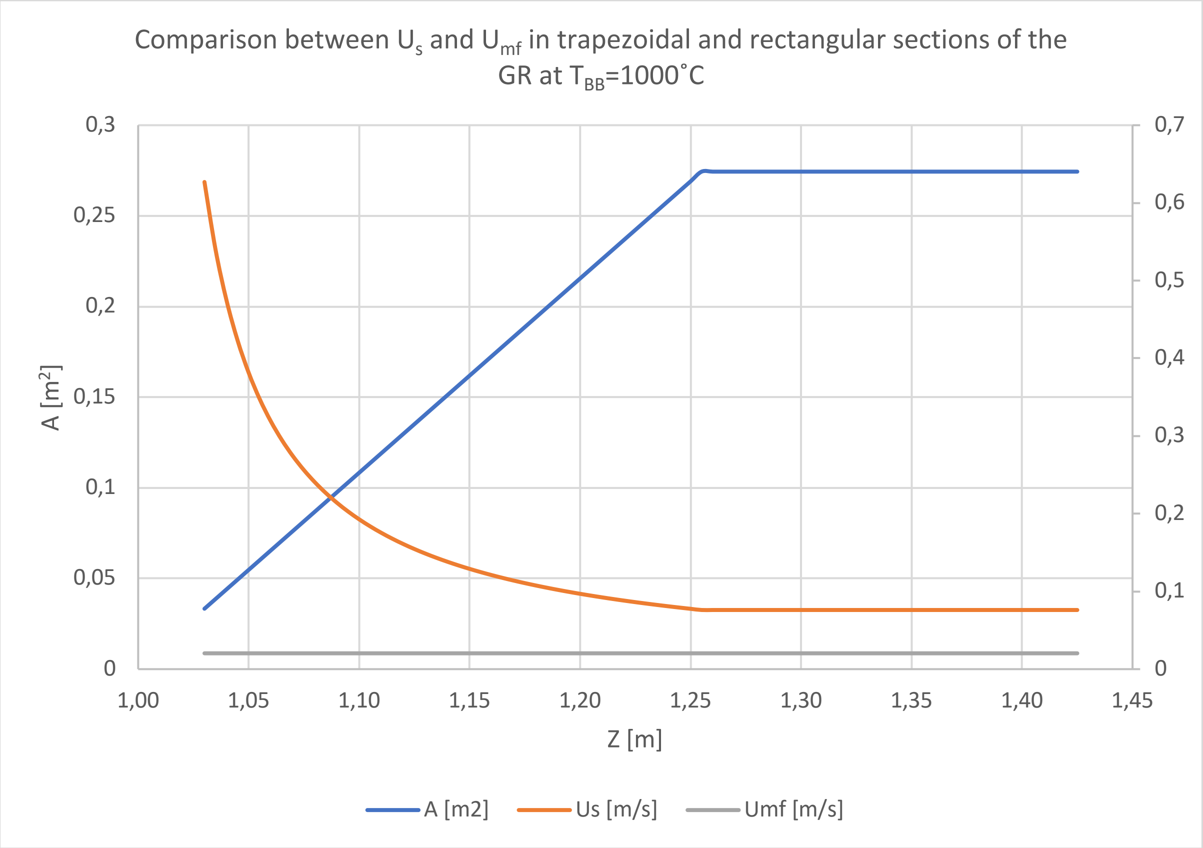

Figure 31 Comparison between superficial velocity and the minimum fluidization velocity in the trapezoidal and rectangular section of the GR at bubbling bed temperature of 1000˚C

It can be concluded that the superficial velocity even at its minimum value, still exceeds the minimum fluidization point. At 600 ˚C, the ratio of U_s/U_{mf} reaches to its minimum value of 1.3, and at 1000˚C this value is 3.7, means $(U_{min}/U_{mf})_{min}$ is increasing by temperature.

Bubble fractions

The porosity in a CFB depends both on the properties of the particles employed and on the gas velocity. In this section bed porosities obtained by semi-empirical correlations.

The porosity at the minimum fluidization point can be derived easily by knowing the minimum fluidization velocity. But in the operational condition, which the velocity is higher than that of minimum fluidization, the bed porosity is the function of the bubble fraction in bed, δ_b, and the porosity of emulsion phase, ε_e. As fluidization between minimum fluidization and minimum bubbling is of the particulate type, for Geldart group B and D, according to (Broadburst and Becker), $\varepsilon_{mf} \cong \varepsilon_{mb}$, and it can be obtained from the Equation 16:

Equation 16 $\varepsilon_{mb} = 0.586\phi_s^{-0.72} Ar^{-0.029} \left(\frac{\rho_g}{\rho_p}\right)^{0.021}$

Equation 16 agreed with the experimental data over the following range:

$$0.85 < \phi_s < 1$$

$$1 < Ar < 10^5$$

$$500 < \frac{\rho_p}{\rho_g} < 50{,}000$$

This correlation is also been compared with the data of (Leva, 1959) for ε_{mf} with satisfactory results.

First one needs to reassure that the range for the validity of the correlations is satisfied for our purpose. The sand here is olivine sand with shape factor of ϕ_s=0.9, Archimedes number varies in a range of 26 to 87 which coincides with the criteria, and finally in our operational range the $\frac{\rho_p}{\rho_g}$ is in the range of 12,000 to 18,000. Now that the criteria are met, we can use the correlation to calculate the ε_{mf} as a function of temperature. The results are shown in the Figure 32:

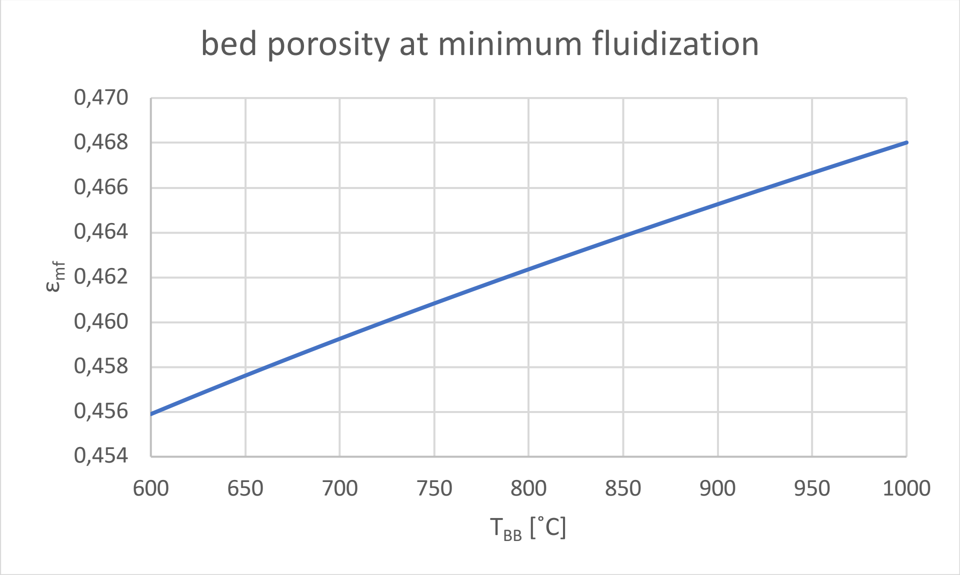

Figure 32 bed porosity at minimum fluidization as a function of bed temperature

Before it was said the ε_{mf} can be estimated like the loosest packing of a packed bed which for uniform spheres is cubic and equals to $\varepsilon_{mf} = \frac{6-\pi}{6} = 0.476$. It can be seen that this estimation due to the consideration of uniformity of the particles, tends to slightly overestimate the results.

Above the fluidization point, only a certain portion of the fluidizing gas flows through the dense particle phase, the remaining gas passes through the fluidized bed in the form of virtually solids-free gas bubbles. There are therefore two distinct phases:

- Emulsion phase
- Bubble phase

The choice of bubbling bed regime is due to the fact that the bubbles in fluidized beds cause for the most part those properties that characterize the fluidized beds:

- good solids mixing
- uniform temperature distribution over the entire fluidized bed

  - good heat transfer between fluidized bed and wall

There are various models proposed by different authors for two-phase models:

  - Model of Davidson and Harrison (1963)
  - Model of Patridge and Rowe (1966)
  - Model of Kunii and Levenspiel (1969)
  - Model of Kato and Wen (1969)
  - Toomey and Johnstone (1952)
  - Model of Hespbasli (1998)
  - Model of Babu et al. (1978)

Different models are briefly described and compared here. The first mentioned model assumes perfect mixing in the dense phase and underestimates the overall conversion for the reactions. The second model allows the calculation of variable bubble sizes and velocities and also considers the presence of clouds but brings more complexity to the numerical calculations. The Kunii and Levenspiel model assume average bubble properties to simulate the entire bed, but in the same time, clouds and wakes and reactions within them are considered. Gives good prediction for bubble phase profiles and overall conversions.

The Kato and Wen bubble assemblage model is suited to represent very complex hydrodynamics due to allowance for variable bubble properties but in the same time tends to overestimate the concentrations in the dense zone.

The Toomey and Johnstone model is relatively simple but it gives an overestimation of the visible bubble flow.

Other methods for calculating the bubble fraction as a function of the bed expansion ratio, R_{bd}, have been proposed Hespbasli, 1998; Babu et al., 1978, which doesn’t take into account the bubble size and tend to overestimate the bubble fractions to compare with other models.

Here for the simplicity only Toomey and Johnstone (1952), Babu et al. (1978) and Hespbasli (1998) models are discussed. The effort of calculating bubble fraction in the bubbling bed and subsequently the bed height, is done to:

- Determining the bed height at operational condition
- Particle distribution over the CFB system
- Pressure drops in the gasification reactor
- Gas residence time in the bubbling bed of the GR
- Gas residence time in the freeboard of the GR

With the application of the two-phase theory of Toomey and Johnstone for fluidized beds, it should be noted that, one part of the gas injected through the distributor tray or the pipes, flows into the bubble phase and one part into the emulsion phase. The part of the volumetric flow which enters the bubble phase, contributes to bubble formation according to the Equation 17:

Equation 17 $\dot{Q}_0 = \frac{Y.(U-U_{mf}).A}{N}$

Where A is the cross-sectional area of the fluidized bed and N is the number of holes in the distributor tray.

The proportion of the bed cross-section which is filled by bubbles ε_b can be written as Equation 18:

Equation 18 $\varepsilon_b = \frac{\dot{Q}_b}{A.u_a}$

u_a denotes the rising velocity of the bubble in the swarm and can be correlated to the corresponding velocity of a single bubble $u_{b\infty}$ with Equation 19. The reason for the higher speeds in the swarm is not clear. They are likely to be due to coalescence processes.

Equation 19 $u_a = u_{b\infty} + (U - U_{mf})$

There are several semi-empirical methods to calculate the velocity of a single bubble in the fluidized bed. The Equation 20 is most frequently used. As some experimental results show, this equation is likely to overestimate the ascent rates of single bubbles in fluidized beds.

Equation 20 $u_{b\infty} = 0.71.\sqrt{g.d_{eq}}$

There are a variety of semi-empirical to empirical equations in the literature that provide more or less good bubble diameter predictions as a function of fluidized bed height. Here is an example of a correlation according to (Darton et al., 1977):

Equation 21 $d_{eq} = 0.54.\left[Y.\left(U - U_{mf}\right)\right]^{0.4}.\left(z + 4.\sqrt{A_0}\right)^{0.8}.g^{-0.2}$

The A_0 is the so-called catchment area for a bubble stream at the distributor plate. It is usually the area of distributor plate per orifice. For a porous plate, $A_0 \approx 0$. Reasonable agreement with several independent data sets is reported (Gas-Solid Phenomena 1984).

z means the distance from the distributor floor, where z = 0 denotes the height directly at the distributor floor.

Applying Darton's equation (Equation 21) one needs to define the catchment area properly $A_0=A/N$ (A_0=catchment area of bubble streams, N=number of nozzles, A=cross-sectional area of the reactor). The typical values are between 0.01 to 0.02 for distributor plates. But since in our system, steam is injected via pipes (5 pipes), it assumed to be zero as in a porous plate. The results from this model will be compared with the models proposed by (Hespbasli, 1998) and (Babu et al. 1978).

Hespbasli, 1998; Babu et al., 1978 methods for calculating the bubble fraction, use a bed expansion ratio, R_{bd}:

Equation 22 $\delta_b = 1 - \frac{1}{R_{bd}}$

(Hespbasli, 1998), gave the following expression, Equation 23, valid for $R_{bd}>1$:

Equation 23 $R_{bd} = 0.5482 d_p^{0.129} (U - U_{mf})^{0.111}$

and (Babu et al. 1978) proposed Equation 24:

Equation 24 $R_{bd} = 1 + \frac{14.31 (U - U_{mf})^{0.738} d_p^{1.006} \rho_p^{0.376}}{\rho_g^{0.126} U_{mf}^{0.937}}$

A correction factor Y=0.8 is applied to the Equation 23 and Equation 24.

And finally, the bed porosity at bubbling bed regime can be calculated by Equation 25:

Equation 25 $\varepsilon_{bed} = (1 - \delta_b)\varepsilon_{mf} + \delta_b$

The Hespbasli correlation gives value of $R_{bd}<1$ in our calculations, therefore, cannot be used.

The Babu correlation was obtained using a large number of literature data obtained for coal and related materials.

Equations 22, 24 and 25 are used to calculate the bed porosity according to Babu et al. model and equations 17, 18, 19, 20, 21 and 25 are used for the Toomey and Johnstone model.

It should be noted that the bubble fraction and bed porosity calculated here are average values over the bed of the GR. Since steam input, superficial velocity, and bubble diameter changes over the height, hence the bubble fraction and bed porosity are also function of height. The mean values are taken into account for simplicity and the results of two models are reported and compared in the Figure 33:

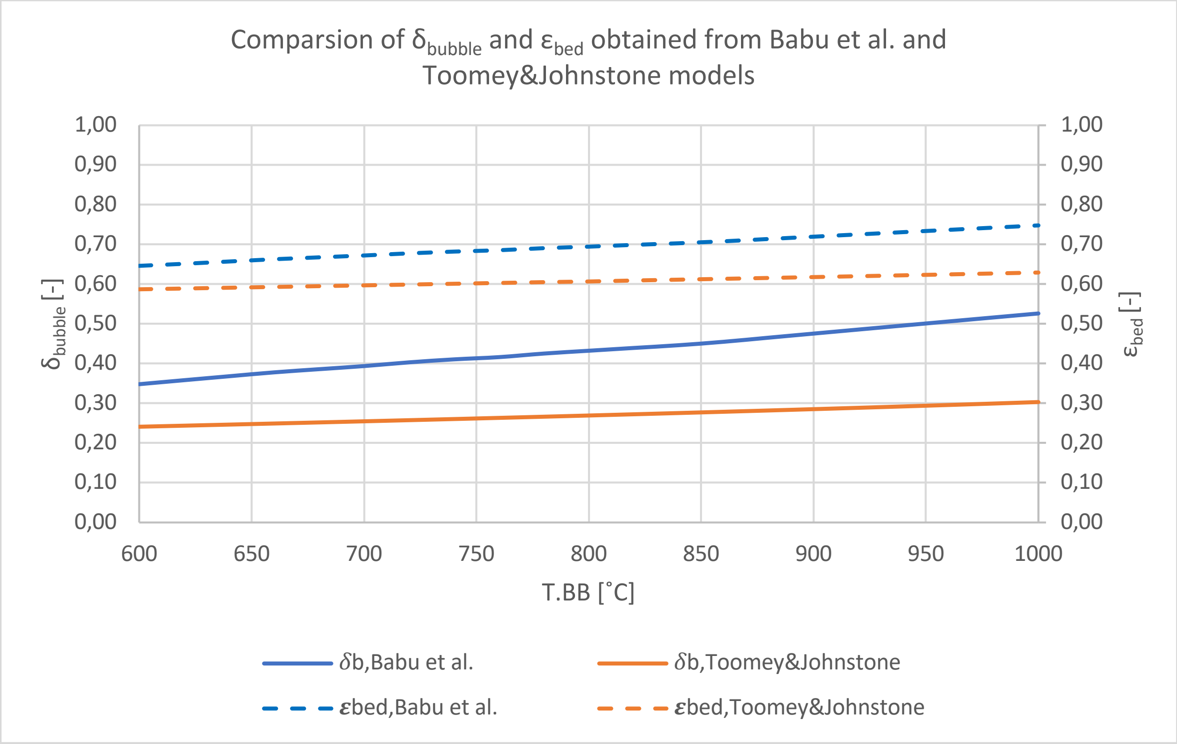

Figure 33 Bubble fraction and bed porosity of the GR according to Babu et al., and Toomey&Johnstone

As it was predicted, Babu et al. model tends to overestimate the bubble fraction and bed porosity due to its simplicity and lack of consideration of bubble diameter. Further for the bed height at operational condition and gas residence time in GR, the results from Toomey & Johnstone are taken into account.

The average bed porosity of different sections of the GR in a separate way is reported in the Figure 34**Error! Reference source not found.**:

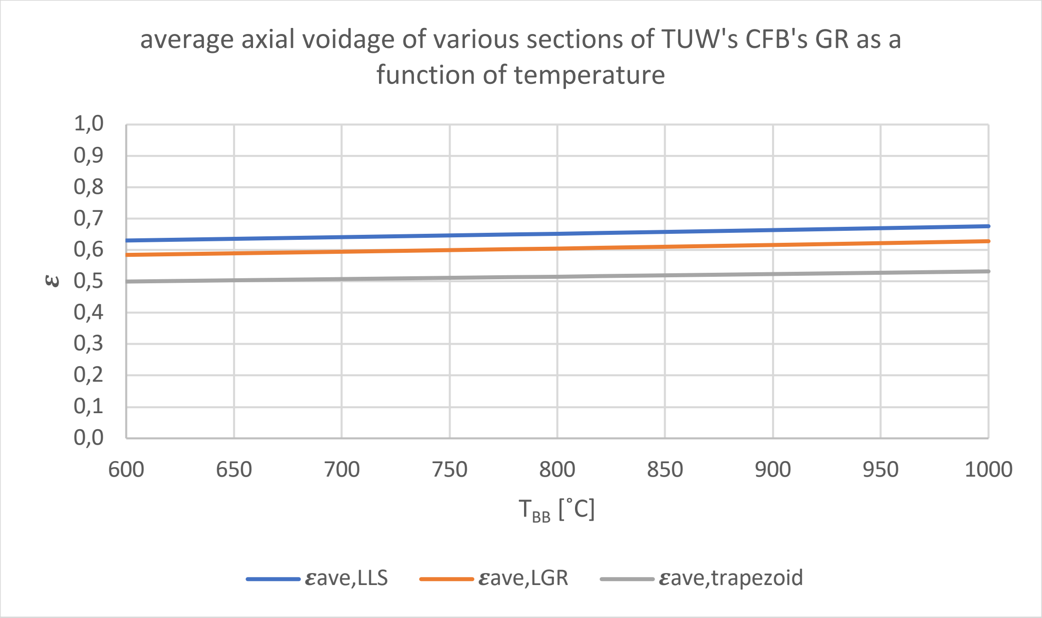

Figure 34 Average bed porosity of various parts of the GR as a function of bed temperature

It can be observed that, the bed porosity in the lower loop seal is higher than that of lower gasification part and trapezoidal section of the GR, due to its lower cross-sectional area. The increasing of cross-sectional area in the trapezoidal section, results to lower bed porosity. The bed porosity at the lower loop seal is considered to be equal on both sides of the GR and the CR. The bed porosity of the CR will be discussed in the next chapter.

Combustion reactor

The bed material passes through the riser while transport the char particles from the GR to adsorb the heat generated by burning the char and take back this heat to the GR to provide the necessary heat for the overall endothermic reactions occurring in the GR.

The riser is a relatively long reactor with narrow section-area (ϕ=125 mm, L=4.5 m) and works in fast fluidization regime to operate in the transport mode, with solids carried over from the top of the riser separated and returned to the GR via non-mechanical connections (loop seals). The transition from low-velocity fluidization to transport operation occurs when significant solid entrainment commences with increasing superficial gas velocity. There some methods proposed to quantify the transition, either based on solid entrainment or solid concentration profile.

The particle characterization has been already done in the particle characterization chapter. In order to define the minimum fluidization, terminal, transport and critical velocities for the CR, first one must define the temperature range for the operational mode of the CR and the fluidization gas characteristics corresponding to the temperature.

In order to proceed with the calculations, first must define the average temperature in the riser with regards to the temperature of the GR.

To find some correlations between temperatures of various parts of the CFB gasifier, the temperature measurements of various experiments are taken into account. Several temperature sensors are implemented over the system as can be seen in the Figure 35:

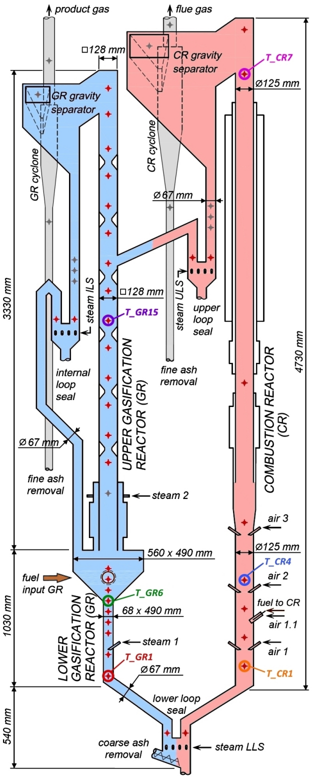

Figure 35 Schematic figure of the100 kWth CFB gasifier of TUW with temperature sensors

Temperature of GR6 is our reference point and represents the temperature of bubbling bed of the GR. Devolatilization products and char gasification rate are calculated based on this temperature, namely "T_{GR6} or T_{BB}".

In the Figure 36, other temperature points are shown as the function of T_{GR6}:

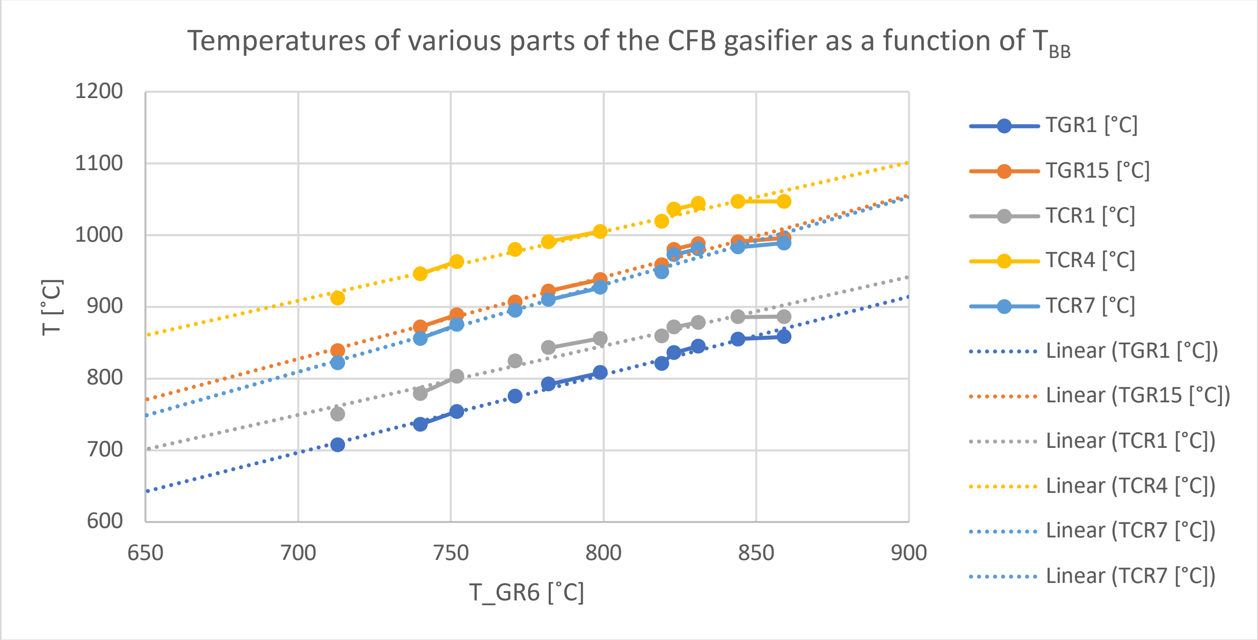

Figure 36 Temperatures of various parts of the CFB gasifier of TUW

As it can be seen, there are almost linear relationships between these values. On the average, T_{GR1} is 5˚C higher than T_{GR6} but for simplification they can be assumed equal: $T_{GR1} \approx T_{GR6}$.

T_{GR15} on average is 140˚C higher than T_{GR6} ($T_{GR15} \approx T_{GR6}+140$˚C) and will be the reference temperature for homogenous reactions in the freeboard.

The relationships between T_{GR1} and T_{CR1} are not very linear and as T_{GR1} increases, the difference between these two values decrease and they get closer. T_{CR4} has a linear relationship with T_{CR1} and on average is 160 ˚C higher. Also, between T_{CR4} and T_{CR7} cannot find a linear relationship, since at higher temperatures their difference decrease.

For simplification, T_{CR} is considered to be average of T_{CR1}, T_{CR4} and T_{CR7}. The $T_{CR}=(T_{CR1}+T_{CR4}+T_{CR7})/3$ shows a linear relationship with TGR6 with a higher value of 125 ˚C on average:

$T_{GR1} \approx T_{GR6}$	temperature of bubbling bed of the GR
$T_{GR15} \approx T_{GR6}+140$˚C	temperature of the freeboard of the GR
$T_{CR}=(T_{CR1}+T_{CR4}+T_{CR7})/3=T_{GR6}+120$˚C	temperature of the CR

Now with knowing the temperature range of the CR in correlation of T_{GR6}, one need to define the operational condition of the CR. The main fluidization agent used in the CR is air, to burn the residual char coming from the GR, plus half of the steam input at LLS that transport the bed material and char towards the CR. The characteristic of the air as a function of T_{CR} is reported in the Figure 37 and Figure 38:

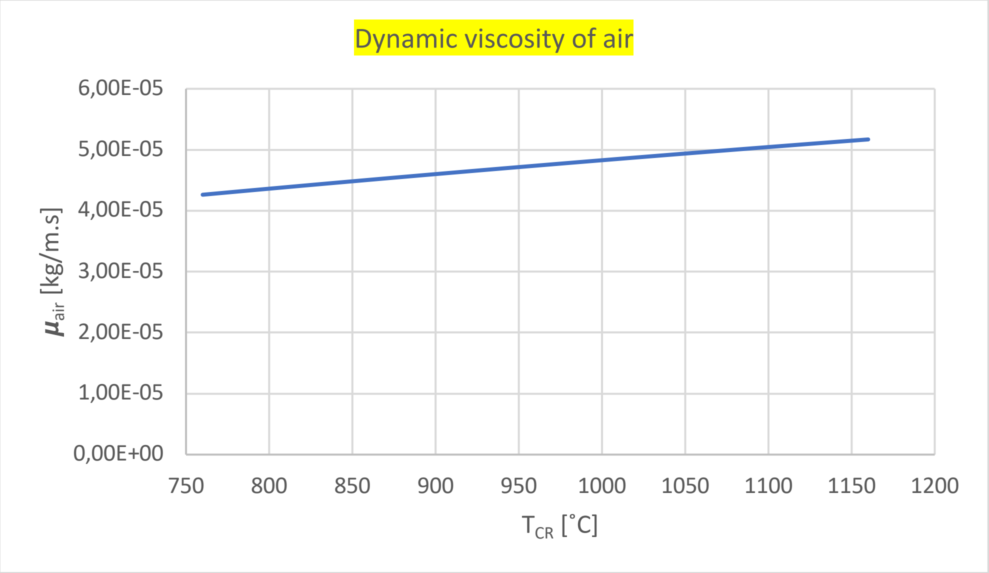

Figure 37 Dynamic viscosity of air as a function of temperature

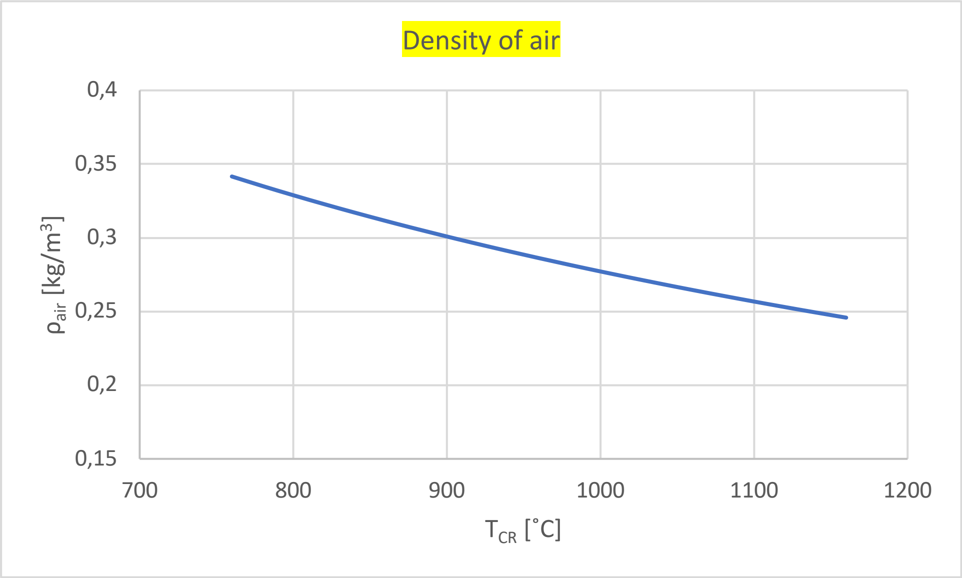

Figure 38 Density of air as a function of temperature

Minimum fluidization velocity

Minimum fluidization velocity for the riser is calculated as a reference point. The results are shown in the Figure 39:

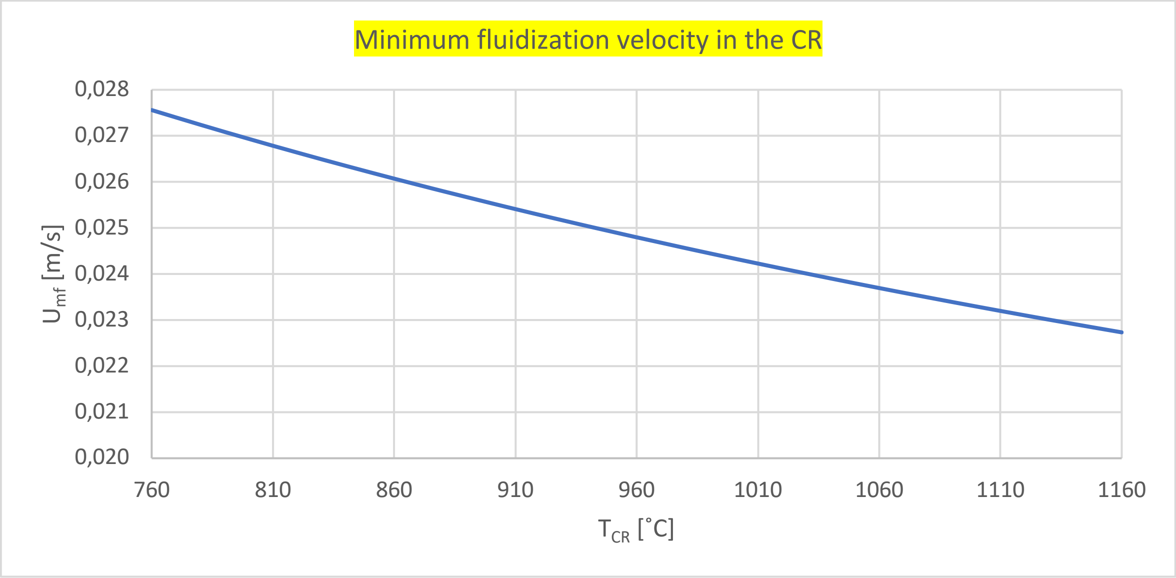

Figure 39 Minimum fluidization velocity in the CR as a function of temperature

Terminal, transport and critical velocities

The terminal velocity of a single particle is an intrinsic characteristic of the particle, and its calculation and measurement are as important as other intrinsic particle properties, such as particle size and density. Calculation of the terminal velocity is explained in the previous chapters. Here are the results for the riser in the Figure 40:

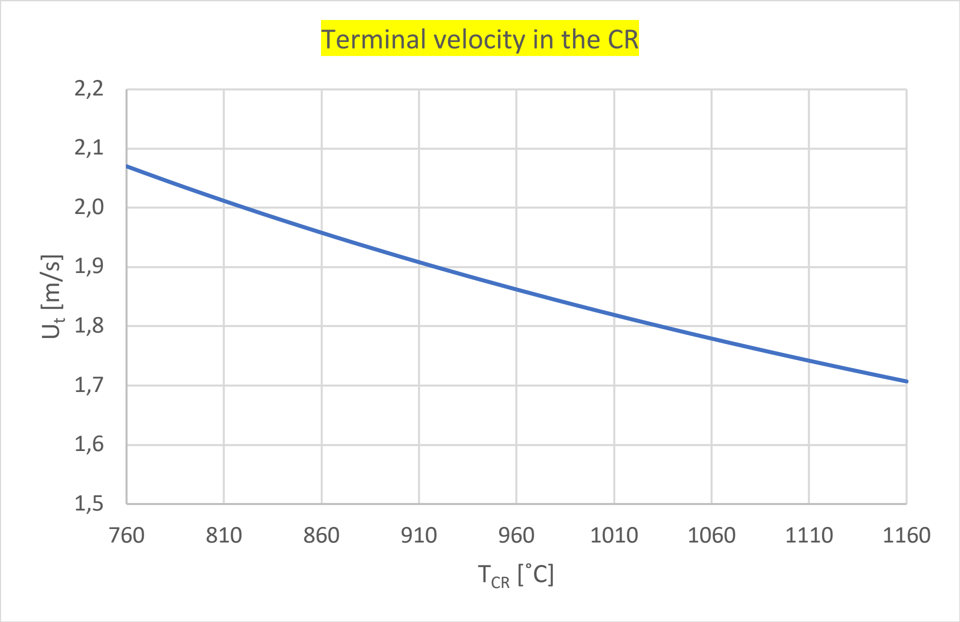

Figure 40 Terminal velocity in the CR as a function of temperature

Checking U_t* on the state diagram, shows that we are still far from fast fluidization. Here we discuss more intrinsic characteristics of particles in the riser to figure out how to determine proper gas velocity and gas flow rate.

U_{se}: Critical velocity, based on solids entrainment:

In the CFB design of the TUW, the scope of the CR (riser) is to provide heat for the GR through circulation of bed material, hence, solid entrainment from the CR is required to achieve. In a gas-solids transport system, solids flux and gas velocity are linearly proportional. This critical velocity, designated U_{se}, (Bi et al 1995), can be considered a hindered or apparent terminal velocity of bed particles because the entrainment of single particles is initiated when the superficial gas velocity reaches the terminal settling velocity, while U_{se} can be considered to correspond to the onset of significant entrainment for the assembly of particles.

To summarize, U_{se} should not depend on column dimensions and geometry (ie. riser height, riser diameter, solids feed device) or on solids inventory when large diameter, tall risers are used. U_{se}, like U_{mf} can thus be considered to characterize the bed material behavior.

U_{se} can also be determined in a batch fluidized bed from the emptying time (Bi et al., 1995). A correlation for U_{se} based on data from relatively tall and large columns (Bi et al., 1995) gives:

$Re_{se}=1.53Ar^{0.5}$

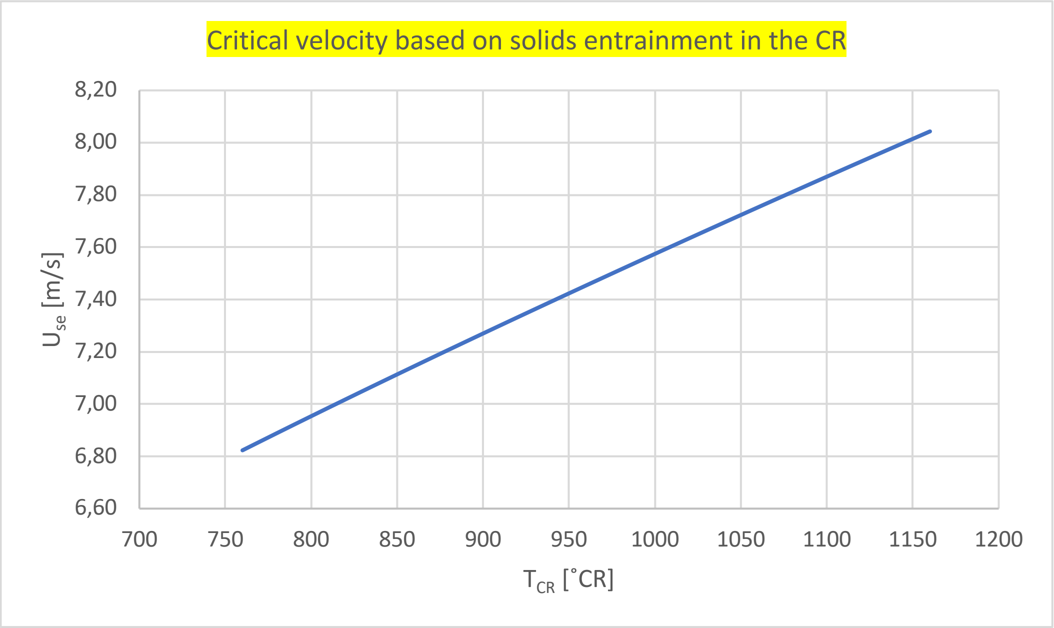

Figure 41 Critical velocity in the CR as the onset of significant entrainment of solid particles

Checking U^*_{se} values on the state diagram, it's noted that we are at the intersection between the turbulent and fast fluidization regime, where a notable solid entrainment begins. To set the operational condition one more intrinsic characteristic will be discussed here to draw the final conclusion.

U_{tr}: Critical velocity based on solid circulation rate

One critical solid circulation rate may exist when a sharp change in pressure drop over the lower part of the riser takes place when varying the solid circulation flux at a given gas velocity, U_s. As superficial velocity increases beyond a certain point, the sharp change in the pressure gradient disappears. The gas velocity at this critical point, defined as the transport velocity U_{tr}, marks the onset of fast fluidization (Yerushalmi and Cankurt, 1979). An examination of pressure gradient profiles (Bi, 2002) reveals that U_{tr} varies with height. U_{tr} may indicate a transition of axial voidage profiles in the riser.

Below this velocity, a distinct interface exists between the top-dilute and bottom-dense regions. Beyond this velocity, the interface becomes relatively diffuse.
To predict U_{tr}, several correlations have been developed, most of the form
$Re_{tr}=kAr^n$
Typical k and n values are given in Bi et al. (2000), with k=2.28 and n=0.419 from Bi and Fan (1992).

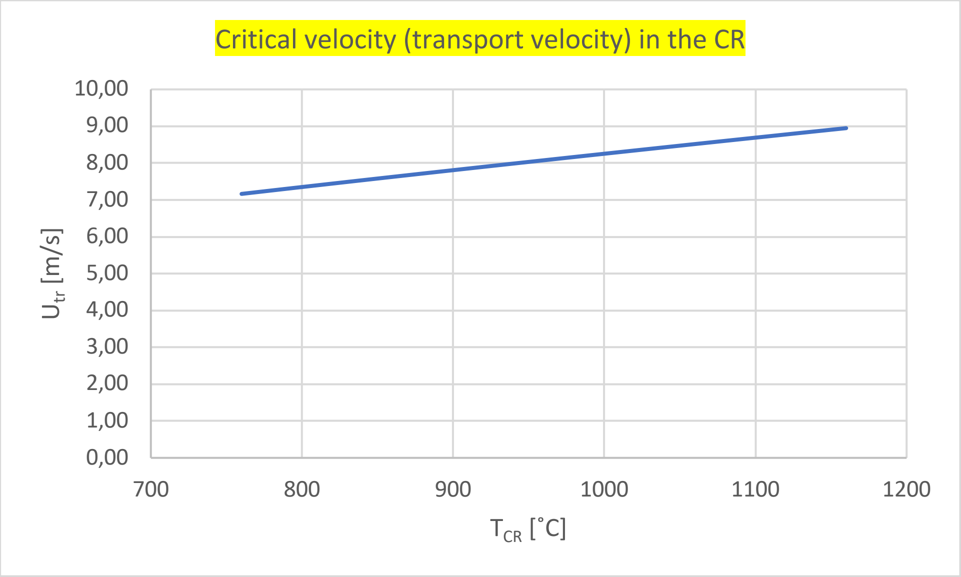

Figure 42 Critical velocity in the CR based on solid circulation rate

U_s: Superficial velocity:

All the above-mentioned superficial velocities are reported in the Figure 43, and their ratios respect to each other are shown in the Figure 44.In the Figure 45 the a-dimensional values for the Reh's state diagram are reported and after investigating these values on the diagram, the superficial velocity for air can be chosen for operational condition.

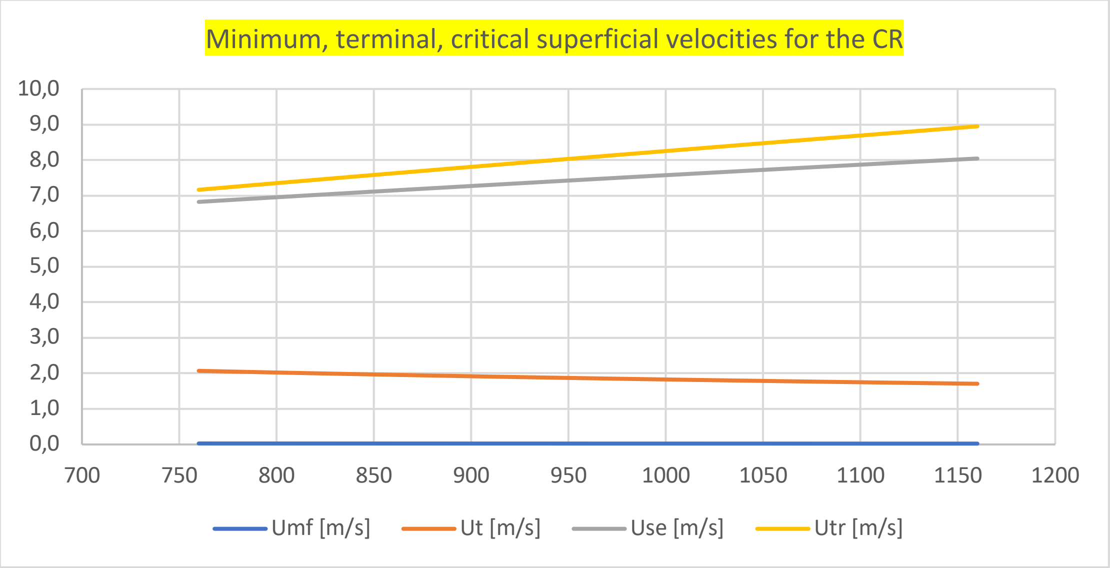

Figure 43 All intrinsic velocities in the CR as a function of temperature

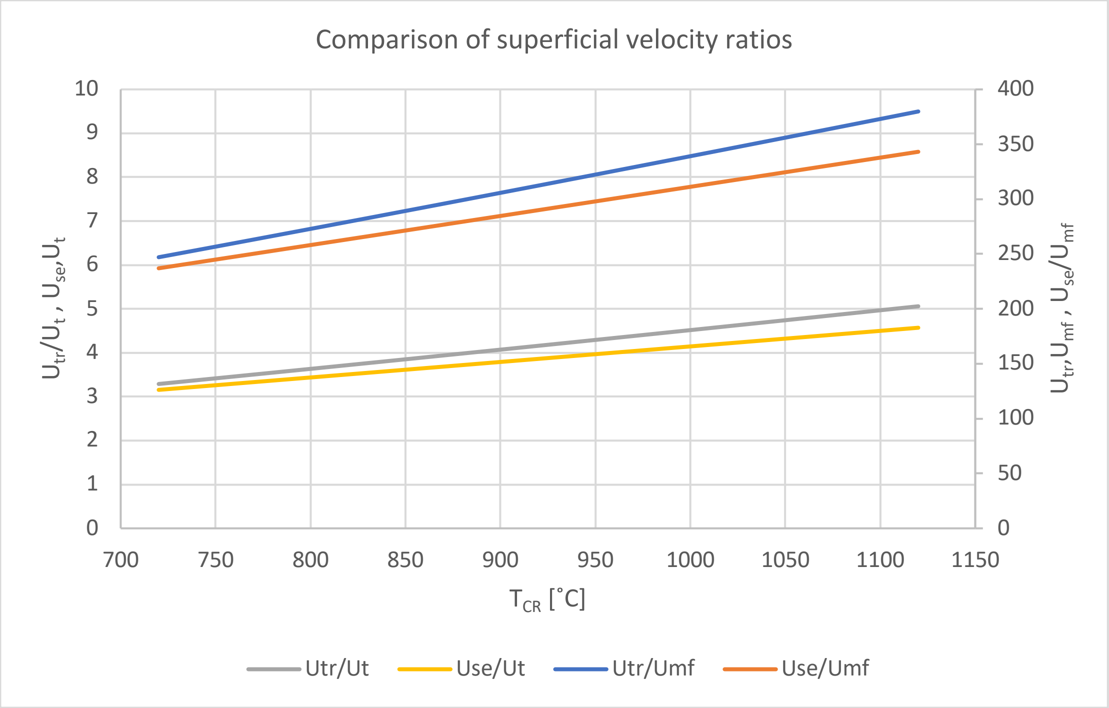

Figure 44 Comparison of superficial velocity ratios in the CR

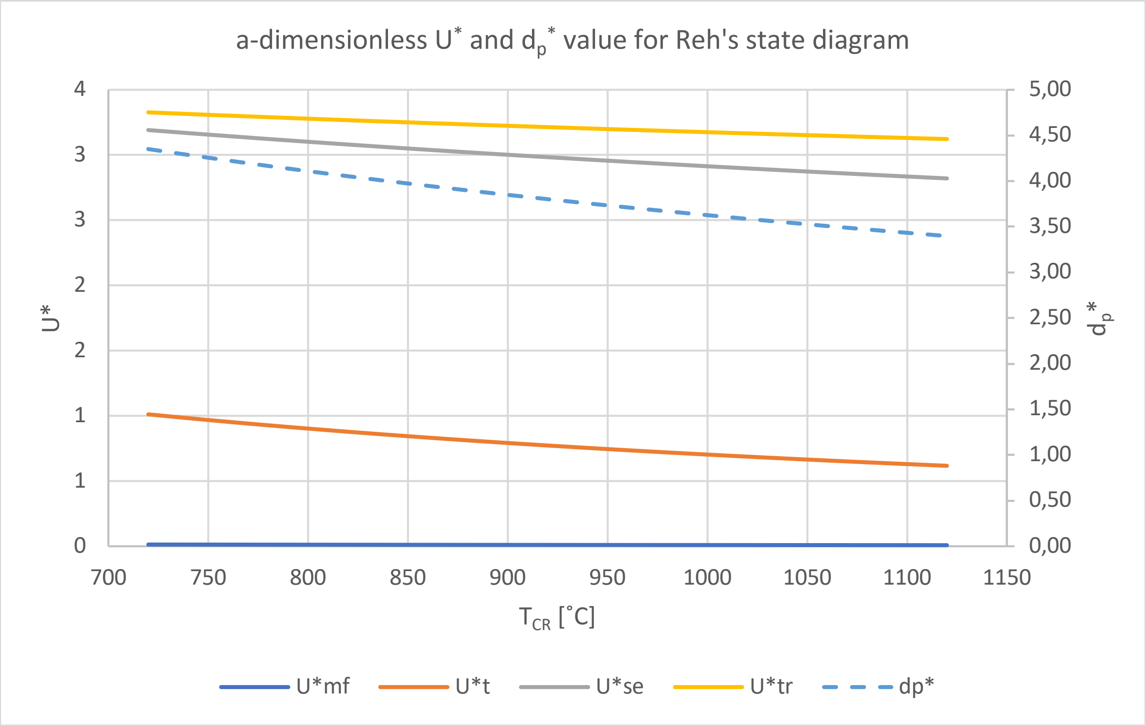

Figure 45 A-dimensional values of the CR for Reh’s state diagram

The dimensionless values reported in the figure above, are investigated on the Reh state diagram to identify their corresponding fluidization regime and the results is shown in the figure below:

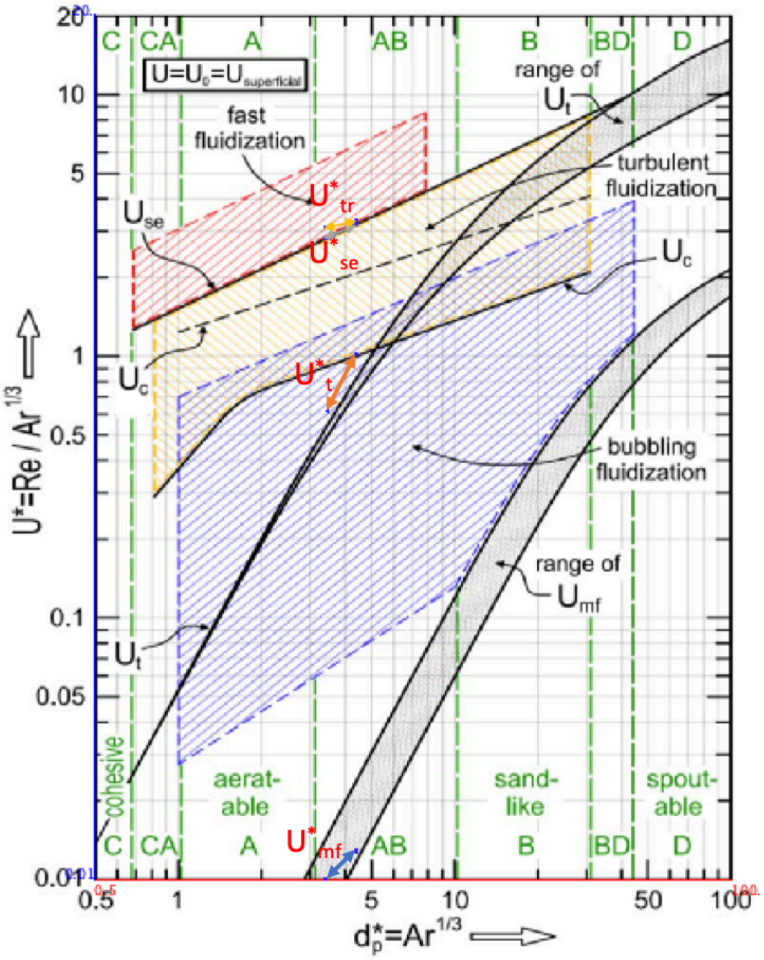

Figure 46 Reh's state diagram to identify fluidization state of the CR

The gas superficial velocity is then considered to be equal to U_{se} as the onset of fast fluidization and noticeable solid entrainment flow and air input is calculated based on this reference velocity. Air on one hand fluidize the bed material in the riser, and on the other hand oxidize the unconverted char coming from the GR to provide heat. In order to have a fully combustion, one must ensure that the calculated air input is higher than of stoichiometric value for burning the residual char. The air in the CFB design of TUW, is injected in three different parts above the LLS in the riser. First air injection is at the height of 690 mm, second one is at 1090 mm and the third and last one at the height of 1490 mm above the ground (base line of the CFB system). Staging the air input helps to better fluidize the bed material, and mitigates creating hot spots at the bottom of the riser, especially in the cases where additional fuel input is required to maintain the heat at the GR. The first and second air input are decided to be equal, but the last one is decided to be half of the 1st and 2nd one, since most of the char is already burned at this point and there is less bed material on top of this point to be fluidized. Therefore:

$Q_{air1}=Q_{air2}=2Q_{air3}$

Air flow input in the riser is more discussed in the section of operational condition of the CR.

Bed porosity

The riser is working in the fast fluidization regime to ensure the bed material circulation. From the bottom of LLS to the point where the first air input is injected to the system, is working at bubbling bed due to half of the steam input at LLS. This lower part of the system is assumed to have the same porosity as the other half of the lower loop seal. As for the fast fluidized section, there are some experimental techniques to measure the bed porosity which is avoided here due to complexity. There are as well some correlations to calculate the bed porosity based on either particle flux or pressure gradient over the height of the riser. The latter is available from the experiments.

In practice, the great majority of measurements of spatial average voidages have been derived from differential pressure measurements. If friction at the wall and acceleration effects are neglected, the vertical gradient of pressure in the upper part of the riser acts like a hydrostatic pressure gradient, so that, for gas-solid systems with $\rho_g \ll \rho_p$, the average voidage and solids hold up over the section in question can be then be estimated with Equation 26:

Equation 26 $\frac{dP}{dz} = -g\left[\rho_p(1 - \varepsilon_{ave}) + \rho_g \varepsilon_{ave}\right]$

In order to apply Equation 26, pressure taps should be provided at regular intervals covering the entire height of the riser, beginning just above the gas distributor at the bottom of the riser, with the distance between successive pressure taps small enough that the pressure gradient term, dP/dz, can be estimated with little errors. Unfortunately, there are only few pressure-taps over the riser (9 sensors), therefore the average axial voidage obtained from the estimated pressure gradient, will be compared with other experiments in the literature and other calculation methods.

Also neglecting wall friction is only reasonable for large columns, but it it can lead to significant deviations for D (or equivalent diameter [=4 x Area/Premier] for non-circular sections) less than 0.1 m. The CFB's riser of TUW has a diameter of 0.125m, but still deviation due to wall friction can be hardly neglected.

In the Figure 47 a typical pressure profile of the CFB at experiments is shown.

Various points at different temperatures from experiments are taken into account to estimate the average riser axial voidage.

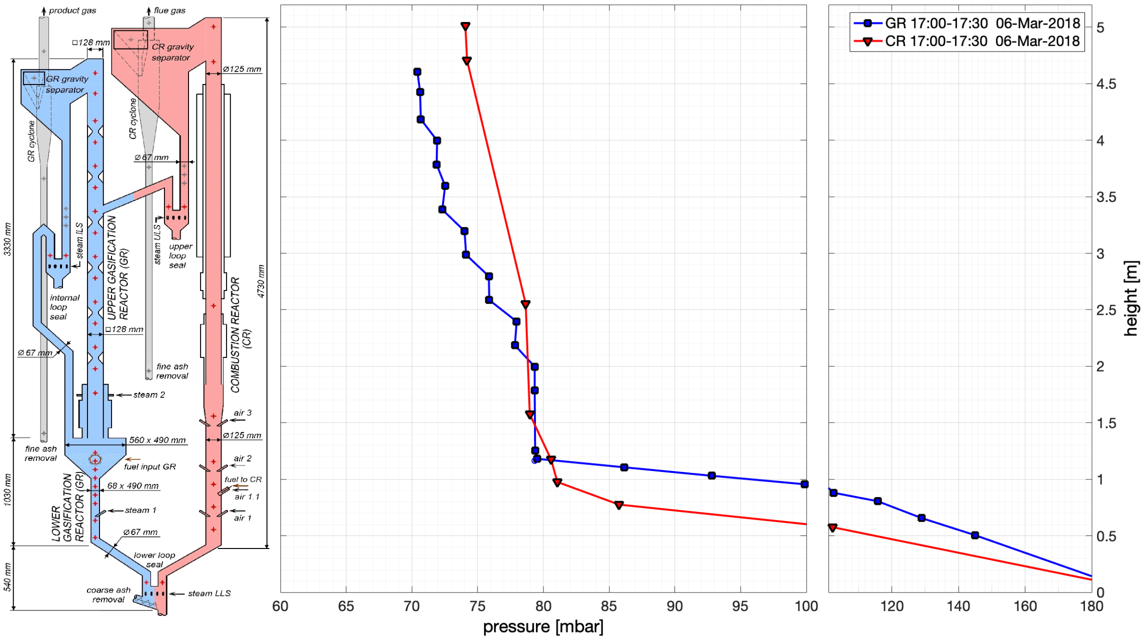

Figure 47 Typical pressure profile measurement of the CFB gasifier of TUW

The results of average axial voidage based on Equation 26 are shown in the Figure 48:

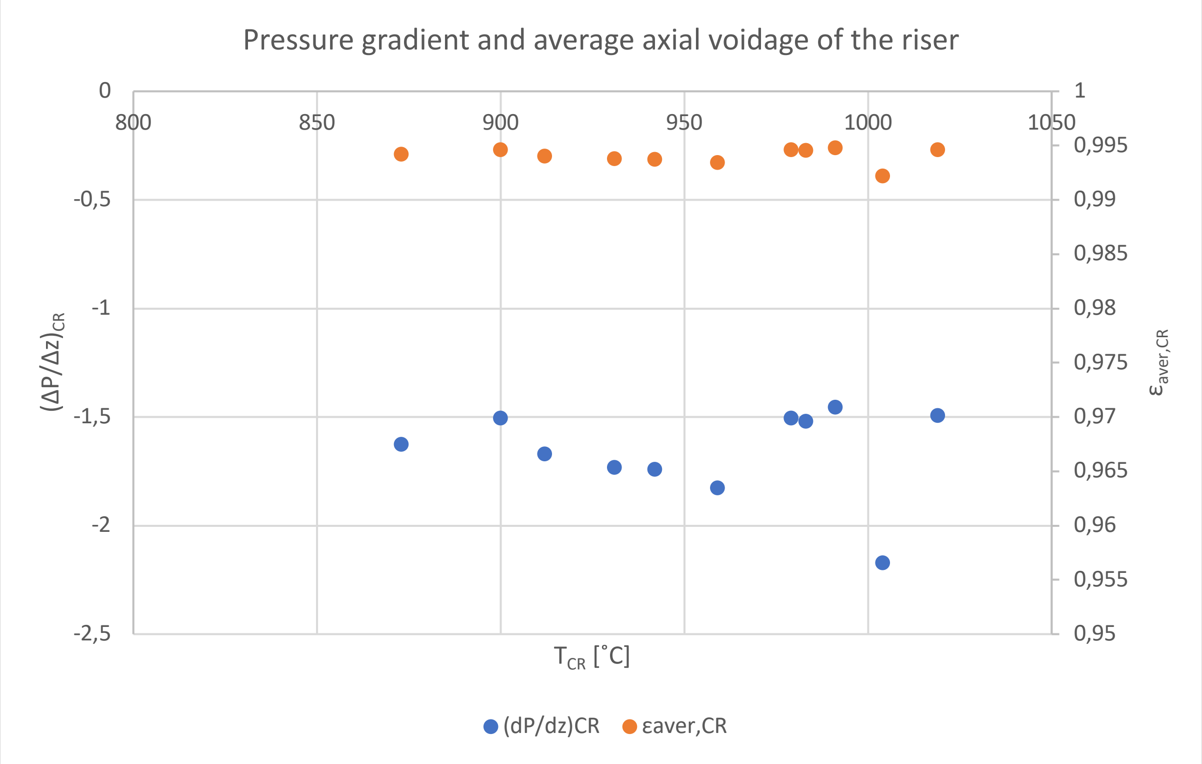

Figure 48 Pressure gradient and average axial voidage of the riser as a function of temperature

The axial voidage in the riser as can be seen from these results is higher than 0.99 (ε_{ave}>0.99 (solid hold up ε^*_s<0.01) which doesn't quite match with the experimental results in the literature.

As it can be seen in the Figure 49 (Figure from book: „Fluidization Engineering“ ed. Kunii & Levenspiel, Butterworth-Heinemann), $\varepsilon^*_s=0.01$ will indicate that the riser is working at pneumatic transport condition and typical values for the solid hold up in the upper part of the riser lies between 0.02 and 0.05. This issue also has been found and discussed in the work of (J. Fuchs et al. 2018), and concluded that for calculating the solid flux from the riser based on the pressure gradient on upper part of the riser, a correction factor must be introduced:

Equation 27 $R = 0.7364 \left(\frac{\Delta P}{\Delta H}\right)^{-0.174}_{upper\ part\ of\ riser}$

Then G_s as solid flux entrainment can be estimated by Equation 28:

Equation 28 $G_s = \left(\frac{\Delta P}{\Delta H}\right) . \frac{Q_g}{A} . \frac{1}{g} . R$

Where ΔP/ΔH refers to the pressure gradient in the upper part of the riser and expressed in (Pascal/m), Q_g is the volumetric gas flow in the riser (m^3/s), g is gravitational acceleration constant (9.81 m^2/s), A is the cross-sectional area of the riser (m^2) and R is dimensionless correction factor. The results, G_s, will obtained as [$kg/m^2.s$], indicating the mass of bed material passing by the cross-sectional area of the riser per second.

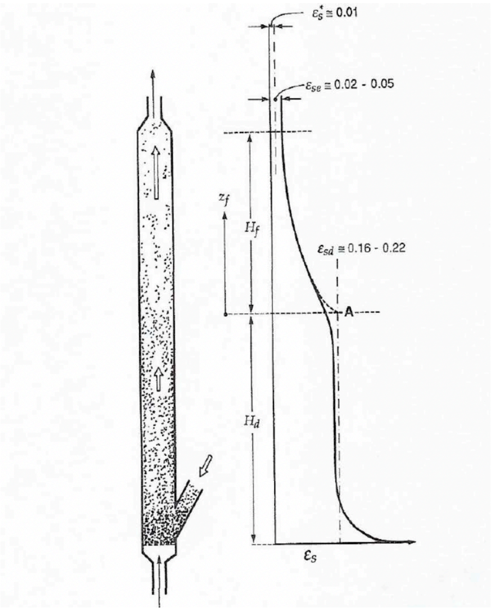

Figure 49 ε_s ... solids fraction, ε_{se} ... solids fraction at exit, ε_{sd} ... solids fraction in dense phase ε_{s^*} ... solids fraction at pneumatic transport

With the method mentioned above, the G_s is calculated based on experimental results, and a linear correlation between G_s and U_s is obtained to use as the basis for the further hydrodynamic characterization of the CFB of TUW. The results and correlation between G_s and U_s are shown in the Figure 50:

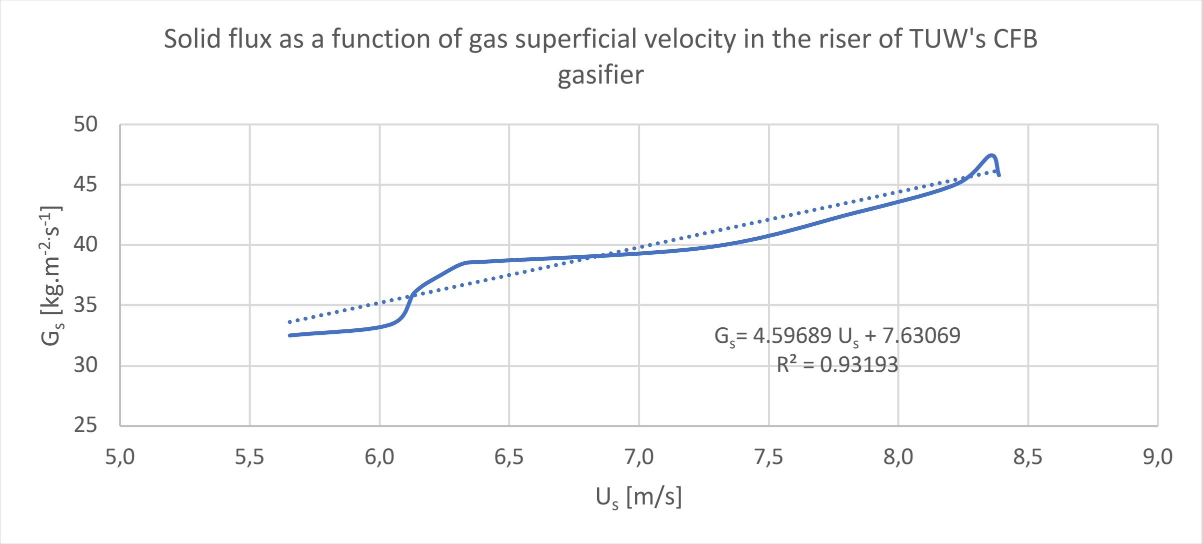

Figure 50 Solid flux out of the riser as a function of gas superficial velocity – TUW's CFB gasifier

In the Figure 50, the X-axis represents gas superficial velocity measured in the experiments, and G_s is calculated from 1.the pressure gradient measured in upper part of the riser, 2.the volumetric air flowrate in the riser, 3.and R as the correction factor. Although the correlation is relatively strong (coefficient of determination R^2=0.93), it's not recommended to conclude that this correlation can be applied to other CFB systems, since it's based on the experimental results of only two plants (TUW's CFB gasifier and an acrylic glass cold flow model). Any extension or extrapolation of this correlation to other system must be well investigated and validated before being applied.

This correlation is used to estimate the net particle flux G_s, with our calculation in the operational condition of the TUW's CFB and the results are shown in the Figure 51:

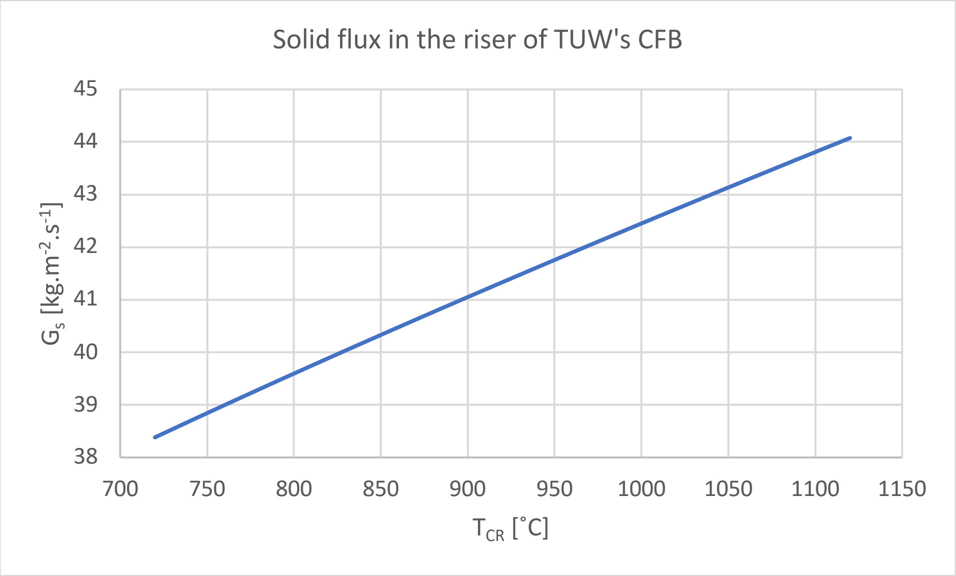

Figure 51 Solid flux in the riser of TUW's CFB as a function of CR's temperature

At this point, after estimating the value of net flux of the particles G_s from the riser, one can calculate the average bed porosity and solid hold ups at lower part and upper part of the riser with two different methods.

In a gas-solid transport system, as mentioned before, solids flux and gas velocity are related by:

Equation 29 $G_s = \rho_p(1-\varepsilon)(\frac{U_g}{\varepsilon} - U_{slip})$

A linear relationship between G_s and U_g in the high velocity range with ε constant (Bie et al. 1995) suggest that U_{slip} in Equation 29 approaches a constant value. This constant value as described before is determined as critical velocity U_{se} and whenever this value is greater than terminal velocity of single particles, should be taken as U_t.

In the Equation 29, G_s is already estimated, superficial gas velocity is set to be equal to the critical velocity, and U_{slip} is equal to the U_{se}. Average bed porosity of the riser then is calculated as a function of temperature:

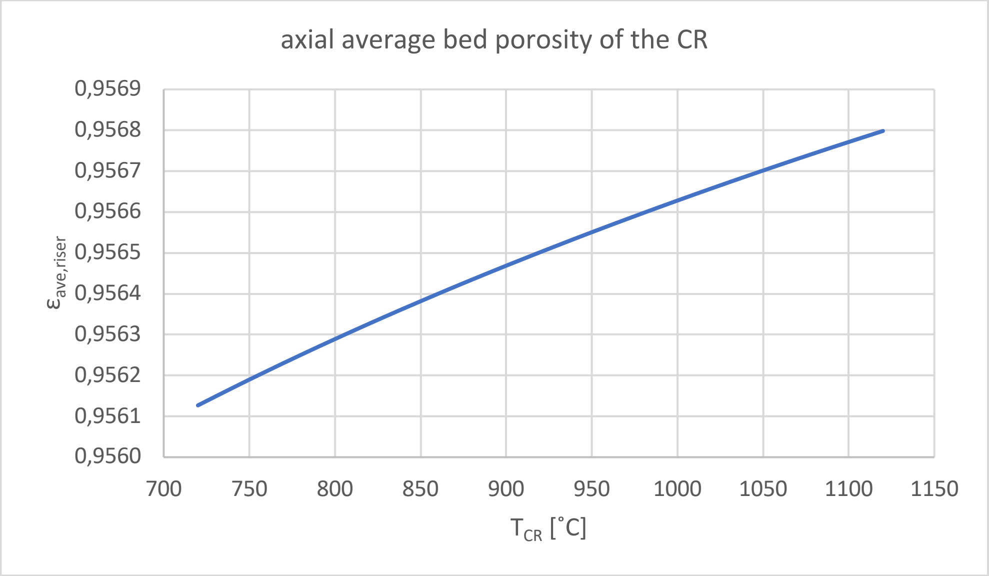

Figure 52 Axial average bed porosity of the CR as a function of temperature

As it can be seen from the results and as it was mentioned earlier, at high superficial gas velocities, bed porosity of the fast-fluidized bed remains almost constant (here it varies between 0.9561 and 0.9568, hence ≈0.956). These obtained values are compared with vast amount of results found in the literatures, and as it can be seen in the Table 12, they quite fit in the range:

Author	H_0 [m]	D [mm]	d_p [µm]	ρ_p [kg/m^3]	U_{se} [m/s]	ε_{ave}
Chang and Louge (1992)	7,00	200	234	1440	4	0,943
			67	7400	2,4	0,995
Bai et al. (1987)	9,00	186	94	1546	1,6	0,932
			187	703	1,6	0,967
Zhang et al. (1990)	6,40	186	384	681	1,9	-
			62	1006	0,8	-
Yerushalmi and Cankurt (1979)	8,40	152	49	1450	1,3	0,976
Rhodes and Geldart (1986b)	6,60	152	42	1020	1,3	0,981
			64	1800	1,3	0,987
			38	1310	1	0,985
Schnitzlein and Weinsten (1988)	8,40	152	59	1450	1,4	0,967
This work	4,6	125	250	2850	7-8	0,956
Zhang et al. (1985)	8,00	115	220	732	1,9	-
Satjia et al. (1985)	6,50	102	155	2446	-	0,994
			245	2446	-	0,996
Bi et al. (1991)	6,40	102	325	660	1,8	0,984
Takeuchi et al. (1986)	5,50	100	57	1050	1,4	0,944
Hirama et al. (1992)	5,50	100	54	750	0,8	0,975
Perales et al. (1991)	2,90	92	80	1715	1,4	-
Chen et al. (1980)	8,00	90	54	3160	2	0,988
			81	3090	2,6	0,985
			58	1780	1,2	0,981
			56	3050	2	0,987
Gao et al. (1991)	8,40	90	62	1020	0,75	0,974
			82	1780	1,5	0,982
			205	760	1,5	0,975
Capes and Nakamura (1974)	9,10	76	256	7510	5,5	0,999
			535	7510	10,4	0,997
			1200	7850	14,5	0,998
			2340	7700	17,1	0,995
			1080	2470	16,1	0,979
			1780	2900	11,1	0,985
Drahos et al. (1988)	2,23	55	120	2550	1,6	0,994
			200	2550	1,7	0,998
Yousfi and Gao (1974)	6,00	50	118	2470	2	-
			143	2470	2,2	-
			183	2470	1,6	-
			290	1060	2,5	-
Horio et al. (1992)	2,40	50	60	1000	0,6	0,921
Zenz (1949)	1,20	44,5	168	2098	1,5	0,98
			587	2483	3,1	0,979
			930	2643	3,4	0,984
			1676	1089	2,7	0,94
Lewis et al. (1949)	3,00	31,8	40	2483	1,3	0,955
			100	2483	1,6	0,938
			280	2483	2,5	0,927
Sun and Yang (1990)	6,00	30	165	794	1,7	-
			325	794	1,9	-
			85	1387	1,7	-
Mok et al. (1989)	9,00	20	210	2620	2,6	0,982

Table 12 average axial bed porosity in the riser from different literature

The average axial bed porosity estimated for the riser in the TUW's CFB gasifier, can also agree with other studies where the axial bed porosity is measured over the height of the riser as a function of superficial gas velocity and solid flux. Two more of these examples are the work of (Brereton, 1987) and (Huang and Zhu, 2001) as can be seen in the Figure 53 and Figure 54 respectively.

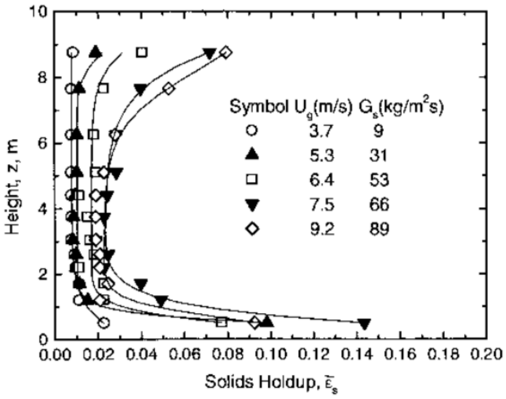

Figure 53 Axial profiles of solid holdup in riser of diameter 152 mm and height 9.3 m with a constricted exit. d_p=148 µm, ρ_p=2650 kg/m^3, air as fluidizing gas (Brereton, 1987)

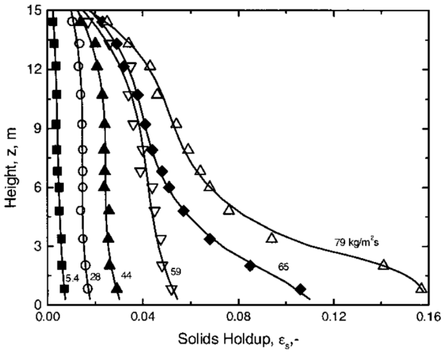

Figure 54 Axial profiles of solid holdup for FCC particles in riser of diameter 0.1 m and height 16 m with a smooth unconstructed exit. d_p=67 µm, ρ_p=1500 kg/m^3, U_g=3.0 m/s. (Huang and Zhu, 2001.)

There are several more method to estimate average axial bed porosity $\varepsilon_{ave}(z)$. Bai and Kato (1999) provide excellent summary tables showing previous correlations and source of data. They also provide useful new correlations based on two cases, one for net circulation fluxes, G_s, less than, and the other for them greater than, the saturation carrying capacity flux, G^*_s, correlated by Equation 30:

Equation 30 $\frac{G_s^* d_p}{\mu} = 0.125 Fr_d^{1.85} Ar^{0.63} \frac{\rho_p - \rho_g}{\rho_g}$

Where:

$4.7 < Ar = Archimedes\ numer < 1020$,

$41 < Fr_d = Froude\ number = {}^{U_g}\!\Big/\!{}_{\sqrt{g d_p}} < 226$,

$607 < density\ ratio = \frac{\rho_p - \rho_g}{\rho_g} < 3610$.

The above-mentioned criteria are satisfied with the characterization of our system. Therefore, the saturation carrying capacity flux, G^*_s, is calculated based on the Equation 30 and compared with the G_s and the results are shown in the Figure 55:

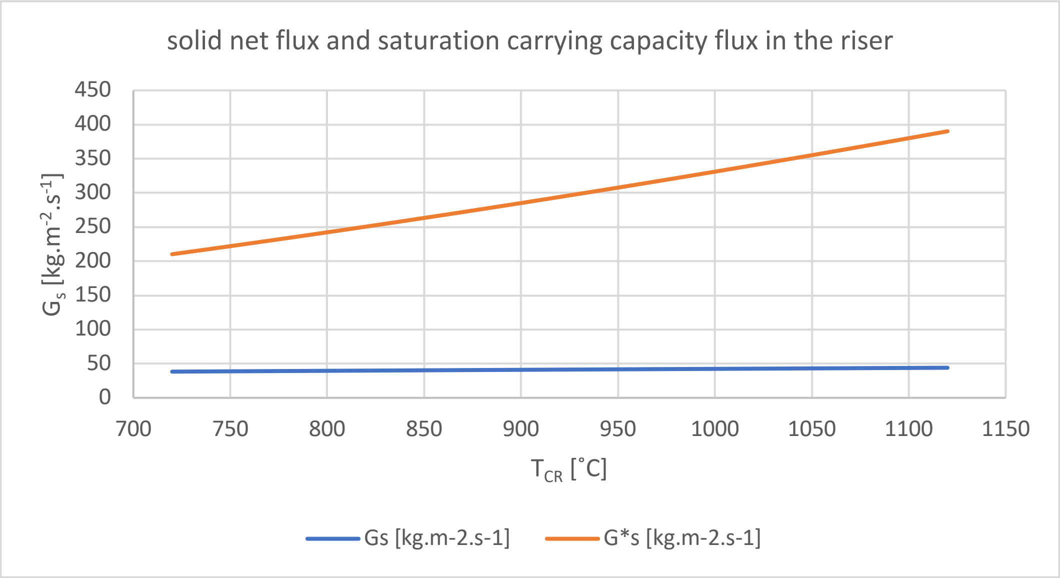

Figure 55 Comparison of solid net flux and saturation carrying capacity flux in the riser

It is obvious from the comparison that G_s is way below the saturation capacity point in our system at operational condition, therefore the following correlations can be used to estimate the solid hold ups at the lower dense part ε_{sd}, and at top exit of the riser ε^*_s:

Equation 31 $\frac{\varepsilon_{sd}}{\acute{\varepsilon}_s} = 1 + 6.14 \times 10^{-3} \left(\frac{\rho_p U_g}{G_s}\right)^{-0.23} \left(\frac{\rho_p - \rho_g}{\rho_g}\right)^{1.21} \left[\frac{U_g}{\sqrt{gD}}\right]^{-0.383}$

Equation 32 $\varepsilon_s^* = 4.04(\acute{\varepsilon}_s)^{1.24}$

Where $\varepsilon'_s = G_s/[\rho_p(U_g - u_t)]$ is the solids holdup excepted for the ideal case where all particles travel with a velocity equal to U_g minus the terminal settling velocity, u_t. The results are shown in the Figure 56:

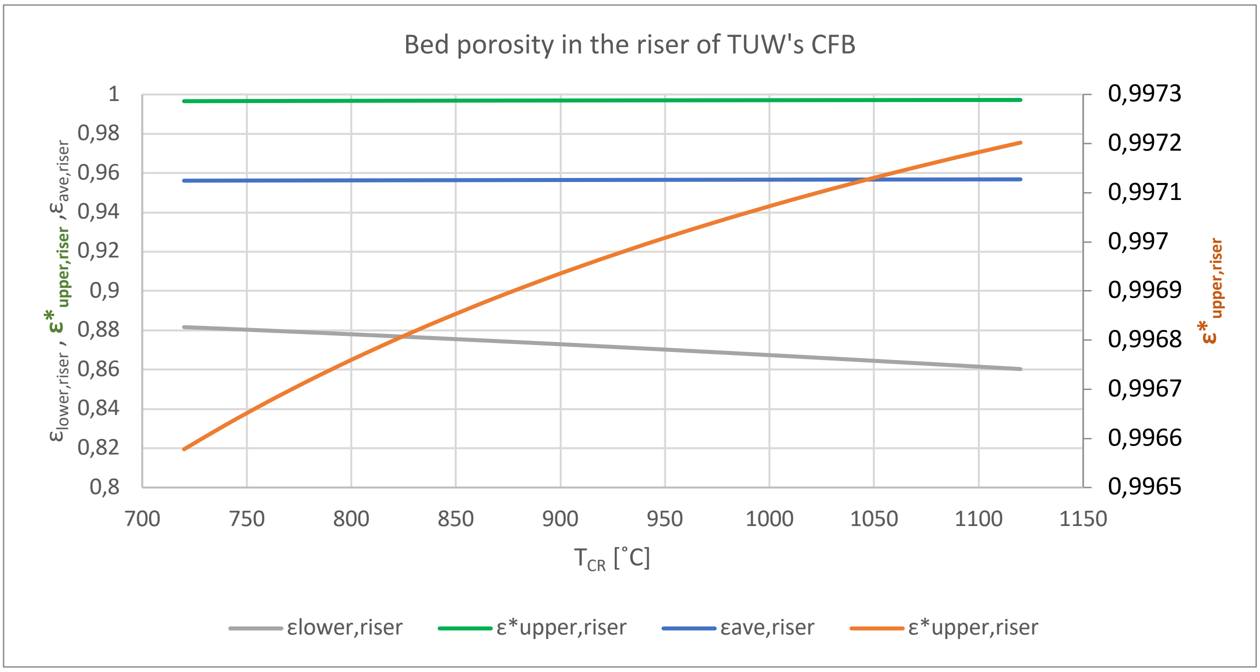

Figure 56 Bed porosity of the riser (TUW’s CFB gasifier) – total average value, at the dense bottom, at the top dilute part

At this point, with knowing the bed porosity of the riser in the dense bottom zone, dilute top zone, and the overall average, one can estimate the point where these two regions of dense and dilute separate:

Equation 33 $Z_i.\varepsilon_{lower,riser} + (L - Z_i).\varepsilon^{*}{}_{upper,riser} = L.\varepsilon_{average,riser}$

The results are shown in the Figure 57:

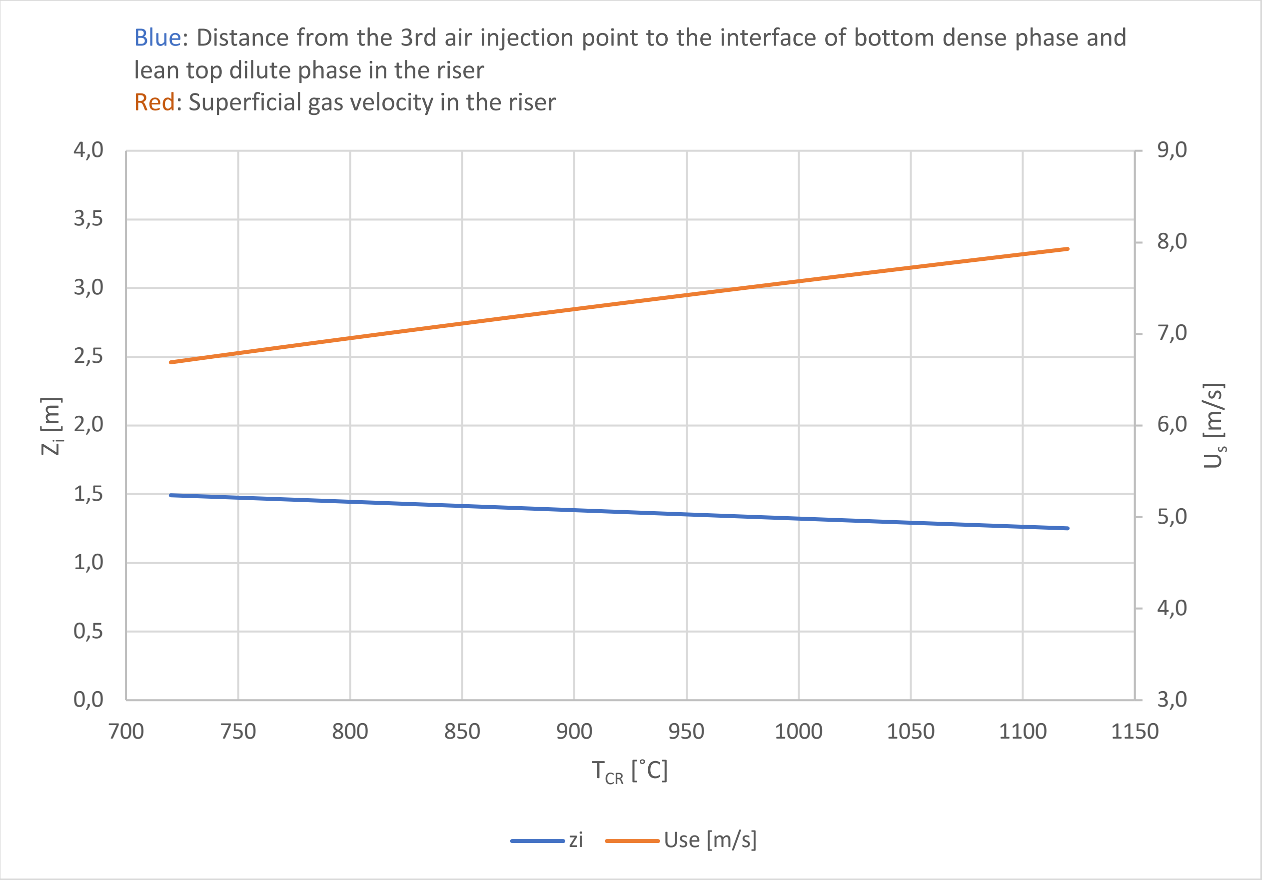

Figure 57 The length of the bottom dense part of the riser in the fast fluidization regime

As it can be seen, with increasing gas superficial velocity, the length of the bottom dense phase of the riser at fast fluidization regime decreases. This founding agrees with the founding of (Haung and Zhu, 2001), that the distance required to achieve fully developed voidage or solids holdup profiles in a riser of small D decreases with increasing U_g.

The implication of these founding on the pressure profile of the TUW's CFB will be discussed in the next chapter.

In the Figure 58, the average axial voidage over the whole CR is summarized:

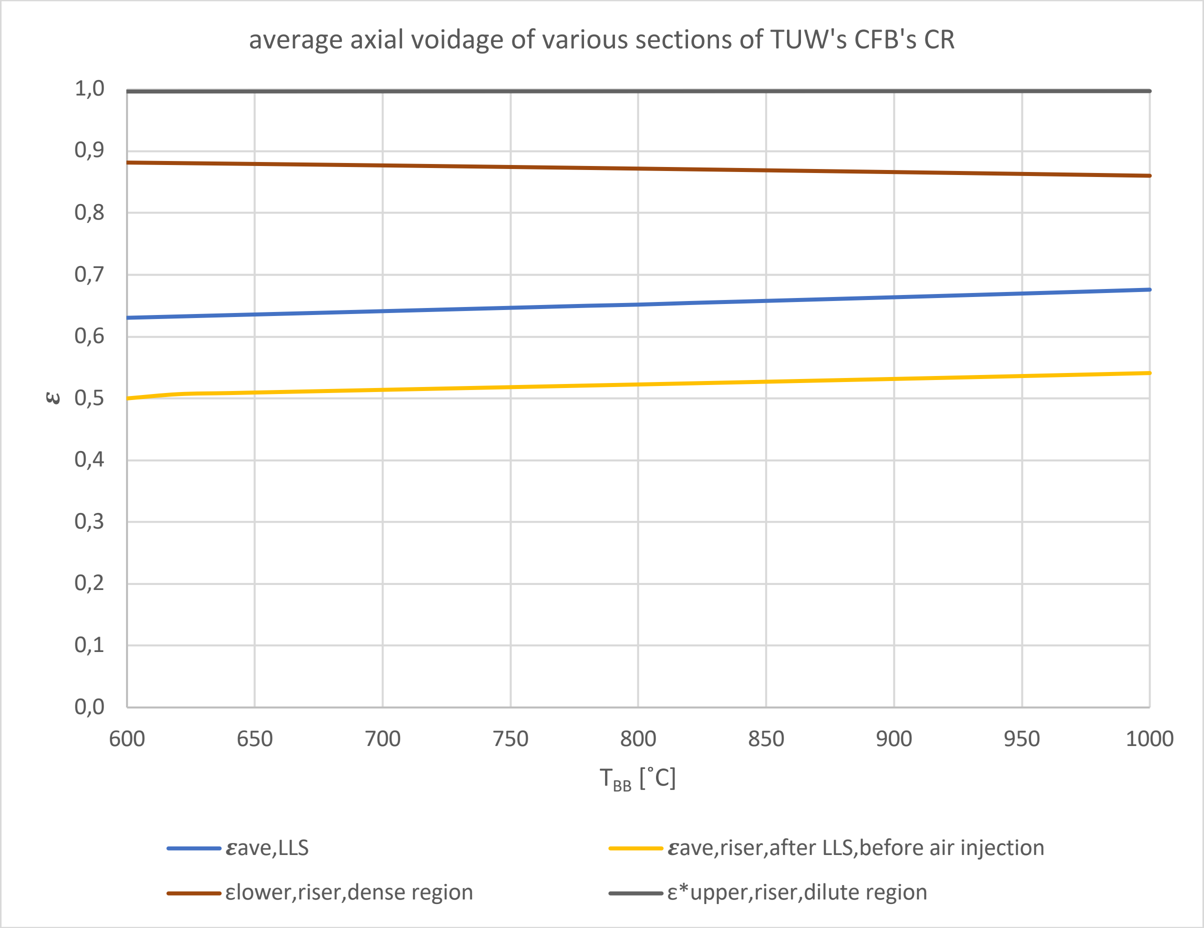

Figure 58 Average axial voidage of various parts of the riser of TUW's CFB as a function of temperature

Operational condition

At this point, one can calculate the total air flow to the system based on the gas superficial velocity as well as staged air flows and compare them with the required amount of air for stoichiometric combustion of char. The feeding rate of softwood pellets as biomass fuel to the CFB system is set to be almost 19 kg/h on dried ash-free basis. According to the proximate analysis of softwood pellets [Table 9], fixed carbon of the SWP is 14.5% on mass (daf) basis. On a very basic assumption, it can represent the amount of char that is going to the CR for combustion. The stoichiometric value for air input to burn the char at CR can be calculated:

$$\dot{Q}_{air,stoi} = \frac{19kg_{biom}}{h} \times \frac{0.14kg_C}{kg_{biom}} \times \frac{kmol_C}{12kg_C} \times \frac{kmol_{O_2}}{kmol_C} \times \frac{5kmol_{air}}{kmol_{O_2}} \times \frac{29kg_{air}}{kmol_{air}} \times \frac{m^3{}_{air}}{1.204kg_{air}} \approx 26\ \frac{m^3{}_{air}}{h}$$

The air input in the system is staged to achieve a better fluidization of the bed material in the riser, as well as having a more efficient combustion and avoiding hot spots as the air is injected in three different sections over the height of the riser as can be seen in the schematic figure of the CFB gasifier (Figure 14).

The results of staged air input are shown in the Figure 59:

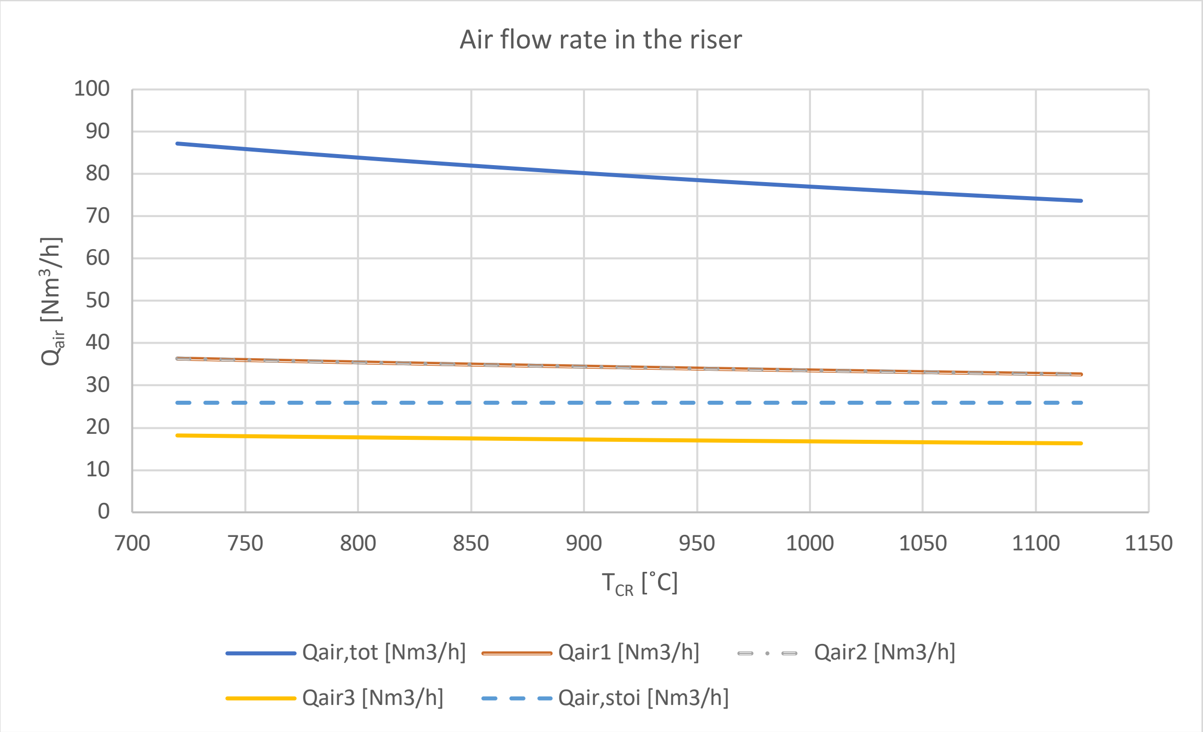

Figure 59 Air flow rate in the riser: total air flow, staged air flow, stoichiometric air flow for char combustion

It can be noted that the total amount of air input is few times higher than the stoichiometric air required for combustion, and even the first stage of air input exceeds the stoichiometric value.

Bed material circulation rate

Knowing the bed inventory in the CFB, one can then calculate the time required for the circulation of the particles and therefore the circulation rate according to Equation 34 and Equation 35:

Equation 34 $\tau_{circulation}=M_{inventory}/(G_s.A_{riser})$ *[time]*

Equation 35 $f=1/\tau_{circulation}$ *[cycle=1/time]*

The bed material inventory in the 100 kWth CFB gasifier of TUW is between 60 to 100 kg. In the long test run on softwood pellets with olivine sand as bed material, the bed inventory was 70 kg. This value is used for the calculation of bed material circulation time and rate. The results are shown in the Figure 60:

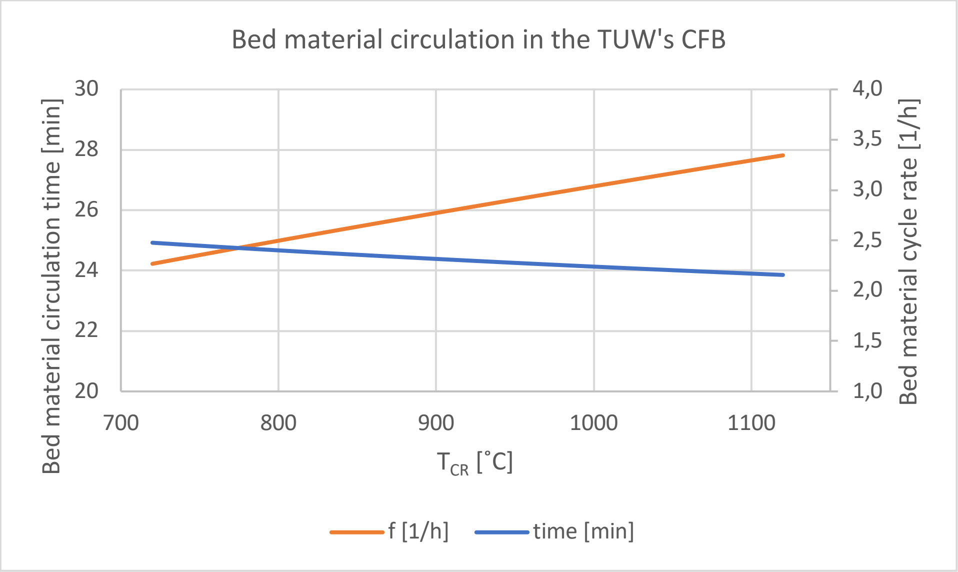

Figure 60 Bed material circulation rate and time required for a cycle, as a function of riser's temperature

Bed material circulation rate is defined as the bed material inventory over the bed material exchanged between GR and CR per unit of time.

Particle distribution

To fully determine particle distribution over the whole CFB gasifier, one needs to know the axial voidage at every point and the total bed material inventory as well as the detailed geometry of the TUW's CFB which is shown in the Figure 35.

In that context, the total bed material inventory $M_{inventroy}$, must be equal to the sum of the mass of the bed material particles at each layer of the CFB gasifier:

Equation 36 $M_{inventory} = \int_{z=0}^{z=L} dM(z)$

Where L is the vertical length of the CFB gasifier and M(z) can expressed as:

Equation 37 $dM(z) = \rho_p . dV(z) . [1 - \varepsilon(z)]$

Where ρ_p is the bed material density, V(z) is the volume of the layer as a function of height "z", and ε is the axial voidage in the CFB as a function of height. In fact, axial voidage ε(z), is as a function of operational condition, but since all the operational conditions are correlated with the temperature in this study, ε here will vary with only temperature and height. At this point ε is calculated for the sections where work in bubbling regime (lower loop seal, lower gasification part, trapezoid section in the GR, in the riser before air injection) with Darthon method; for the riser (dense and dilute phase) based on Baio and Kato (1999), but still two more sections are remaining to cover: rectangular part and the freeboard in the GR.

The rectangular part of the GR has a very high cross-sectional area ($A_{LLS}/A_{rectangular}$=0.07, $A_{LGR}/A_{rectangular}$=0.375, $A_{freeboard}/A_{rectangular}$=0.135), and the bed porosity can be calculated with

Darthon's method as well. But since experiments show that even with maximum loading of 100kg of bed material, the bubbling bed doesn't reach this part, for simplification, this section of the CFB gasifier is assumed to be virtually solid particle free ($\varepsilon \rightarrow 1$). As for the freeboard section of the system, since the bed material circulating back the GR from this part, an estimation of the $\varepsilon_{freeboard}$ is made based on the pressure gradient measurements in the experiments, using the Equation 26 and the results are shown in the Table 13:

Table 13 Estimation of bed axial bed porosity in the freeboard of the CFB gasifier

$T_{GR.BB}$ [˚C]	839	872	889	907	922	934	956	980	988	991	996
(dP/dz)GR	-1,760	-1,827	-2,338	-2,662	-2,720	-2,630	-2,484	-2,779	-2,659	-2,712	-3,059
$\varepsilon_{freeboard,GR}$	0,994	0,993	0,992	0,990	0,990	0,991	0,991	0,990	0,990	0,990	0,989

For simplification $\varepsilon_{freeboard}$ is decided to be equal to 0.99 for all operational temperatures on average.

Now one can rewrite the Equation 36 with combining it with Equation 37 :

Equation 38 $M_{inventory} = \int_{z=0}^{z=L} \rho_p . dV(z). [1-\varepsilon(z)] = \int_{z=0}^{z=L} \rho_p . [A(z). dz]. [1-\varepsilon(z)]\Big|_{GR\&CR}$

We can divide this integral form into different sections (LLS_{GR}, LGR, Trapezoid, Rectangular, Freeboard, LLS_{CR}, $Riser_{before\ air\ injection}$, $Riser_{dense\ region}$, $Riser_{dilute\ region}$). When A(z) is constant, can be taken out of integral, and as for $\varepsilon(z)$, it also can be substitute with average value at each section, except for the trapezoidal section where A(z) varies with height. Rewriting the Equation 38:

Equation 39 $M_{inventory} = \sum_i \rho_p . (1-\hat{\varepsilon}_i). V_i + \rho_p . (1-\hat{\varepsilon}_{trapezoid}). \int_{z=z_0}^{z=bed\ surface} A(z) dz$

Where i=LLS_{GR}, LGR, LLS_{CR}, $Riser_{before\ air\ injection}$, $Riser_{Dense\ phase}$, $Riser_{Dilute\ phase}$, and A(z) is the cross-sectional area in the trapezoidal section and can be written as:

$$A(z) = \left(b_1 + (b_2 - b_1)\frac{z_{BB}}{h}\right). L$$

Where b_1 and b_2 are the lower and upper length of the trapezoid respectively, h is the total height of the trapezoid, z_{BB} is the height of the bubbling bed surface from the bottom of trapezoid, and L represent its depth. The schematic of the trapezoid is shown in the Figure 61:

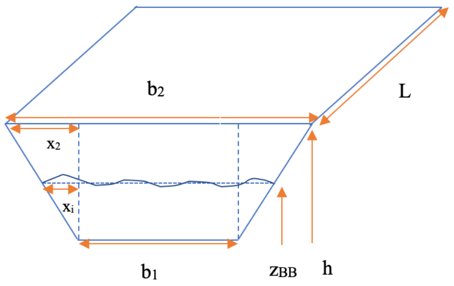

Figure 61 Trapezoidal section of the TUW's CFB gasifier in the GR

Solving the Equation 39, gives us the position of the bed surface, the particle distribution in the CFB system, as well as pressure drops in the sections where the superficial gas velocity is less than terminal velocity by the Equation 40Equation 5 and in dilute phases with the Equation 41:

Equation 40 $\Delta P = (1-\varepsilon).\left(\rho_p - \rho_g\right).g.H$

Equation 41 $\Delta P = \Delta Z.g\left[\rho_p(1-\varepsilon_{ave}) + \rho_g \varepsilon_{ave}\right]$

Typical bed inventory for the CFB gasifier of TUW is between 60 to 100 kg depending on the bed material. For olivine sand, the amount of 70 kg is chosen. When system is loaded with the bed material, at the fixed bed condition with pressure balance between the gasification reactor and the riser, the height of the bed material should be equal in both reactors. In order to calculate the bed height at the fixed bed condition, first step is calculating the total volume that will be occupied by 70 kg of olivine sand:

M=70 kg, ρ_{bulk}=1500 kg/m^3, ρ_p=2850 kg/m^3

$$V_{tot} = \frac{M}{\rho_{bulk}} = \frac{M}{(1-\varepsilon).\rho_p} = 0.046 \quad m^3$$

The bed height at static condition (fixed bed) results to 1.141 m. Then $\Delta H_{operational}/H_{static}$ will be evaluated as a function of gasification temperature. The results are shown in the Figure 62:

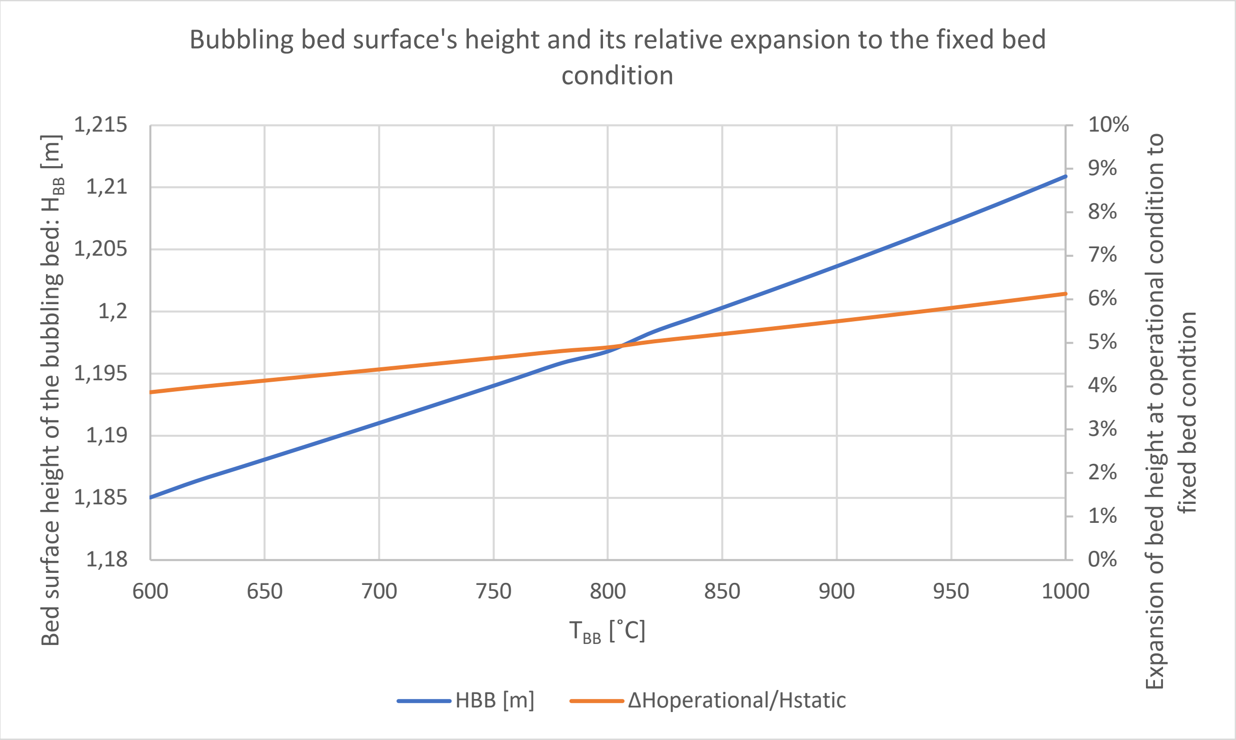

Figure 62 Bubbling bed surface's height and its relative expansion to the fixed bed condition

It's evident from the results that with increasing the temperature and subsequently increasing superficial velocity, the expansion of the bed increases. From 600 to 1000 ˚C, the height of the bed surface increases almost 25 cm. The relation between the bed surface at operational condition and static condition indicates that at operational condition the bed surface is 4 to 6% higher than that of static condition. The latter agrees with the founding of (Kunii and Levenspiel 1991) that estimates the bed height at operational condition to be 5% bigger than that of fixed bed condition. In the Figure 63, a schematic of the 100 kWth CFB gasifier of TUW with a qualitative representation of the bed material distribution over the system is shown.

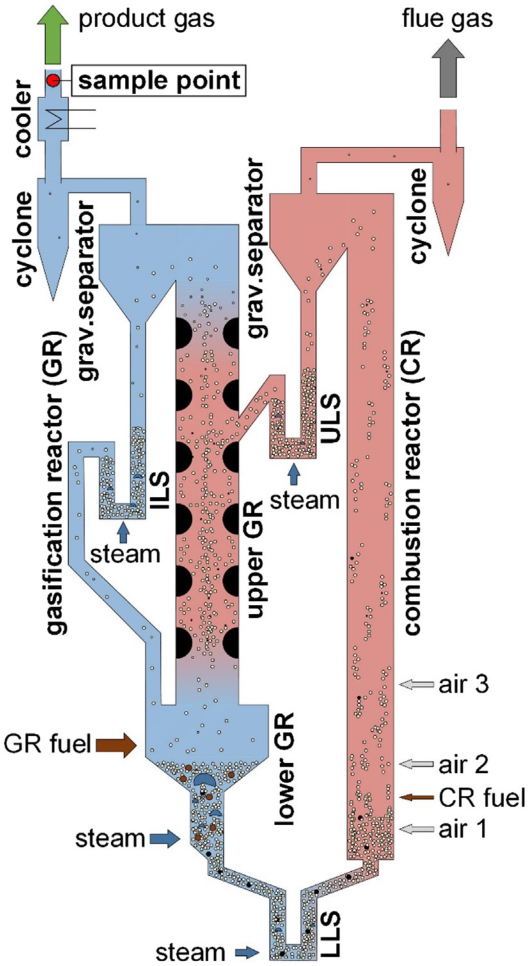

Figure 63 Schematic of TUW's 100 kWth CFB gasifier with qualitative representation of the bed material particle distribution

Pressure drops

The pressure drops in the GR and the CR are calculated as explained in previous chapters. The results are shown in the Figure 64 and later all the calculated and assumed values for the CFB gasifier at operational mode are compared with the experimental set up and measurements.

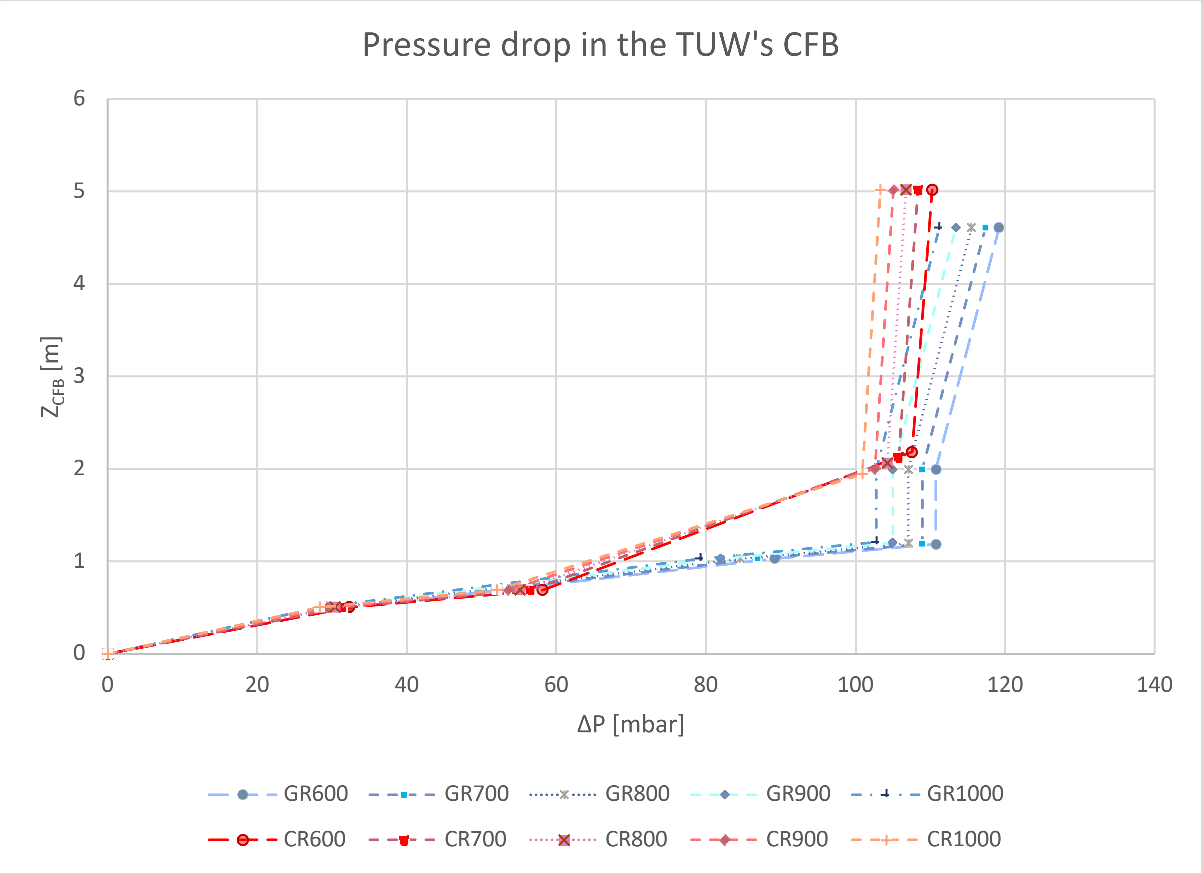

Figure 64 Pressure drop in the 100 kWth CFB gasifier of TUW

It can be noted that with increasing the temperature, which in the model set up coincides with increasing the superficial gas velocity, the total pressure drop in the CFB decreases.

Gas and char residence time

Knowing the volume of various parts of the reactor, as well as the bed height of the bubbling bed in the operational condition, one can calculate the gas and char residence time for various parts. The gas residence time at this point, doesn't take into account the products of the biomass drying and devolatilization. The gas residence time can be easily derived from the Equation 42:

Equation 42 $\tau_{gas} = \frac{V}{Q_{gas}}$

Since the gas input changes in different sections of the CFBG as explained in the previous sections, therefore it's calculated for each part separately. The results are shown in the Figure 65:

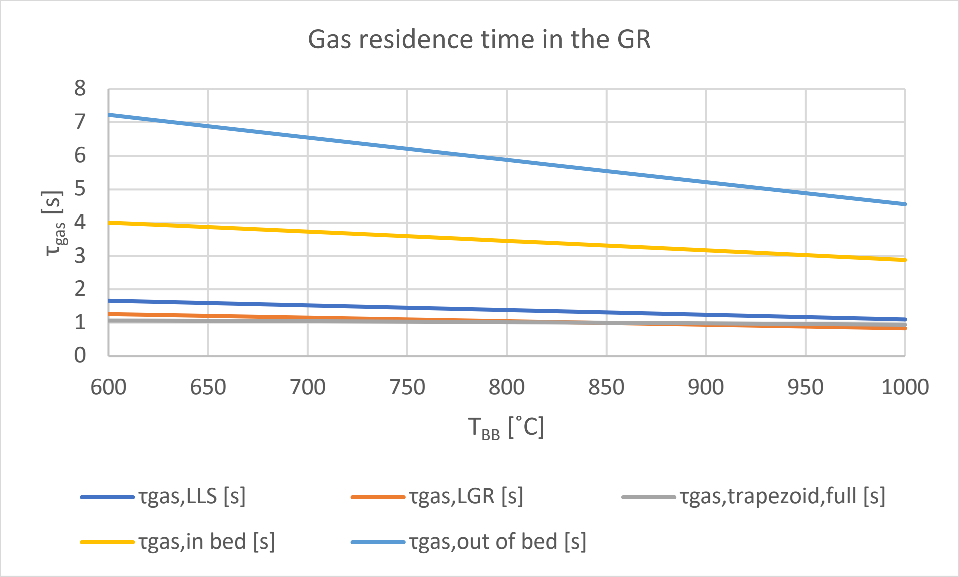

Figure 65 Gas residence time in the GR

In both the freeboard and the bubbling bed, homogenous gas-gas reactions will occur but with two different sets of kinetics, since the bed materials themselves will act as catalyst, also the temperature plays a role which is more than a 100˚C different between the bubbling bed and the freeboard.

Drying is assumed to happen instantaneously on top of the bed, and the biomass devolatilization is assumed to happen in a linear way from top of the bed to the bottom of the lower gasification part. Therefore, the char reaction may occur from the first point of the devolatilization up to the lowest part of the lower loop seal (LLS). The residence time for the char is different than for the gases. Assuming that the char particles are moving with the bed material, the residence time for the char gasification will be the same as bed material through their circulation in the bubbling bed. It would be the total time of the circulation of the bed material in the CFB gasifier minus the time that is passed in the riser and the freeboard of the gasifier:

Equation 43 $\tau_{char,BB}=\tau_{p,circulation}-\tau_{p,riser}-\tau_{p,freeboard}$

Equation 44 $\tau_{partcile,riser} = \frac{L_{riser}}{\upsilon_{particle}} = \frac{L_{riser}}{\frac{G_S}{\rho_p(1-\varepsilon_{ave})}}$

The upper limit of counter-current flow is set by the terminal velocity (Wilhelm and Valentine, 1951; Lapidus and Elgin, 1957). When the bed material comes back from the riser with solid flux G_s, the superficial gas velocity inside the freeboard is much less than terminal velocity of the single particles, therefore it’s assumed here that they just drop down to the bubbling bed:

Equation 45 $\tau_{partcile,freeboard} = \frac{L_{freeboard}}{u_t}$

The char residence time in the riser can be calculated with the same approach:

Equation 46 $$\upsilon_{char} = \frac{G_s}{\rho_{char}(1-\varepsilon_{ave})}$$

But in this equation defining the density of char can have complication, since assuming a shrinking model, based on conversion rate of the char in the GR, this density will change. For simplification, a constant density for char is assumed with the following correlation:

$$\rho_{char} = FixedCarbon_{Biomass}\%.\rho_{Biomass} = 0.144 \times 640 = 128\ kg/m^3$$

The results of bed material particle and char residence time in the TUW's CFB in shown in the Figure 66:

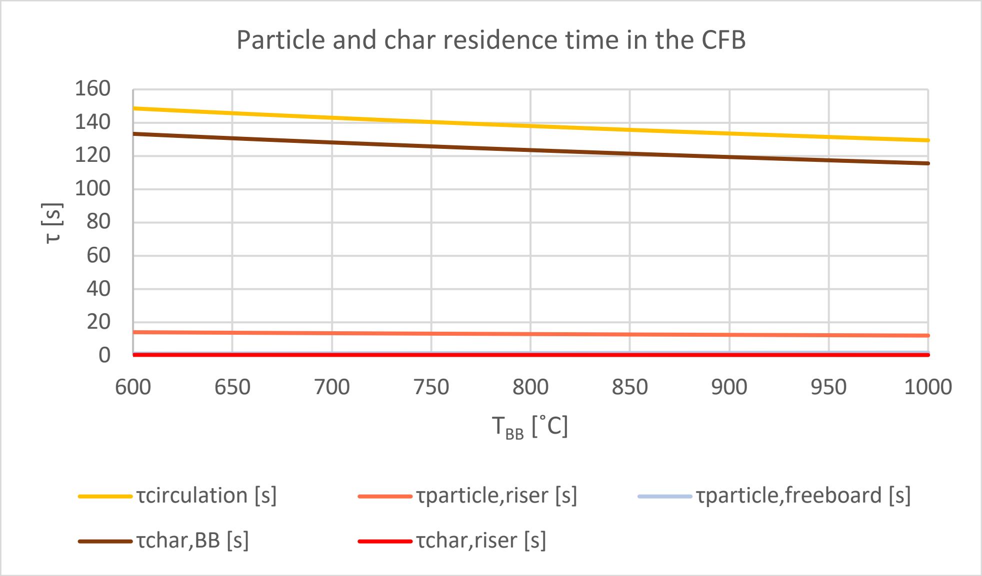

Figure 66 Particle and char residence time in the CFB gasifier

The char residence time in the riser is less than residence time in the bubbling bed of the GR with orders of magnitude (0.4˜0.5 sec in the riser, 2˜3 min in the BB). But there's also the fact that in the riser char is oxidizing with air which has a much higher kinetics that char gasification with steam and CO_2 which happens inside the bubbling bed of the GR.

Compare with the operational conditions at experiments

A long test run with temperature variation from 650 to 900 ˚C has been performed with the CFB gasifier of TUW, with softwood pellets feeding above the bed as the fuel, and olivine sands as bed materials. The experiment is a basis for validation of the model. The experimental values as input condition for the long test run is compared with the calculated values for the system and reported below:

1. Biomass feeding rate

In the model development it’s assumed a constant feeding rate of 20.4 kg/h (19 kg/h dry ash-free) with corresponding thermal power of 100 kW. In the experiments this value varies in a narrow range. The comparison between set up of the model and experimental values are shown in the Figure 67:

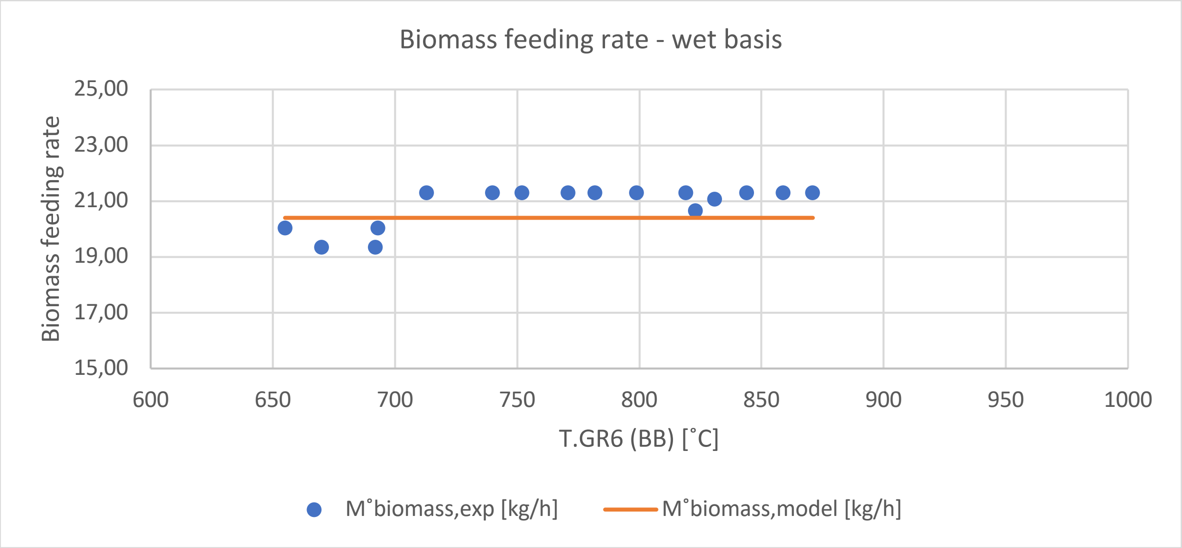

Figure 67 A comparison between biomass feeding rate in the model development and experimental condition

Solid line indicates the model and the points represent experimental values. The values are in good agreement.

2. Steam flow rates:

Steam input in the lower loop seal (LLS), lower gasification part (LGR), total steam to the bubbling bed (BB) and total steam to the gasification reactor (GR) are reported in the Figure 68 below. The solid lines represent the model values and the points are experimental values.

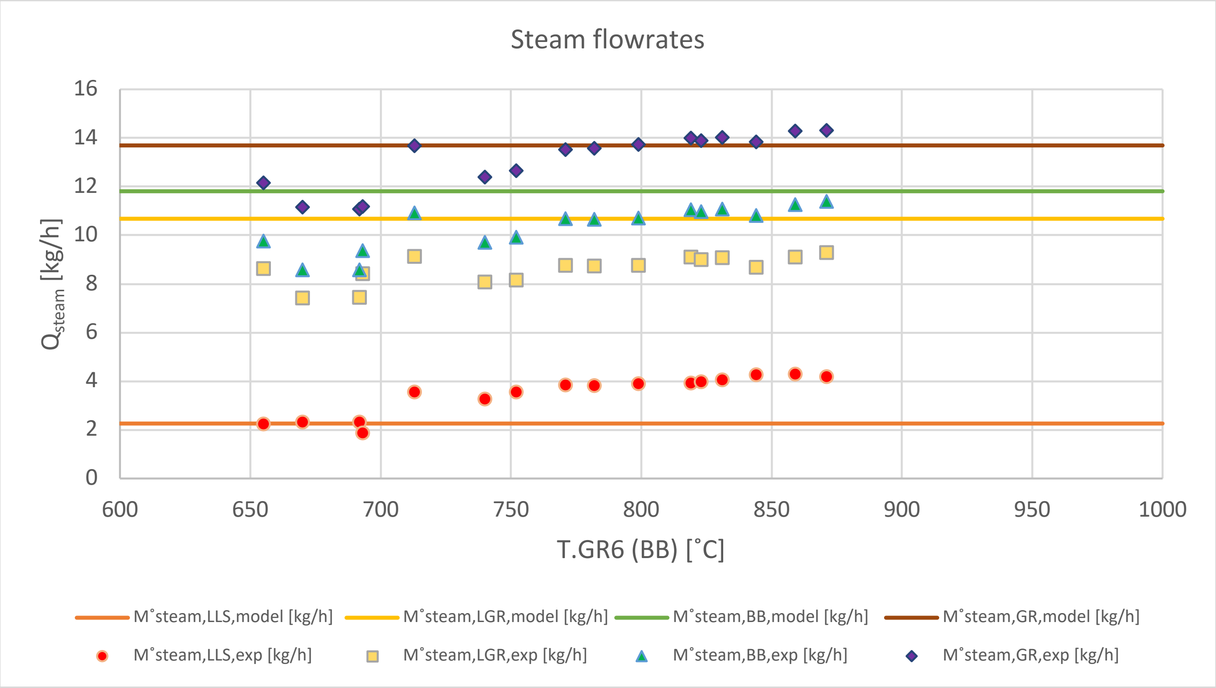

Figure 68 Steam flowrates in various parts of the CFB gasifier as a function of temperature: model vs experiment

There's a good agreement between model and experiment, especially for the overall steam input to the CFB gasifier.

3. Steam to Biomass ratio:

Steam to biomass ratio is considered in two different ways, once without taking the steam released from moisture content of the biomass "StB" and secondly with considering this value "StB*". The results are shown in the Figure 69:

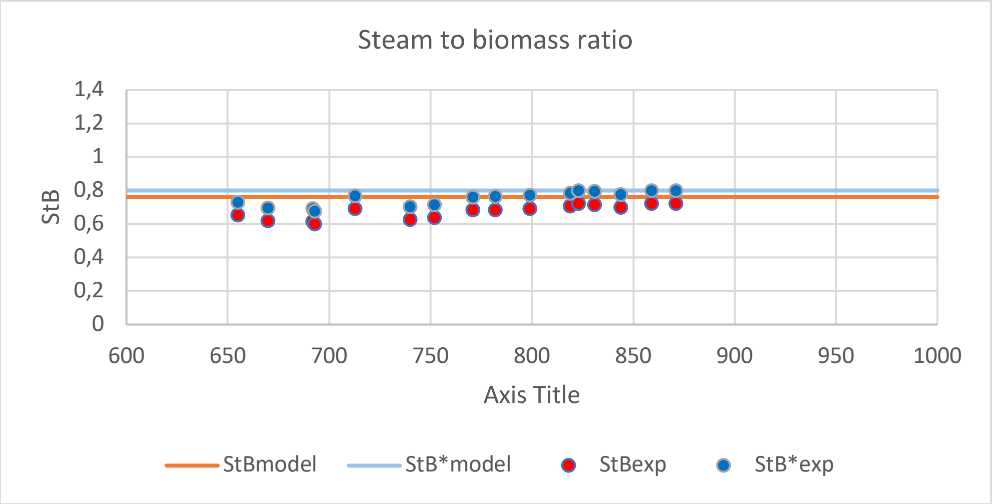

Figure 69 Steam to biomass ratio: a comparison between the model and experimental values

4. Air flow rate and the superficial gas velocity in the CR (riser):

As for the experiments, both air inflow at normal condition (Q_N [Nm^3/h] and superficial velocity are rising with temperature. In the set-up of the model, the superficial velocity (U_g=U_{se}) is increasing, therefore the air flow in the riser at operational condition ($Q_{air,operational\ mode}$=$Q_T$ [m^3/h]) rises subsequently. The air input must then be calculated based on normal condition, and the relation between normal and operational condition is as follows:

Equation 47 $Q_N = Q_T.\frac{\rho_T}{\rho_N} = Q_T.\frac{T_{normal\ condition}}{T_{operational\ condition}}$

Although the superficial gas velocity increases in the model, the air inflow at normal condition decreases, due to the fact that the factor of $\frac{T_{normal\ condition}}{T_{operational\ condition}}$ is decreasing.

The results are shown in the Figure 70:

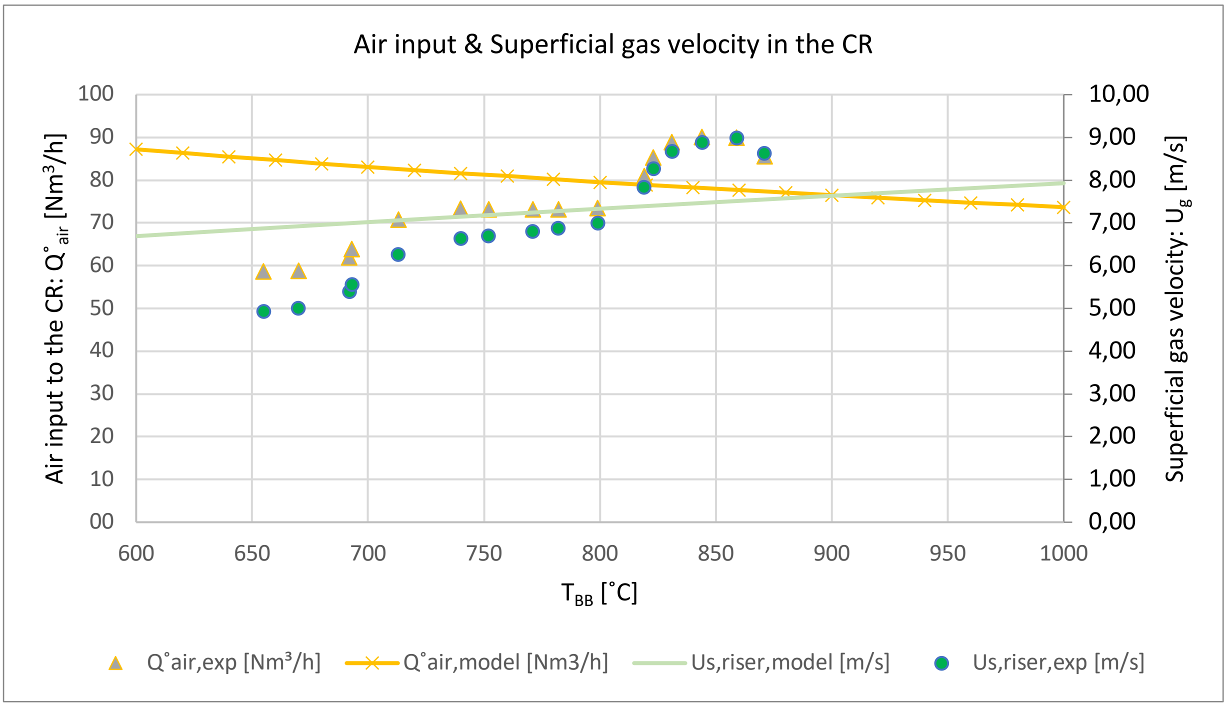

Figure 70 Air inflow and superficial gas velocity in the CR: model vs experiment

There's some discrepancy between the model and experiment in terms of total air inflow, but in terms of gas superficial velocity there's a better agreement.

5. Pressure drops in the CFB: ΔP_{CFB}

The pressure drops in the CFB is defined based on the fluidization regime in various parts of the CFB as well as total amount of bed material inventory. Three examples of comparisons between experimental measurements and model results are shown in the Figure 71, Figure 72 and Figure 73 for the GR bed temperature of 740, 800 and 860 ˚C respectively:

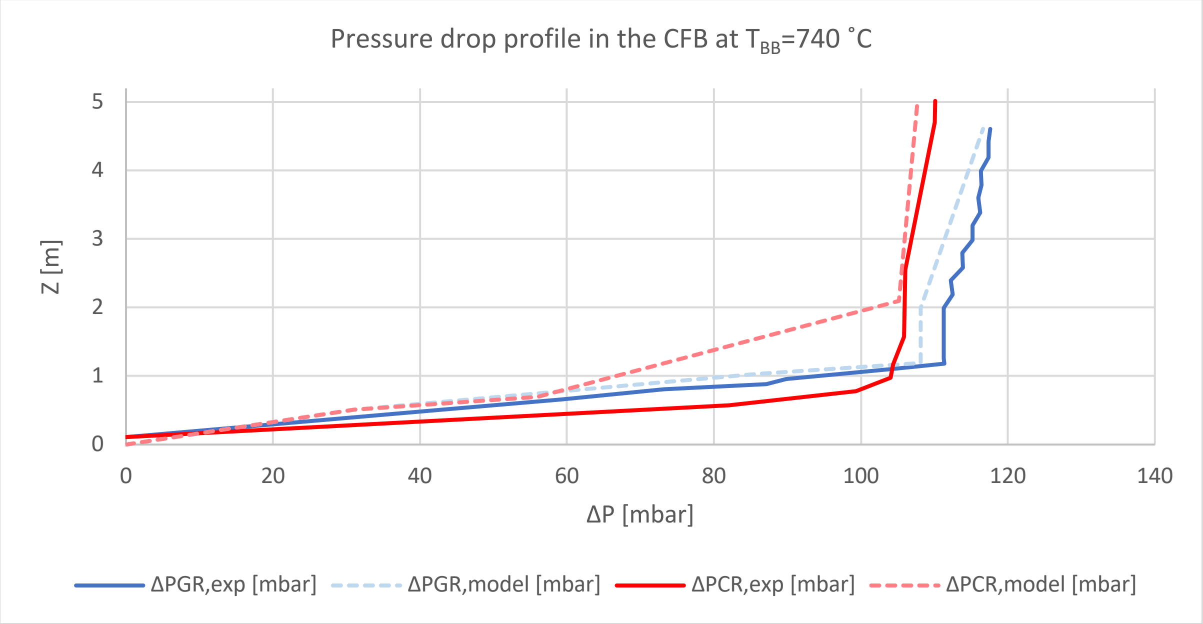

Figure 71 Pressure drop profile in the CFB gasifier at T_{BB}=740 ˚C: model vs experiment

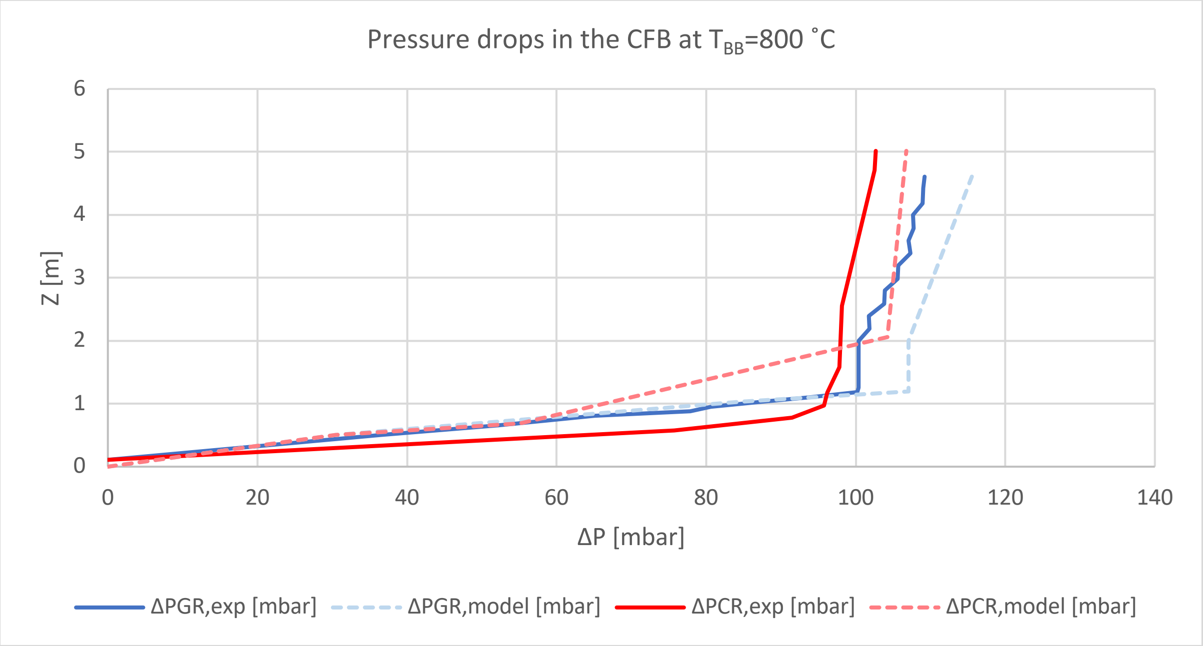

Figure 72 Pressure drop profile in the CFB gasifier at T_{BB}=800 ˚C: model vs experiment

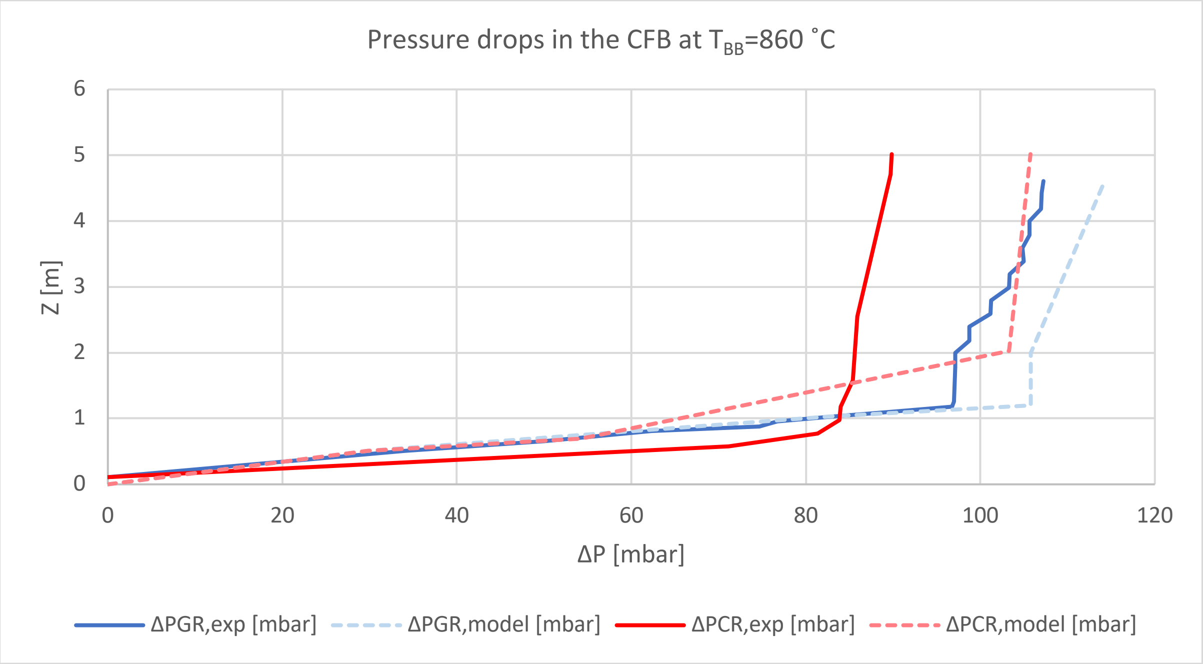

Figure 73 Pressure drop profile in the CFB gasifier at T_{BB}=860 ˚C: model vs experiment

It can be seen that with increasing temperature, the relative errors are increasing. The errors in the GR are generally lower, since calculating the pressure drop in the GR is more straightforward due to its bubbling bed fluidization state. The total pressure drops in the GR and the CR, as well as pressure drop only in the bubbling bed as a function of GR's temperature, are shown in the Figure 74. In the Figure 74, the lines indicate the results from the model, and the points representing the experimental values. On each experimental value point, the relative error with the model is reported. It can be noticed that the relative error for the total GR, CR and bubbling bed pressure drops lies between -8.5% to 0.9%, -21% to 2.8% and -10.1 to 2.8% respectively. The higher relative errors for the CR are due to difficulty of estimating pressure drops in the dense phase of the fast fluidization state.

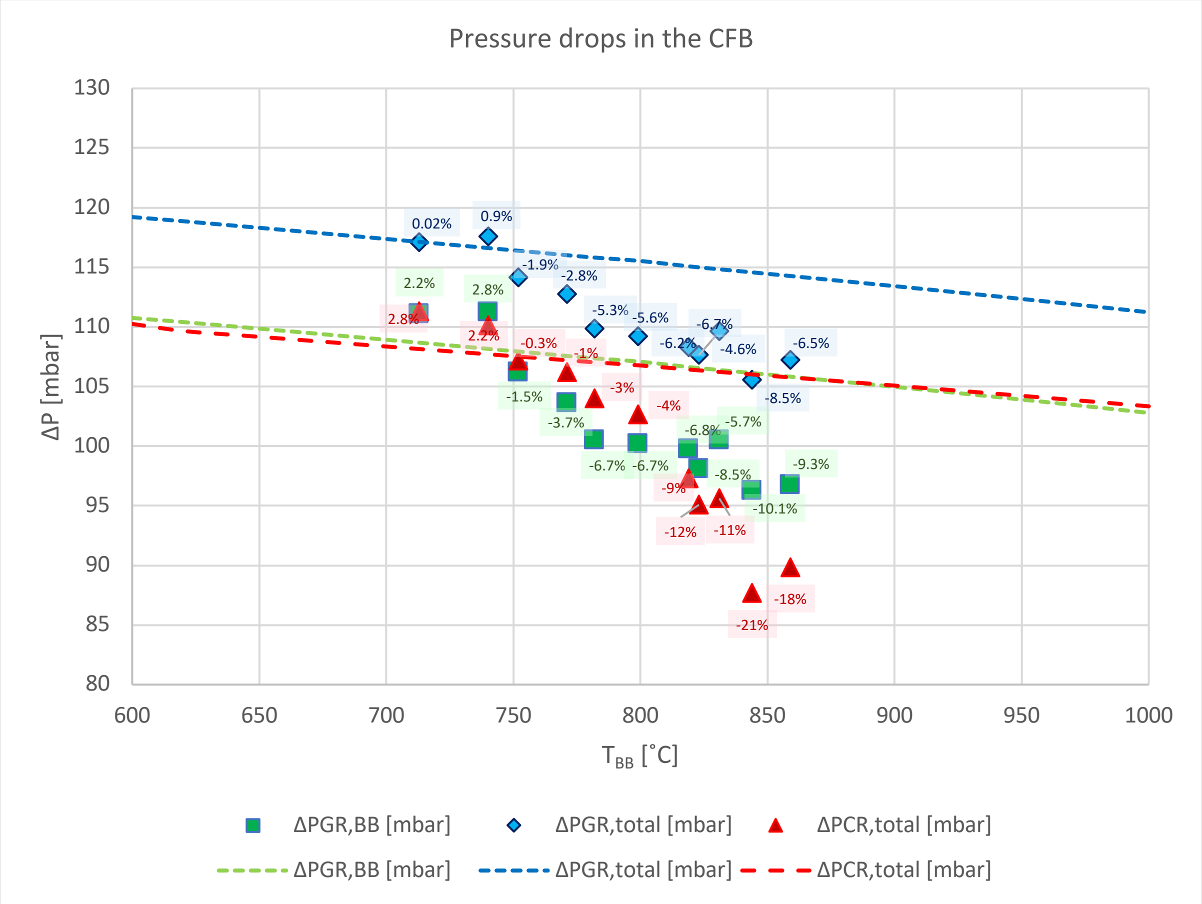

Figure 74 Pressure drops in the bubbling bed, in the whole GR, and the whole CR of TUW's CFB as a function of bed temperature

A summary of the typical operational condition of TUW's CFB gasifier is reported in the Table 14. The highlighted values are from the experiments and non-highlighted are values in the model. One has to consider that the superficial velocities that have been calculated so far, don't take into account the gas coming from biomass drying and devolatilization products, as well as the gas producing/consuming in heterogenous reactions between gas and char. The latter will be discussed later on in the next chapter.

parameter/name	unit	general		
feedstock to gasification	kW	90 – 110: 100		
typical feedstock properties	-	fuel as pellets		
heat losses of the reactor	kW	25 – 30: neglected		
additional fuel input for	kW	30 – 57: neglected		
pressure	bar	ambient conditions		
bed material	-	olivine sand (gasifier)		
Amount of bed material	kg	75 – 100: 70 (olivine)		
design	**unit**	**lower gasification**	**upper gasification**	**Combustion reactor**
range of temperature	°C	655 – 870 (600-1000)	800 – 1000 (700-1100)	840 – 1060 (760-1160)
regime of fluidization	-	bubbling bed	turbulent zones	fast bed
input gas for fluidization,	-	steam	steam	air
inner diameter/dimension	mm	560 x 490	128x128	ø125
characteristic inner height	m	1.03	3.33	4.73
mean bed material diameter	µm	250 (243)	250 (243)	250 (243)
cross section for calculation	mm	68 x 490	128 x 128	ø125
superficial gas velocity, U	m/s	0.47 – 0.93 (0.42-0.63)	1.7 – 2.1 (1.0-1.4)	6.3 – 7.6 (6.7-7.9)
minimum fluidization	m/s	0.037 (0.020-0.030)	0.037 (0.02-0.03)	0.028 (0.023-0.028)
fluidization ratio, U/U_{mf}	-	13 – 25 (13-30)	40 – 55 (32-68)	220 – 270 (230-340)
terminal velocity, U_t	m/s	2.06 (1.8-2.7)	2.06 (1.8-2.7)	1.61 (1.7-2.1)
fluidization ratio, U/U_t	-	0.23 – 0.45 (0.16-0.35)	0.8 – 1.1 (0.37-0.77)	3.8 – 4.8 (3.15-4.6)

Table 14 Summary of the operational condition of the CFB gasifier of TUW

4. Devolatilization of biomass in fluidized bed

Devolatilization is a key conversion stage during gasification and combustion of biomass fuels. Biomass devolatilization is a thermal decomposition, where the biomass yields into liquid organics, permanent gases and carbonaceous solid residual namely char. Knowledge of yields and composition of biomass devolatilization products is critical to understand the whole process of gasification and its modeling. Liquid organic fraction of these products contains heavy hydrocarbons (tar) and pyrolytic water which arises from chemically bounded water in the biomass and it's different than the moisture content. Permanent gases can be lumped into CO, CO_2, CH_4, C_2H_4 and H_2 as main products. And finally, the solid residual (char) can be represented as pure carbon, even though there are small percentage of hydrogen and oxygen in the char, depending on the temperature at which devolatilization occur, and the nature of biomass itself. When biomass is devolatilized, light gases and tars represent 70–90% of the total mass fed, whereas only 10–30% is char (Neves et al., 2011). In a circulating fluidized bed gasifier, the yield of char is useful for the riser and the carbon conversion efficiency achieved in the reactor. Determination of the tar yield is essential since high tar content limits the gas application.

The yield and composition of devolatilization products depend on many variables, such as: nature of the biomass feedstock, the size of the biomass particles, the temperature, residence time, heating rate, the type of instrument in use, gas medium and etc. There are numerous studies in attempt to find the correlations for biomass devolatilization products like the works of (Neves, Thunman, Matos, Tarelho, & Gómez-barea, 2011), (Neves et al., 2017a) and (Zhang & Pang, 2017).

(Gómez-barea, 2011) concludes that regardless of fuel type, operational condition and methodologies, there are general trends for both the products and their properties as a function of temperature. The latter can be due to the fact that most biomass fuels lie in a relatively narrow range of elemental composition (40-60% carbon, 30-50% oxygen and 5-8% hydrogen, mass% of dry ash-free). However a more detailed study may be needed due to the different chemical structures in the biomass such as cellulose, hemicellulose and lignin. (Gómez-barea, 2011) gathers the results of more than 300 experiments on devolatilization to find semi-empirical correlations to approximately the behaviour of biomass through the process of devolatilization. His founding can be used for a more generic approach to model the steam gasification of biomass, but here the focus is on the specific process of softwood gasification in the CFB gasifier of TUW with olivine sand as bed material.

(Neves et al., 2017a), instead of more generic approach, performed woody biomass devolatilization in a similar condition of bubbling fluidized bed reactors. In his work, he gathered data for two types of wood (eucalyptus and pine) and two types of pellets (forest residues and wood) with particles of 6-8 mm in diameter fed over the hot bubbling bed at temperature range of 600 to 975 ˚C. These founding can be representative of the softwood pellet gasification in the CFB gasifier of TUW in terms of fluidization state, biomass fuel type, particle size and the temperature range. A comparison between the elemental composition of the fuels used in (Neves et al., 2017a)'s work and softwood pellets used in this work has been made and shown in the Table 15:

Fuel	*Carbon*^{a}	*Hydrogen*^{a}	*Oxygen*^{b}	*Nitrogen*^{a}	*Ash*^{a}
Eucalyptus wood	46.3±0.5	6.4±0.1	46.8±0.6	0.1±0.0	0.4±0.0
Pine wood	48.0±1.2	6.3±0.1	45.1±1.2	0.1±0.0	0.5±0.0
Wood pellets	49.1±1.0	6.6±0.1	43.5±1.1	0.1±0.0	0.7±0.0
Forest pellets	49.8±0.8	6.3±0.1	42.7±0.8	0.3±0.0	1.0±0.0
Softwood pellets	50.7	5.9	43.0	0.2	0.2

Table 15 Ultimate analysis of biomass fuels used in (Neves et al., 2017) and Softwood pellets in this work; a: mean value ± one standard deviation from replicate samples; b: determined by difference method.

The proximate analysis of the samples in (Neves et al., 2017) is not reported, but it assumed that all the wood samples have similar chemical structures. The ultimate analysis of the samples shows very similar elemental compositions, therefore, the results of devolatilization products and their composition are used for the modeling of softwood gasification in CFB gasifier of TUW. The experimental set up, methodology and data treatment of (Neves et al., 2017) is briefly explained here.

A stationary fluidized bed reactor is used to simulate the condition of industrial fluidized bed gasifiers. The experiments are in batch condition, with fast pyrolysis of solid biomass under inert atmosphere at the beginning, followed by combustion of the residual char during pyrolysis stage. The bed material used in the experiments is silica sand with particle size of 180 to 250 µm. The particle size is similar to olivine sand used in the CFB gasifier of TUW. The biomass fuel is dried in the oven up to 105 ˚C and then cooled down in room temperature. The dry fuel is fed over the hot bubbling bed. The gases from devolatilization are measured by gas analyzer and tars are collected from impinger bottles. When the pyrolysis stage is completed, the residual char is measured then combusted in an oxidizing environment. The pyrolytic products are reported as yields, $Y_{i,F}$, with the unit of $kg_i/kg_{daf\ fuel}$. The yield of char is obtained from the amount of char particles recovered from the bed, with the assumption of all ash content from biomass remaining in the char. The amount of carbon in the char is evaluated during the combustion phase. The material trapped in the impinger bottles are defined as pyrolytic liquids which contains organic compounds as well as pyrolytic water. The gases are collected in sampling bags and their yield is determined from a known amount of inert gas N_2 that is injected to the system. In this work, the amount of pyrolytic water is not measured, since it was diluted with the water inside the impinger bottles. To include the pyrolytic water, the founding of (Gómez-barea, 2011) is taken into account.

Despite all the efforts in precise measurement of the devolatilization products, a mass balance of 100% is barely achieved. The mass balance closure results are shown in the Figure 75:

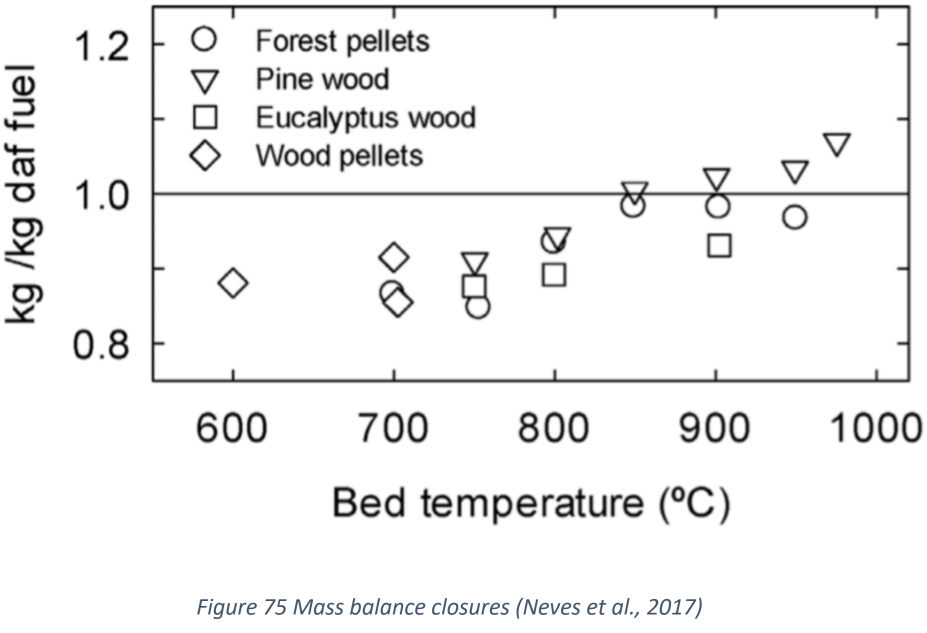

Figure 75 Mass balance closures (Neves et al., 2017)

One issue that can contribute to the temperature dependency of the mass balance closure can be measuring limited sets of light hydrocarbons. The values in the Figure 75 are based only on six main gas specieies of H_2, CO, CO_2, CH_4, C_2H_4 and C_2H_6.

The results of major devolatilization products from the wood and pellets based on (Neves et al., 2017) as a function of temperature is reported in the Figure 76 and Figure 77:

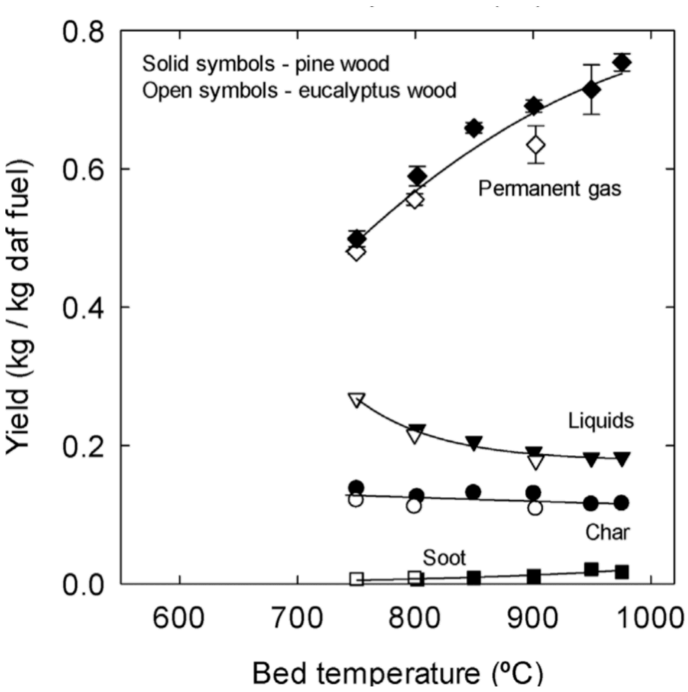

Figure 76 yield of major products from the wood as a function of temperature (Neves et al., 2017)

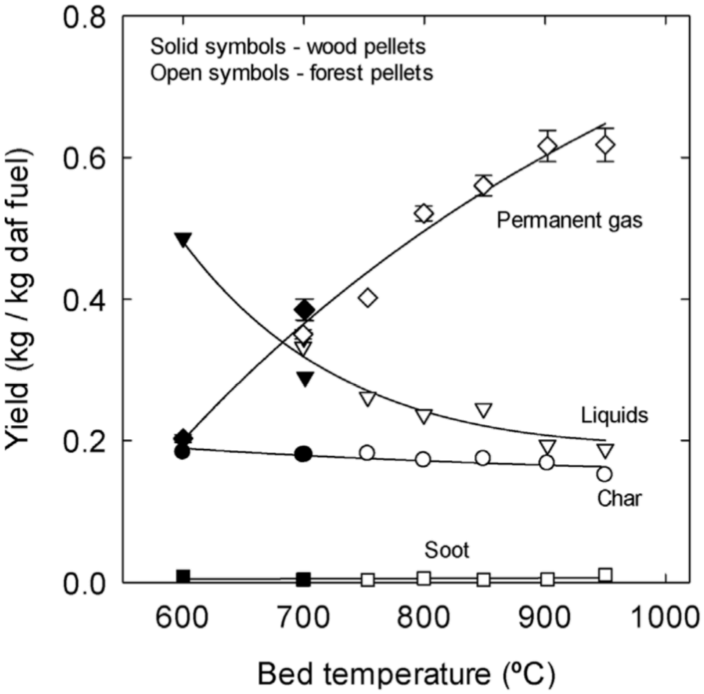

Figure 77 yield of major products from the pellets as a function of temperature (Neves et al., 2017)

The trends show that pyrolysis is progressing mostly in gas phase. By increasing the temperature, the amount of inorganic decreases, but after 800 ˚C the rate of decreasing slows down, which may indicate that these groups of tars are more stable and harder to convert thermally. The yield of char from pellets are higher which may be due to higher carbon content in the biomass fuel. The yield of char must not be misunderstood as pure carbon, since the char itself contains some amount of hydrogen and oxygen and its composition varies with temperature. Therefore, the amount of carbon in the char is obtained by combusting the char and the results are shown in the Figure 78:

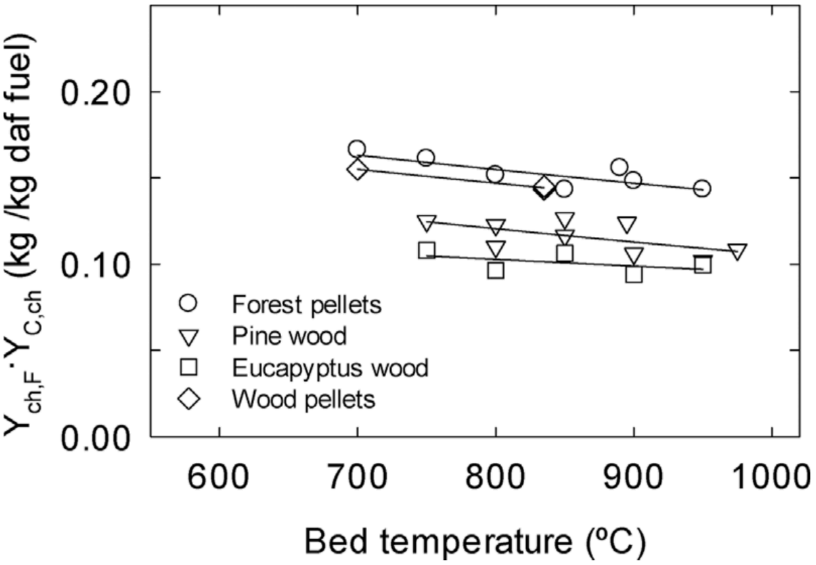

Figure 78 Total amount of carbon remaining in bed as char particles and fines per unit mass of dry ash-free fuel as a function of bed temperature (Neves et al., 2017)

In the development of simulation model, the char is assumed to be pure carbon for simplicity, therefore, the yield of char is obtained from Figure 78. The data doesn't cover the whole range of 600 to 1000 ˚C temperature as required for the model; therefore, an extrapolation of the data will be made.

The yield of permanent gases is reported in the Figure 79. It's worth mentioning that the devolatilization process approximately completes at 600 ˚C and from this point on, the temperature dependency of the permanent gases is mainly due to the secondary gas reactions between the volatiles. Carbon monoxide is the major compound and its yield strongly depends on the temperature. Carbon dioxide is the second major gas species in the volatiles with less temperature dependency. Carbon dioxide exhibits a peak value around 850 ˚C with maximum yield of 12-15% mass basis. Even the influence of the nature of the biomass can be evident of the yield of different permanent gases, therefore, in the model, either average values are taken into account as the trend, or the specific values for wood pellets. The trend of methane yield is similar to carbon monoxide as it increases with increasing the temperature.

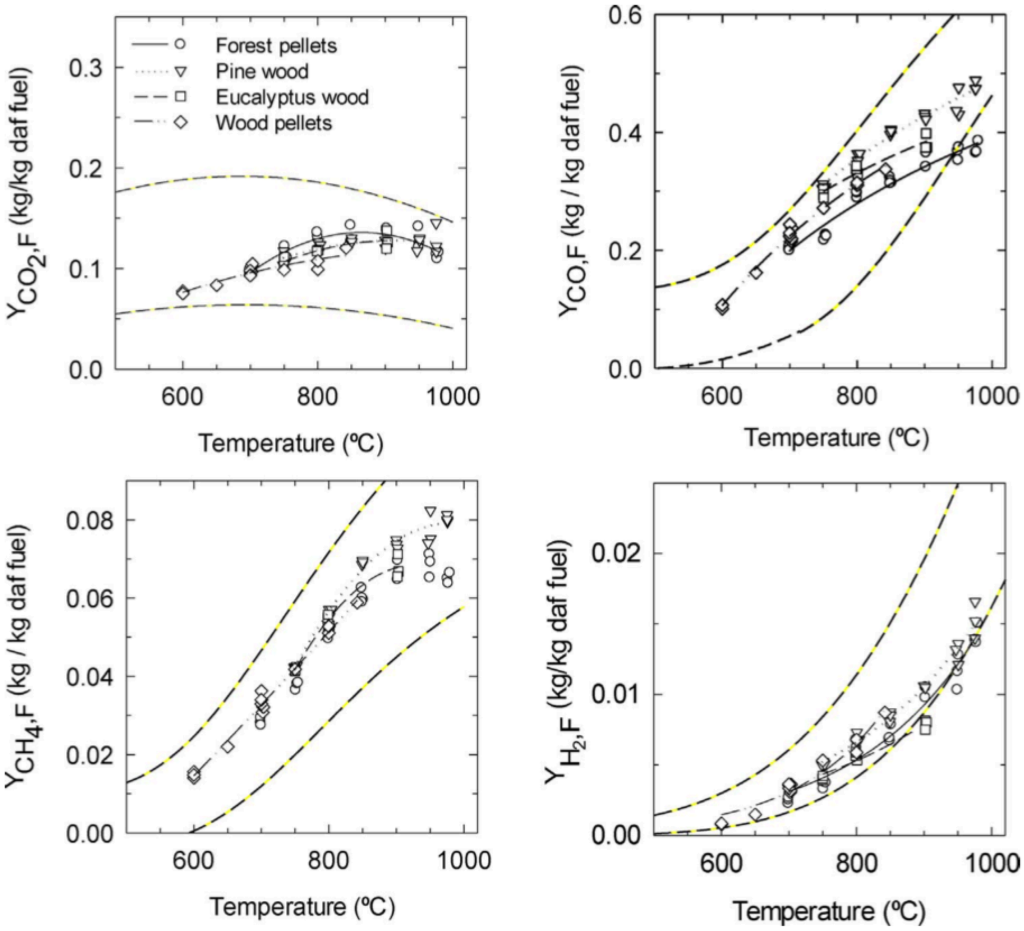

Figure 79 Yield of CO, CO_2, CH_4 and H_2 as a function of bed temperature (Neves et al., 2017)

As mentioned earlier, the yield of pyrolytic water is not quantified in the work of (Neves et al., 2017), and tar and pyrolytic water are lumped into liquid. The results from (Gómez-barea, 2011) are used to obtain the yield of pyrolytic water from devolatilization process of biomass as a function of temperature as shown in the Figure 80:

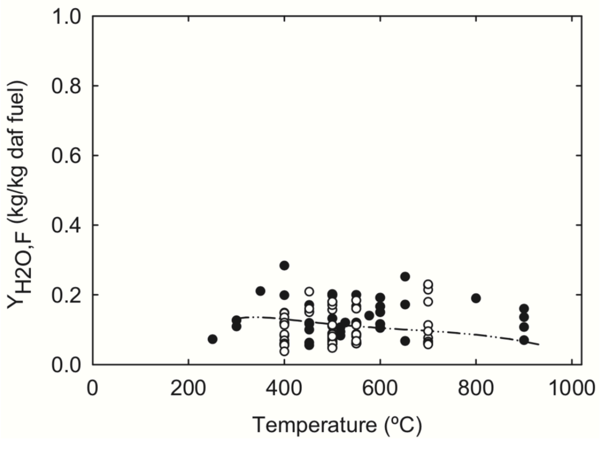

Figure 80 Yield of pyrolytic water as a function of pyrolysis peak temperature. Solid circles represent fast heating rate and hollow circles represent slow heating rate (Gómez Barea, 2011)

The trend line in the Figure 80 represents the trend line of pyrolytic water yield as an average value of many experiments taking into account, both with fast heating rate and slow heating rate. The pyrolytic water yield from fast heating process is higher than of low heating process, therefore, the overall average tends to slightly underestimate the pyrolytic water yield from fast devolatilization.

Devolatilization products

At this point, the yield of char, permanent gases, liquids (tar and pyrolytic water) can be defined as a function of temperature in the process of woody biomass devolatilization in a representative condition of fluidized be gasifier. The results of main devolatilization products (char, permanent gases and liquids) to incorporate in the model is shown in the Figure 81:

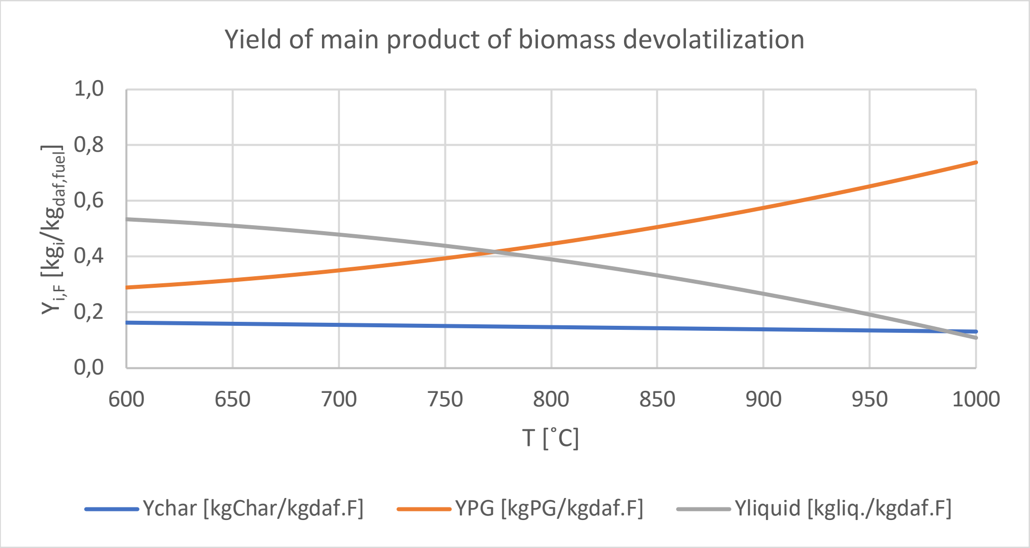

Figure 81 Yield of char, permanent gases and liquids (tar + pyrolytic water) from biomass devolatilization as a function of temperature

As it can be noticed in the Figure 81, the yield of liquids (tar and pyrolytic water) has a significant share at lower temperatures and neglecting them in the development of a simulation model can results significant errors. As temperature rises, the yield of tar and pyrolytic water decreases, and yield of permanent gases increases. The char yield slightly decreases with temperature, with values higher than the fixed carbon of softwood pellets.

Despite the increase of permanent gas yield with temperature, different gas compounds show different trend with temperature. While carbon monoxide as the dominant compound increases with temperature, carbon dioxide as the second major gas compound tends to decrease.

Methane and ethylene are less temperature dependent, while hydrogen also shows increasing with temperature. The results of different gas compounds from biomass devolatilization are shown in the Figure 82:

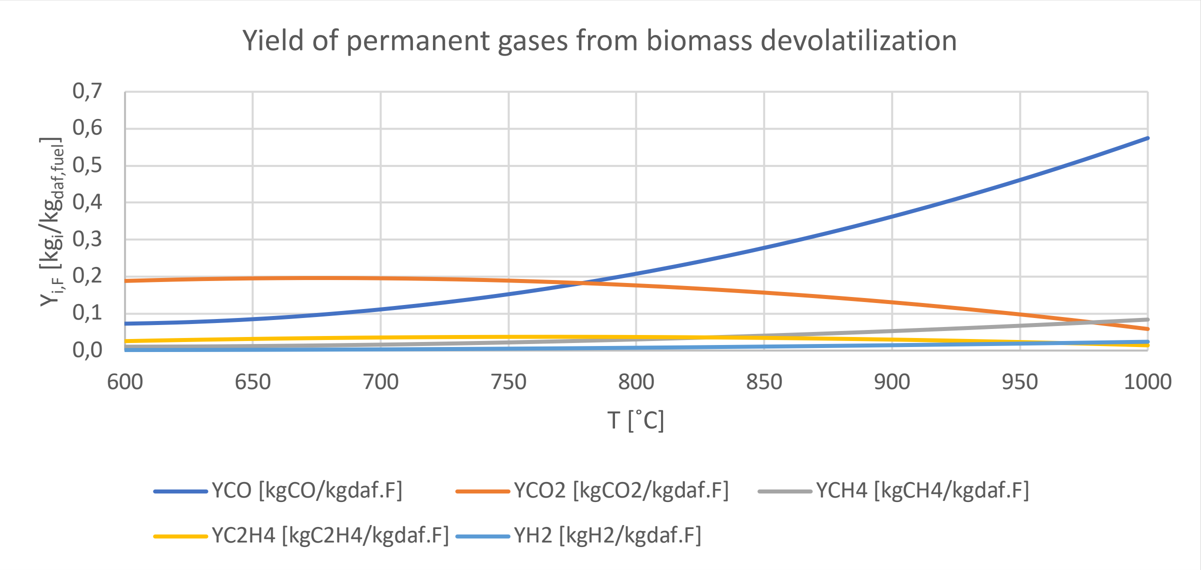

Figure 82 Yield of permanent gases from biomass devolatilization as a function of temperature

The yield of devolatilization products are shown so far on mass basis for its conservatory characteristic, but as for the gases it's worth look at their evolving with temperature based on their volume fraction in the gas. The gas composition after devolatilization, without considering tar cracking and reforming, is shown in the Figure 83. It can be seen that ethylene has the lowest share in the mixture.

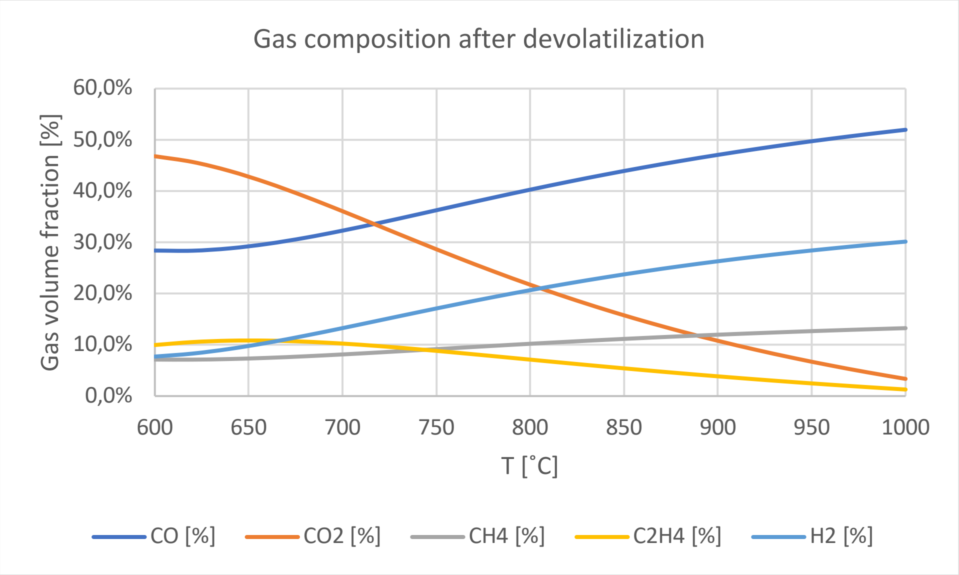

Figure 83 Gas composition after devolatilization without considering secondary reactions of tar compounds

The mixture of liquid products of devolatilization, which will be in gaseous form in high temperature, contains tar compounds as well as pyrolytic water. Their yield will decrease with increasing the temperature and their trend is shown in the Figure 84:

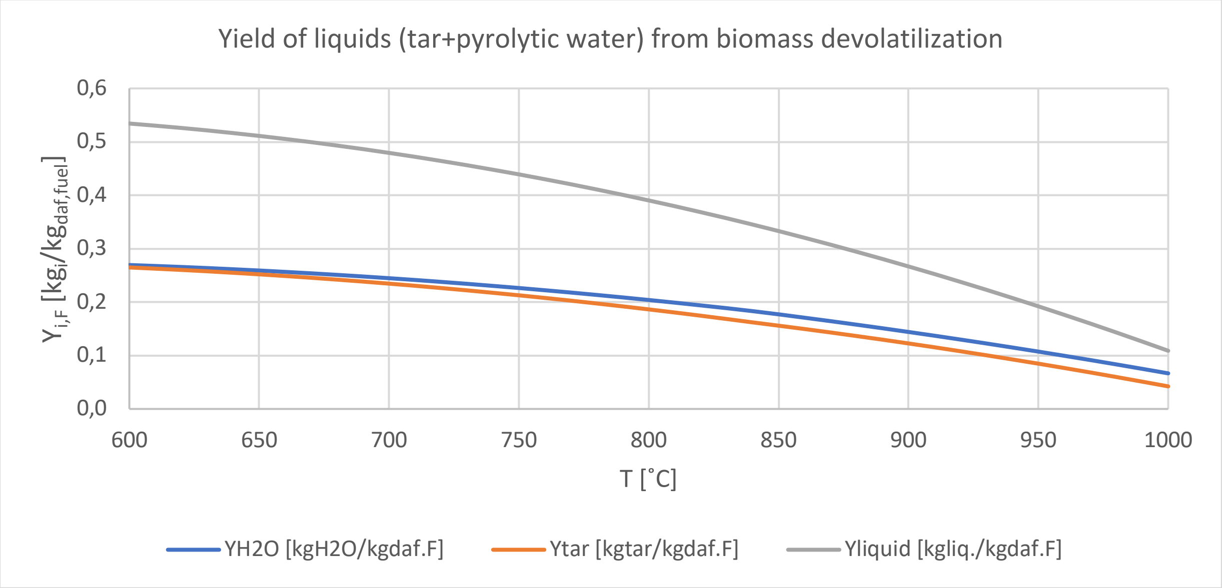

Figure 84 Yield of pyrolytic liquids (water and tar) from biomass devolatilization as a function of temperature

The remaining question would be the composition of the tar in order to proceed with the developing of the simulation model. In the work of (Gómez Barea, 2011), some correlations are proposed for carbon, hydrogen and oxygen content of the tar as a function of temperature, but the correlation factors are very low, therefore an average of the data in the literature is used to obtain the following correlation for the elemental composition of the tar: $Y_{C,tar}/Y_{C,F}$=1.14, $Y_{H,tar}/Y_{H,F}$=1.13 and $Y_{O,tar}/Y_{O,F}$=0.8. Considering the elemental composition of tar, their yield from biomass devolatilization as well as atom balance between biomass and the products, the tars are lumped into two group compounds of phenols and toluene to represent the primary and tertiary tars. The results are shown in the Figure 85:

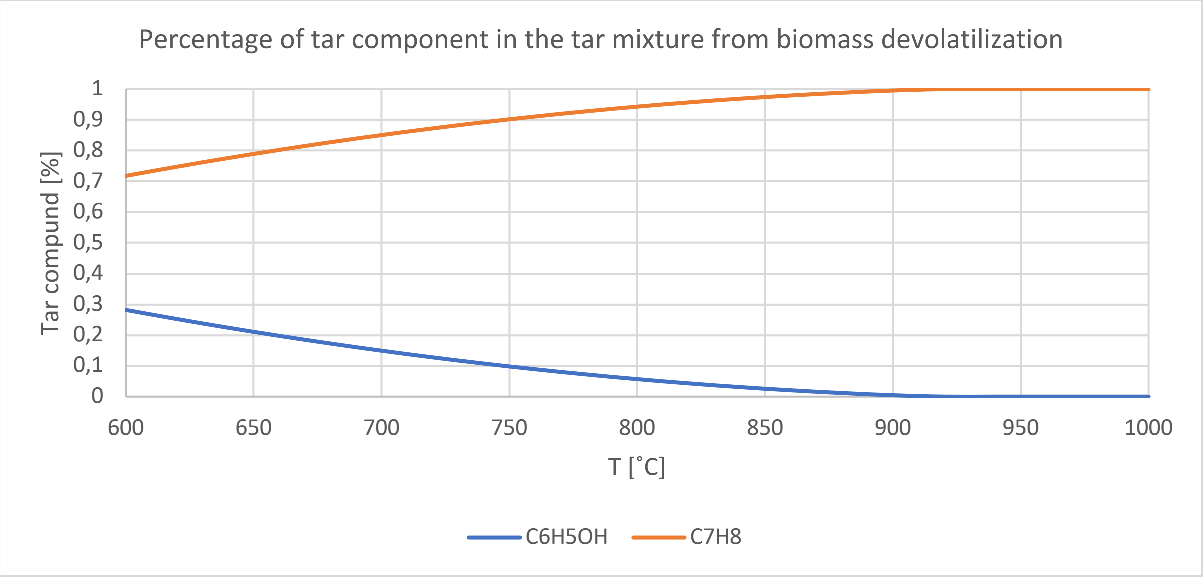

Figure 85 Percentage of the different tar compounds from biomass devolatilization

Phenol and toluene are taken into acount as tar models since their pathway of decomposition and reforming is studied in the works of (Nguyen, Sengupta, Raspoet, & Vanquickenborne, 1995) and (Fuentes-cano, Go, Nilsson, & Ollero, 2016) respectively and can represent the primary and tertiary tar groups. As it can be seen in the previous figure, the yield of phenol as a primary tar group is declining by increasing the temperature and the share of the toluene is rising. This behaviour is also predicted and reported in the work of (Fjellerup, Ahrenfeldt, Henriksen, & Gøbel, 2005) and shown in the Figure 13 previously.

The reaction pathways for model tar compounds are summerized in the Table 16:

Table 16 Stoichiometric for the reactions of the secondary conversion submodel (Srinivas, Field, & Herzog, 2013)

REACTION	**STOICHIOMETRY**	
R-1	$C_6H_5OH+3\ H_2O \rightarrow 2\ CO+CO_2+2.5\ CH_4+0.05\ C+0.1\ H_2$	Steam reforming
R-2	$2\ C_7H_8+21\ H_2O \rightarrow 7\ CO_2+29\ H_2+7\ CO$	Steam reforming
R-3	$C_7H_8+2\ H_2 \rightarrow CH_4+C_6H_6$	Hydrodealkylation
R-4	$C_6H_6+2\ H_2O \rightarrow 1.5\ C+2.5\ CH_4+2\ CO$	Steam reforming

Two more assumption have been made to simplify the modelling; firstly, the thermal cracking of the tar model compounds is neglected. Thermal cracking of the tar is achieved by raising the temperature of the gas to a point at which thermal cracking occurs of the tars. Temperatures for thermal cracking depend on the nature of the tars, and there is great inconsistency in the literature of an appropriate temperature, although a common conclusion is that temperatures exceeding 1100 ˚C are required (Donnot, Reningovolo, Magne, & Deglise, 1985). Since in our model, temperatures above 1000 ˚C is not considered, this assumption can be justified. The second simplification is that the reactions are considered to be at equilibrium in the CFB gasifier of TUW. In the work of (Mauerhofer et al., 2019), evolution of gas and tar composition over the reactor height of CFB gasifier of TUW is studied. According to this work, the yield of different tar compounds at few centimetres above the bubbling bed, varies in the range of 0.05 to 4 $g/m^3_{gas,db}$ which is in order of magnitude lower than the predicted tar yield from devolatilization process. The latter can suggest that the significant amount of secondary tar reactions can occur from the lowest point of the devolatilization in the GR (somewhere in the bubbling bed), up to the rectangular section of the GR. For simplification, in the model development, it will be assumed that all the secondary tar reactions occur in the bed, hence, in the freeboard of the GR, only gas-gas reactions between the permanent gases will occur. This statement means that the gas composition derived from the devolatilization yield products and secondary tar reactions discussed before, must represent the gas composition at the GR slightly above the bubbling bed. These results are only available for the bed temperature of 850 ˚C from the work of (Mauerhofer et al., 2019) and can be a hint of validation to the previous assumptions. The results of gas composition on top of the bubbling bed from the model are shown in the Figure 86 and the gas composition from the experimental work of (Mauerhofer et al., 2019) is shown on the same figure with dots.

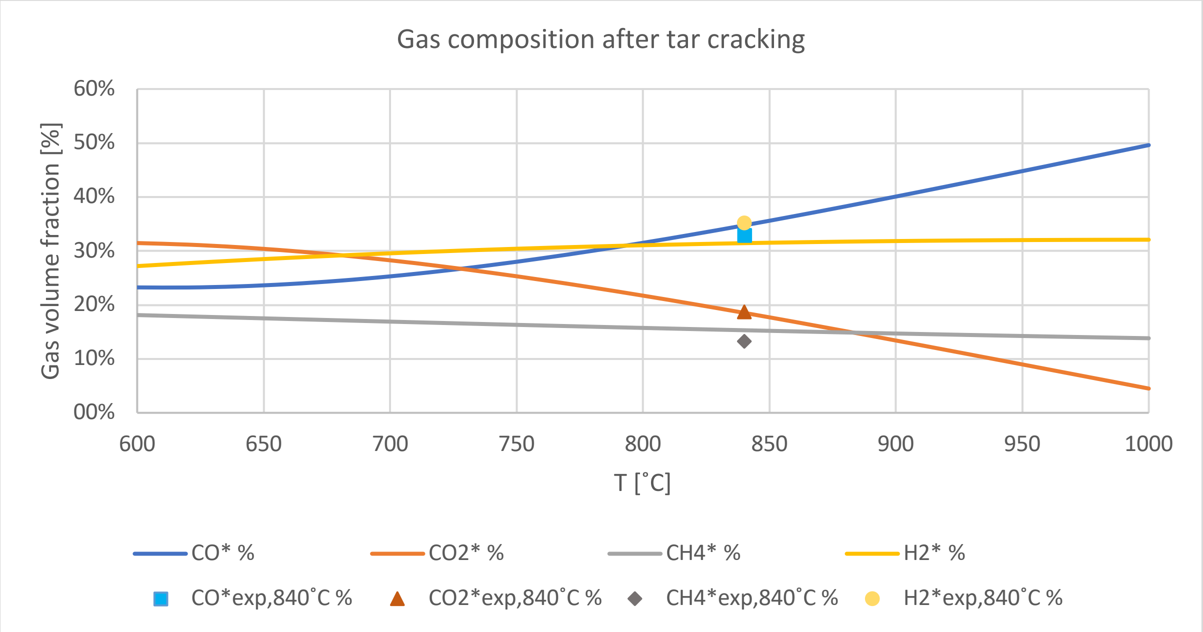

Figure 86 Gas composition after devolatilization and secondary tar reactions; solid lines=model, dots=experimental data for softwood pellet gasification at TUW's CFB gasifier at 840 ˚C with olivine and limestone as bed material, source:(Mauerhofer et al., 2019)

The experimental data available are only for one temperature and they are in good accordance with the model pointwise, but the trends can't be validated due to lack of experimental measurements. Instead, the final gas composition at the outlet of the gasifier will be validated against the long test run of softwood pellets with temperature variation.

Effect on StB

So far, the steam to biomass ratio is discussed in two cases of considering solely the steam as fluidization agent to the dried ash-free fed biomass, and the case where the moisture content released from the biomass itself taken into account for the expression of steam to biomass ratio. Further on, the pyrolytic water formed through process of devolatilization can also be taken into account and its effect on the overall StB ratio will be discussed. The yield of pyrolytic water is a temperature dependent variable, therefore, the new expression of StB** which concludes this valuable is as a function of temperature. Since the yield of pyrolytic water decreases with temperature, the StB** is also expected to decrease with temperature but remains always higher than the StB ratio where the pyrolytic water is neglected. The results of new expression of StB** is shown in the Figure 87 and is compared to the previous StB expressions. The new expression shows an increase between 14% and 40% respect to StB.

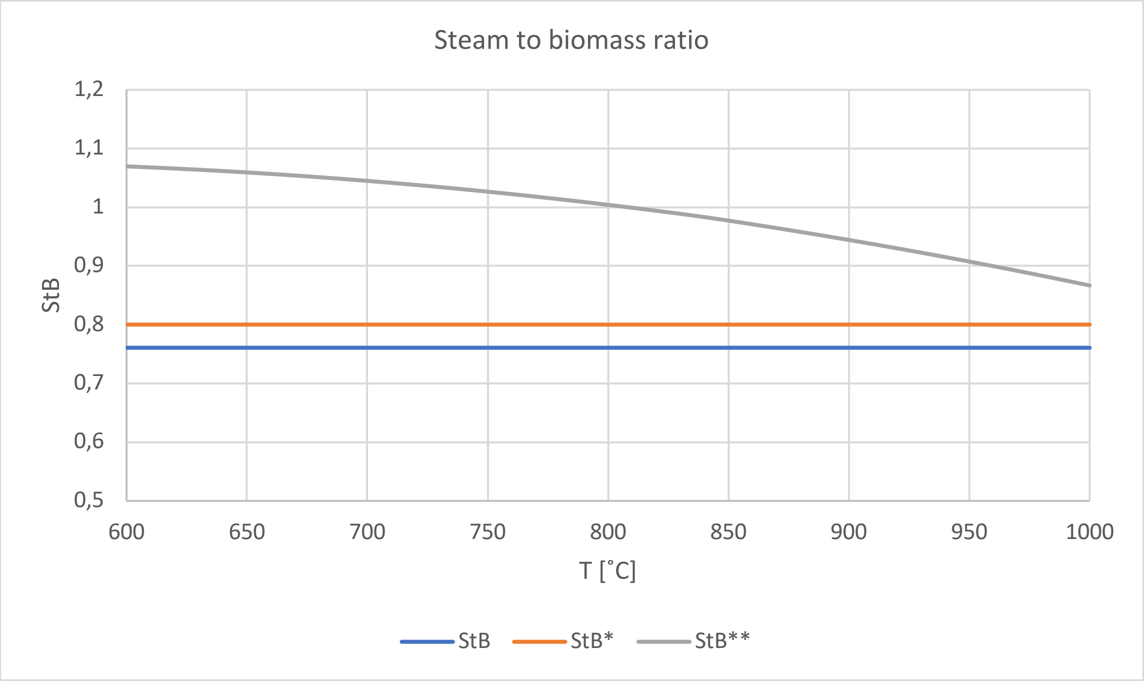

Figure 87 Steam to biomass ratio; StB=$H2O_{fluidization}/M_{biomass,daf}$, StB=($H2O_{fluidization}+H2O_{moisture\ content}$)/$M_{biomass,daf}$, StB**=($H2O_{fluidization}+H2O_{moisture\ content}+H2O_{pyrolytic\ water}$)/$M_{biomass,daf}$*

Effect on gas residence time

The gas residence time in the key for kinetic modeling of the reactions occurring in a reactor. Previously it was calculated based on the gas input as fluidization agent which is shown with blue line in the Figure 88. Considering the amount of gas released from the devolatilization process and secondary tar reactions, the volume of the gas will increase and subsequently the gas residence time will decrease. The effect of gas coming from biomass devolatilization is shown in the Figure 88. The orange line indicates the gas residence time in the freeboard of the GR as a function of temperature. The results show that the gas residence time almost half, when considering the devolatilization products.

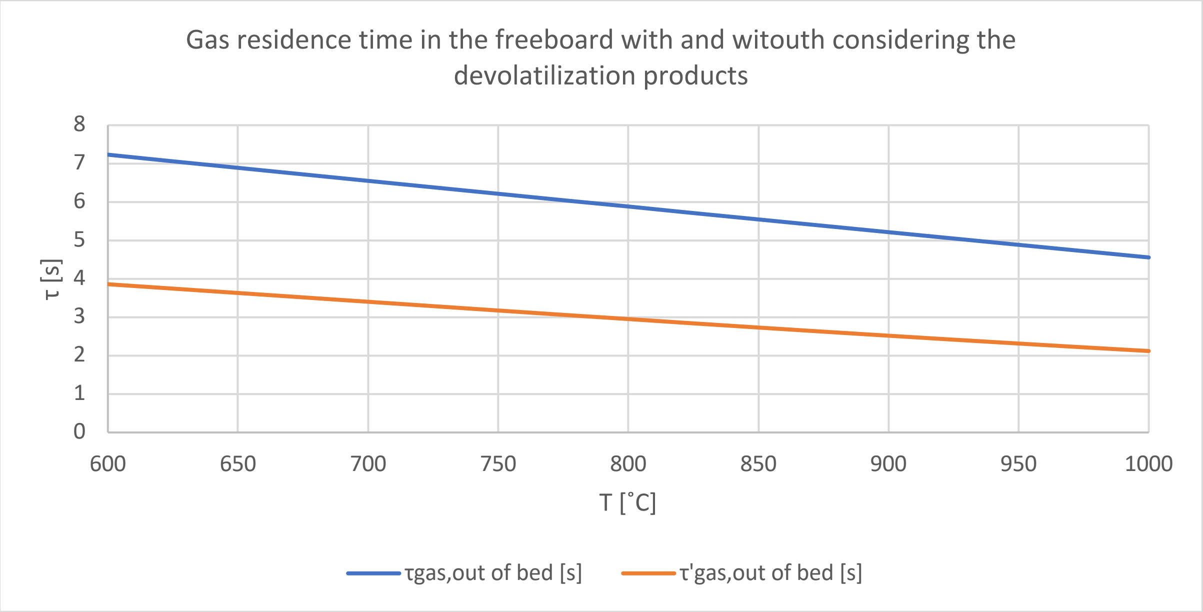

Figure 88 Gas residence time in the freeboard of the GR as a function of temperature; blue: only steam, orange: steam plus devolatilization products

5. Char conversion in fluidized bed gasification

The kinetics of char gasification is an important aspect to study and model the biomass gasification. In the CFB gasifiers where the gasification reactor is fed only by steam as fluidization agent, the reaction of char with H_2O and CO_2 is by orders of magnitude slower than the devolatilization process and gas-gas reactions. Therefore, only a fraction of char will be gasified in the GR, and the rest is carried away with circulating bed materials to the CR to be combusted and provide the heat for the GR. Maximizing the char gasification in the GR will increase the efficiency of the process, but it's limited to its kinetics and the gasification design.

In this chapter, the kinetics of the char derived from softwood pellets are experimentally investigated to be implemented in the model. Softwood pellet is chosen because it's the reference fuel for this model and the standard fuel for most of the commercial gasification plants. The reaction of char derived from SWP will H_2O and CO_2 are investigated separately in two different TGA devices at Technical University of Denmark (DTU) at different temperatures. The gasification of gas mixtures and gas combustion wasn't technically possible; therefore, the related data are chosen from relative literature. Further on, the effect of presence of bed material such as olivine sand on the kinetics of char gasification is also investigated experimentally.

The rate of char gasification is influenced by temperature, partial pressure of the gas reactants as well as the products, the fuel parent, the process from which the char is produced, its ash content and their composition, particle size, its porosity (surface area and volume of the pores), and finally number of active sites on the char particle. Therefore, obtaining the rate expression based on all the possible variables is very complicated and beyond the scope of this work. The rate of char gasification here is simply expresses as its mass loss over the time:

Equation 48 $r = -\frac{1}{m_{C0}}\frac{dm_C}{dt} = \frac{dx_C}{dt}$

In the Equation 48, m_{C0} stands for the initial mass of the char, and m_C represents the mass of char particle at conversion x_C. Then the term of reactivity can be defined by the conversion rate at time t with referring to the mass of char particle:

Equation 49 $R = \frac{1}{1-x_C}\frac{dx_C}{dt}$

As said earlier, the char reactivity does depend on many variables, and even shrinking the char particle through the process of gasification, can affect the mass and heat transfer limitations for the reaction and hence constantly changing the rate of reaction. Shrinking of the particle has also another effect on the process. The inorganic content of the char, can either catalytically enhance the process or inhibits it, based on their composition. With reducing the particle size over the process of gasification, the ratio between the total amount of inorganics to the char particle itself changes and can be a changing factor to the reaction rate.

The char gasification experiments in the TGA devices to be fully representative of char gasification in the CFB gasifier, the char must be produced from the same process. But since the char in the CFB gasifier will go through the CR to be combusted, collecting it from the same process was difficult and it was decided to produce the char in a small reactor from pyrolysis at the same temperature of the CFB gasifier. (Gomez-Barea and Leckner, 2009b) concluded in their study that the most important factors on the properties of the char generated after devolatilization are the temperature and particle heating rate, therefore in the process of char generating they were taken into account. Other affecting parameters in this study is cooling the char particles after generating them, which was inevitable, and will reduce the char reactivity as also reported in the works of (Miura et al., 1989; Liu et al., 2003). The last factor would be lower activation sites on the char particles that are produced from pyrolysis to compare with the char produced in the CFB gasifier.

Most authors investigated the char reaction with steam and carbon dioxide separately without using the mixture of gases. There are two arguments for char gasification with steam and CO2. One is the different active sites on the char particle reacts with different gases, therefore there's no race between H_2O and CO_2 to compete for the same active site; and second argument is contrary to the first one, which indicates that H_2O and CO_2 have to compete against each other to reach the same active site on the char particle. Both arguments are investigated by different authors, and (Everson et al., 2006; Huang et al., 2010) concluded that the char gasification with H_2O and CO_2 occurs at different sites, therefor a sum of kinetics of these two separate reactions can be taken into account and the same time author (Umemoto et al., 2011) concluded that the active sites are shared between gases. Since for almost all chars, the gasification rate with H_2O is much higher than CO_2 (Robert and Harris, 2007), in this work it's assumed that the reaction happens at different active sites, therefore the overall gasification reaction rate would be the sum of reactions with H_2O and CO_2. There are also studies that suggest the inhibitive effect of CO and H_2 on the gasification reaction, since they can also be adsorbed at the surface of the char pores. These effects have been studied by (Di Blasi, 2009; Ollero et al., 2002). At moderate condition with atmospheric pressure and relatively low partial pressure of CO and H_2, their inhibitive behaviour on the char gasification can be neglected.

To obtain the kinetic expression of char gasification at temperature T, according to (Gomez-Barea and Leckner, 2010), the following expression can be used:

Equation 50 $r = r_{x_c}(T,P).F(x_c)$

Where r_{xc} can be expressed with two parts; first the Arrhenius equation that takes into account the dependency on temperature, and the second part which takes into account the partial pressure of reactant gases. In this study only pure gases are used as the reactants; therefore, the second term of the r_{xc} that takes partial pressures into account will be irrelevant at this point. The last term of the equation, $F(x_c)$, will take into account the variation of reaction rate with respecting to the conversion, which can include the effect of shrinkage of the particle and the proportion of the inorganics to the char particle as reaction is progressing. Assuming that the order of reaction doesn’t change with neither temperature nor degree of conversion, then r_{xc} can be expressed as:

Equation 51 $r_{x_c} = k_0 e^{\left(\frac{-E_a}{R_g.T}\right)}.P(CO_2, H_2O)$

The second part as discussed before, will be neglected here, since the reactant gases are used in pure form without any dilution. Equations 50 and 51 are practical expression to fit the experimental measurements.

Experimental set up

The softwood pellets are pyrolyzed at the Technical University of Vienna (TUW) and char gasification performed in two separate Thermogravimetric Analyzers (TGA) at Technical University of Denmark (DTU). Char gasification with CO_2 has been performed in a micro-TGA heated at 20 ˚K/min to reach the peak temperature and then the char sample has been held at peak temperature for 30 minutes. During the heating up, N_2 as an inert gas is used to evaporate the remaining moisture and volatile content in the sample, then at the peak temperature the gas is switched to CO_2 for initiating the reaction. The samples (20~25 mg) is placed in the crucible, on a horizontal balance arm with the precision of 0.1 µg. The accurate sample temperature is detected by a thermocouple in direct contact with the sample crucible. The gases are introduced in the chamber at atmospheric pressure with the flowrate of 30 ml/min. The experiment was repeated at 4 different temperature of 650, 750, 850 and 950 ˚C. Once the reaction rate of char gasification with CO_2, namely Buoduoard reaction was obtained, olivine sand was added to the sample to assess the enhancement of the reaction in presence of olivine sand.

The second TGA device where steam gasification is performed, is a macro device with a bigger crucible (sample size 15~30 gr) and higher steam flowrate of 150 ml/min. The experiment has been conducted at three temperatures of 650, 750 and 850 ˚C, without presence of olivine sand. In order to assess the remaining moisture content and volatile matter in the char, a proximate analysis has been performed. The repeated experiments showed that the samples contain around 0.8% moisture content and 2.5% volatiles. The amount of moisture content and volatile (sum<2.3%) may be adsorbed by the char sample during the handling after pyrolysis, while it was cooled down and transferred. The result of char proximate analysis is shown in the Figure 89:

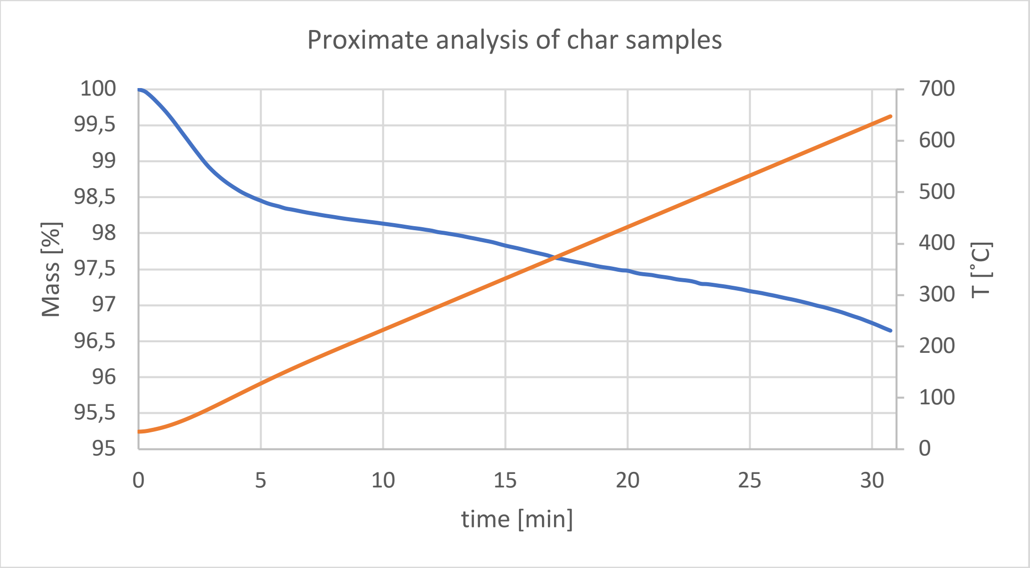

Figure 89 Proximate analysis of char samples

As it can be seen, up to 100 ˚C the moisture content is vaporized, and with increasing the temperature the volatile content has been released.

In this work, the reactivity is measure by the mass loss of the sample over time and the method of the experiments is ex-situ, meaning the char is produced in a different laboratory apparatus and cooled down to the ambient temperature before conducting the char gasification reaction. In a study of (Nilsson S. 2012), the author compares both ex-situ method with in-situ where the char produced from biomass is being gasified without cooling down. She concludes that the thermal history of char is an important factor on reactivity of in-situ char can be much higher. In her study he shows that the char gasification rate with CO_2 at 800 ˚C, at conversion of x_c=0.2 is two times higher for ex-situ char, and the gasification rate with H_2O at the same temperature is 3 times higher. In this work due to technical limitation only the ex-situ method is employed, therefore an underestimation of char reactivity is expected.

Specific surface area and volume of pores has been measured for the char sample with BET analysis and compared to the data from literature (Lundberg et al., 2016), where the char sample from softwood pellet is collected directly from the fluidized bed gasifier at 850 ˚C with steam as gasification agent. The results show that the char sample from SWP from ex-situ method has a specific surface area of 384 m^2/g to compare with the work of (Lundberg et al., 2016) which has a surface area of 1581 m^2/g. Having a higher surface area for (4.1 times higher) can be an indication for the difference between char reactivity of ex-situ and in-situ char.

Char gasification with CO_2

The results of char gasification with CO2 in form of mass loss is shown in the Figure 90. It can be noted that at temperatures below 950 ˚C, the kinetics of the Buoduoard reaction is so low, that in 30 minutes it barely reaches 2% conversion, but at 950 ˚C a significant increase can be observed. It can be also attributed to activation of the char at higher temperatures.

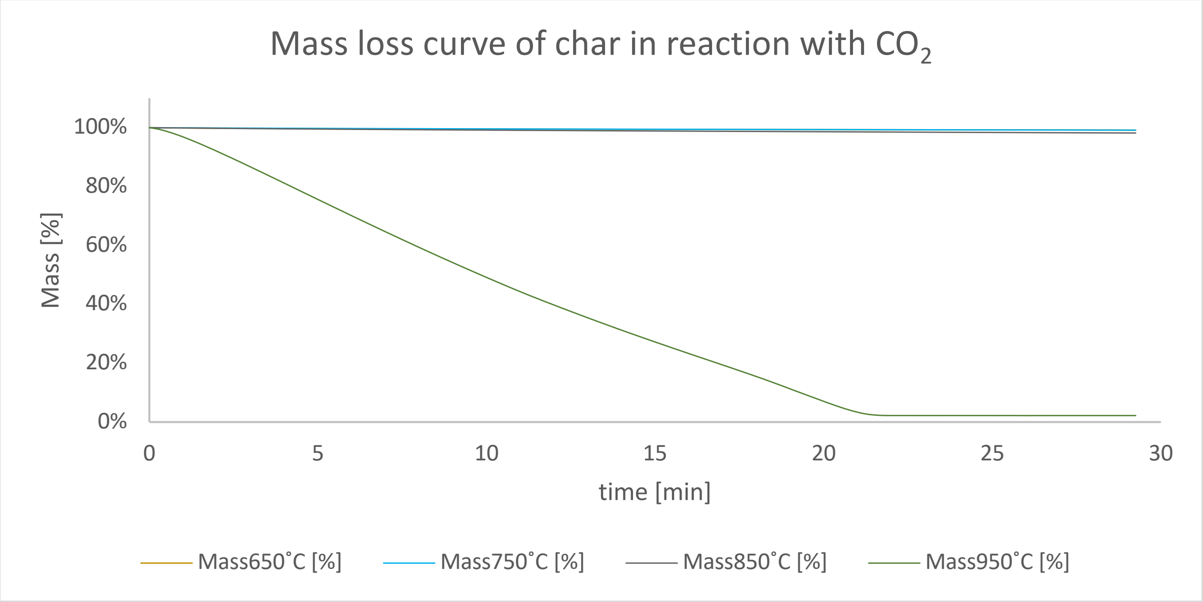

Figure 90 Mass loss curve of char samples in reaction with CO_2 at temperatures of 650, 750, 850 and 950 ˚C

For a better and distinguishable visualization, the results for the temperatures of 650, 750 and 850 ˚C are put together in the Figure 91.

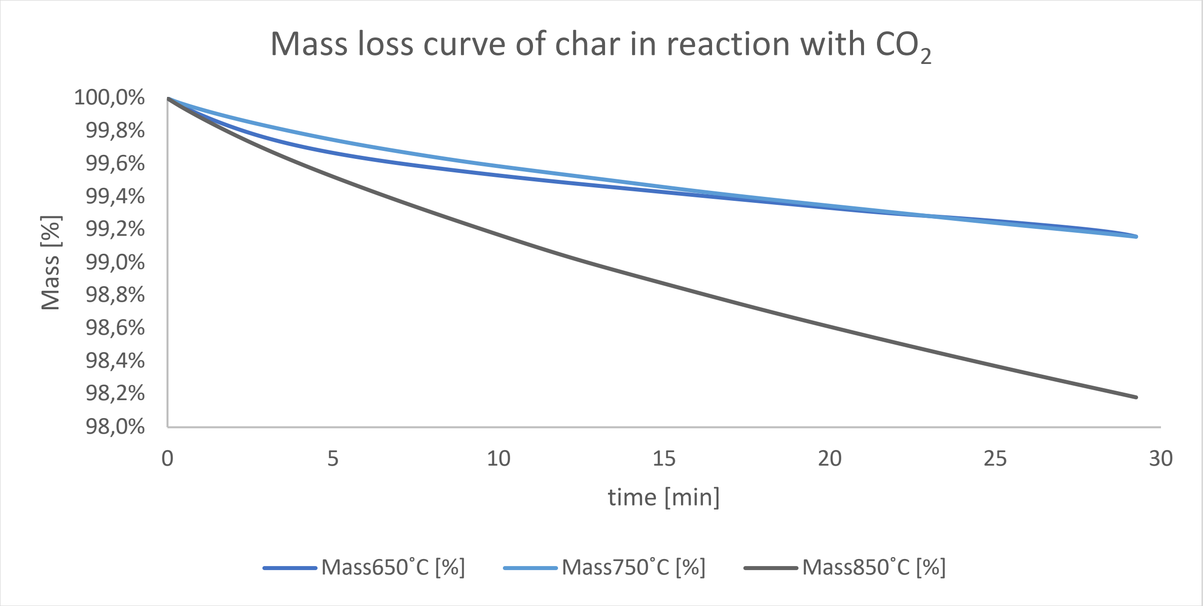

Figure 91 Mass loss curve of char samples in reaction with CO_2 at temperatures of 650, 750 and 850 ˚C

It's evident from Figure 91 that within 30 minutes of reaction, the conversion doesn't exceed 2% (X_C<0.02). A longer time for test run was avoided since in industrial CFB gasifiers char residence time does not reach such time scale. In order to obtain the rate of reaction as a function of conversion, full conversion at all temperatures are needed. Therefore, for implementation of the results in the model, according to char residence time, corresponding conversion to that time is taken into account according to the results of mass loss over time. The char conversion results are summarized in the Figure 92. But further on the effect of adding olivine sand to the samples are investigated to assess the enhancement of the process.

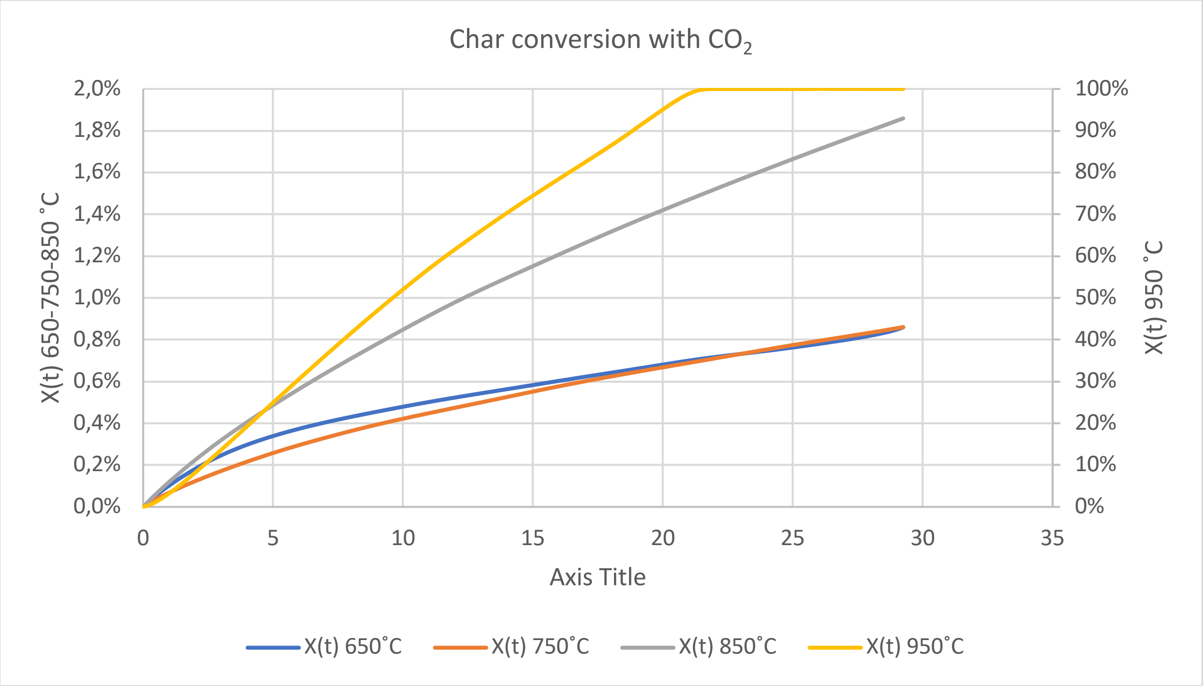

Figure 92 Char conversion in TGA with CO2 at different temperatures

After mixing char particles with olivine sand, experiments have been repeated with the same procedure. The results show drastic increment in the char conversion which can be attributed to the higher heating exchange when the olivine sand is added (Koppatz, Pfeifer, & Hofbauer, 2011). The results are shown in the Figure 93, where the solid lines represent char conversion without olivine sand, and the dashed lines show the char conversion in presence of olivine sand.

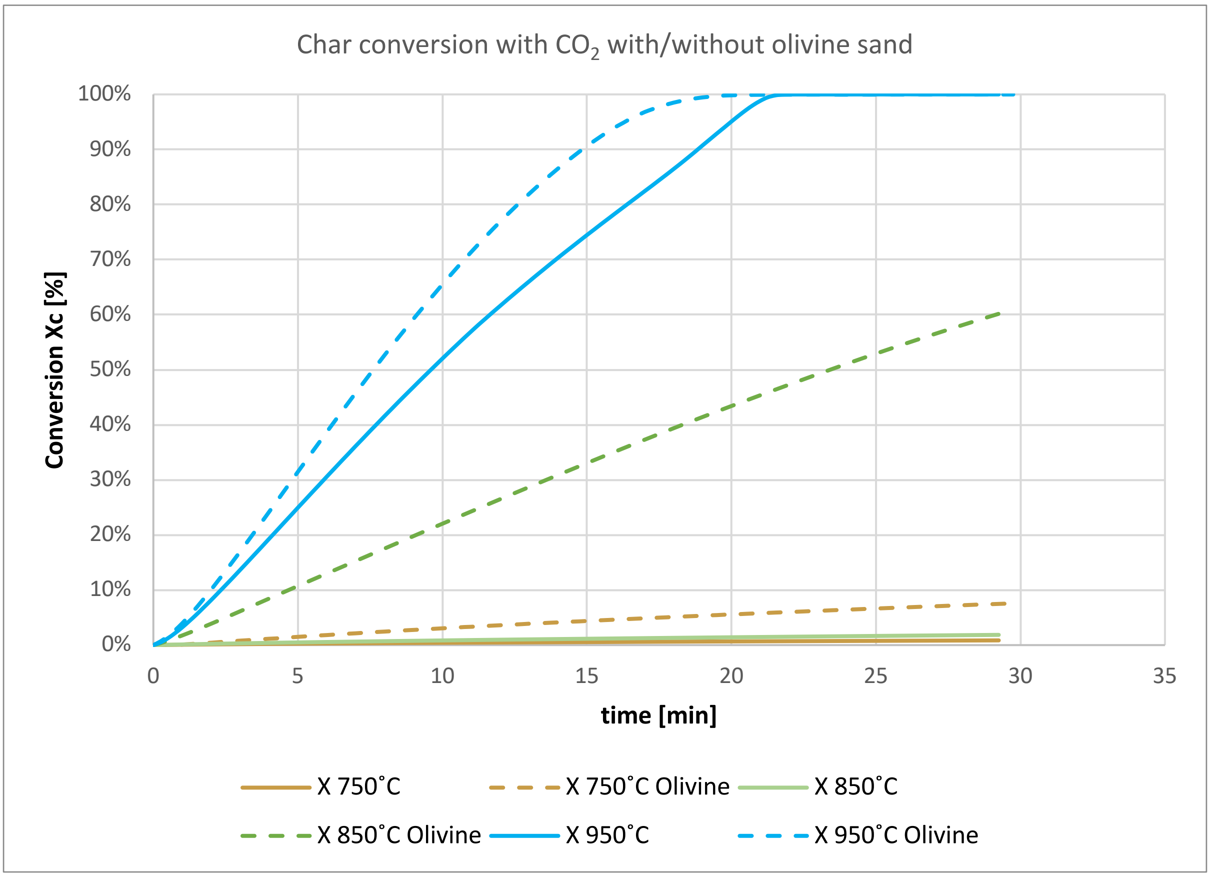

Figure 93 Char conversion with CO_2 with and without olivine sand at 750, 850 and 950 ˚C

Trying to fit the experimental data to the Arrhenius kinetic expression for char gasification with CO_2 results to activation energy of E_a=169 kJ/mol and frequency number of k_0=5.17x10^6 in the case of pure char, and E_a=20 kJ/mol and of k_0=1.57x10^6 when olivine sand is added to the sample. It's evident that both activation energy and frequency number reduce in presence of olivine sand. The kinetic values obtained in these experiments are compared to (Nilsson et al. 2010). In her study, the order of the reaction was also investigated, but since here the partial pressure of the CO_2 is not changed during the experiments, order of the reaction couldn't be obtained, and it's assumed that the reaction is 1^{st} order. (Nilsson et al, 2010) found the kinetic parameters for char gasification with CO_2 to be E_a=163.5 kJ/mol and of k_0=6.33x10^4. It's evident that the activation energies are very close and match with a narrow margin. The frequency number is lower in the founding of (Nilsson et al., 2010) which can be attributed to the higher ash content of their char.

Char gasification with steam

Char gasification with steam has been investigated with the same method explained previously but in a different TGA device. Raw data were not available and instead a dedicated software to the TGA device generates the figures. An example of the results, only for temperature of 850 ˚C is shown in the Figure 94 and Figure 95. The mass loss curve shows a conversion of 78% in 23 minutes at 850 ˚C, with maximum reactivity of 17.5 %/min. The maximum conversion at 650 and 750 ˚C in 23 minutes are 7.2% and 20% respectively. The kinetic parameters obtained from the results for char gasification with steam are E_a=240 kJ/mol and of $k_0=8.9x10^6$. The obtained value are in good agreements with the founding of (Barrio et al., 2008).

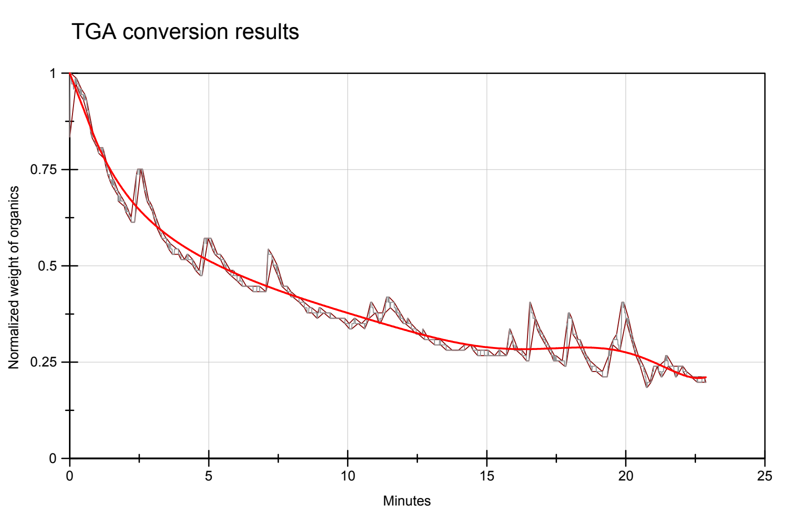

Time of operation: 23 min
Residual organic material after operation: 20.48 wt% of total organics
Reactivity at 50% conversion (R50): 8.18 +/- 0.02
Time used at 50% conversion: 5.38 min.

Figure 94 Mass loss curve of char gasification with steam at 850 ˚C

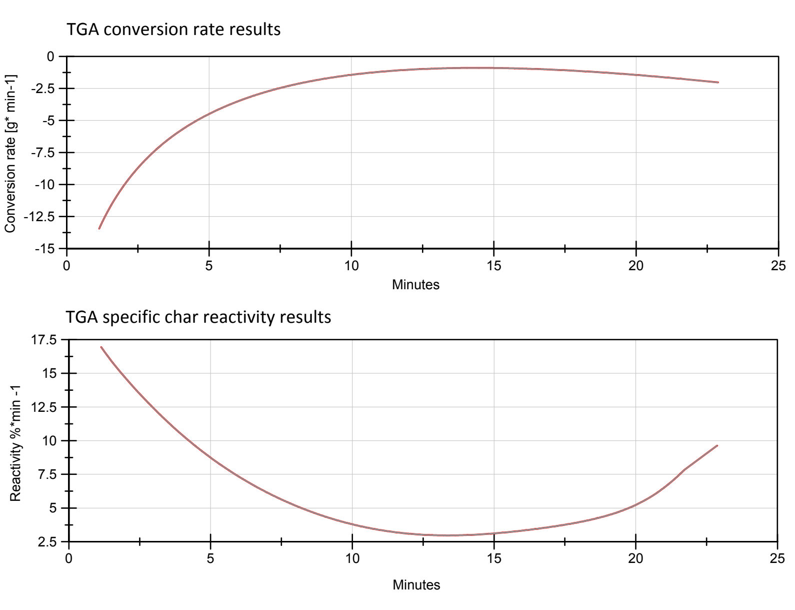

Figure 95 Conversion rate and reactivity of the char gasification with steam at 850 ˚C

Char oxidation

Instead of measuring the rate of combustion of char, respective values are searched and compared from literature. The kinetic values are investigated in lower temperatures (around 500 ˚C) and then interpolated for higher temperatures. In the Table 17 a comparison has been made between five literature models for the kinetics of wood char combustion.

Table 17 Comparison of the kinetic parameters of wood char combustion from literature

Model	k_0 (s^{-1})	E_A (kJ/mol)	n	r^2
homogeneous rate equation	1.064×10^5	124.8	0.529	0.941
Simons and Finson (1979)	2.332×10^5	125.0	0.530	0.950
Bhatia and Perlmutter (1980)	4.434×10^5	124.9	0.529	0.943
Gavalas (1980)	4.434×10^5	124.9	0.529	0.943
Tseng and Edgar (1989)	4.434×10^5	124.9	0.529	0.943

Homogeneous rate reaction model considers the particle consisting of one phase. Instead, methods proposed by authors mentioned in the Table 17, pore models are taken into account. The model equations of Bhatia and Perlmutter (1980), Gavalas (1980), and Tseng and Edgar (1989) have the same mathematical form and therefore shows exact results for kinetic parameters. The model of Simons and Finson (1979) considers a very low value of initial char porosity and therefore it is not well suited for modeling the char combustion. These kinetic values also have been compared with the results of (Dennis et al., 2005) where the intrinsic kinetics of char combustion with char produced from sewage sludge is measured. In (Dennis et al., 2005) work, the activation energy is calculated to be 114 kJ/mol which is about 9% lower than that of char from wood, and the kinetic constant is measured to be 1.16×10^4 (s^{-1}) which shows a higher deviation from k_0 of char wood. The latter can be explained by much higher ash content of the char from sewage sludge.

The data from CFB gasifier of TUW, shows that flue gas from combustion reactor is virtually CO free ($N_2\approx80$ to 85%, $CO_2\approx10$ to 15% and the rest is O_2), therefore, one can assume that the combustion is happening completely and kinetic modeling can be simplified to equilibrium model.

The founding in this chapter is later used to simulate the process of steam biomass gasification in the dual fluidized bed gasifier of TUW.

Results

In the CFB gasifier of TUW, with increasing temperature of the GR, the air input in the riser increases. Increased superficial velocity in the riser causes higher circulation rate of bed material and subsequently less residence time for the char in the bubbling bed of the GR. An estimation of the char residence time in the GR as a function of bubbling bed temperature has been made in the Chapter 2. Based on the char residence time and kinetics of the char gasification, the converted char in the GR and the unconverted char going to the riser has been calculated and are shown in the Figure 96 below:

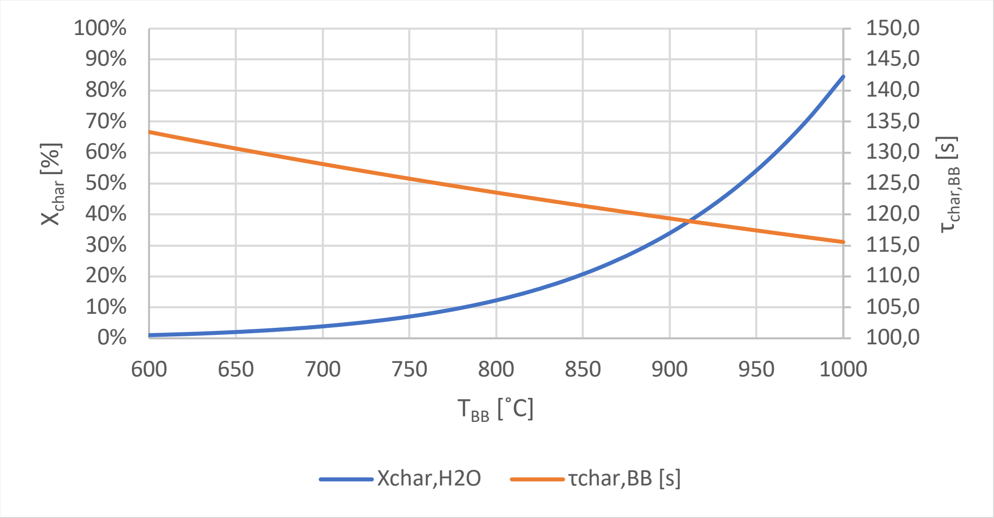

Figure 96 Char conversion in the gasification reactor of TUW's CFB as a function of bubbling bed's temperature and corresponding char residence time

It can be noticed that even though the char residence time slightly decreases with temperature, the higher increase in the kinetics of the char gasification results to a very notable increment of char gasification. Higher char gasification inside the GR is desired since it raises the carbon conversion and efficiency of the process. As more char in converted, less char is going to the riser. The amount of converted char in the GR and unconverted char going to the CR as a function of gasification temperature is shown in the Figure 97 below:

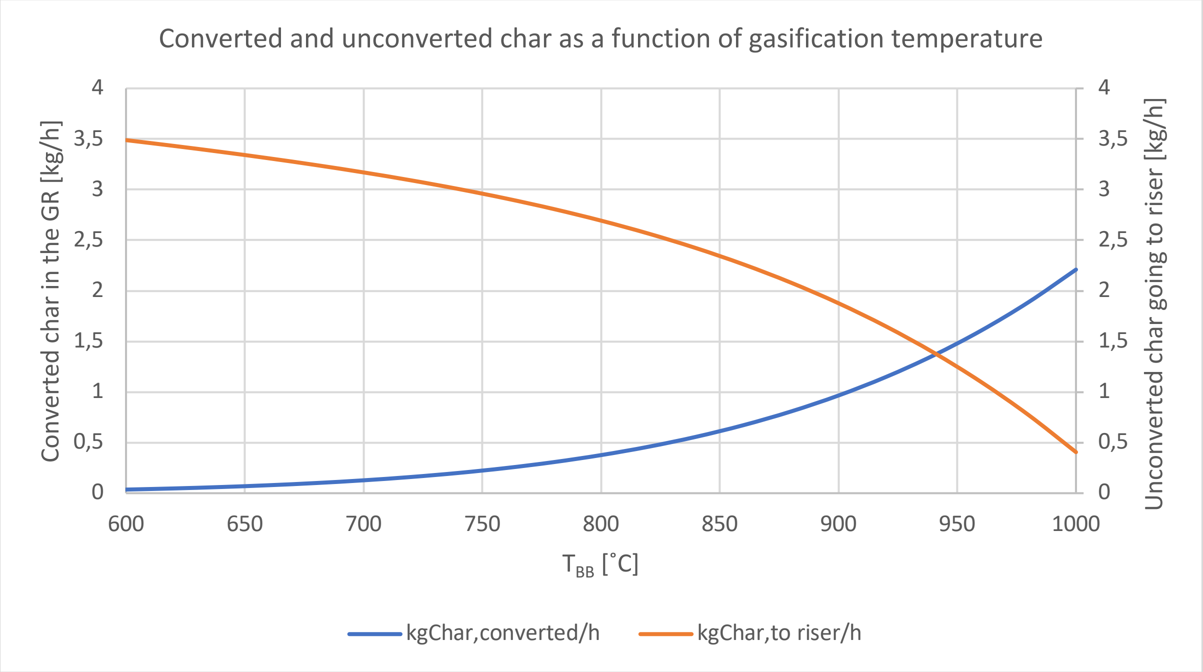

Figure 97 Converted char in the GR vs Unconverted char going to the CR

Increasing the char gasification in the GR, require steam for the reaction and subsequently increases the carbon and water conversion. Carbon conversion in the gasification reactor is one of the key figures for the efficiency of the system. Steam in the GR participates in different reactions, such as char steam gasification, tar reforming and reactions with permanent gases for which water gas-shift reaction is the dominant one.

As it can be observed from the results, assuming a StB* ratio of 0.8, for which also the moisture content of the biomass is included, results to a total steam input to the GR of 15 kg/h (steam for fluidization + steam from moisture content of the biomass= 15 kg/h). With increasing the temperature of the gasification, more char is gasified with steam and it can require up to 3.3 kg/h of steam which accounts for 22% of the total steam input in the system. The results of the amount of steam needed for the complete char steam gasification and subsequent water conversion in the gasification reactor for the whole range of gasification temperature is shown in the Figure 98 below:

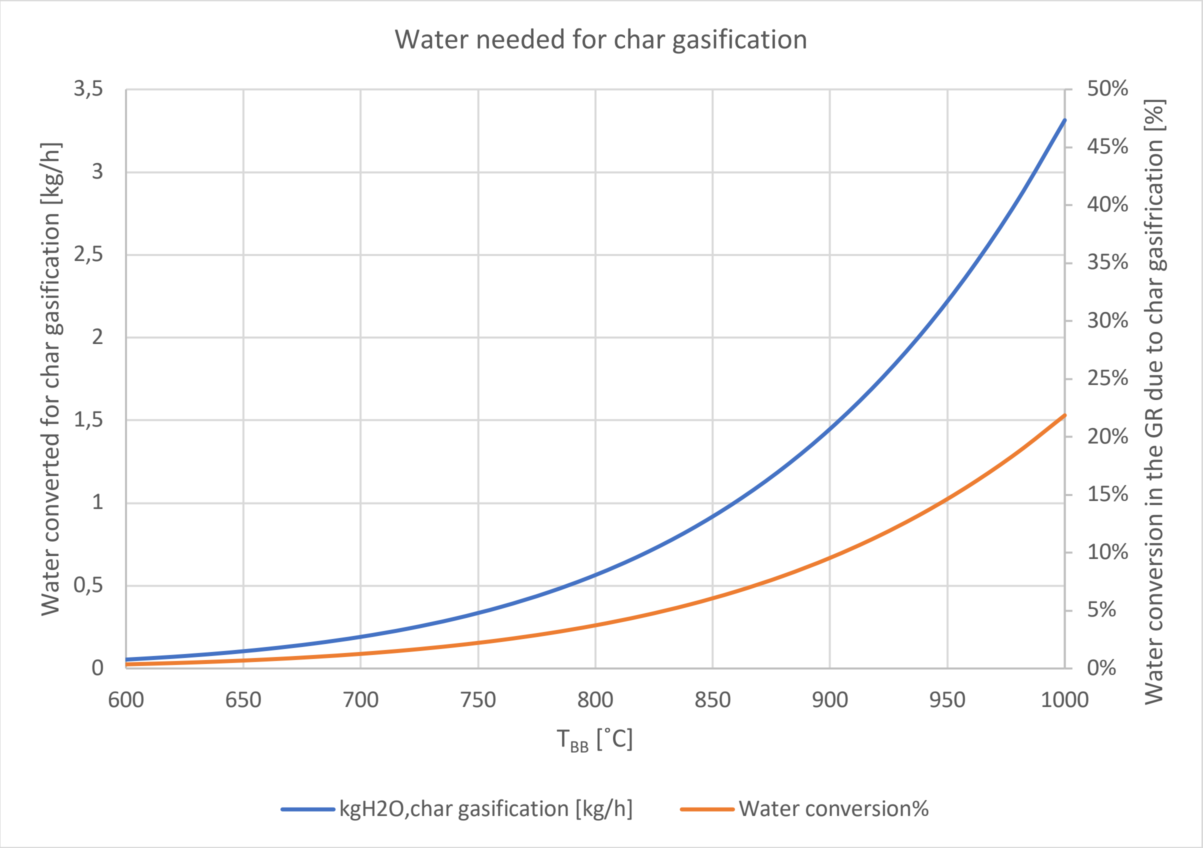

Figure 98 Water converted with the char inside the GR as a function of temperature

6. Water gas-shift reaction in the process of biomass gasification

The solid biomass in the high temperature of the reactor turns into permanent gases, tar and char. The tar over its dew temperature will be found in vapor phase and will ascend with the permanent gases through the freeboard of the reactor. Possible gas-gas reactions are water gas-shift reaction which leads to production of hydrogen, and methane steam reforming reaction which also leads to hydrogen production with consuming methane. (Kjell-Arne Solli et al., 2016) gathers the kinetic parameters of these reactions and run simulations to compare their relative speed. He sets rate of reactions from (Thapa et al., 2014) together with calculated typical molar concentrations after devolatilization process of biomass at inlet feed conditions. The simulations are performed under plug flow reactor condition. He sets two different residence times of 12 and 300 seconds to study the importance of these two reactions proceeding in parallel. He concludes that within 12 seconds residence time, including or neglecting the methane steam reforming reaction, has no noticeable effect on the final gas composition. Since gas residence time in the dual CFB gasifier of Vienna calculated to be lower than 7.5 seconds, the methane steam reforming reaction is neglected in the development of the simulation for simplicity. This assumption is validated by the founding of (Kjell-Arne Solli et al., 2016). He concludes that, the water gas-shift reaction is the dominant reaction and other reaction doesn’t contribute significantly in CH_4 concentration, although at 300 second residence time, the effect of methane steam reforming reaction can be more evident.

Water gas-shift reaction

Water gas-shift reaction (WGSR) is the most important and dominant gas-gas reactions in the process of steam biomass gasification which increases the hydrogen content in the product gas. In the literature, this reaction is widely studied at lower temperatures and in presence of metal catalysts, since WGSR is favored in those conditions. But the kinetics of WGSR at higher temperatures (above 650 ˚C) which is typical for biomass gasification has only been investigated by few authors. In fact, WGSR in the fluidized bed reactors, can be considered a gas-gas-solid reaction, where the solid part is either the char, ash, or bed material which can change the kinetic rate. Therefore, the kinetics have to be chosen with caution because the composition of the ash and char, and so their catalytic activity, depend greatly on the parent fuel. In this work, an experimental investigation has been done to obtain the kinetics of homogeneous WGSR in typical conditions of biomass gasification reactors without interference of any catalyst. Further on, a factor can be introduced for the catalysts added into the system.

The experiments to investigating the kinetics of WGSR are conducted in 3 different temperatures (700, 800 and 900 ˚C) in a non-catalytic reactor (quartz) to avoid any catalytic effect of the reactor walls. Even the thermocouples are covered with quartz.
WGSR requires steam as one of the reactants, which producing steam and injecting with high precision to the system is difficult, it’s decided to perform the reverse-WGSR with feeding the reaction hydrogen and carbon monoxide. After obtaining the kinetic expression of reverse-WGSR, one can correlate the results with the forward WGSR, using the equilibrium constant. There are various equations for equilibrium constant K_{eq} of WGSR in the literature and some of them are reported and compared here and the results are shown in the Figure 99:

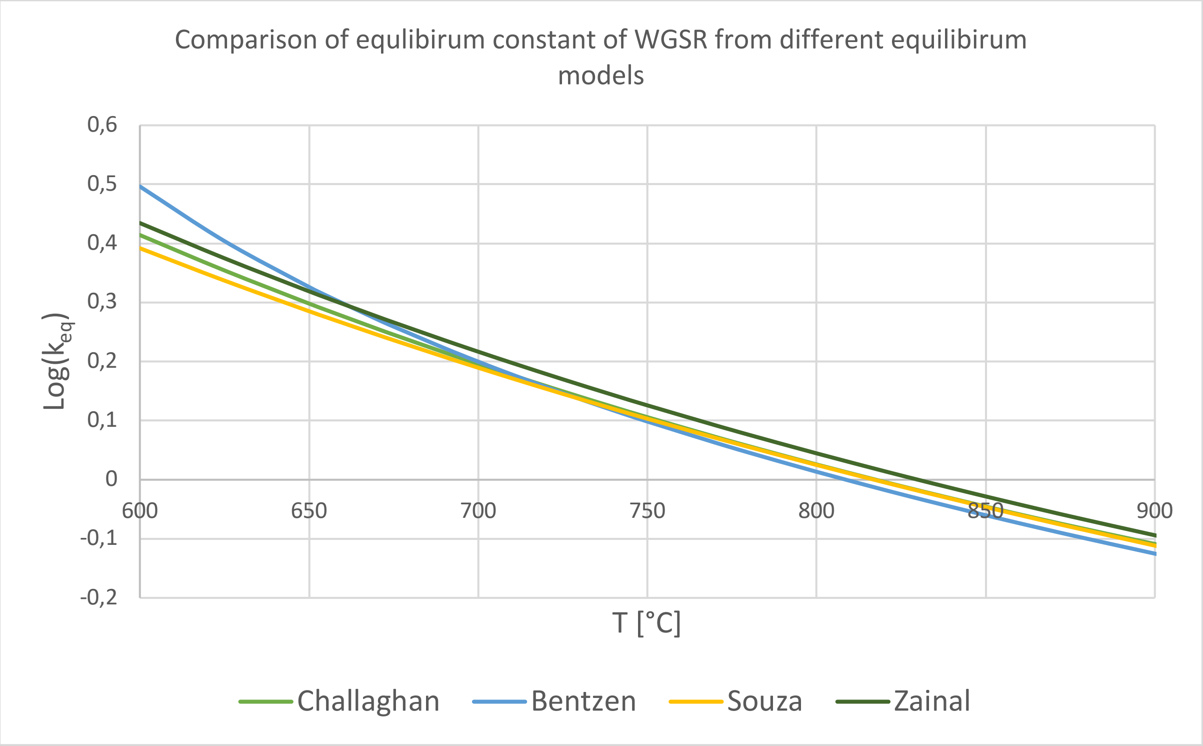

Figure 99 Equilibrium constant of water gas-shift reaction based on different models

Challaghan: $K_{eq} = 10^{-2.4198+0.0003855T+2180.6/T}$

Bentzen:$K_{eq} = ((0.000001303T + 0.000717)T - 1.3006)^{-1}$

Souza:$K_{eq} = 0.0265e^{3958/T}$

Zainal*:$K_{eq} = e^{\frac{5870.53}{T}+1.86\ln(T)-0.00027T-\frac{58200}{T^2}-18.007}$ (most accurate one)

Temperature in the equations are in Kelvin: T [˚K]
The results from different models are in good agreement and there’s a very low discrepancy. Here the model from Souza is taken into account. With taking one of these models in account, one can calculate the equilibrium composition of the gases at outlet as well as correlating the kinetic parameters of reverse-WGSR with forward-WGSR when needed.
The equilibrium constant can be written as a function of partial pressures of the reactants and products of the reaction:

WGSR: $CO+H_2O \rightarrow H_2+CO_2$; $\Delta H_{850^{\circ}C}$=-33.6 [kJ/mol]
r-WGSR: $H_2+CO_2 \rightarrow CO+H_2O$

$$K_{eq,WGSR} = \frac{[CO_2].[H_2]}{[CO].[H_2O]} = \frac{P_{CO_2}.P_{H_2}}{P_{CO}.P_{H_2O}}$$

Partial pressures will be equal to the molar fraction of the gas components multiply the total pressure of the mixture in case of ideal gases:

$$K_{eq,WGSR} = \frac{[CO_2].[H_2]}{[CO].[H_2O]} = \frac{P_{CO_2}.P_{H_2}}{P_{CO}.P_{H_2O}} = \frac{P.y_{CO_2}.P.y_{H_2}}{P.y_{CO}.P.y_{H_2O}}$$

Since in the experiments, the reverse-WGSR (r-WGSR) is investigated, one can obtain the equilibrium constant of r-WGSR based on the forward one:

$$K_{eq,r-WGSR} = \frac{[CO].[H_2O]}{[CO_2].[H_2]} = \frac{1}{\frac{[CO_2].[H_2]}{[CO].[H_2O]}} = \frac{1}{K_{eq,WGSR}}$$

In order to study the kinetics of a reaction, one must make sure that the experimental measurements are far from equilibrium. For that matter, the equilibrium composition must be calculated. Assuming the CO_2 conversion to be X_{CO2}, the conversion of hydrogen and production of steam and carbon monoxide can be correlated to the CO_2 conversion based on stoichiometric values and relative molar ratios in the feed stream. In the experiments, hydrogen bottle is diluted with nitrogen for safety measurements. Therefore, the gas composition at the outlet can contain the following components: CO_2, CO, H_2, H_2O and N_2.

At the inlet, the reactor is fed with the mixture of CO_2, H_2 and N_2. Carbon dioxide and hydrogen reacts to produce carbon monoxide and steam and nitrogen acts as an inert. The amount of steam produced in the reaction will be condensate in a cooling bath and the rest of the gas is sent to the gas analyzer to measure the gas composition.

Molar flow rates of the gas components at the inlet are known and measured and can be denoted as: F°_{CO2},F°_{H2},F°_{N2} [mol/min]. At the outlet two more components will be added as the products of the reaction and therefore the flowrates of the gas components at the outlet are: F_{CO2},F_{CO},F_{H2},F_{H2O},F_{N2}.

Then the conversion of CO_2 can be written as:

$$X_{CO_2} = X_A = \frac{F^{\circ}_{CO_2} - F_{CO_2}}{F^{\circ}_{CO_2}}$$

The relation between molar flows at the inlet can be defined by introducing a ratio between molar fraction of either hydrogen or nitrogen to the molar fraction of CO_2, which is measured and controlled in the experiments:

F°_{H2}=a F°_{CO2}, F°_{N2}=i F°_{CO2}

With setting the CO_2 conversion at equilibrium as a variable, the conversion of H_2 and production of CO and H_2O can be correlated to this variable via stoichiometric coefficients of the reaction and therefore the molar flowrate of the gas components at the outlet can be re-written as:

$F_{CO2}=(1-X_A)\ F^{\circ}_{CO2}$
$F_{H2}=(a-X_A)\ F^{\circ}_{CO2}$
$F_{CO}=(X_A)\ F^{\circ}_{CO2}$
$F_{H2O}=(X_A)\ F^{\circ}_{CO2}$
$F_{N2}=(i)\ F^{\circ}_{CO2}$

Total molar flowrate of inlet and outlet doesn't change since reactants and products are equimolar and therefore:

$F^{\circ}_{tot}= F_{tot}= (1+a+i)\ F^{\circ}_{CO2}$

Letting the molar fraction be $y_i=F_i/F_{tot}$, one can obtain the following expressions for the molar fraction at the outlet:

$y_{CO2}=(1-X_A)\ /(1+a+i)$
$y_{H2}=(a-X_A)\ /(1+a+i)$
$y_{CO}=(X_A)\ /(1+a+i)$
$y_{H2O}=(X_A)\ /(1+a+i)$
$y_{N2}=(i)\ /(1+a+i)$

Since in the experimental measurements, the steam condensate in the cooling bath and only the rest of gas components are being measured, one need to obtain normalized value for molar fraction with taking out the steam (Y):

$Y_{CO2}=(1-X_A)\ /(1+a+i-X)$
$Y_{H2}=(a-X_A)\ /(1+a+i-X)$
$Y_{CO}=(X_A)\ /(1+a+i-X)$

Y_{N2}=(i) /(1+a+i-X)

A summary of this procedure is reported in the Table 18:

Table 18 Inlet and outlet condition of the reverse WGSR experiment

	$F°_i$ [mol/min] (inlet)	$y°_i$ [%]	F_i [mol/min] (outlet)	y_i [%]=F_i/F_{tot} (outlet)	F^G_i [mol/min] (outlet without steam)	Y_i [%]=F^G_i/F^G_{tot} (outlet without steam)
A (CO_2)	$F°_A$	1/(1+a+i)	$(1-X_A)F°_A$	$(1-X_A)/(1+a°+i)$	$(1-X_A)F°_A$	$(1-X_A)/ (1+a+i-X_A)$
B (H_2)	$F°_B$=a. $F°_A$	a°/(1+a+i)	$(a°-X_A)F°_A$	$(a°-X_A)/(1+a°+i)$	$(a-X_A)F°_A$	$(a-X_A)/(1+a+i-X_A)$
C (CO)	0	0	$X_AF°_A$	$X_A/(1+a°+i)$	$X_AF°_A$	$X_A/(1+a+i-X_A)$
D (H_2O)	0	0	$X_AF°_A$	$X_A/(1+a°+i)$	0	0
I (N_2)	i.$F°_A$	i/(1+a+i)	i.$F°_A$	i/(1+a°+i)	i.$F°_A$	$i/(1+a+i-X_A)$
tot	(1+a+i) $F°_A$	1	(1+a+i) $F°_A$	1	$(1+a+i-X_A)$ $F°_A$	1

From the experimental measurements, Y_{CO2}, Y_{CO}, Y_{H2} and Y_{N2} are known. Therefore, there five equations that can lead to the calculation of X_{CO2}.

$$Y_{CO2}^{exp} = \frac{1 - X_{CO2}}{1 + a + i - X_{CO2}}$$

$$Y_{CO}^{exp} = \frac{a - X_{CO2}}{1 + a + i - X_{CO2}}$$

$$Y_{H2}^{exp} = \frac{X_{CO2}}{1 + a + i - X_{CO2}}$$

$$Y_{N2}^{exp} = \frac{i}{1 + a + i - X_{CO2}}$$

$$X_{CO2} = \frac{F°_i - F_i}{F°_i}$$

Although the most straight-forward way to calculate the CO_2 conversion is using the molar fraction of nitrogen in the gas composition at outlet, this value is calculated based on all means and the results have been compared.

As mentioned earlier, before proceeding with the processing the measurement data from r-WGSR experiments, one need to assure that the gas composition at outlet is still far from equilibrium and is controlled by the kinetics. In order to do so, the CO_2 conversion at equilibrium must be calculated:

$$K_{eq,r\_WGSR} = \frac{[CO].[H_2O]}{[CO_2].[H_2]} = \frac{P_{CO}.P_{H_2O}}{P_{CO_2}.P_{H_2}} = \frac{P.y_{CO}.P.y_{H_2O}}{P.y_{CO_2}.P.y_{H_2}} = \frac{X_{eq,A}.X_{eq,A}}{\left(1 - X_{eq,A}\right).\left(a - X_{eq,A}\right)}$$

$$\rightarrow \left(1 - K_{eq,r\_WGSR}\right){X_{eq,A}}^2 + \left[K_{eq,r\_WGSR}.(a + 1)\right]X_{eq,A} - aK_{eq,r\_WGSR} = 0$$

$$K_{eq,r\_WGSR} = 1/K_{eq,WGSR}$$

$$\rightarrow X_{eq} = \frac{-[K_{eq,r}(a+1)] \pm \sqrt{[K_{eq,r}(a+1)]^2 - 4(1-K_{eq,r})(-aK_{eq,r})}}{2(1-K_{eq,r})}$$

Equilibrium constant, K_{eq}, is already known, therefore based on the feeding composition one can calculate the equilibrium composition at the outlet.

The gas bottles used for the experiments are a pure carbon dioxide cylinder and a cylinder where 80% consists of nitrogen and 20% hydrogen for safety reasons. Pure CO_2 is fed 0.3 NL/min, and the mixture of N_2 and H_2 with 1.8 NL/min which results to 0.6 NL/min of hydrogen flowrate. Based on these values, one can calculate the ratios of "$a= F^{\circ}_{H2}/F^{\circ}_{CO2}$" and "$i= F^{\circ}_{N2}/F^{\circ}_{CO2}$". Based on the experimental condition, CO_2 conversion and gas composition at equilibrium can be calculated and the results are shown in the Figure 100:

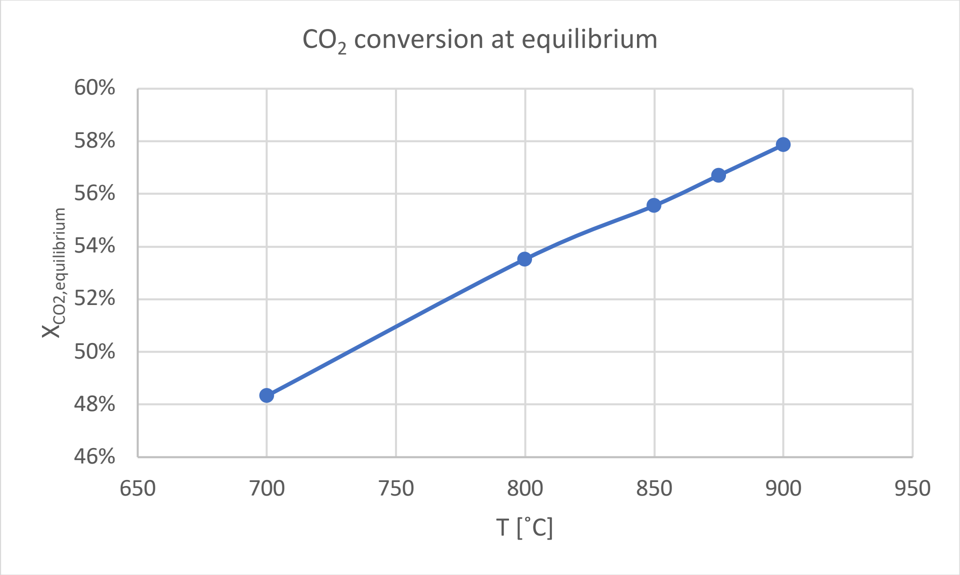

Figure 100 CO_2 conversion of r-WGSR at equilibrium state based on the gas feed composition in the experiment

It is evident that with increasing temperature, the conversion of CO_2 will increase. Since WGSR is slightly exothermic, it's expected that reverse-WGSR to be endothermic. Endothermicity of the reaction explains increasing of reactant conversion with increasing the temperature.

With knowing the conversion, the composition of the gas at equilibrium based on the feeding condition now can be calculated and the results are shown in the Figure 101:

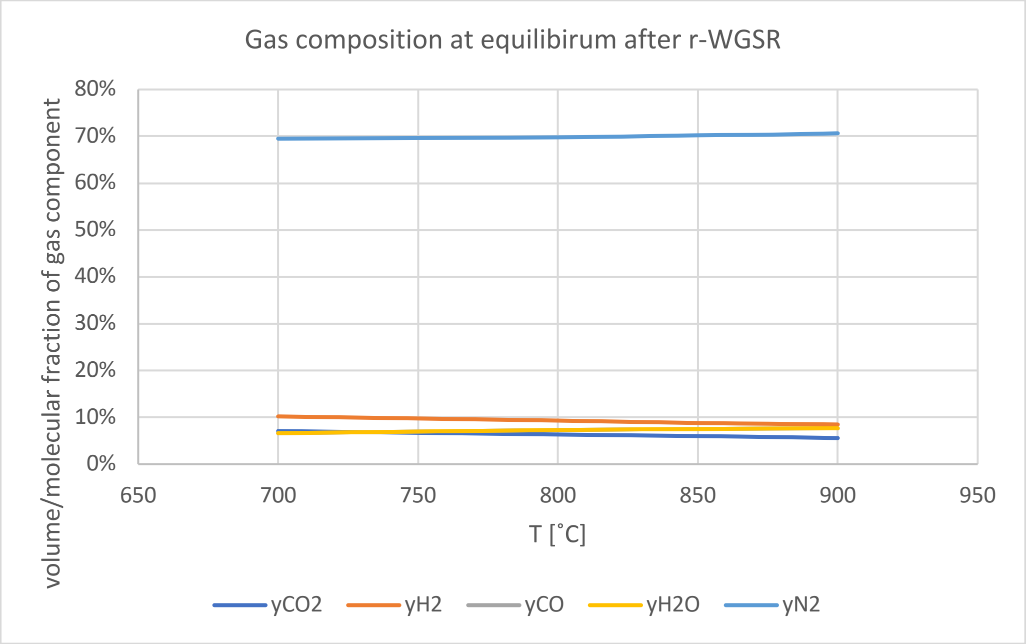

Figure 101 Outlet gas composition of r-WGSR at equilibrium state based on the gas feed composition in the experiment

The gas analyzer measures the gas composition after water condensation in the cooling bath, therefore one needs to normalize the above values with taking out the volume fraction of the steam in the gas composition and to assess dry gas composition. The results are shown in the Figure 102:

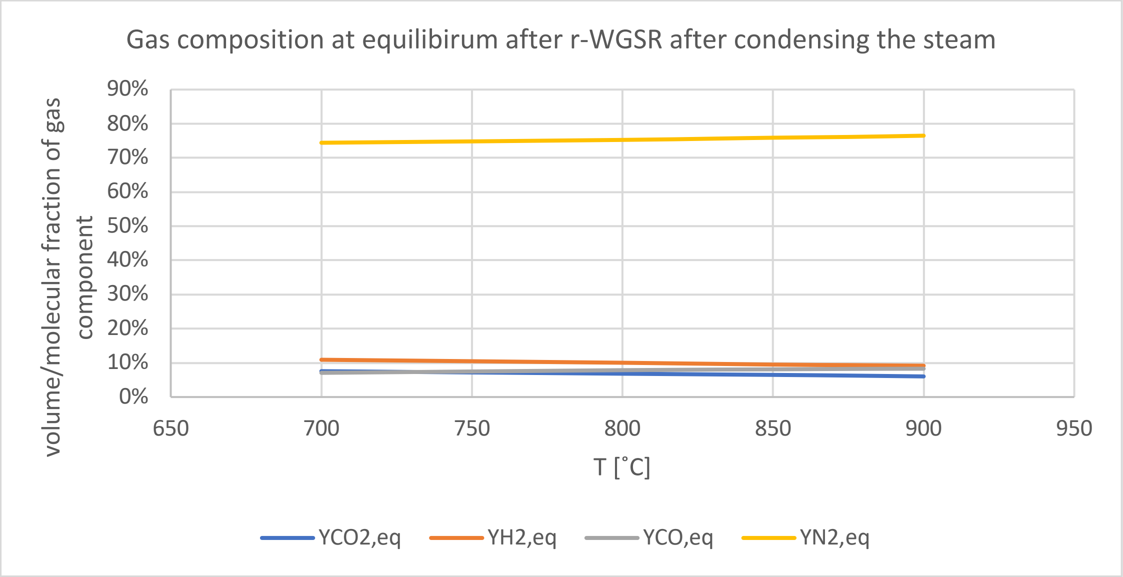

Figure 102 Outlet gas composition (dry basis) of r-WGSR at equilibrium state based on the gas feed composition in the experiment

The equilibrium composition will be used as the reference point. The gas composition in the experiments must be far from equilibrium to study the kinetics of the reaction.

The results of the experiments are shown in comparison to the equilibrium composition in the Figure 103:

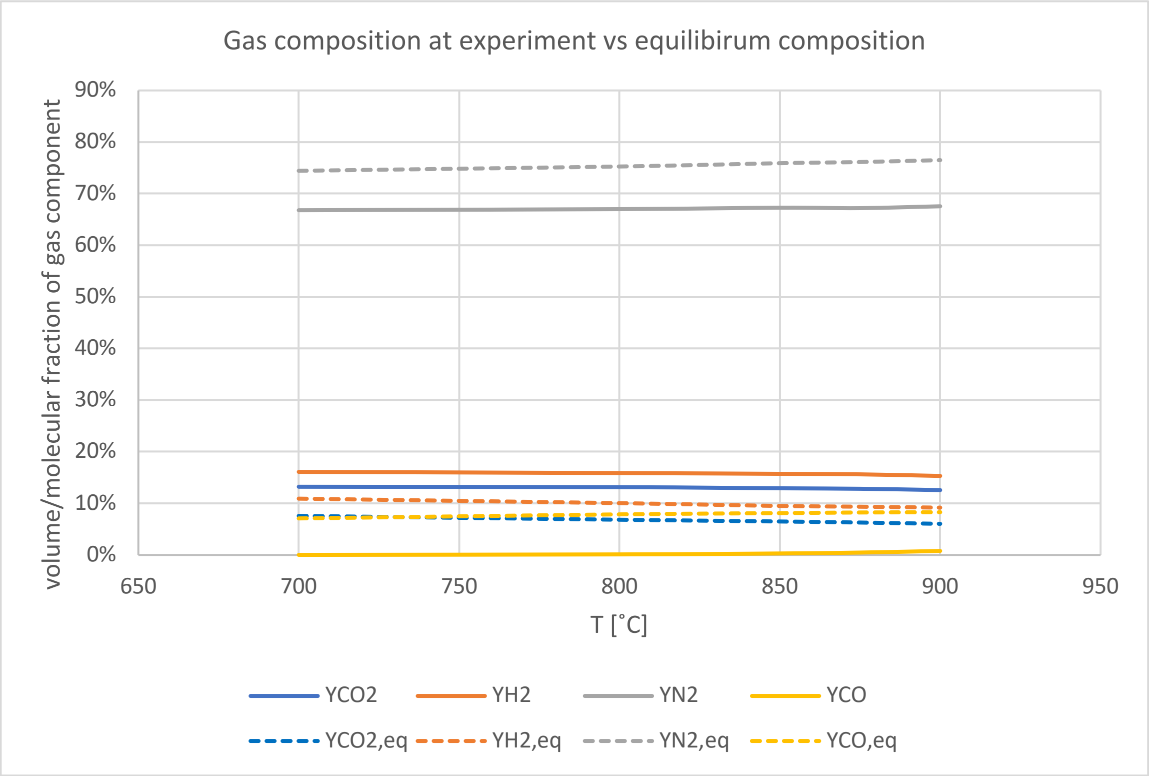

Figure 103 Outlet gas composition of r-WGSR at equilibrium state based on the gas feed composition in the experiment comparing to the measured gas composition at the outlet

The distance between measured values and equilibrium composition allows us to study the kinetics of the reaction.

At this point the conversion of CO_2 in the experiments can be calculated based on the inlet and outlet composition of the gas mixture and the results are compared in the :

Table 19 CO_2 conversion in the r-WGSR: experiments vs equilibrium

T [˚C]	X_{CO2}	$X_{CO2,\ equilibrium}$
700	0,00%	48,33%
800	0,00%	53,52%
850	1,412%	55,56%
875	2,322%	56,71%
900	4,451%	57,87%

It’s evident that at lower temperatures with the current residence time in the reactor almost no reaction occurs. The three conversions obtained at 850, 875 and 900 ˚C are enough to calculate the kinetic parameters.

Some assumptions will be considered through the interpreting the data:

- Steady-state and isothermal operation
- Elementary reaction (first order)

- Negligible mass and heat transfer resistances
- Ideal gas behavior

The quartz reactor that we use in the experiments has an inner diameter of 34 mm and a height of 60 cm resulting to the volume of 0.0005 m^3.

The volume of the reactor can be correlated to the rate of reaction with design equation:

$$V = \frac{F_{0,CO_2} - F_{CO_2}}{-r_{CO_2}}$$

Substituting:

$$F_{CO_2} = F_{0,CO_2} - F_{0,CO_2}.X_{CO_2}$$

Will result to:

$$V = \frac{F_{0,CO_2} X_{CO_2}}{(-r_{CO_2})_{exit}}$$

$F_{0,CO2}$ is the molar flowrate and can be correlated with volumetric flowrate in case of ideal gases:

$$F_{0,A} = v_0 \frac{y_{A0} P_0}{RT_0}$$

At this point, the rate of reaction for each temperature can be calculated. The results are shown in the Figure 104:

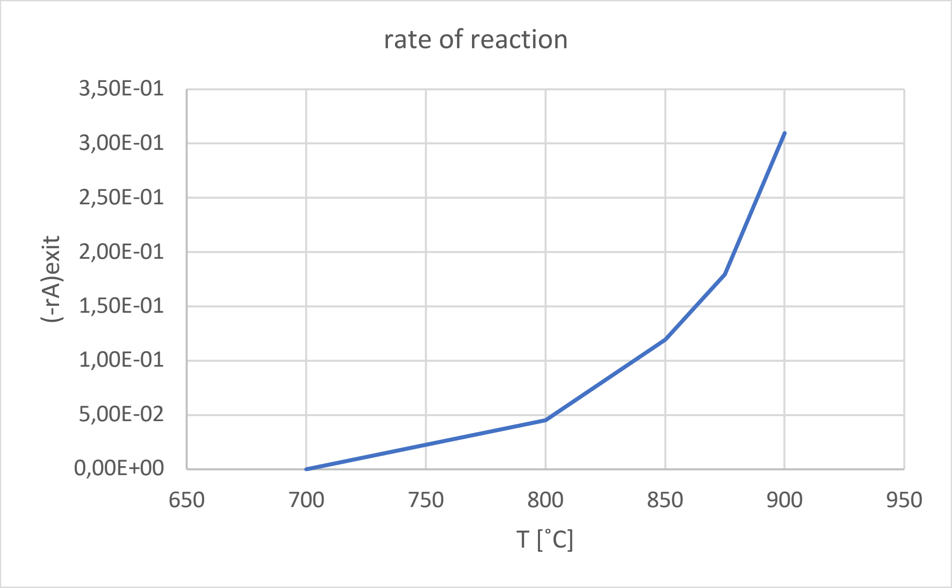

Figure 104 Rate of the r-WGSR obtained in the experiment

Now, based on the rate of reaction, the kinetic parameters can be obtained using the following expression:

$$-r_A = k.[CO_2][H_2]$$

Where the brackets indicate molar concentration and k is expressed with Arrhenius expression:

$$[A] = {}^{F_{0,A}}/_{\nu_0}$$

$$k = k_0.e^{\frac{-E_a}{RT}}$$

Where k_0 is the pre-exponential factor, a constant for each chemical reaction. According to collision theory, k_0 is the frequency of collisions in the correct orientation, and E_a is the activation energy (in the same unit as RT).

Applying logarithm to the equation of rate constant one can derive the following equation:

$$\log k = \log k_0 - \frac{E_a}{R}.\frac{1}{T}$$

The equation above is a linear correlation between log(k) and (1/T). With plotting the experimental data, the pre-exponential factor and activation energy of the r-WGSR can be obtained. The results are plotted and shown in the Figure 105:

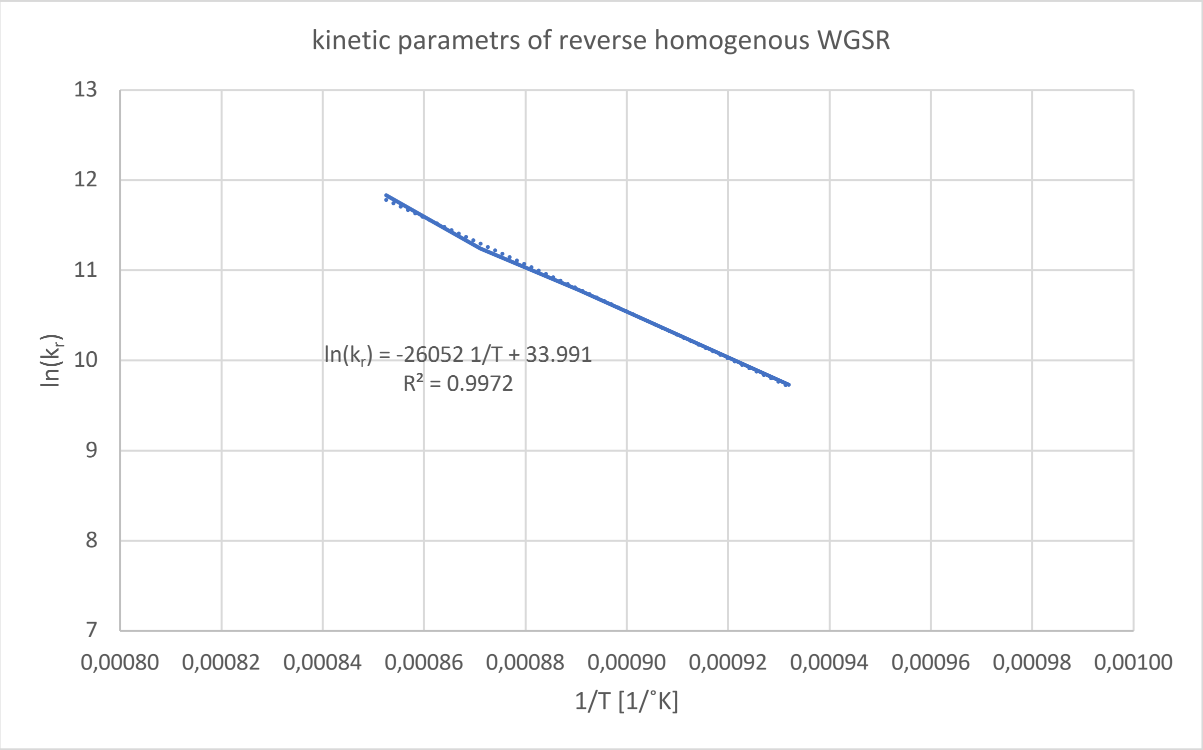

Figure 105 Kinetic parameters of the homogenous r-WGS reaction obtained from the experiment

The kinetic parameters for the reverse water gas shift-reaction based on the experiments are:

$k_{0,r}$=5.78×10^{14}

$E_{a,r}$=216.6 kJ/mol

The kinetic parameters of reverse and forward reaction are correlated with the equilibrium constant through the following equation:

$$K_{eq} = \frac{k_f}{k_r}$$

Applying the equation above can results the kinetic parameters of forward WGSR:

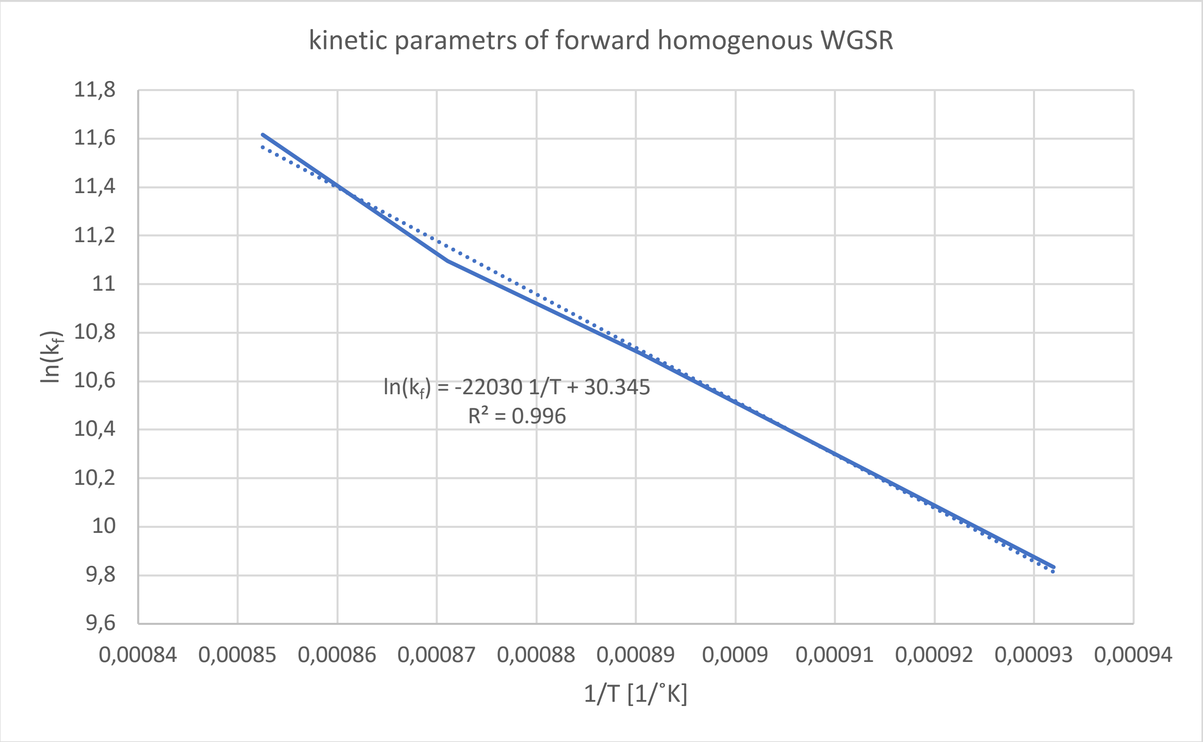

Figure 106 Kinetic parameters of the homogenous WGS reaction obtained from the experiment

$k_{0,f}$=1.51×10^{13}

$E_{a,f}$=183.15 kJ/mol

Results and discussion

Here the power law-type rate equations are used to describe the experimental data. Podolski and Kim analyzed several kinetic expressions of the Langmuir-Hinshelwood and power law (exponential) types. They concluded that power law-type rate equations describe the experimental data more accurately and are more suitable for reactor design. On the other hand, Fott et al. studied the kinetics of the WGSR using a differential reactor at pressures up to 10 bar and found that Langmuir-Hinshelwood kinetic model fits the experimental data better. Since here the experiments were conducted at atmospheric pressure and high temperatures, power law type has been chosen.

The results of experiments are compared with literature. The assumption that reaction is elementary has been used and proved by various authors Parent and Katz (1948), (Gomez-Barea et al., 2010), (Yoon et al., 1978), (Jones and Lindstedt, 1988), (Kuo, 1986), (Wang et al., 2012). (Smith R J, Loganathan, & Shantha, 2010) made a review of the WGSR kinetics in both micro and macro scale. In their work kinetic parameters of the WGSR are listed which is also reported here in the Table 20:

Pre-exponential factors are in orders of magnitude different from various sources. It's due to the condition of the experiments, which is mostly due to presence of catalyst or kinetics of reaction at much lower temperatures. Activation energies on the other hand shows less deviation from our results. Higher activation energy obtained in our experiments indicates absence of catalyst, which when is present provides and alternative route for the reaction with lower activation energy.

Catalyst	**Operating Conditions**	**Arrhenius Parameters**		**Order of reaction**				**Reference**
		Ko	**Ea**	**l**	**m**	**n**	**q**	
High Temperature Catalyst								
Fe_3O_4/Cr_2O_3 8 wt% Cr_2O_3	1 atm, 350^{0}C - 440^{0}C	lnKo=11.5	112 (kJ/mol)	-	-	-	-	Rhodes et al (2003)
Fe_3O_4/Cr_2O_3 180 -250µm	1 bar, 380^{0}C – 450^{0}C	lnKo=10.1±0.2	118±1 (kJ/mol)	-	-	-	-	Rhodes et al (2003)
Fe_3O_4/Cr_2O_3 180 -250µm	6 bar, 380^{0}C – 450^{0}C	lnKo=12.0±0.2	124±1 (kJ/mol)	-	-	-	-	Rhodes et al (2003)
Fe_3O_4/Cr_2O_3 180 -250µm	27 bar, 380^{0}C – 450^{0}C	lnKo=7.4±0.1	111±1 (kJ/mol)	-	-	-	-	Rhodes et al (2003)
Fe_3O_4/Cr_2O_3	3 – 5 bar 573^{0}C - 633^{0}C	2.16 x 10^{11} (s^{-1}) (lnKo=26.1)	95 (kJ/mol)	1.1	0.53	-	-	Keiski et al. (1996)
89%Fe_2O_3, 9% Cr_2O_3	575 to 675 K	ln k0 = 14.78	E/R = 9598	0.74	0.47	-0.18	0	Keiski et al. (1992)
80-90%Fe_2O_3, 8-13% Cr_2O_3, 1-2%CuO,	1 atm, 450^{0}C 6mm x 6mm	$10^{2.845}$ (mol/ gcat s)	111 (kJ/mol)	1	0	-0.36	-0.09	San et al. (2009)
80-95%Fe_2O_3, 5-10% Cr_2O_3, 1-5%CuO,	1 atm, 450^{0}C 6mm x 6mm	$10^{0.659}$ (mol/ gcat s)	88 (kJ/mol)	0.9	0.31	-0.156	-0.05	San et al. (2009)
$CuO/Fe_3O_4/Cr_2O_3$ 180 -250µm	1 bar, 380^{0}C – 450^{0}C	lnKo=2.0±0.1	75±1 (kJ/mol)	-	-	-	-	Rhodes et al (2003)
$CuO/Fe_3O_4/Cr_2O_3$ 180 -250µm	6 bar, 380^{0}C – 450^{0}C	lnKo=5.5±0.1	85±2 (kJ/mol)	-	-	-	-	Keiski et al. (1992)
$CuO/Fe_3O_4/Cr_2O_3$ 180 -250µm	27 bar, 380^{0}C – 450^{0}C	lnKo=4.0±0.1	85±1 (kJ/mol)	-	-	-	-	Keiski et al. (1992)

Table 20 Power law parameters for various WGSR catalysts and operating conditions

Although no studies were available on homogenous WGSR in high temperature, (Bustamante et al., 2004) has evaluated the kinetics of homogenous reverse-WGSR in quartz reactor and compared it with other studies. The activation energy and pre-exponential factors associated with each study of homogeneous r-WGSR are summarized in the Table 21:

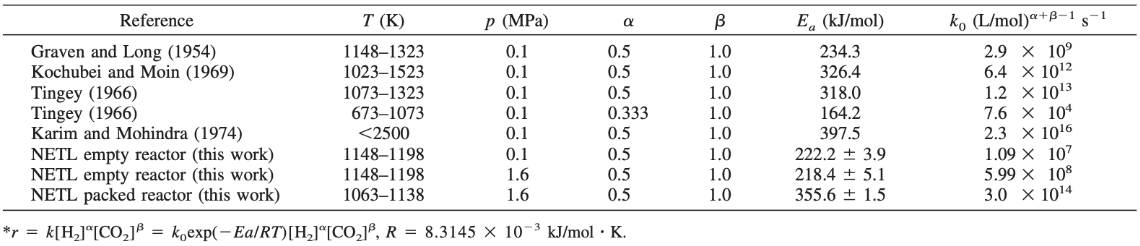

Reference	T (K)	p (MPa)	α	β	E_a (kJ/mol)	k_0 (L/mol)$^{\alpha+\beta-1}$ s^{-1}
Graven and Long (1954)	1148–1323	0.1	0.5	1.0	234.3	2.9×10^9
Kochubei and Moin (1969)	1023–1523	0.1	0.5	1.0	326.4	6.4×10^{12}
Tingey (1966)	1073–1323	0.1	0.5	1.0	318.0	1.2×10^{13}
Tingey (1966)	673–1073	0.1	0.333	1.0	164.2	7.6×10^4
Karim and Mohindra (1974)	<2500	0.1	0.5	1.0	397.5	2.3×10^{16}
NETL empty reactor (this work)	1148–1198	0.1	0.5	1.0	222.2 ± 3.9	1.09×10^7
NETL empty reactor (this work)	1148–1198	1.6	0.5	1.0	218.4 ± 5.1	5.99×10^8
NETL packed reactor (this work)	1063–1138	1.6	0.5	1.0	355.6 ± 1.5	3.0×10^{14}

*$r = k[H_2]^\alpha[CO_2]^\beta = k_0\exp(-Ea/RT)[H_2]^\alpha[CO_2]^\beta$, $R = 8.3145 \times 10^{-3}$ kJ/mol · K.

Table 21 Kinetic expressions for the rWGSR in quartz reactors

Activation energy obtained from the work of Bustamante et al. in similar condition as our experiments (atmospheric pressure and temperature range of 875 to 900 ˚C) is 222.2±3.9 kJ/mol which is in great accordance to our result of 216.6 kJ/mol. In terms of pre-exponential factor some deviation can be noted which might be due to assumption of elementary reaction in our case, where Bustamante et al. assumed the reaction order of 0.5 for H_2 instead of 1.

At this point, necessary information is available to model the process of steam biomass gasification in the CFB gasifier of TUW. The development of the model is explained in the next chapter.

7. Modeling of the DFB gasifier of TUW

Developing the model

Simulating the process of gasification in circulating fluidized bed (CFB) gasifiers is very challenging, due to various reactions occurring in parallel and interacting with each other. Here a new method is developed on the basis of the experimental data set. The aim is to tune with literature experiments a physically based model to obtain a better prediction of the gas composition and a better insight on char reactivity in CFB gasifier. Biomass can be defined as a non-conventional heterogenous compound, being described with its ultimate, proximate analysis. Therefore, in order to implement the reactions, the model has to turn heterogeneous non-conventional biomass into either constituent elements or product yields after devolatilization. The assumption that the biomass turns into its constituent elements (CHON) will lead to very unrealistic results, since it cannot consider the temperature effect on the pyrolysis yields, as well as it cannot represent the chemical bonds in the biomass. The proposed model considers a separation between parallel reactions in the gasifier trying to represent them in a realistic way on the basis of experimental data. In the DFB gasifier the biomass is inserted on top of the bubbling bed, typically at a temperature around 800 °C, then it is dried, the moisture content evaporates and rises in the freeboard of the gasifier. Dried biomass goes through devolatilization and the volatiles leave, while the char remains and reacts with the gases. The unconverted char will be dragged by the bed material to the combustor via a loop to be burned there and provide the heat needed for the overall endothermic reactions in the gasification reactor (GR).

Several assumptions are made when developing the model aiming at obtaining accurate prediction at a reduced computational cost:

- The amount of nitrogen, sulphur and chlorine in the biomass is neglected. In fact, their amount is less than 0.2% of the biomass considered in this work.
- Drying and devolatilization occur instantaneously.
- Amongst the cited homogenous reactions, only water-gas shift reaction is relevant for hydrogen production according to (Pala, Wang, Kolb, & Hessel, 2017).
- The char is assumed to be pure carbon. In fact, the carbon content in the char in the simulated temperature range is between 85 and 95%.
- Char conversion rates are based on thermogravimetrically analysis (TGA) of ex-situ char with pure gases.
- Tar is also considered, and it is represented as lumped groups (Hydroxyacetaldehyde and catechol), since their pathway of decomposition is studied in the works of (Nguyen et al., 1995) and (Fuentes-cano et al., 2016) respectively.
- Heat losses are not considered in the model.

When biomass is fed into the gasifier, the free water evaporates. Although biomass (wood pellets) drying is not normally considered as a chemical reaction, a stoichiometric reaction can be used in to convert a part of the biomass to form water. The following equation represents the drying process for the initial softwood pellets:

$$\text{Biomass (wet)} \rightarrow 0.0555084\ H_2O + \text{Biomass (dry)}$$

The reaction indicates that 1 mole of biomass reacts to form 0.0555084 mole of water which corresponds to the water content of the biomass. The conversion for this reaction must be set to achieve the proper amount of drying. At code start-up, the fractional conversion is set to be 0.2 but its value is later overridden by using a calculator box.

After being dried, the model arranges the decomposition of biomass through the pyrolysis process, turning into char ($CH_pO_q \approx C$), volatiles (CO, CO_2, CH_4, C_xH_y, H_2), non-condensable gases tar and pyrolytic water (H_2O). The water arises from several pyrolysis reactions and is chemically bound in the biomass.

Modelling this process is the most challenging task in a biomass gasification simulation and, for such reason, it is neglected in many other works such as (Suwatthikul, Limprachaya, Kittisupakorn, & Mujtaba, 2017) pertinent to biomass gasification, where the biomass is assumed to yield to its constituent elements of CHNO, eventually leading to inaccurate results.

Defining the pyrolysis reaction requires the known yields of the products in either mass or mole basis. The true yields of the components after pyrolysis depends however on many variables such as the temperature of the reactor, the heating rate, the particles size, the residence time and the amount of fuel according to studies such as (Babu & Chaurasia, 2004). An attempt to find the empirical correlations between the yield of the components and the temperature was done by (Neves et al., 2011) using about 300 different experimental investigation on the process. The investigations were classified in fast and slow pyrolysis. Since in the DFB gasifier at TU Wien, the pyrolysis happens in less than few seconds, only the correlations for the fast pyrolysis are considered. According to this research, there are correlations expressing: the yields of CH_4 and CO as reported in the work of (Di Blasi et al., 2001), or Scott et al; the yields of H_2 and CO; the yield of H_2 as a function of pyrolysis peak temperature according to (Scott, Piskorz, Bergougnou, Graham, & Overend, 1988), or the relation between the volatile products based on the work of (Funazukuri, Hudgins, & Sllveston, 1986); the yield of Char and its elemental composition as a function of pyrolysis peak temperature (Wang, Kersten, Prins, & Van Swaaij, 2005), also for secondary biomass (Zanzi, Sjöström, & Björnbom, 2002) and dedicated cultivation (Encinar, González, & González, 2000); the elemental composition of the Tars (Dupont et al., 2008), and the thermal cracking (Fagbemi, Khezami, & Capart, 2001) as well as the lower heating value in the function of temperature (Di Blasi, Signorelli, Di Russo, & Rea, 1999). For the mentioned empirical correlations, the coefficient of the determination "R^2" is always high enough to be taken as a reference for the further calculations. Since these correlations are over a wide range of biomass, they've been corrected with the results of (Neves et al., 2017b) which is specifically related to woody biomass. The yield of products from fast pyrolysis has been already discussed with details in Chapter 3, here the results will be implemented for the model.

The char composition as function of peak temperature according to (Neves et al., 2011) contains mostly C (85-95%) with a small amount of H and O. Therefore, to overcome the complications in the modeling, it was decided to model the char as pure carbon (homogeneous compound) instead of a heterogeneous nonconventional compound in the simulation (see the modelling assumptions cited before).

The same type of correlation exists also for the CHO content in the tar according to (Scott, Plskorz, & Radleln, 1985). There is a weak relationship between the elemental composition of tar and pyrolysis temperature.

It is possible to write the atom balance and energy balance for the pyrolysis products. A system of linear equations with 4 equations (atom balance CHO, energy balance) is obtained and the yields of other four components (CO_2, C_xH_y, H_2O, TAR) can be calculated. Despite the effort of complete mass and energy balance between biomass and devolatilization products, some slights errors have been noted over the range of temperature. The mass balance shows an error less 2.3% and energy balance has a discrepancy of maximum 7%. In order to examine the energy balance, the heating value of char and tar are considered 30 and 33 MJ/kg respectively.

Furthermore, by analyzing the literature results (Schmid, Müller, & Hofbauer, 2016), one can notice that the amount of C_2H_6 is negligible. Therefore, for the modelling of other light hydrocarbons (C_xH_y), only Ethylene (C_2H_4) is considered here.

The temperature below 600 °C is not considered here, since literature shows (Ahrenfeldt, Henriksen, Gøbel, & Fjellerup, 2005b) that below this temperature some tar remains as residue in the char thus affecting the model predictions. However, this is not a real limitation as this temperature is not typical of the operational condition for the CFB gasifier. When increasing the temperature, the amount of CO is rising, and the amount of CO_2 is decreasing. Considering the water gas shift reaction as the most important reaction in the process, and if the provided steam is always enough for this reaction, in steam gasification a rise of CO_2 and decreasing of CO is expected when increasing the temperature. Then, the nonconventional heterogeneous biomass is transformed in conventional components except for the tar.

Some authors neglect the tar contribution in the simulation of the CFB gasifier because of the modelling complexity as shown in the two examples reported in (Abdelouahed et al., 2012) and (Paviet, Chazarenc, & Tazerout, 2009). The tars amount at the outlet of the CFB gasifiers is very low and usually in the range of few milligrams to few grams per normal cubic meter of gas. However, the tars formed after the pyrolysis are not negligible. The yield of tars in the temperature range of 600-900 °C ranges between 40-20% of the dried-ash free fuel on mass basis.

In the developed model, the amount of tars for different temperatures, and their composition in a correlation with ultimate analysis of the biomass is assumed. Therefore, a simple algorithm was developed of a system of equations, based on the previous calculations, to calculate the sum of different tar groups corresponding to the amount of tar and its composition after pyrolysis. The tar groups were lumped in 2 groups: Hydroxyacetaldehyde and catechol. This assumption can be valid, since all the tar are assumed to be either cracked thermally or reformed with steam.

The yield of different tar groups with the temperature is described in detail in previous chapters.

The solid residual of the biomass after devolatilization, namely char, goes through the bubbling bed of the GR and is transported with the bed material to the CR where it is burnt. During its passage, a char fraction reacts with other gases such as steam and CO_2 with different reaction rates. The reaction with steam is much faster than that with CO_2 but still many times slower than gas-gas reactions (Klose & Wölki, 2005). Since the kinetics of these reactions are slow and the residence time is limited to the circulation rate of the bed material, a high conversion rate is not expected. The reactions are reported below:

$C \text{ (solid)} + H_2O \text{ (gas)} \rightarrow CO \text{ (gas)} + H_2 \text{ (gas)}$

$C \text{ (solid)} + CO_2 \text{ (gas)} \rightarrow 2CO \text{ (gas)}$

The measurement of char conversion cannot be done directly inside the plant under experimental investigation, and in the literature reaction kinetics show great differences in terms of the activation energy and frequency number from different findings by various authors (Kramb, Konttinen, Gómez-Barea, Moilanen, & Umeki, 2014).

In this work, after separating all the main reactions in the simulation, the reactivity of char with the CO_2 and steam have been investigated with thermogravimetric analysis (TGA) in the laboratory of Technical University of Denmark (DTU) with the same biochar obtained in the previous experiments at TU Wien.

To measure the reactivity of char, a sample is loaded in the crucible of TGA, heated up to the peak temperature at which the reactivity is investigated (650, 750, 850 and 950 °C) with the heating rate of 20 ˚K/min in an inert atmosphere with N_2 gas to evaporate the moisture in the char and release the remaining volatiles, then the gas is switched to CO_2 and the sample is being held for 30 minutes to assess its reactivity over time. This residence time is in the same range for char in the GR during experiments according to IPSEpro data.

The char does not contain any moisture since it is produced at a temperature above 650 °C, but in the process of collecting, sampling and transporting, an average amount of 0.08% of moisture content was adsorbed and observed in the test runs. The char samples also showed a volatile content of about 2.7%.

The same approach was adopted to measure the char reactivity with steam. The results show a much higher reactivity between char and steam if compared to that with char and CO_2, in agreement with literature data.

The experiments with steam were conducted in a macro TGA, where more fluctuations in the mass loss curve was noticed. The results are explained in further detail in chapter 4.

The understanding of the char reactivity with H_2O and CO_2 is not enough to calculate the amount of char gasified with these gases and the effective residence time of the char in the bubbling bed of the GR needs to be considered as well. Char residence time has been already calculated and discussed in the Chapter 2. At this point, the amount of gasified char and the fractional conversion with H_2O and CO_2 are defined.

The most important homogeneous reaction in the process of steam gasification is the water-gas shift reaction (WGSR). According to different studies (Smith R J et al., 2010) this reaction can easily reach the equilibrium at high temperature with about 1 second of residence time (Wheeler, Jhalani, Klein, Tummala, & Schmidt, 2004b). There are various kinetic models available for this reaction, but they are mostly developed in presence of different catalysts and low temperatures (Lima, Zanella, Lenzi, & Ndiaye, 20012). Here, the kinetic of this reaction is obtained experimentally as described in the previous Chapter. The model firstly assumes equilibrium then replace it with kinetics.

In order to have a vision whether the actual product gas from the 100 kW_{th} CFB gasifier reach the equilibrium or not, the deviation of the actual product gas composition according to the WGS equilibrium must be assessed by means of the logarithmic deviation from the WGS using Equation 52:

Equation 52
$$p\delta_{eq,CO-shift}(P_i,T) = log_{10}\left[\frac{\Pi_i p_i^{v_i}}{K_{p,CO-shift}(T)}\right]$$

This equation relates the actually measured gas phase partial pressures of species *i* (CO, H_2O, CO_2 and H_2) to the equilibrium constant K_p calculated from pure substance thermodynamic data.

The deviation calculated from the equilibrium for the experimental results of 100 kWth gasifier of TUW and presented in the Figure 107. The results indicate that around 820 to 850 °C WGSR is very close to the equilibrium in agreement with the prediction of models in (Callaghan, 2006). The findings on CO conversion in WGSR corresponds with the investigation of (Wheeler et al., 2004b). These founding hint that in order to properly model the process of biomass steam gasification, for typical temperature of the fluidized bed gasifiers (800-850 ˚C) assumption of equilibrium state for WGSR can be valid, but for temperatures outside of this range a kinetic model is suggested.

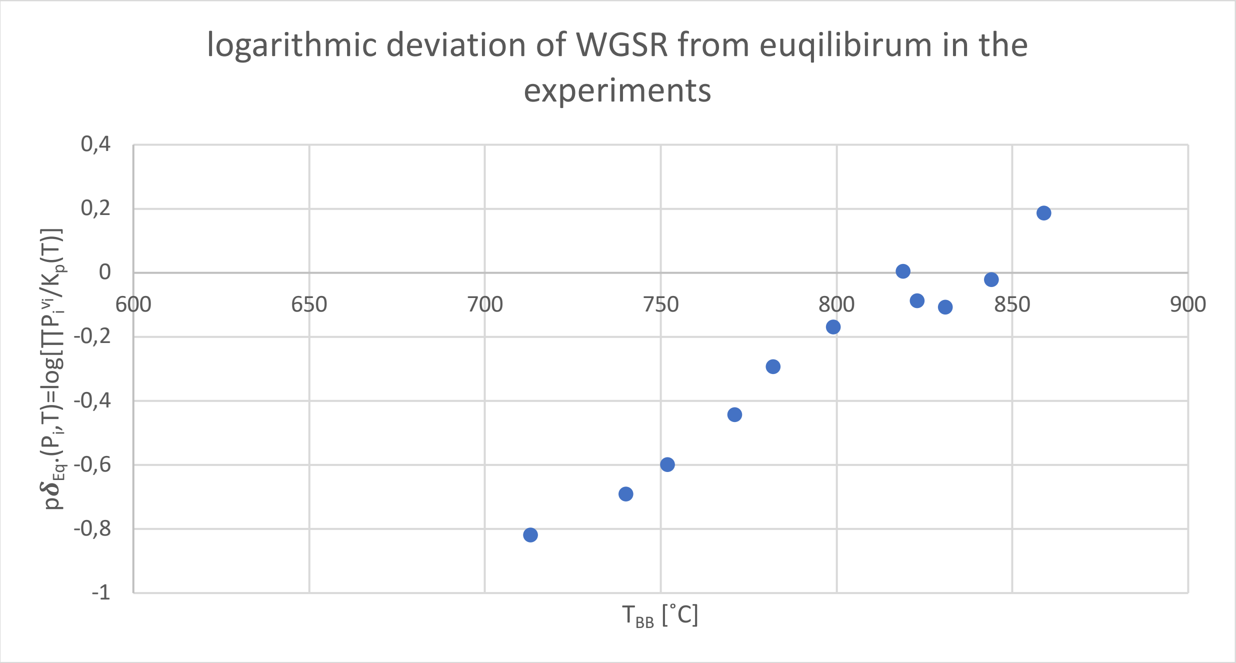

Figure 107 Logarithmic deviation from WGSR equilibrium in experimental results

At first step, equilibrium state is considering for the WGSR in the whole operational range and results are compared with the experimental measurements and later the kinetic expression obtained for WGSR in a non-catalytic and high temperature condition will be applied to improve the results.

In summary, in the model biomass after being fed to the system is dried and the moisture content of the biomass is added to the reactants. Then, the dry biomass stream is turned into the pyrolysis products using the empirical correlations and the calculations mentioned previously. After the pyrolysis the streams are separated into the solid fraction char, volatiles (H_2, CO, CO_2, CH_4, C_2H_4) and the liquids (Tar and pyrolytic water). Tars are cracked and reformed with steam and the products are sent with other components to a reactor where also the products of char gasification are added. The unconverted char is extracted from the stream and then sent to the CR. Finally, all the gas species are sent to the water gas-shift reactor (WGSR).

The key figures in the results are discussed and compared with the experimental measurements. These key variables are the gas composition at the outlet, the water conversion during the process, the cold gas efficiency and product gas yield.

Results and Conclusion

The modelling of biomass gasification enables the optimization of the process designs, but it is a challenge due to its high complexity. Here a model for prediction of the performance of a 100-kW dual bed fluidized biomass gasifier is derived and implemented in the excel sheet environment. Detailed pyrolysis modelling is properly addressed as well as a mechanism for secondary tar conversions and heterogenous reaction of the char, and this is believed to be a key factor of this approach and enables more accurate results. The proposed model and its basic assumptions were extensively validated on a range of operating temperature by conducting experiments using softwood pellets as fuel and fresh olivine sand as bed material. The impact of the gasifier temperature variation on the final product gas composition as well as on the other key figures such as the cold gas efficiency, product gas yield, water conversion and the deviation from equilibrium of the water gas- shift reaction are measured in the experiments and compared to the simulation results.

The study of the dual CFB gasifier behavior is divided into two categories of hydrodynamic and the thermo-chemical reactions. The former is discussed thoroughly in the second chapter and the latter is discussed in the chapters 3, 4 and 5. Each chapter contains the detailed results of that specific chapter and the collective results lead of previous chapters lead to completion of the simulation model. Here in the result and discussion section, only the summary results of the past chapters have been reported again and finally the results of the complete simulation is reported and compared with the experimental results.

The initial condition of the system are explained in the second chapter and has been set based on the thermal power of the gasifier, heating value of the biomass, the optimal steam to biomass ratio, desired fluidization regime in the combustion and gasification reactors, and they are compared with the experimental condition. The initial conditions for the simulation and the experiments are based on the same logic but in the experiments some value diverges slightly from the theoretical values.

The biomass feeding rate is set to correspond to the nominal thermal output of the CFB gasifier and based on the heating value of the biomass and its percentage of ash and water content, but in the experiments some minor divergences have been noticed. The comparison between experimental condition and simulation regarding the biomass feeding rate is shown in the Figure 67:

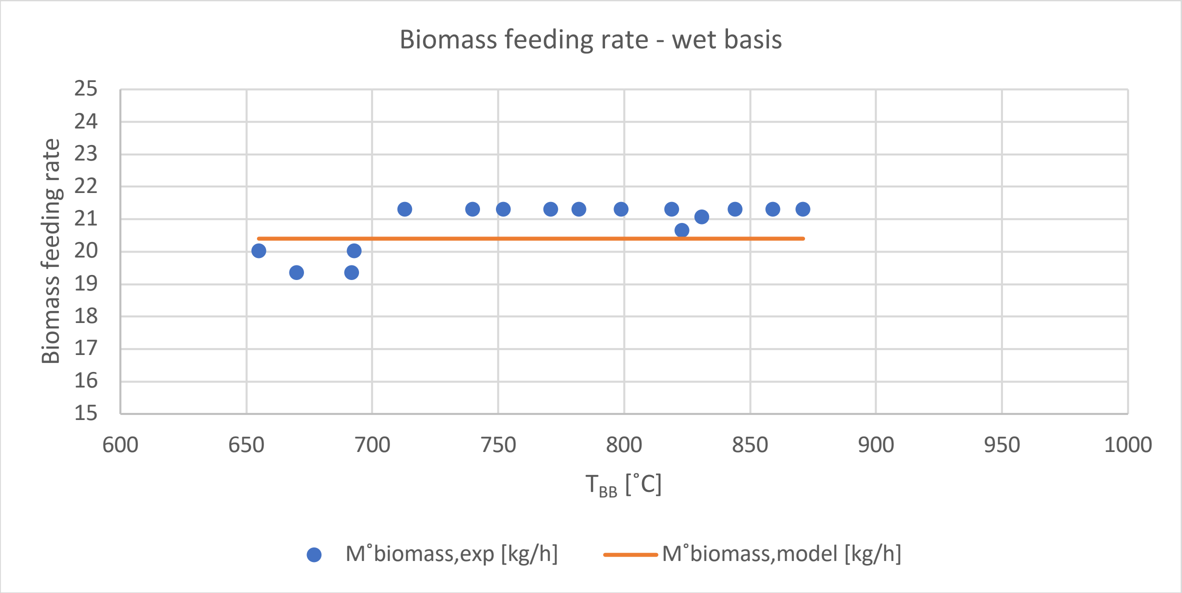

Figure 108 A comparison between biomass feeding rate in the model development and experimental condition

The small difference between the theoretical values and experimental measurements of the biomass feeding rate can be explained by the fact that the flux of solid biomass feedstock with a variation in size particles in practice is very difficult to have a constant rate, and the feeding rate is a time-averaged values. In advance to the experiments, the feeding system is calibrated for such biomass but still in practice a small difference is noted.

Later, based on the steam to biomass ratio, the total steam input to the gasifier has been calculated. The total steam input is the sum of the steam injected in the lower loop seal (LLS) which helps the circulation of the unconverted char and bed material particles, lower gasification reactor part (LGR) which fluidize the bed bubbling bed and upper loop seal (ULS) which helps recirculation of the hot bed material. The amount of the steam inserted in the bubbling bed is the sum of the steam input to the LLS and the LGR. In the Figure 68 the theoretical values for the simulation and the experimental condition are compared:

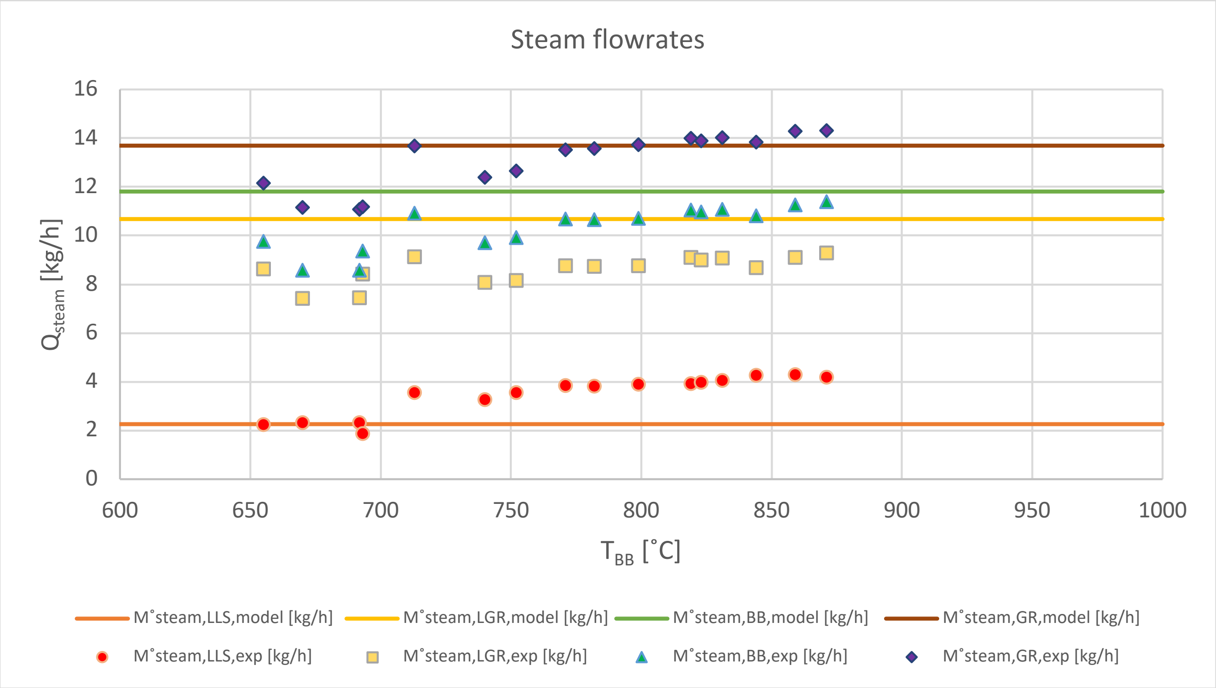

Figure 109 Steam flowrates in various parts of the CFB gasifier as a function of temperature: model vs experiment

Even though there are some differences for the steam input in the LGR between experiments and the simulation condition, the overall steam input to the steam has good accordance for both experiments and the simulation. The steam to biomass ratio is set to be equal to 0.8 which included the moisture content of the biomass and shows a good agreement between experiments and the simulation condition.

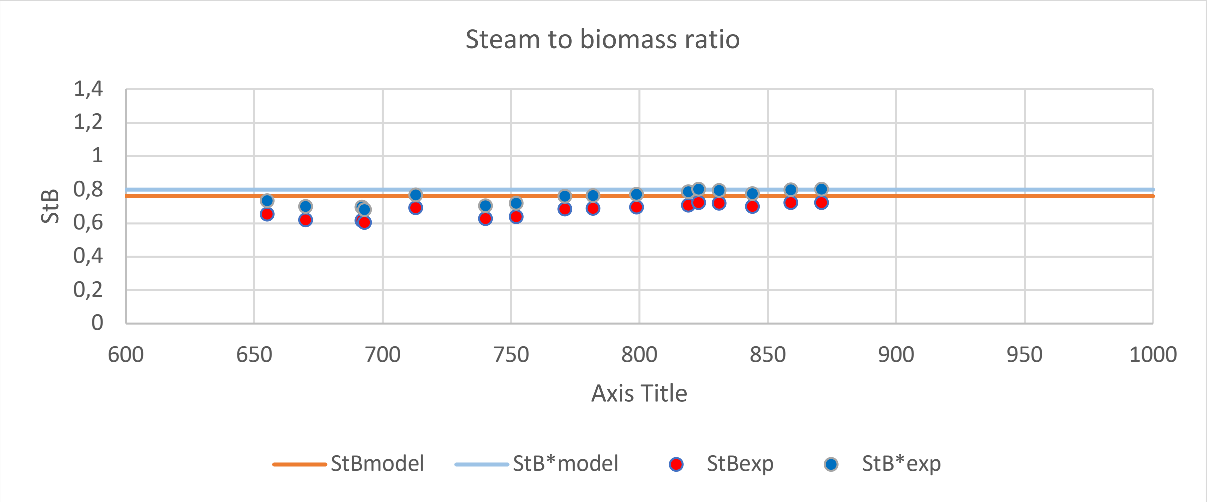

Figure 110 Steam to biomass ratio: a comparison between the model and experimental values

Air input to the combustion reactor must satisfy the fast fluidization regime in the CR for a continuous circulation of the bed material and provide the necessary heat for the overall endothermic reactions inside the GR. Theoretical values are calculated based on the terminal and critical superficial velocities of air. In practice, the values show some differences, but they are not a concern for the simulation process since the product of the CR is a flue gas mainly composed of CO_2, N_2 and H_2O and not a key factor of the system.

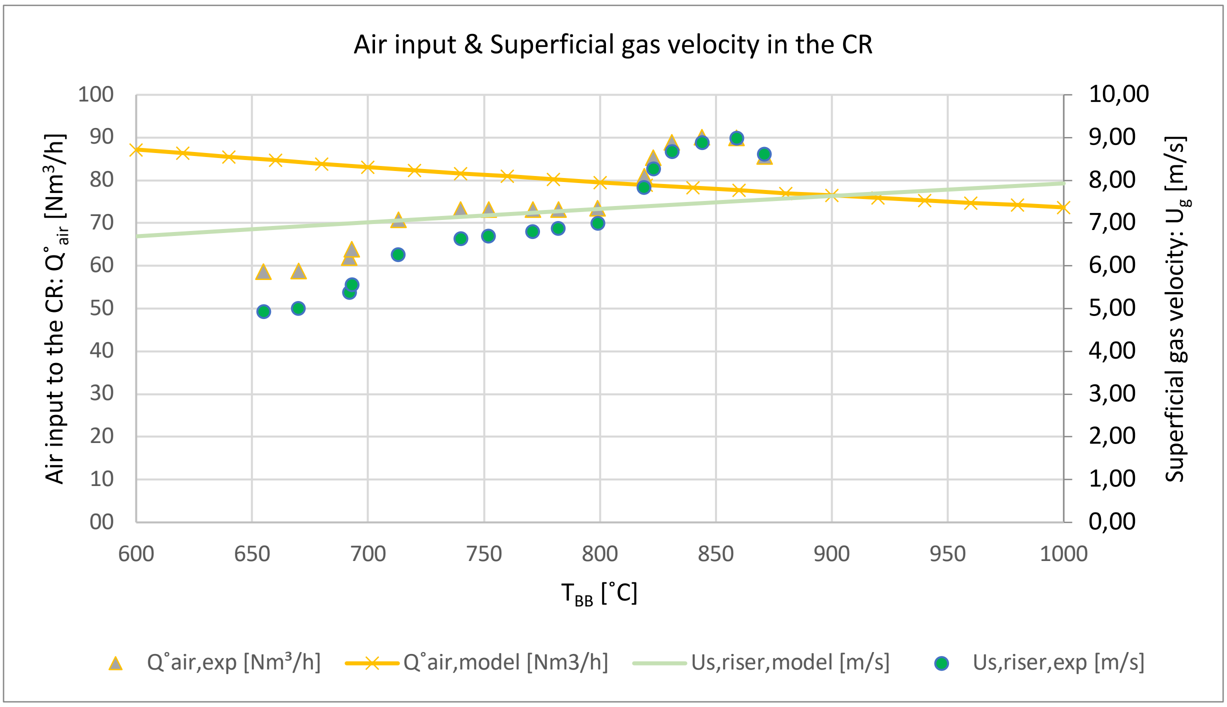

Figure 111 Air inflow and superficial gas velocity in the CR: model vs experiment

Based on the calculated hydrodynamic of the system discussed in the second chapter, pressure drops inside the system have been compared with the experimental results. The good accordance shows a positive sign for the validity of the assumptions that have been made in the model and can be based for a further deeper modelling of the system to integrate the heat transfer and particle transfer in the system. In the following figures the results have been showed. For more information see Chapter 2.

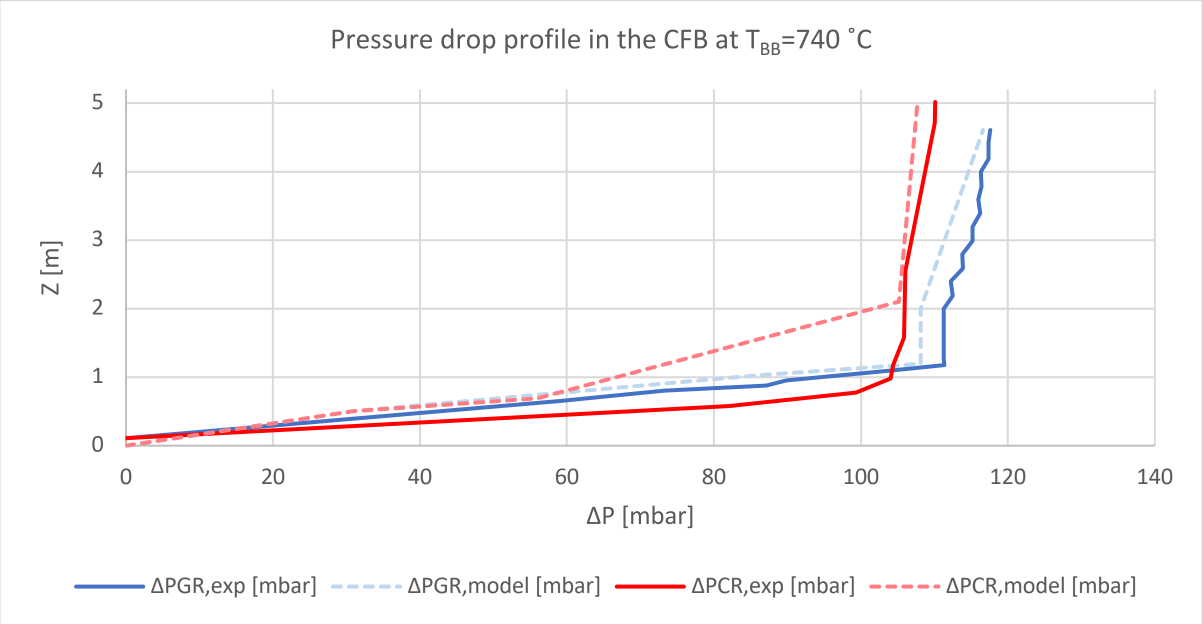

Figure 112 Pressure drop profile in the CFB gasifier at T_{BB}=740 ˚C: model vs experiment

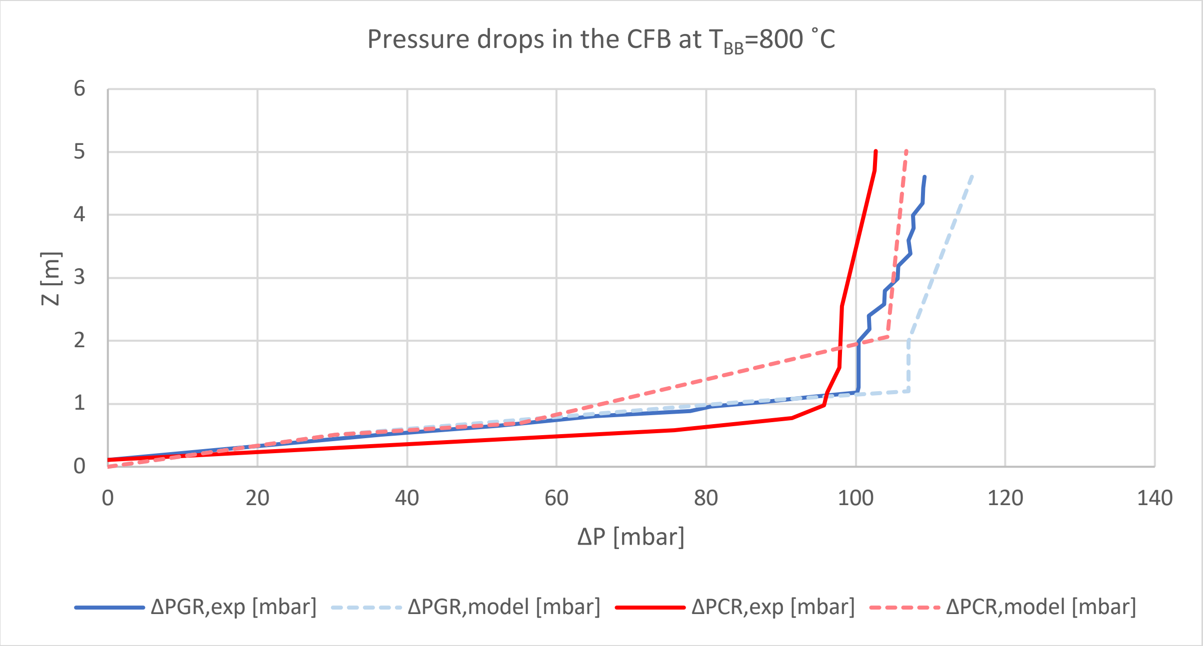

Figure 113 Pressure drop profile in the CFB gasifier at T_{BB}=800 ˚C: model vs experiment

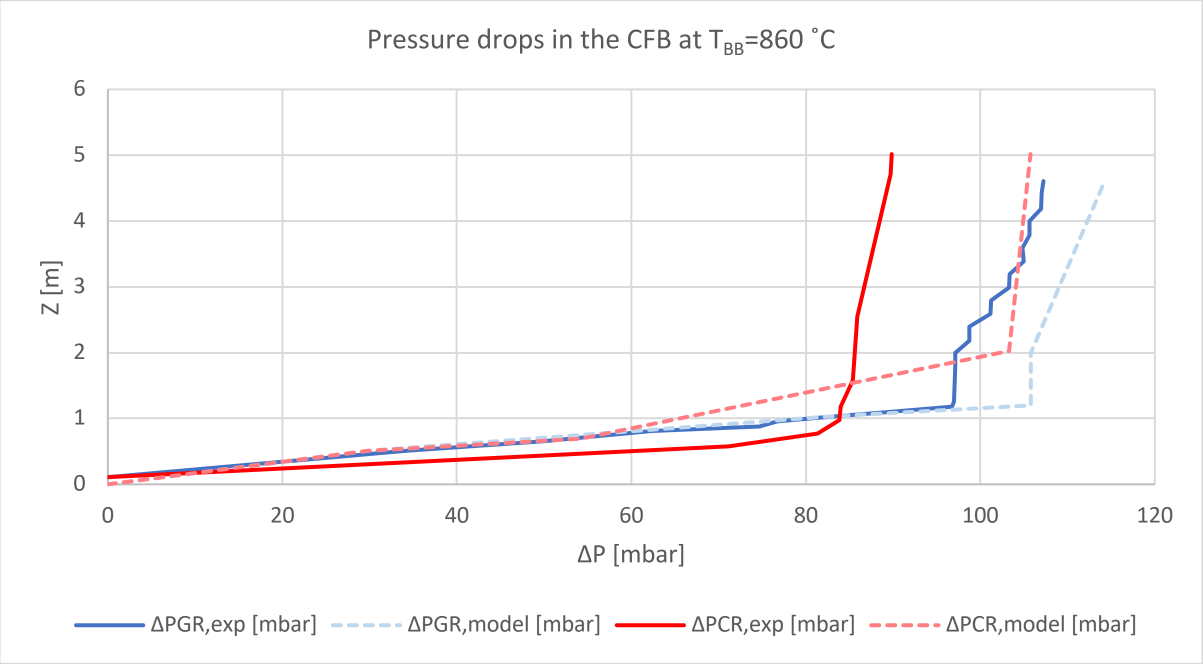

Figure 114 Pressure drop profile in the CFB gasifier at T_{BB}=860 ˚C: model vs experiment

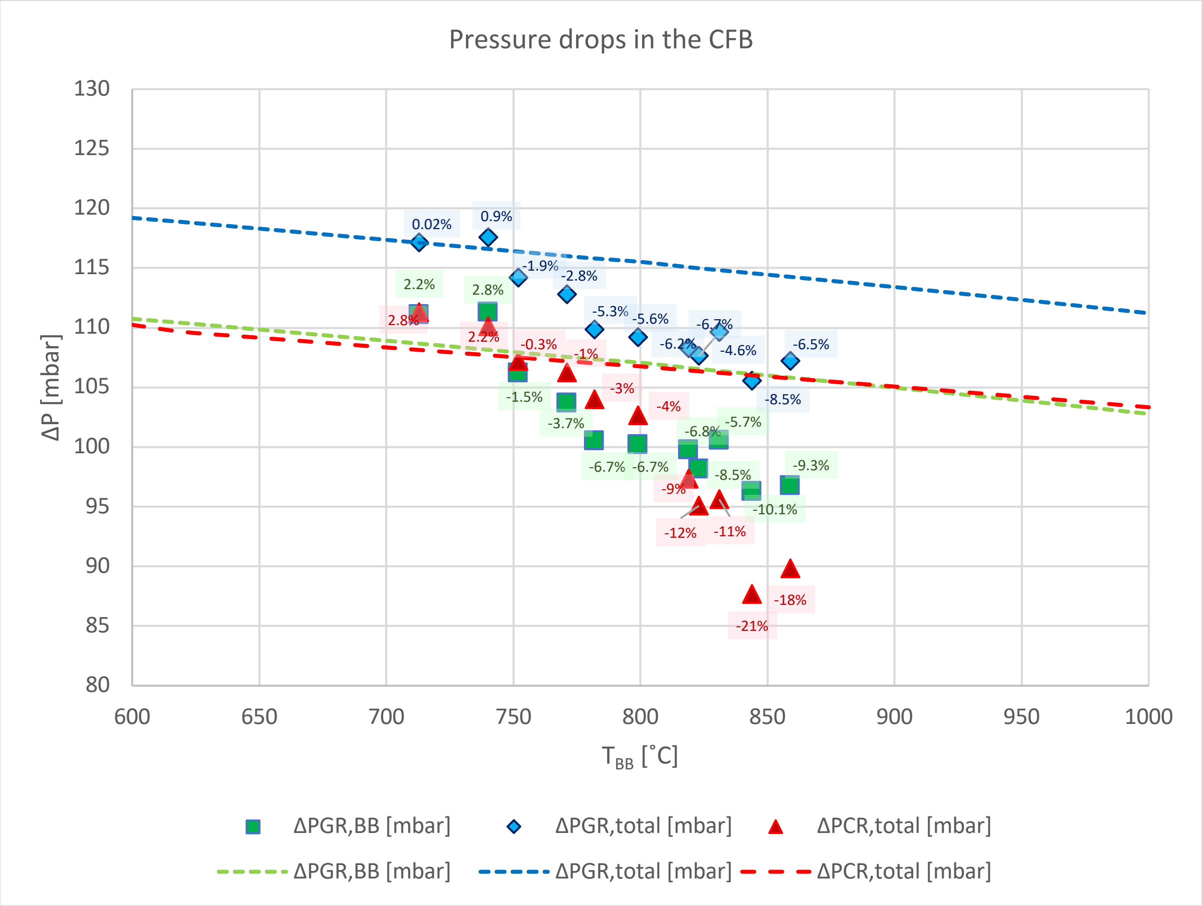

Figure 115 Pressure drops in the bubbling bed, in the whole GR, and the whole CR of TUW's CFB as a function of bed temperature

Up to this point, the initial condition and the hydrodynamic of the system have been discussed. The concept behind the modeling approach of the thermochemical conversion and chemical reactions is shown in the Figure 116 schematically.

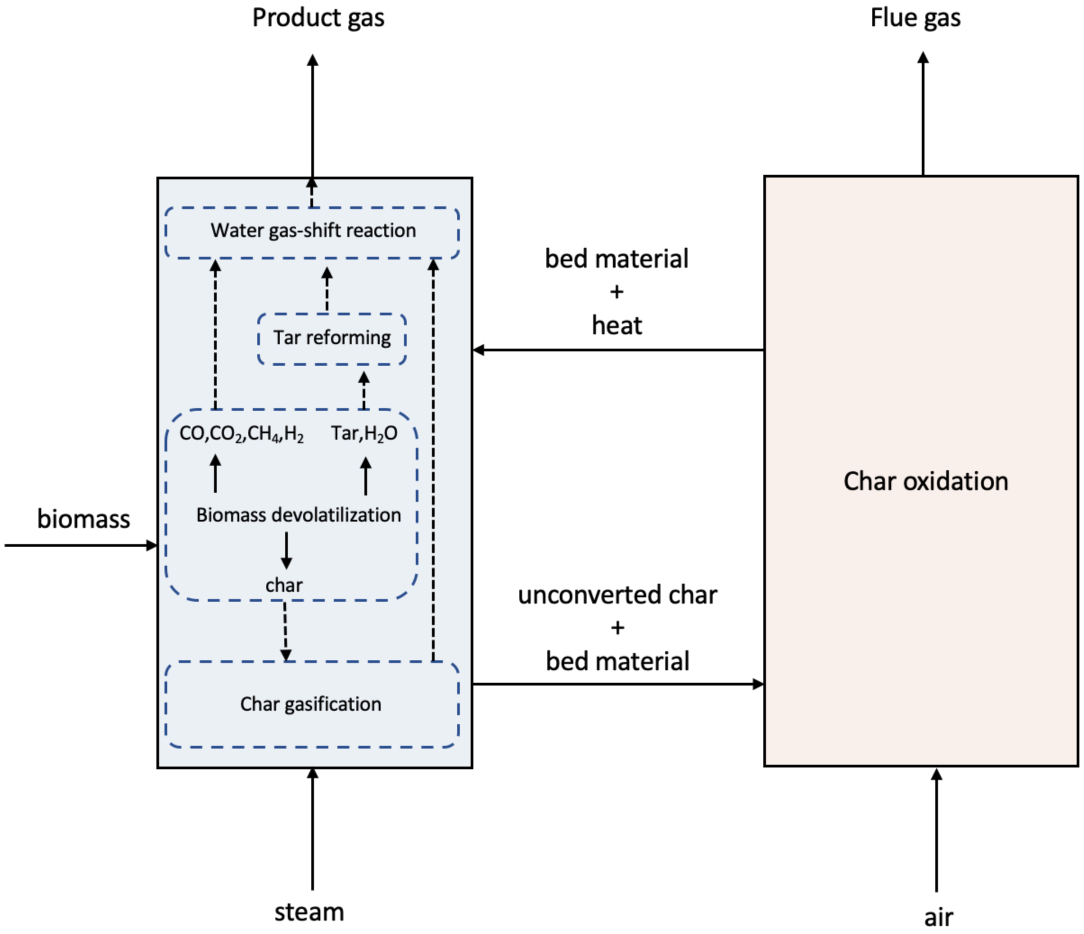

Figure 116 Concept of the modelling process of the dual CFB gasifier of TUW

The biomass is inserted on top of the bubbling bed in the gasification reactor (GR) and goes through devolatilization which is a thermo-chemical conversion. The solid biomass first releases its moisture content and then turns into some permanent gases (CO, CO_2, H_2, CH_4, ...), condensable gases namely tar and H_2O, and solid fraction of char which is mostly carbon. The yield of these components is based on the nature of the biomass itself, the temperature and pressure at which the devolatilization is occurring, the particle size, residence time and some other minor factors. The empirical correlations are taken from literatures are discussed in the third Chapter of the thesis. Here a summary of the results is reported. For more information read the third Chapter. Yield of the main products of the devolatilization as a function of temperature is shown in the Figure 81. Yield of char is decreasing with rising the temperature and is slightly below the fixed carbon amount of the biomass. Permanent gases are increasing with rising the temperature while the liquid fraction shows an opposite trend.

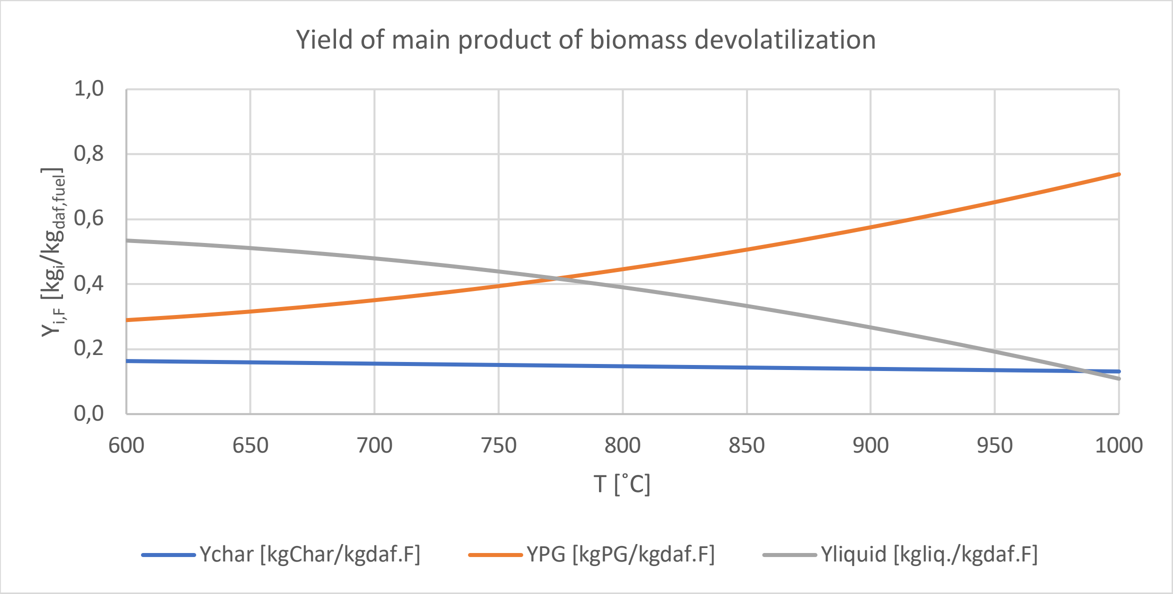

Figure 117 Yield of char, permanent gases and liquids (tar + pyrolytic water) from biomass devolatilization as a function of temperature

Major components of permanent gases released from devolatilization of biomass are CO, CO_2, H_2, CH_4 and some little amount of higher C_xH_y components. The correlations implemented in the model for these gas components are shown in the Figure 82. They have been explained and discussed in the third Chapter thoroughly.

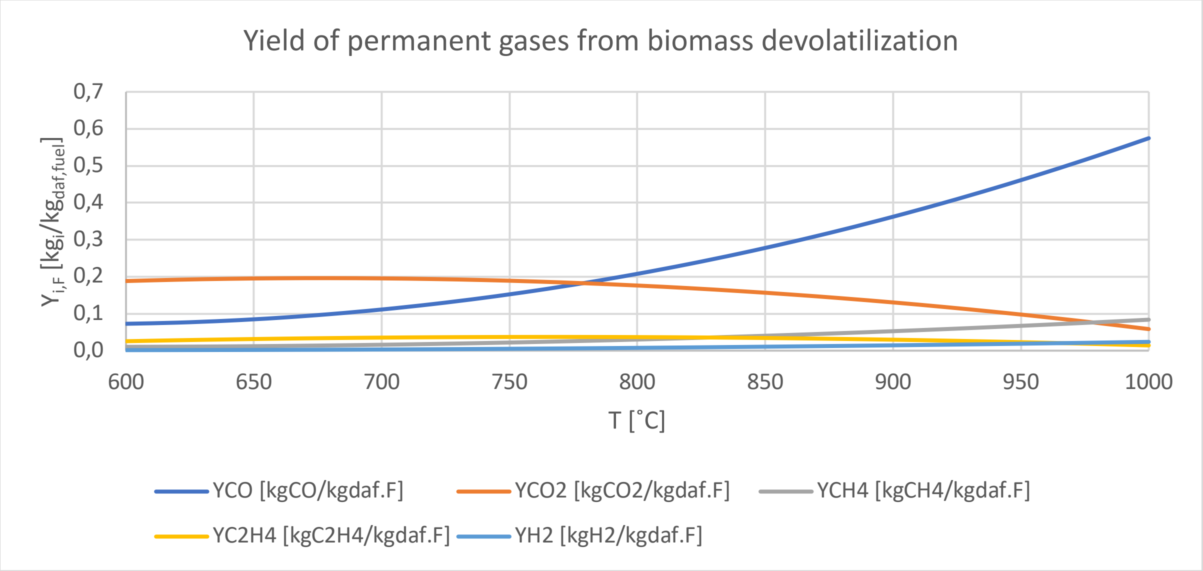

Figure 118 Yield of permanent gases from biomass devolatilization as a function of temperature

Due to the complexity of defining the liquid fraction in the modeling process, it is avoided in most attempts of simulating the biomass gasification process. This neglection specially at lower gasification temperatures can lead to significant error in the results. With increasing the gasification temperature, both the yield of pyrolytic water and the tar decrease. The yield of the tar and pyrolytic water of woody biomass as a function of temperature is shown in the Figure 84:

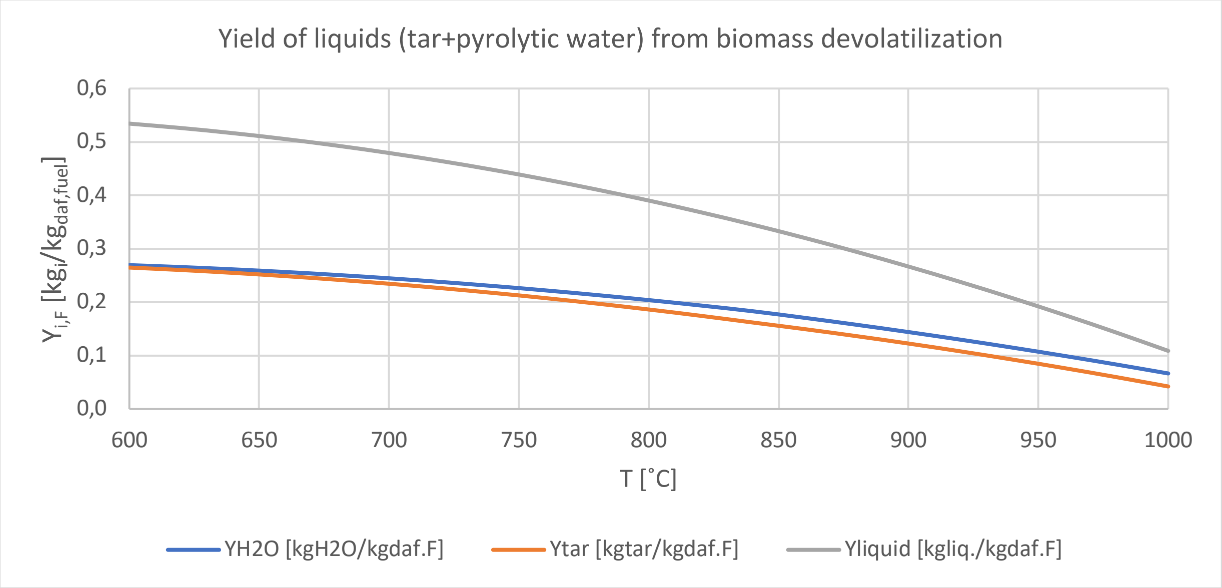

Figure 119 Yield of pyrolytic liquids (water and tar) from biomass devolatilization as a function of temperature

The big challenge regarding the tar fraction of devolatilization products is defining the tar classes and compounds. Here they have been lumped into two categories of primary and tertiary tars of Toluene and Phenol groups. Phenol and toluene are taken into acount as tar models since their pathway of decomposition and reforming is studied in the works of (Nguyen, Sengupta, Raspoet, & Vanquickenborne, 1995) and (Fuentes-cano, Go, Nilsson, & Ollero, 2016) respectively. As it can be seen in the Figure 85, the yield of phenol as a primary tar group is declining by increasing the temperature and the share of the toluene is rising. This behaviour is also predicted and reported in the work of (Fjellerup, Ahrenfeldt, Henriksen, & Gøbel, 2005) and shown in the Figure 13 previously.

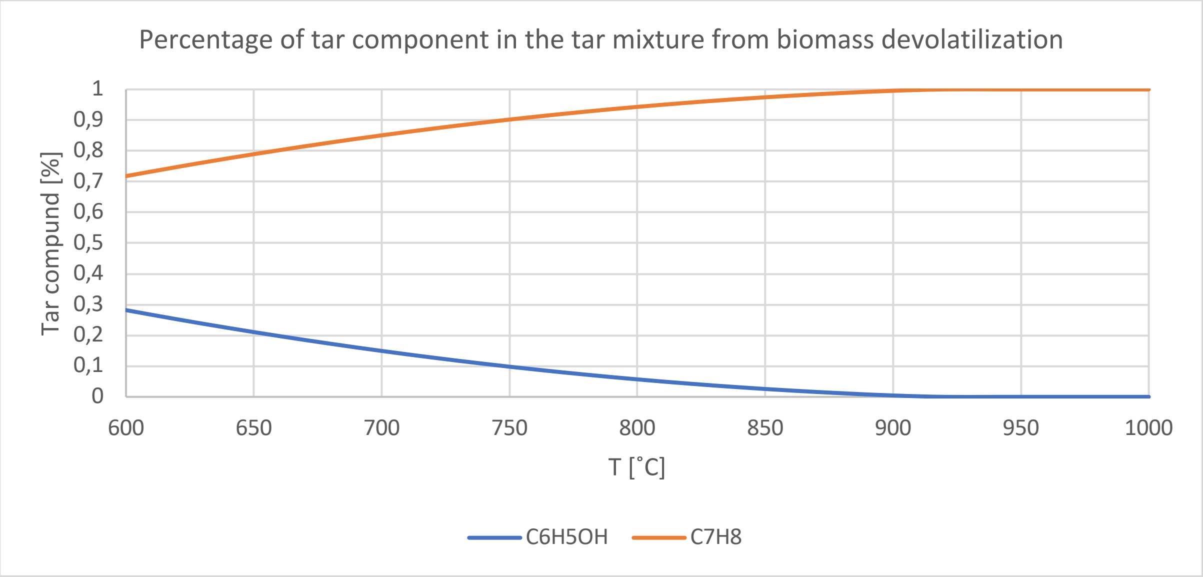

Figure 120 Percentage of the different tar compounds from biomass devolatilization

In the final gas product from the gasification reactor of TUW, the amount of tars present in the gas are very low and up to few milligrams per cubic meter of gas. Therefore, the tars inside the gasification reactor are supposed to completely converted through secondary reactions. The pathways for reforming and converting the tars inside the gasifier are adopted from the work of (Srinivas, Field & Herzog, 2013) and summarized in the table below.

Table 22 Stoichiometric for the reactions of the secondary conversion submodel (Srinivas, Field, & Herzog, 2013)

REACTION	STOICHIOMETRY	
R-1	$C_6H_5OH+3\ H_2O \rightarrow 2\ CO+CO_2+2.5\ CH_4+0.05\ C+0.1\ H_2$	Steam reforming
R-2	$2\ C_7H_8+21\ H_2O \rightarrow 7\ CO_2+29\ H_2+7\ CO$	Steam reforming
R-3	$C_7H_8+2\ H_2 \rightarrow CH_4+C_6H_6$	Hydrodealkylation
R-4	$C_6H_6+2\ H_2O \rightarrow 1.5\ C+2.5\ CH_4+2\ CO$	Steam reforming

At this point, initial conditions of the simulation have been described and the solid heterogenous biomass is turned into homogenous chemical compounds through devolatilization. The next step is defining the chemical reactions that are occurring inside the gasification reactor. Char is the solid fraction of the biomass devolatilization products and is containing mostly carbon with very low amounts of hydrogen, oxygen and inorganic fraction of the biomass which is the ash. In the simulation, for the simplicity the char is assumed to be pure carbon and homogenous. The yield of the char has been already obtained with the empirical correlations, but the reactivity of the char with gases is another issue and a key variable for the efficiency of gasifiers. More char conversion can lead to a higher efficiency of the gasification process. The char gasification is a highly endothermic reaction which depends on many factors such as the fuel parent, the process of devolatilization, particle sizes, residence time, the ash content in the char and so on. In this work, char gasification has been investigated in a thermo-gravimetrical analyzer (TGA) and has been discussed in the Chapter 4. In the experiments, the char reactivity has been analyzed but in order to estimate the amount of char gasified in the gasification reactor, the char residence time in the reactor is needed. The latter is previously discussed and calculated with the knowledge of the hydrodynamic behavior of the system. In the Figure 96 the percentage of the char gasified in the gasification reactor based on its reactivity and the corresponding residence time is reported.

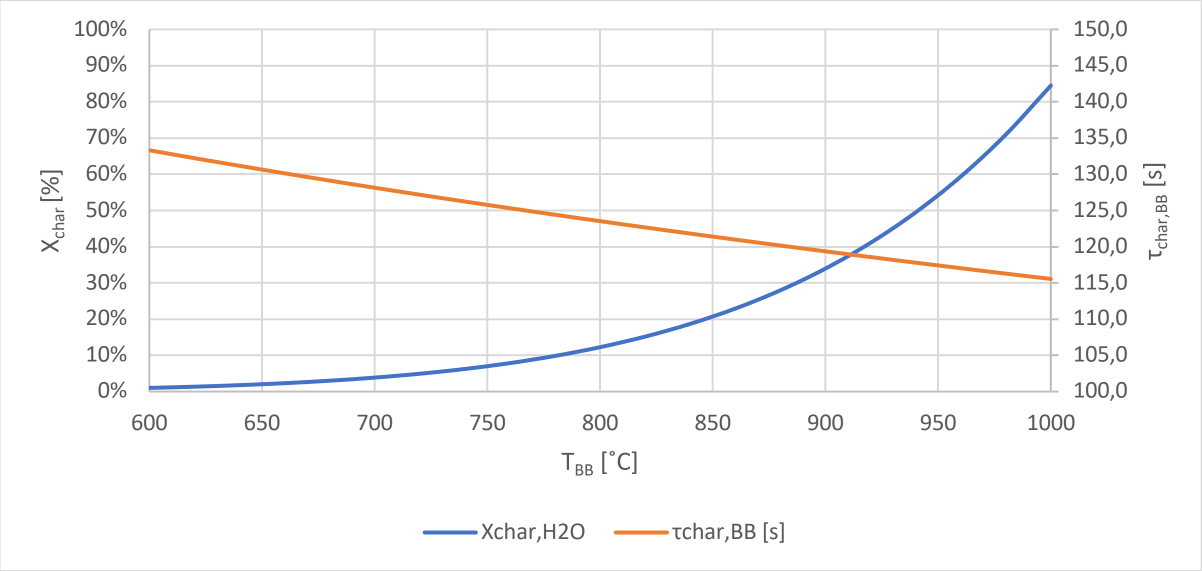

Figure 121 Char conversion in the gasification reactor of TUW's CFB as a function of bubbling bed's temperature and corresponding char residence time

Furthermore, in the Figure 97, based on the biomass input rate, the char yield through devolatilization, char reactivity and char residence time in the gasification reactor, the amount of char which is gasified and the unconverted char which is carried to the combustion reactor is shown. With increasing the gasification temperature, the amount of gasified char is increasing dramatically. It means, at the cost of increasing the gasification temperature, the char conversion goes up. Increasing the gasification temperature requires more energy, therefore there must be an optimal point for the efficiency which is a compromise between char conversion and gasification temperature.

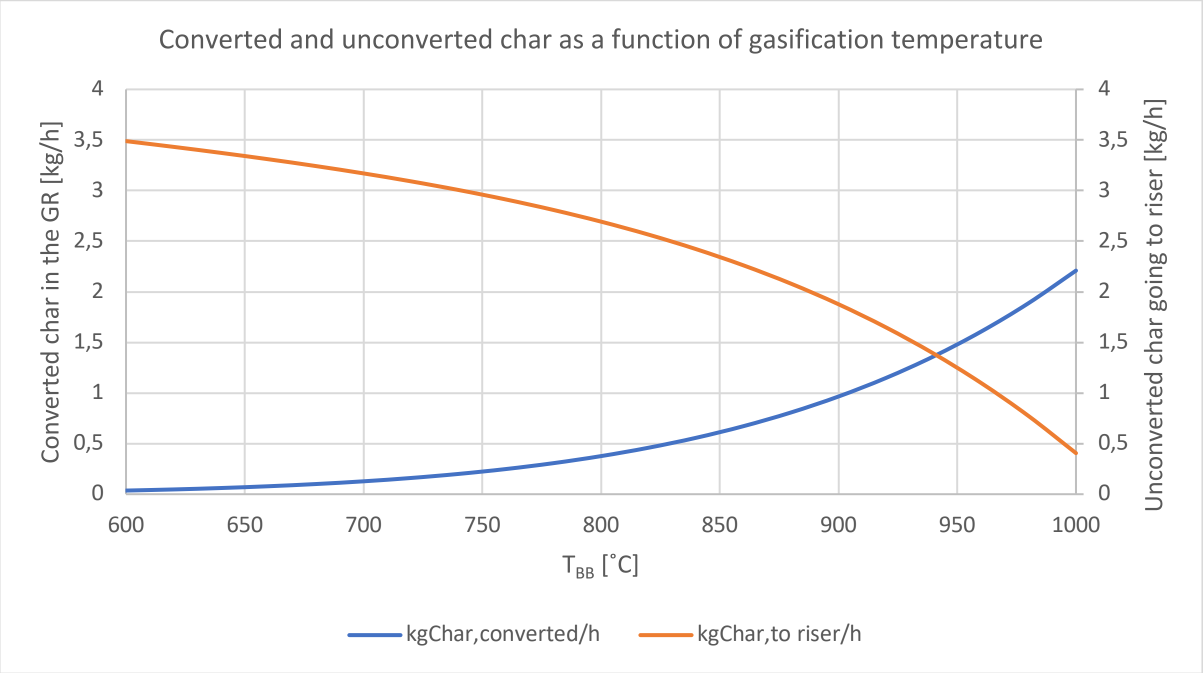

Figure 122 Converted char in the GR vs Unconverted char going to the CR

The last chemical reaction to be defined in order to be able to run the simulation is the water gas-shift reaction "WGSR". This reaction is assumed firstly at equilibrium and secondly with the kinetic expression obtained through the experiments done in this work and explained thoroughly in the Chapter 5. The results of both conditions are later compared and discussed whether there's an improvement. As far as the equilibrium modeling, the information required are the gas composition inside the gasification reactor after the devolatilization, char gasification and secondary tar conversions, as well as the equilibrium constant of the WGSR. The former is obtained through the previous steps of the development of the model and the latter is obtained from the literature and reported in the Figure 99 in Chapter 5. The kinetic of the WGSR in a non-catalytic environment and high temperature is desired for the completion of this simulation model but it's very scarce in the literature. In this work, the kinetic of WGSR in a non-catalytic environment and high temperature is experimentally investigated in a non-direct way. In the experiments, the reverse-WGSR is investigated and later, using the equilibrium constant of the reaction, the kinetic expression of the forward-WGSR has been obtained. The procedure of the experiments and details of the results are explained in the Chapter 5. Here only the final kinetic expression, pre-exponential factor and the activation energy, is reported:

$k_{0,f}=1.51\times10^{13}$

$E_{a,f}=183.15$ kJ/mol

Another essential variable for modeling the WGSR inside the gasification reactor with regarding to its kinetic, is the gas residence time. The gas residence has been calculated with the knowledge of the hydrodynamic behavior of the system in the previous chapters and implemented here.

At this point, all the steps mentioned in the Figure 116 as the concept behind the modeling of the biomass gasification process inside the CFB gasifier of TUW are completed. Before presenting the final results, which include the product gas composition, cold gas efficiency, product gas yield and the water conversion, a summary of the sensors implemented in the system and the data acquired through experimental measurements are explained.

As mentioned in the second Chapter, more than 200 sensors are implemented in the plant to measure and monitor numerous variables. The experimental results have been studied and analyzed separately for each temperature point, but due to the very large volume of data, the temperature and pressure profiles of the gasification and combustion reactors are shown here only for one temperature point as an example.

In the right side of the Figure 123, the temperature profile over the height of the combustion reactor is shown. At the bottom point, the temperature immediately rises as a result of burning of the unconverted char with the primary air injected to the system, and it further rises burning additional fuel being fed to the system with two more air injections for more efficient combustion and better fluidization. Above the last air injection point, the temperature is almost steady (minor temperature decreases due to heat loss). At the top of the riser, hot bed material is being circulated to the gasification reactor to provide the heat for the overall endothermic reactions. Therefore, at about 3.5 m height on the gasification reactor, the temperature is almost equal to the temperature at outlet of the riser. From the entrance point of the circulating bed material in the gasification reactor towards its outlet, the temperature decreases almost 100 °C which can be attributed to both heat loss as well as reforming the tar with steam. The trend of temperature profile from the entrance point of the hot circulating bed materials towards the bottom of the system is less uniform when compared with the upper side. At the height of about 2 m, a steep decrease is observed due to the introduction of secondary steam which has an initial temperature of around 135 °C and needs to be heated up immediately to the reactor temperature. The temperature continues to decrease up to the top of the bubbling bed. This is the point where the biomass is being fed to the system. At this point the moist biomass is heated up to the wet bulb temperature, then further heat is required to evaporate the moisture content, and eventually both dry biomass and water vapor are heated up to the bed temperature. The heat required to satisfy such processes causes this notable system temperature-drop (around

100 °C). Inside the bubbling bed, the char gasification occurs as well as heating up steam as fluidization system which can explain the fluctuations of the temperature inside the bed.

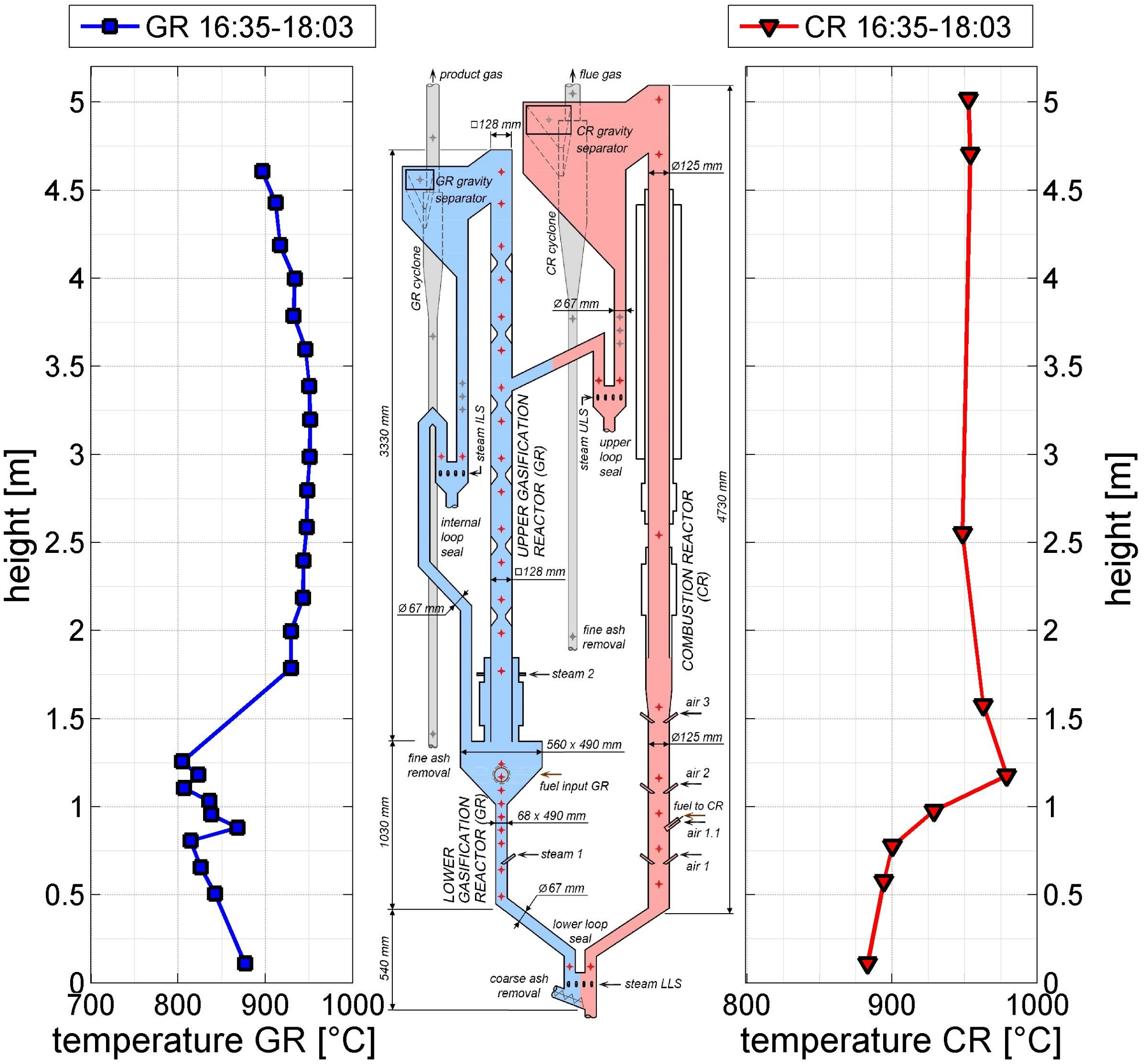

Figure 123 Temperature profiles of the gasification (left) and combustion (right) reactors

In the Figure 110 static gauge pressure measurements are shown over the height of the gasification and combustion reactors with square and triangular points respectively. Below 1 m height, the pressures are higher due to injection of steam and air in the gasification and combustion reactors respectively.

The pressure drops from the bottom of the GR up to a height around 1 meter (above the bubbling bed) indicates the weight of the bed material which is supported with the fluidization gas. A very small pressure drop can be observed over the freeboard of the gasification reactor and also in the riser due to its fast fluidization state.

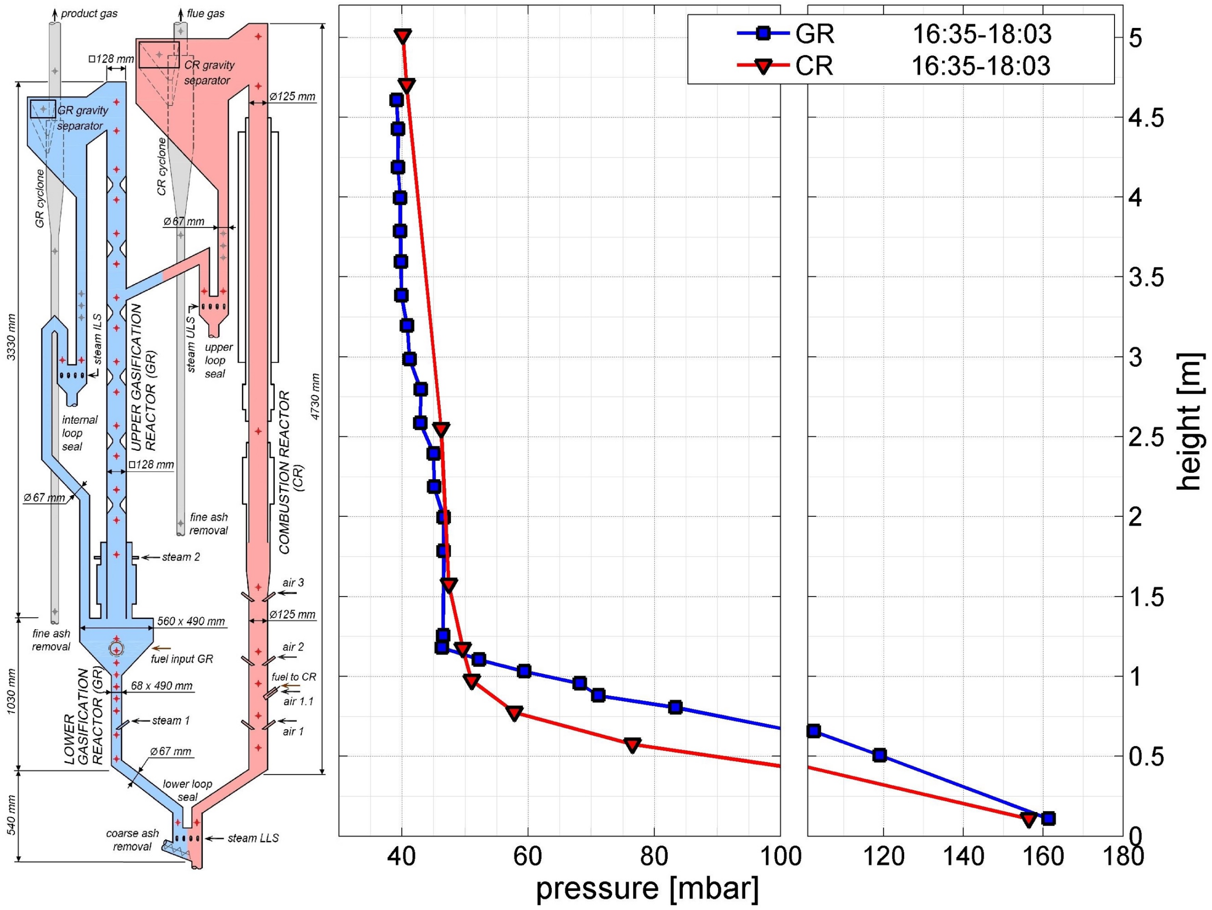

Figure 124 Gauge pressure profile of the gasification (square points) and combustion (triangular points) reactors

Hydrodynamic of the gasifier and pressure drops are discussed thoroughly in the second Chapter.

In Figure 125 and Figure 126, the temperature profiles of various temperature sensors over the GR and CR are shown as a function of time. As it can be seen towards the top of the reactor columns there are less fluctuations and temperatures are more stable. But in contrary at GR3 and GR5, where the steam is inserted to fluidize the bed and the biomass is fed, some fluctuations are noticed.

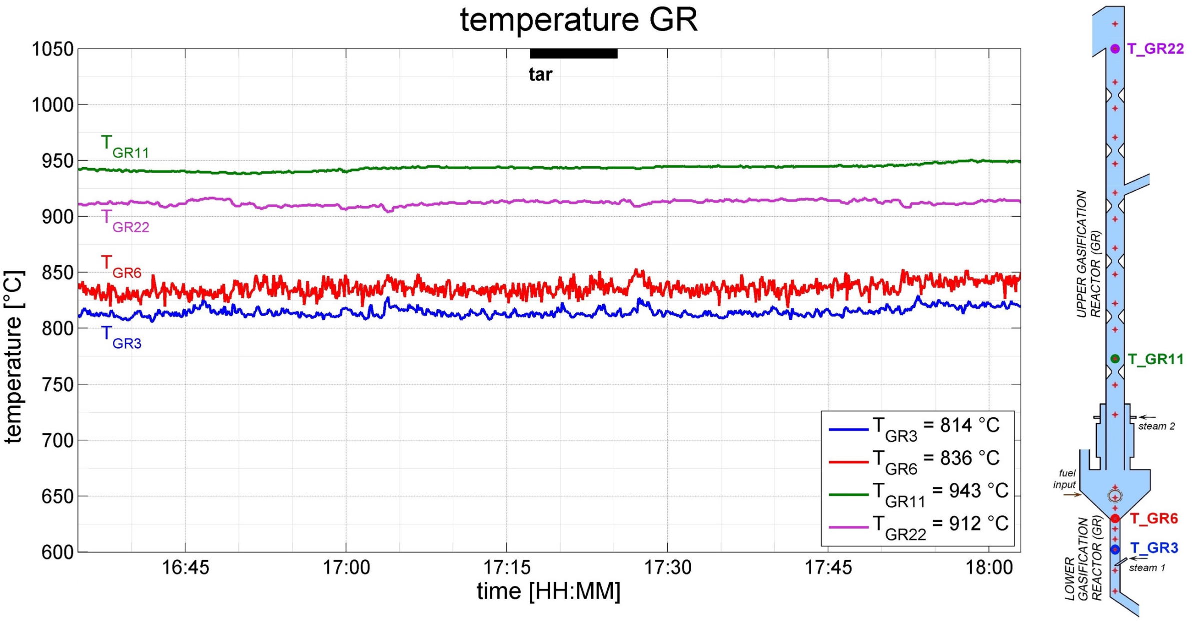

Figure 125 Temperature profile as a function of time over the GR height

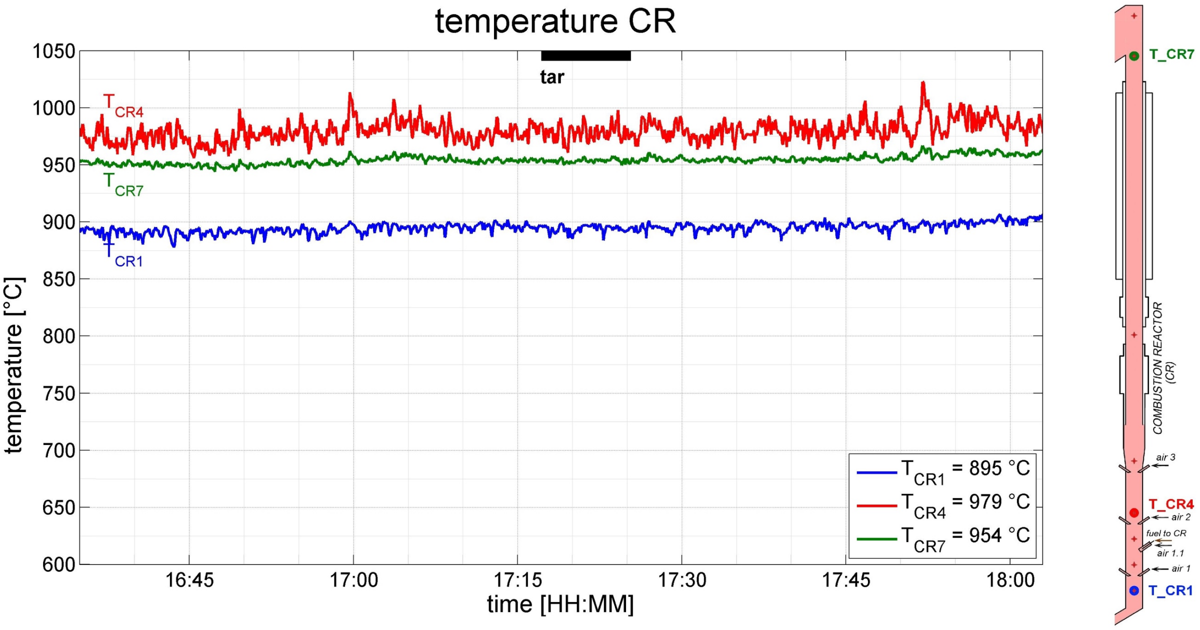

Figure 126 Temperature profile as a function of time over the CR height

Experimental and simulation results of the product gas composition in function of temperature, with assumption of equilibrium state for the WGSR are shown in Figure 127. In this figure, the dots refer to the experimental results and the continuous lines indicate the simulation with the assumption of equilibrium state for the WGSR, and the dash lines indicate the product gas composition before any WGSR. After pyrolysis, the yield of H_2 increases with temperature, and after introducing the steam to fluidize the bed, there is always enough H_2O for the WGSR, but it’s not the case for the residence time. Higher hydrogen productivity at higher temperature can be explained by advancement of WGSR, and lower hydrogen productivity at lower temperature can indicate that the kinetics of WGSR are low and to reach equilibrium more gas residence time in the gasifier is needed. The WGSR is slightly exothermic and thermodynamically more favorable at higher temperature even if the reaction kinetic is slower (Wheeler, Jhalani, Klein, Tummala, & Schmidt, 2004a). At higher temperature, the CO content starts to increase, and the CO_2 content will decrease with increasing gasification temperature. The yield of CH_4 and C_2H_4 from pyrolysis decreases with temperature. Also, these compounds are produced when the tar are cracked and reformed by either steam or CO_2. In the equilibrium model, C_2H_4 and C_2H_6 have been neglected in the producer gas, but we still notice some percentage of these compounds in the real product gas. The interesting observation in the Figure 127 is that at the lower temperatures, the real gas composition is more closer the gas composition after the devolatilization and tar cracking before any water gas-shift reaction. With increasing the temperature, the real gas composition corresponds much better with the simulated gas composition with assumption of WGSR being at equilibrium. This result indicates that at lower operational temperatures of the CFB gasifier of TUW, almost no WGSR occurs and around typical operational condition (T_{GR}~850˚C) WGSR reaches equilibrium. In order to simulate the transient part between these two points, using a proper kinetic model is suggested. Another small discrepancy between the experimental results with simulation can be due to neglecting some side reactions that could produce more of CH_4 and C_2H_4.

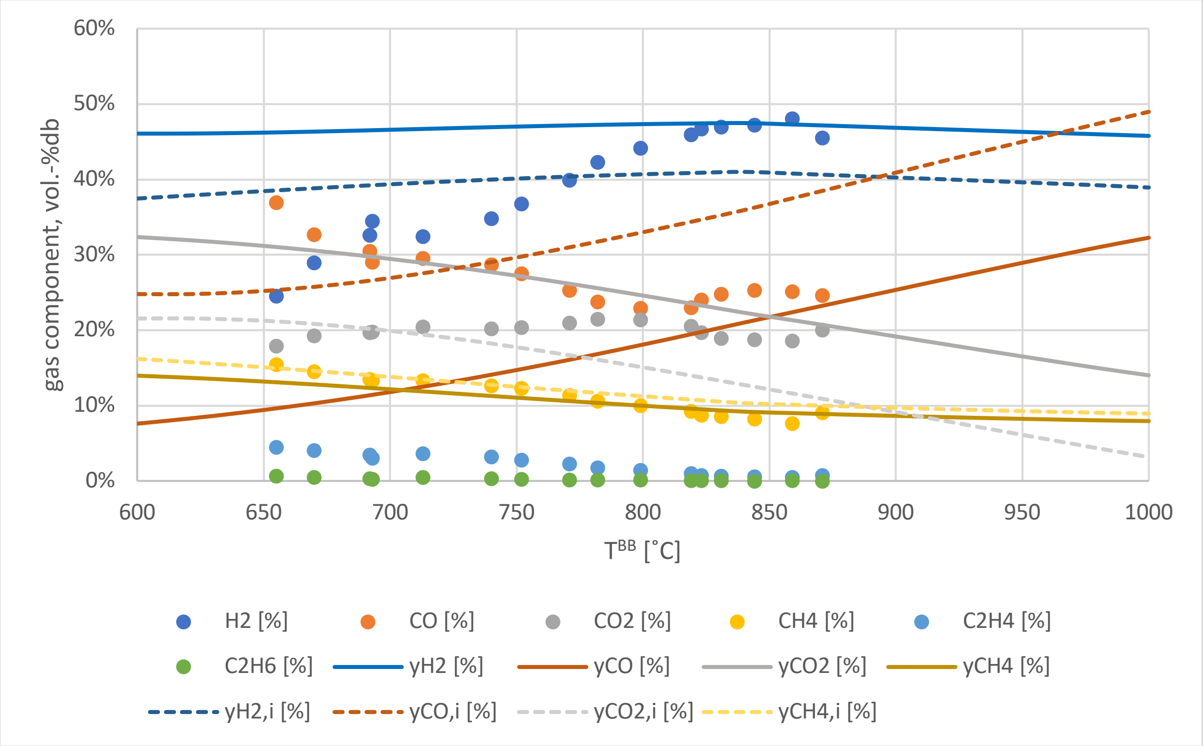

Figure 127 Comparison of product gas composition between experimental measurements and simulation results – assumption of equilibrium state for WGSR

More key figures of the CFB gasifier are evaluated here based on the previous assumptions. Later the results will be compared to the kinetic modeling to assess the improvement. Product gas yield is another important key figure which also is an indication of the efficiency of the system and the process is shown in the Figure 128. The value is the amount of dry product gas volume produced in the gasifier per kilogram of dried and ash free biomass fed to the system.

$$PGY = \frac{\dot{Q}_{pg}}{\dot{m}_{biomass-daf}} \qquad \left[\frac{Nm^3_{pg_{dry\ basis}}}{kg_{bm_{dry\ ash-free}}}\right]$$

There's a good accordance between the simulation results and the experiments. At higher temperatures the model shows less product gas yield (PGY) which can be due to the fact that methane steam reforming is neglected and therefore less water is converted to permanent gases and the yield of dry product gas is a little bit lower.

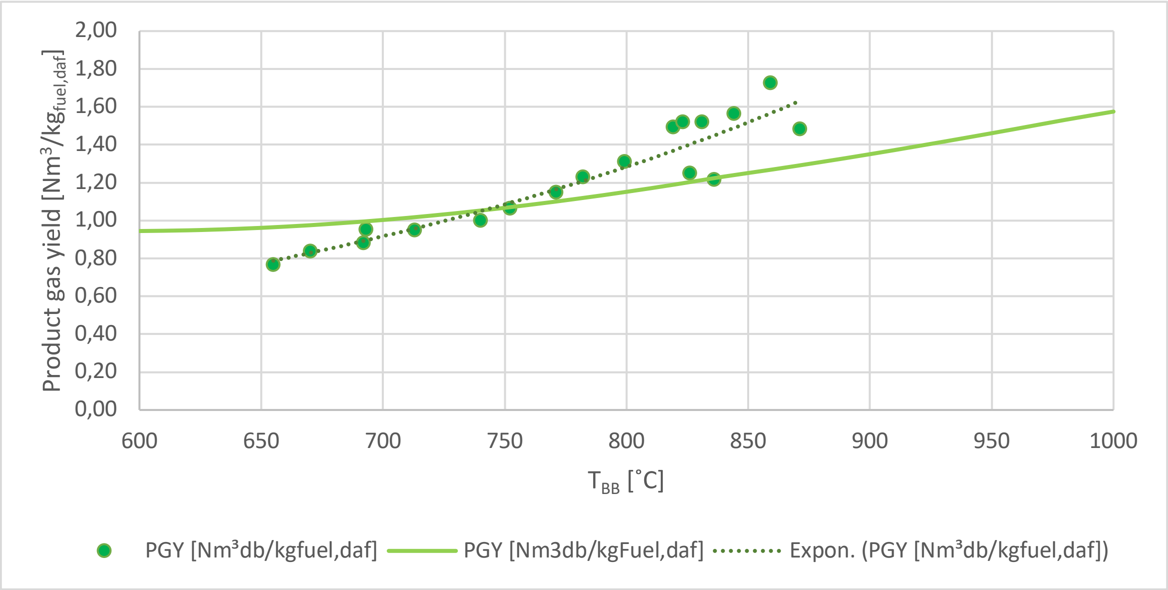

Figure 128 Product gas yield based on equilibrium modeling of the WGSR compared with the experimental results

Another key figure is the water conversion in the system which also can be an indication to the efficiency of the system. This value is based on the difference between the overall steam input to the system as fluidization/gasification agent and the amount of steam present in the product gas.

$$water\ conversion\% = \frac{\dot{Q}_{steam,input} - \dot{Q}_{steam\ in\ the\ PG}}{\dot{Q}_{steam,input}}$$

More water conversion means more char steam gasification, more tar steam reforming and WGSR closer to the equilibrium. The result of this variable is shown in the Figure 129. At lower temperature the model predicts more water conversion which can be due to the fact that in the WGSR equilibrium modelling even at lower temperatures this reaction is considered to be at equilibrium (infinite time for the reaction), but in the real system the gas residence time is not enough for the reaction to proceed. At higher temperatures the model shows less water conversion which again can be attributed to the negligence of methane steam reforming.

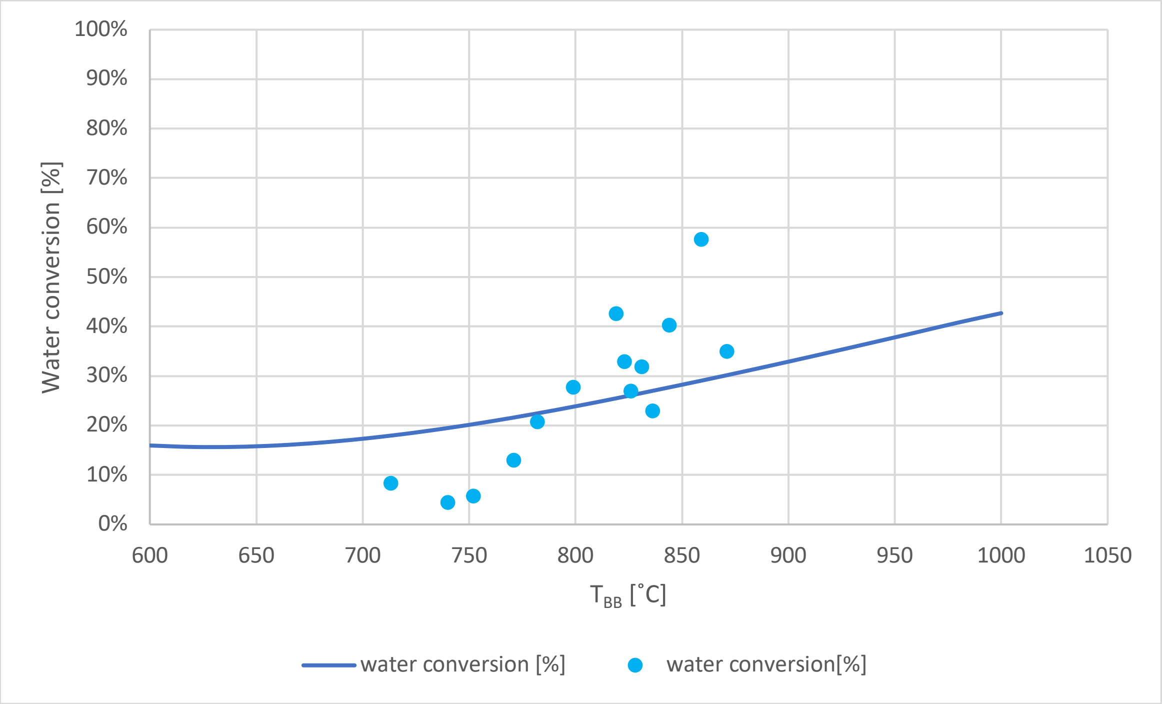

Figure 129 Water conversion based on equilibrium modeling of the WGSR compared with the experimental results

Last key figure to be discussed here is the cold gas efficiency which represent the ratio between the heating value output of the product gas and heating value input of the biomass as feedstock.

$$CGE\% = \frac{LHV_{pg_{db}} \cdot \dot{Q}_{pg_{db}}}{LHV_{bm_{daf}} \cdot \dot{m}_{bm_{daf}}}$$

The results are from the model are in an accepting range in regards to the experimental data, but the small difference can be attributed to the fact that the model predicts more CO_2 and less CO which lowers the heating value of the gas and also it predicts less product gas yield in the higher temperatures.

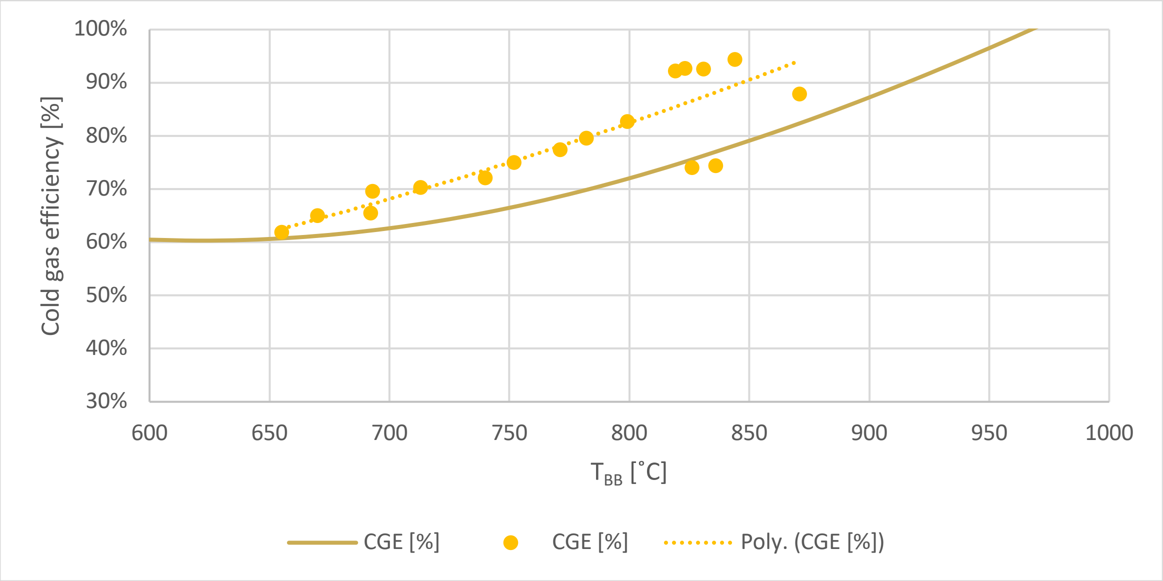

Figure 130 Cold gas efficiency based on equilibrium modeling of the WGSR compared with the experimental results

The kinetic expression obtained through the experiments for the homogenous WGSR in high temperatures is used to assess the improvement in the model to predict the product gas composition as well as key figures of the gasifier such as product gas yield, water conversion and cold gas efficiency. The results for the product gas composition are shown in the Figure 131.

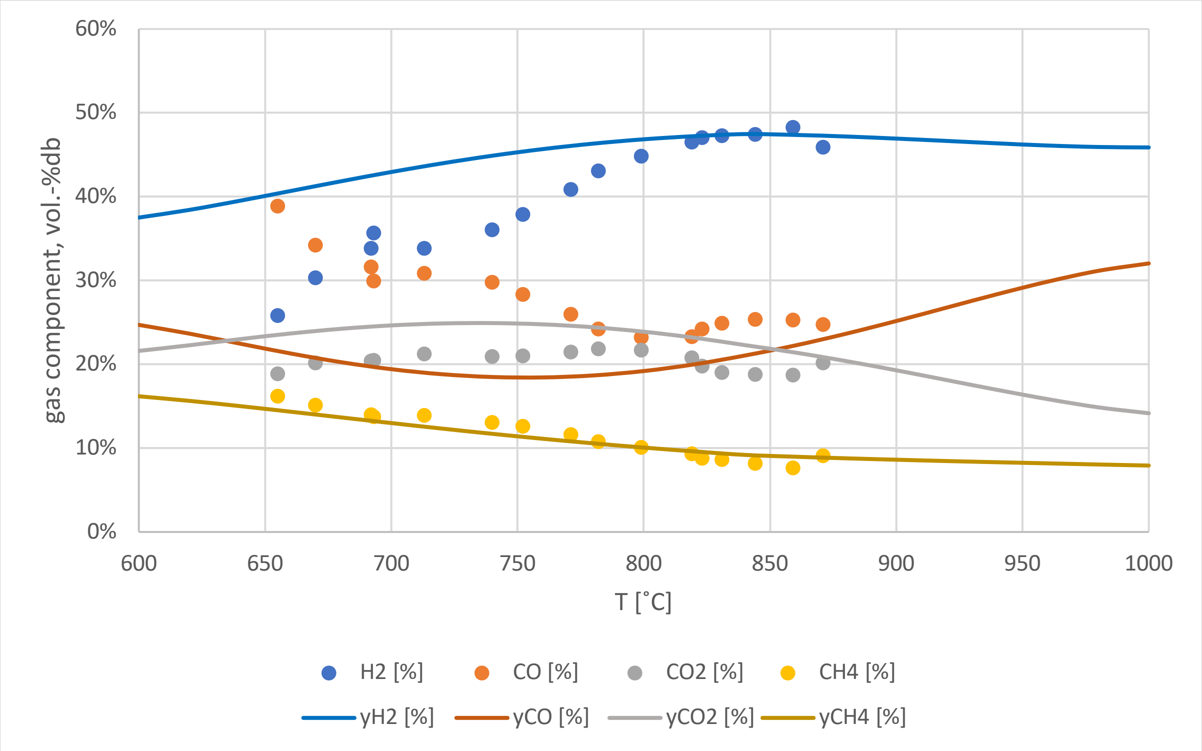

Figure 131 Comparison of product gas composition between experimental measurements and simulation results –kinetic modelling for the WGSR

An immediate improve in the results can be noticed. The model predicts the CH_4 amount and its trend very well, the H_2 results are improved even though there's still a gap at lower temperatures. CO and CO_2 still show some discrepancies, but with a major change and it's predicting a maxima and minima value for gases. When increasing the temperature, the reverse WGSR occurs in parallel and finally after about 830 ˚C, the reverse reaction exceeds. This explains the minimum of CO around this temperature in the results. At higher temperature, the CO content starts to increase, and the CO_2 content will decrease with increasing gasification temperature. This CO minimum (respectively CO_2 maximum) was previously reported in different studies of (Schmid et al., 2016) and (Ahrenfeldt et al., 2005a) but never been predicted by the simulation.

Other key figures such as product gas yield (PGY), water conversion and cold gas efficiency (CGE) as a result of kinetic modeling of the WGSR are reported in the Figure 132, Figure 133 and Figure 134 respectively.

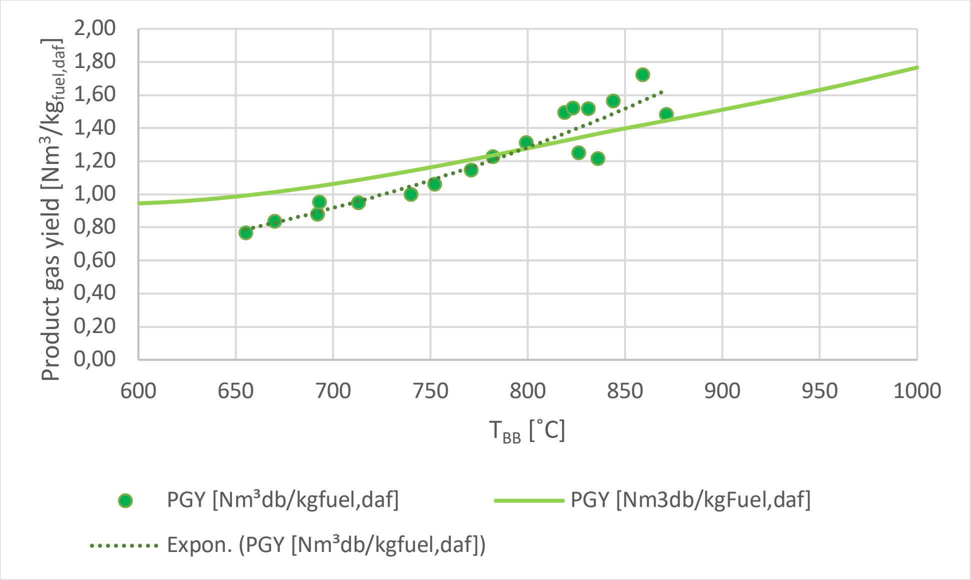

Figure 132 Product gas yield based on kientic modeling of the WGSR compared with the experimental results

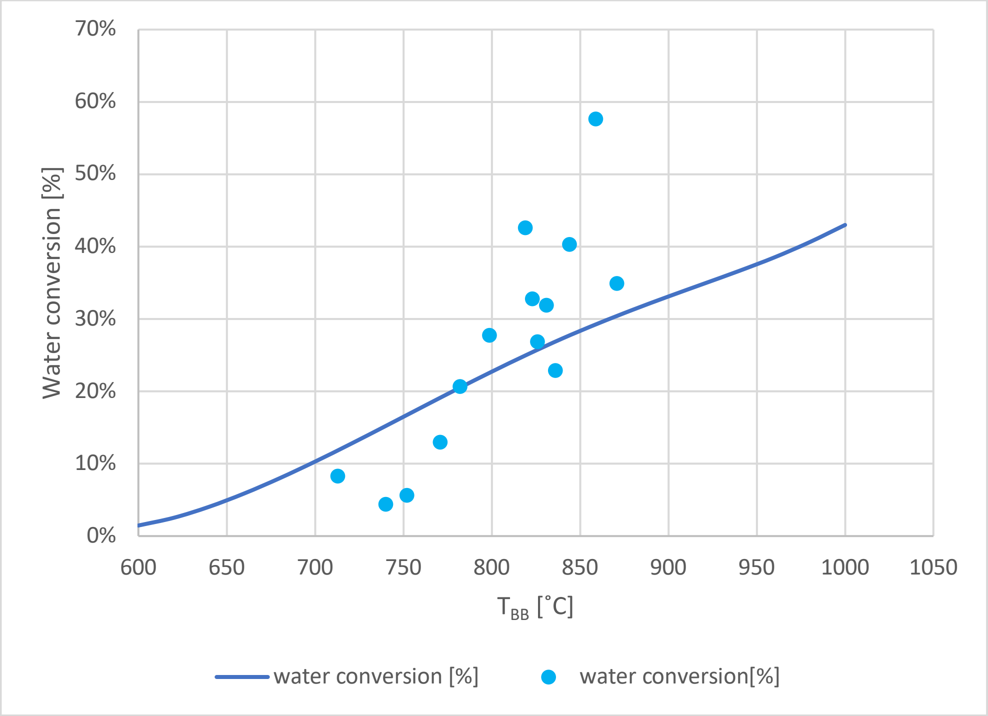

Figure 133 Water conversion based on kinetic modeling of the WGSR compared with the experimental results

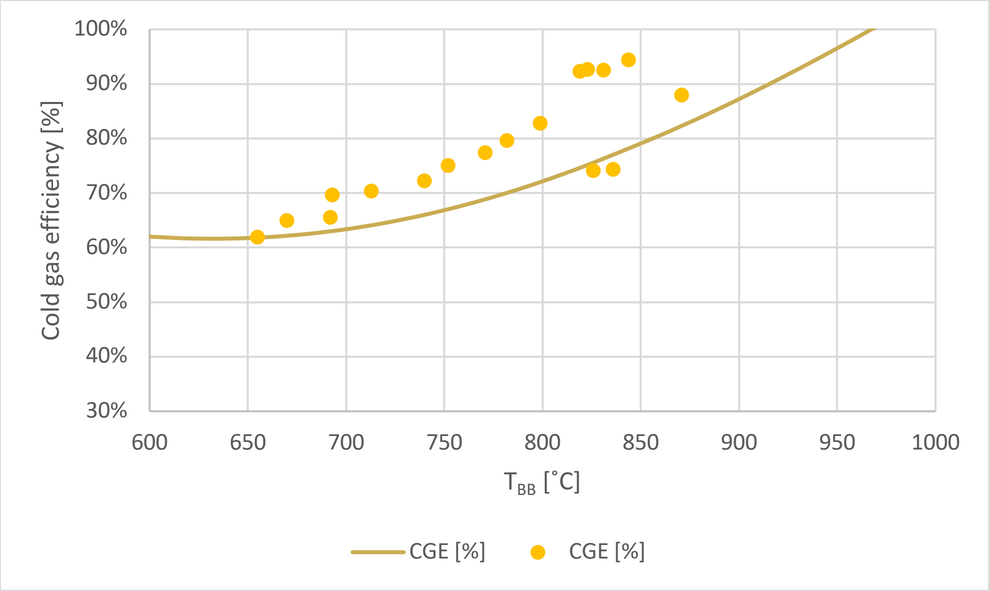

Figure 134 Cold gas efficiency based on equilibrium modeling of the WGSR compared with the experimental results

In order to assess the improvement of the prediction of these values with incorporating the kinetic expression in the model, their values based on the equilibrium and kinetic modeling of the WGSR are reported in the following Figure 135, Figure 136 and Figure 137.

In the results of product gas yield, it can be noted the model has a more accurate prediction at higher temperatures, but no improvement has been made at the lower temperatures.

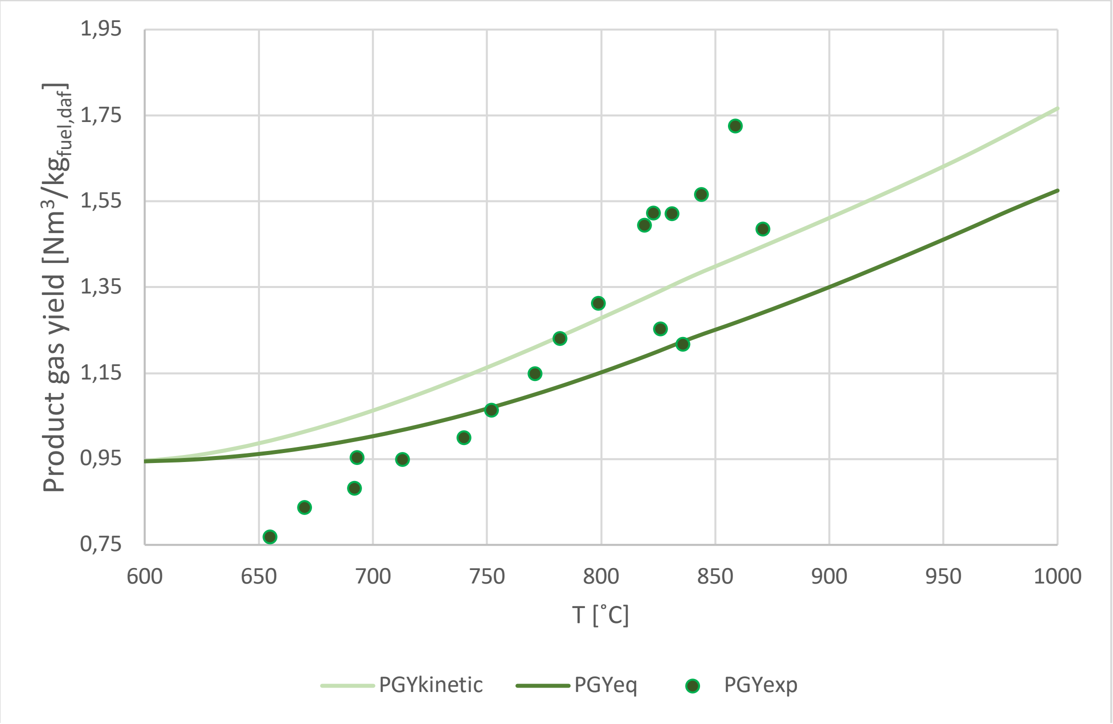

Figure 135 Product gas yield based on compared kinetic model with equilibrium model and the experimental results

The results of the water conversion have been improved as well. The equilibrium model predicts a total WGSR at lower temperatures, hence, it predicts higher water conversion which is not feasible in the CFB gasifier of TUW. Lower kinetic of the WGSR and the low gas residence time doesn’t allow this reaction to reach the equilibrium.

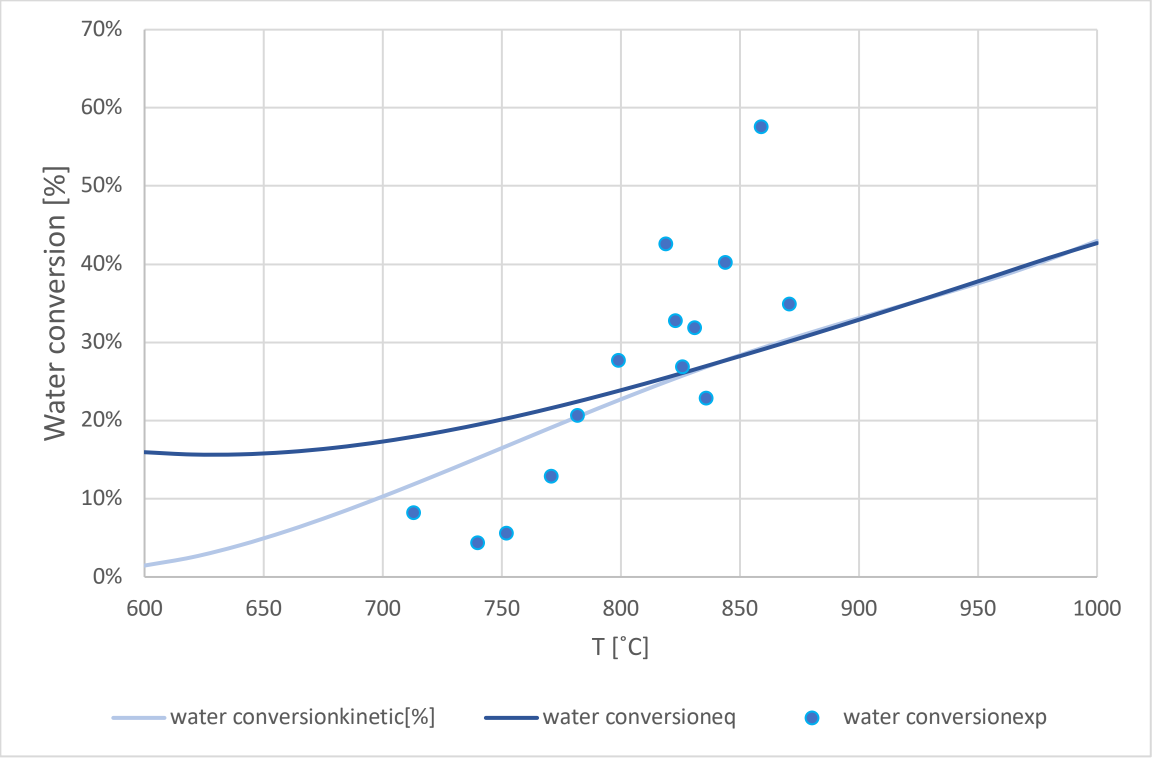

Figure 136 Water conversion based on compared kinetic model with equilibrium model and the experimental results

The results of the cold gas efficiency show only a small improvement at lower temperature and at higher temperatures there's almost no changed noted.

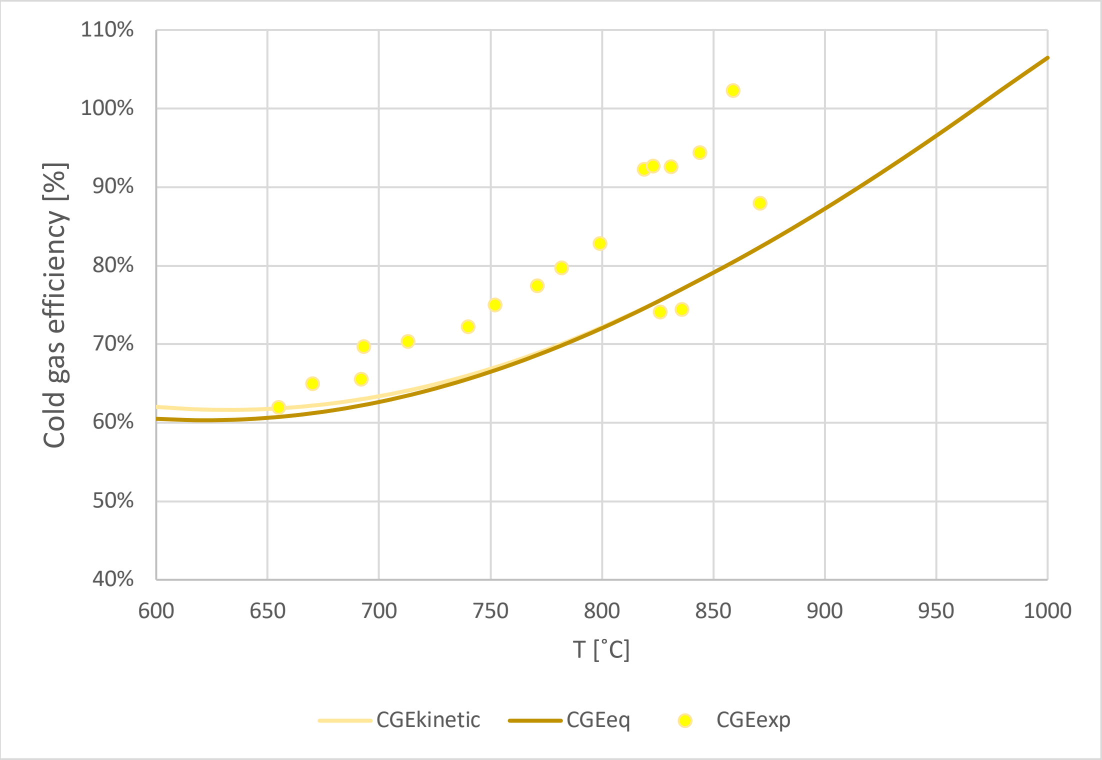

Figure 137 Cold gas efficiency based on compared kinetic model with equilibrium model and the experimental results

The individual gas components also have been studied to visualize better the improvement of the prediction of the model with incorporating the kinetic expression of the WGSR. The results are shown in the following figures.

The equilibrium model predicts much higher H_2 productivity which is due to the assumption of infinite gas residence time and subsequently proceeding with WGSR completely. Even though the kinetic model shows improvement of the prediction at lower temperatures, still there's a gap to fill between simulation results and experimental measurements. This gap can be due to some simplifications and assumptions that made through the process of the modeling such as H_2 and tar yields from the devolatilization of the biomass, and the kinetic expression of the WGSR as well neglecting some minor possible homogenous gas-gas reactions in the freeboard of the gasifier.

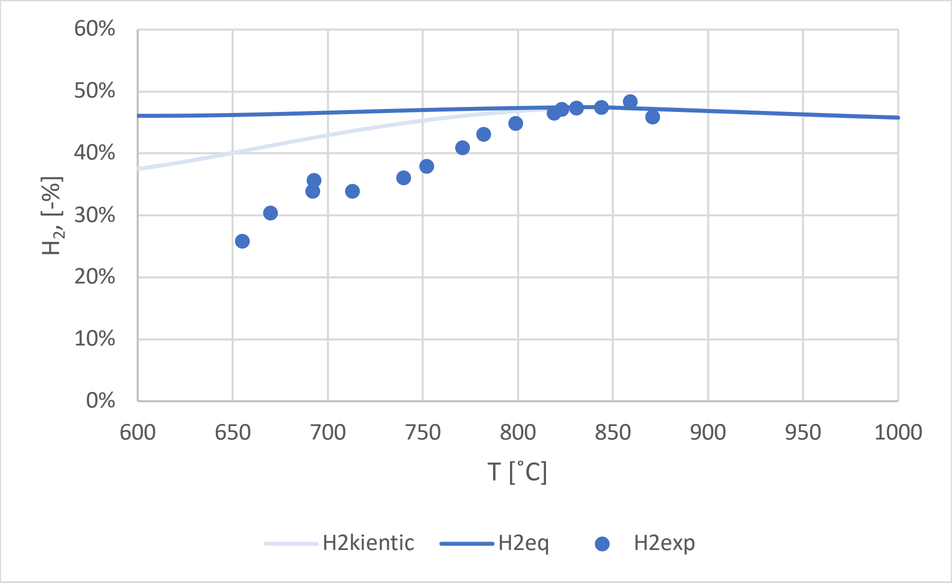

Figure 138 Comparison of H_2 gas composition between experimental measurements and simulation results –kinetic and equilibrium modelling for the WGSR

CO and CO_2 prediction based on the kinetic modelling are drastically improved at the lower temperatures. The major improvement is predicting a curvy behaviour which explained earlier and only have been reported in the experimental measurements and not with simulation models.

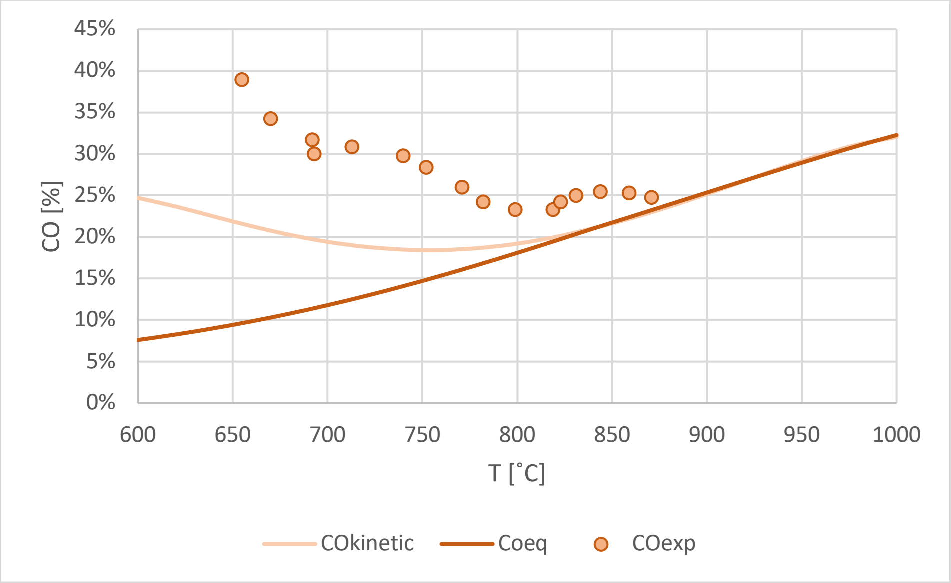

Figure 139 Comparison of CO gas composition between experimental measurements and simulation results –kinetic and equilibrium modelling for the WGSR

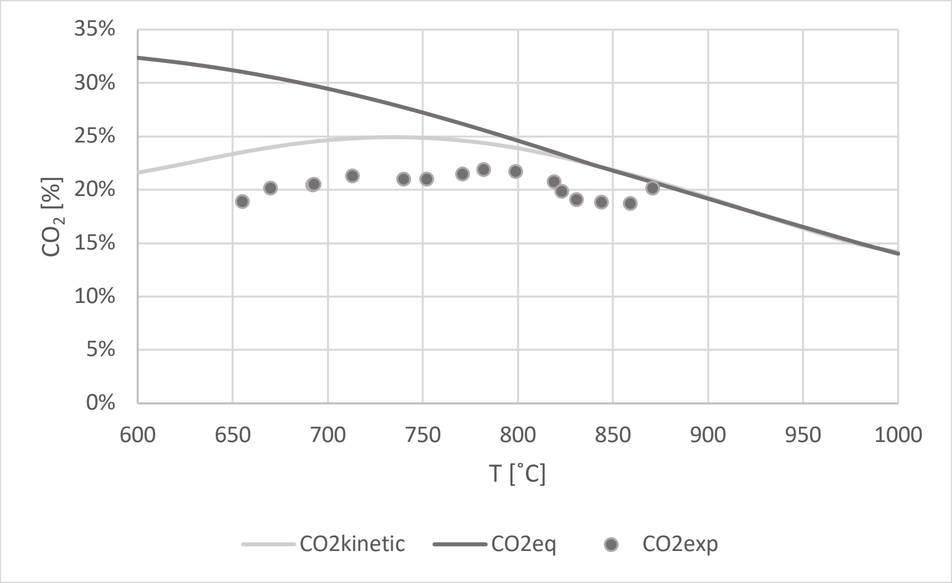

Figure 140 Comparison of CO_2 gas composition between experimental measurements and simulation results –kinetic and equilibrium modelling for the WGSR

The trend and composition of the CH_4 has the best agreement with the simulation results in both lower and higher temperatures. The small gap can be due to the negligence of the methane steam reforming in the gasifier.

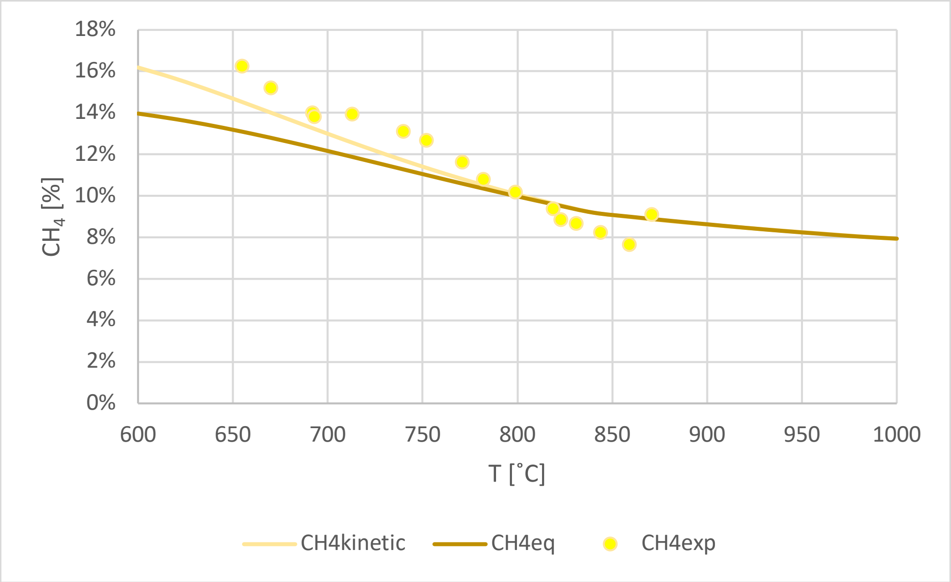

Figure 141 Comparison of CH_4 gas composition between experimental measurements and simulation results –kinetic and equilibrium modelling for the WGSR

In Figure 142 the results are presented in a different perspective. The horizontal and vertical axis represent experimental and simulation results, and the numbers 1, 2, …, 16 represent the temperatures at which there's experimental results available. A ratio between simulation and experimental results are reported for the gas composition at above-mentioned temperatures. The solid line with 45° in the figure indicates that values from simulation equals exactly to the measured values from experiments, and the dashed lines in above and below this line show and area with maximum 30% error (the simulation values in these regimes show maximum either 30% over-estimation or under-estimation). As it can be noticed, almost everything coincides in a margin of less than 30% error except few cases of CO at lower temperatures.

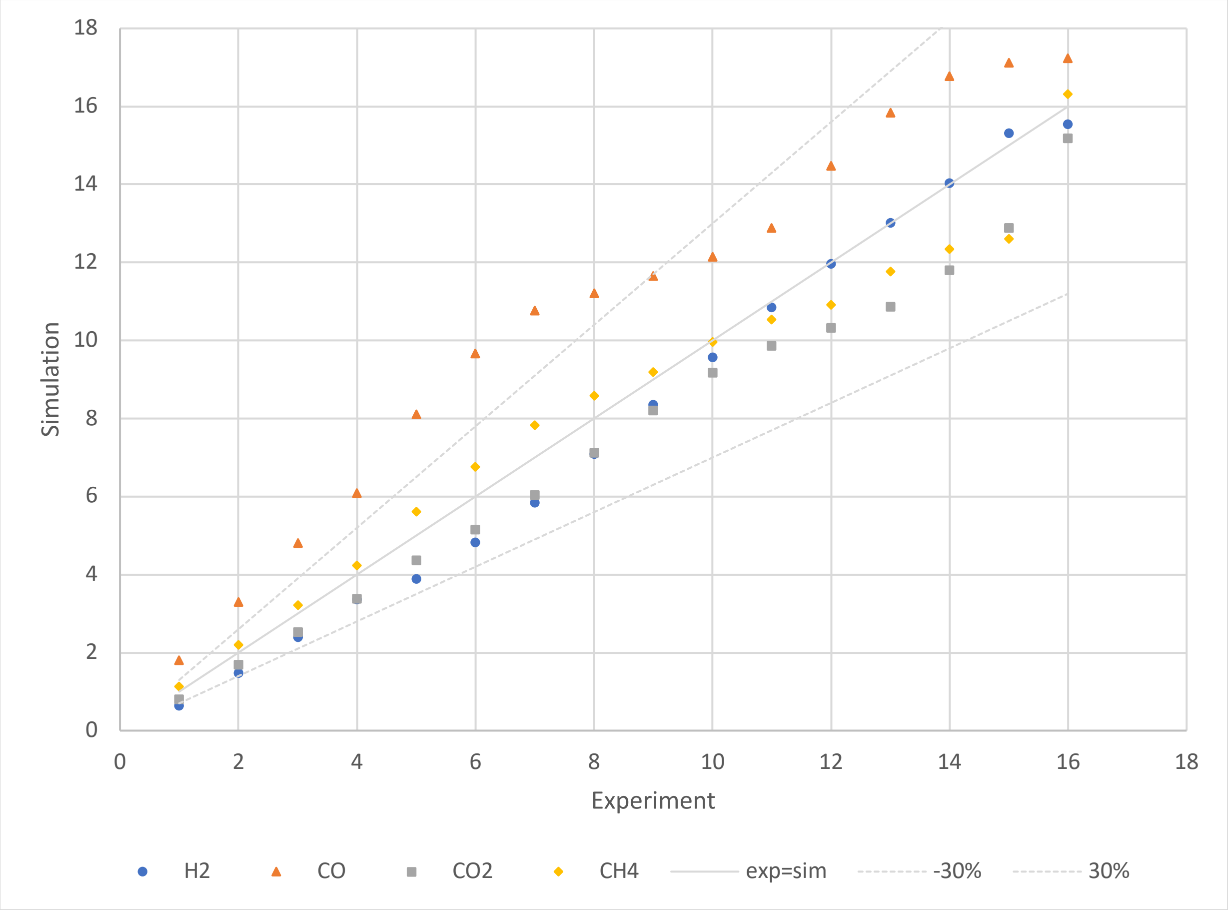

Figure 142 Comparison between the results of simulation model and measurement data of the steam gasification of softwood pellets with olivine sand as bed material in the 100 kW DFB gasifier

A methodology is developed to model a CFB gasifier of TUW using excel spreadsheets proper developed to separately reproducing pyrolysis, including an extensive investigation on char reactivity as well as the kinetics of the WGSR. The method is based on separating the main reactions -pyrolysis, char gasification, water-gas shift reaction, tar formation and conversion, and char combustion- in different reactors.

Pyrolysis product yields (char, volatiles, pyrolytic water, tar species) and their composition are implemented in in the model prior to heterogenous reactions of char and homogenous gas-gas reactions. Water-gas shift reaction is modeled with kinetic approach based on the experimental measurements in a non-catalytic environment.

This method allows having an insight on the mechanism of the reactions that occur inside the gasifier as a result of suitable pyrolysis correlation and kinetic approach of WGSR.

In successive works, one can introduce the fully detailed kinetic of pyrolysis and side reactions to fully integrate the heat balance of the system; implementing of kinetics of tar cracking/reforming can enhance the prediction of gas composition and can include the remaining tar based on the operational condition in the product gas; implementing other parallel reactions can close the gap between experimental measurements and simulation results specially at lower temperatures. The results show very good accordance for the key figures of the gasifier such as product gas yield, water conversion and cold gas efficiency. These figures are either impossible or very difficult to predict by a simulation based on only equilibrium modeling without a detailed modeling of the sub-processes of devolatilization, char gasification and tar reforming.

The presented model constitutes a proper tool to be used for predicting future test runs and, by changing the bed material, the effect of catalytic conversion can be assessed. This model can be also used to optimize the performance of the plant and finally with the acquired knowledge from the sub-processes in the system, improvement of current designs or make innovative designs are feasible.

Then, it will be possible to determine the operating conditions under which the DFB can operate by maximizing the LHV and/or minimizing the tar compounds production and delivering, thus aiming to increase the overall efficiency and reduce the environmental impact of a biomass-based power plant, eventually enhancing overall sustainability.

The features of the present approach constitute the base for developing a black-box model of the pyrolysis/gasification process that is based on physically sound approaches (for any step of the process) more than on the empirical correlation that are usually considered. It is expected that such models can properly predict the gas yields as well as the mass and energy balance of the gasifier.

This is considered a key factor for a proper prediction of the operative conditions of poly-generation power plants, aiming at overcoming the usual limitation of the model currently available in the open literature.

References

1. IEA, Market Report Series: Renewables 2018, Analysis and Forecasts to 2023. Paris, France, 2018.
2. Asadullah, M.; Barriers of commercial power generation using biomass gasification gas: A review; Renewable and Sustainable Energy Reviews, 2014, 29, 201-215
3. Ferreira, L.R.A.; Otto, R.B.; Silva, F.P.;, De Souza, S.N.M.; De Souza, S.S.; Ando Junior, O.H.; Review of the energy potential of the residual biomass for the distributed generation in Brazil, Renewable and Sustainable Energy Reviews, 2018, 94, 440-455
4. Karl, J.; Pröll, T.; Steam gasification of biomass in dual fluidized bed gasifiers: A review, Renewable and Sustainable Energy Reviews, 2018, 98, 64-78.
5. Hamelinck, C.N.; Faaij, A.P.; Future prospects for production of methanol and hydrogen from biomass. J Power Sources 2002; 111:1–22.
6. Levin, D.B.; Chahine, R.; Challenges for renewable hydrogen production from bio-mass. Int J Hydrog Energy, 2010; 35: 4962–9.
7. Larsson, A.; Seemann, M.; Neves, D.; Thunman, H. Evaluation of Performance of Industrial-Scale Dual Fluidized Bed Gasifiers Using the Chalmers 2−4-MWth Gasifier. Energy Fuels 2013, 27, 6665−6680.
8. Borello D., De Caprariis B., De Filippis P., Caucci M., Pantaleo A. M., Shah N., Modeling and experimental study of a small scale olive pomace gasifier for cogeneration: Energy and profitability analysis, Energies, 2017
9. Schmid, J.C., 2014, "Development of a novel dual fluidized bed gasification system for increased fuel flexibility", doctoral thesis, Wien University of Technology, Wien, ISBN 978-3-9502754-6-9
10. Di Carlo, A., Borello, D., Bocci, E., 2013, 'Process simulation of a hybrid SOFC/μGT and enriched air/steam fluidized bed gasifier power plant', International Journal of Hydrogen Energy, 38 (14) pp. 5857 - 5874, doi:10.1016/j.ijhydene.2013.03.005.
11. Nikoo, M.B.; Mahinpey, N.; Simulation of biomass gasification in fluidized bed reactor using ASPEN PLUS, Biomass and Bioenergy, 2008, 12, 1245-1254
12. Jana, K.; De, S. (2014). Biomass integrated gasification combined cogeneration with or without CO_2capture - A comparative thermodynamic study. *Renewable Energy*. doi.org/10.1016/j.renene.2014.07.027

13. Suwatthikul, A., Limprachaya, S., Kittisupakorn, P., & Mujtaba, I. M. (2017). Simulation of steam gasification in a fluidized bed reactor with energy self-sufficient condition. *Energies*. doi.org/10.3390/en10030314
14. Pala, L. P. R., Wang, Q., Kolb, G., & Hessel, V. (2017). Steam gasification of biomass with subsequent syngas adjustment using shift reaction for syngas production: An Aspen Plus model. *Renewable Energy*. doi.org/10.1016/j.renene.2016.08.069
15. Adeyemi, I., & Janajreh, I. (2015). Modeling of the entrained flow gasification: Kinetics-based ASPEN Plus model. *Renewable Energy*. doi.org/10.1016/j.renene.2014.10.073
16. Wang, H., Yan, J., & Dong, L. (2016). Simulation and economic evaluation of biomass gasification with sets for heating, cooling and power production. *Renewable Energy*. doi.org/10.1016/j.renene.2016.07.001
17. Puig-Arnavat, M., Bruno, J. C., & Coronas, A. (2010). Review and analysis of biomass gasification models. *Renewable and Sustainable Energy Reviews*, *14*(9), 2841–2851. doi.org/10.1016/j.rser.2010.07.030
18. Abdelouahed, L., Authier, O., Mauviel, G., Corriou, J. P., Verdier, G., & Dufour, A. (2012). Detailed modeling of biomass gasification in dual fluidized bed reactors under aspen plus. *Energy and Fuels*, *26*(6), 3840–3855. doi.org/10.1021/ef300411k
19. Kaushal, P., & Tyagi, R. (2017). Advanced simulation of biomass gasification in a fluidized bed reactor using ASPEN PLUS. *Renewable Energy*. doi.org/10.1016/j.renene.2016.09.011
20. Neves, D., Thunman, H., Matos, A., Tarelho, L., & Gómez-barea, A. (2011). Characterization and prediction of biomass pyrolysis products. *Progress in Energy and Combustion Science*, *37*(5), 611–630. doi.org/10.1016/j.pecs.2011.01.001
21. Report, P. (2016). Technical Report of Scientific Experimental Research Steam gasification of EXHAUSTED OLIVE POMACE with a dual fluidized bed pilot plant at TU Wien (Vol. 605357), Wien, Austria.
22. Schmid, J.C., Wolfesberger, U., Koppatz, S., Pfeifer, C., Hofbauer, H., 2012, "Variation of Feedstock in a Dual Fluidized Bed Steam Gasifier - Influence on Product Gas, Tar Content and Composition", Environmental Progress & Sustainable Energy, Vol. 31 (2), pp. 205-2015, July 2012, Wiley, doi.org/10.1002/ep.11607
23. Benedikt, F., Schmid, J.C., Fuchs, J., Mauerhofer, A., Müller, S., Hofbauer, H., 2018, "Fuel Flexible Gasification with an Advanced 100 kW Dual Fluidized Bed Steam Gasification Pilot Plant", Energy, Vol.164, pp. 329-343, doi.org/10.1016/j.energy.2018.08.146
24. Pröll, T.; Hofbauer, H. Development and Application of a Simulation Tool for Biomass Gasification Based Processes. Int. J. Chem. React. Eng. 2008, 6, Article 89.

25. Prins, M. J., Ptasinski, K. J., & Janssen, F. J. J. G. (2003). Thermodynamics of gas-char reactions: First and second law analysis. *Chemical Engineering Science*, *58*(3–6), 1003–1011. doi.org/10.1016/S0009-2509(02)00641-3
26. Pearson, R. G., & Williams, E. L. (1987). A comparison of heterogeneous and homogeneous kinetics in the formation of a polyurethane. *Journal of Polymer Science Part A: Polymer Chemistry*, *25*(2), 565–573. doi.org/10.1002/pola.1987.080250210
27. Pala, L. P. R., Wang, Q., Kolb, G., & Hessel, V. (2017). Steam gasification of biomass with subsequent syngas adjustment using shift reaction for syngas production: An Aspen Plus model. *Renewable Energy*, *101*, 484–492. doi.org/10.1016/j.renene.2016.08.069
28. Milne, T. A., Evans, R. J., & Abatzaglou, N. (1998). Biomass Gasifier "'Tars'": Their Nature, Formation, and Conversion, (November). NREL Report, Golden, Colorado, doi.org/10.2172/3726
29. Babu, B. V., & Chaurasia, A. S. (2004). Dominant design variables in pyrolysis of biomass particles of different geometries in thermally thick regime. *Chemical Engineering Science*, *59*(3), 611–622. doi.org/10.1016/j.ces.2003.10.014
30. Di Blasi C, Branca C, Santoro A, Hernandez EA. Pyrolytic behavior and products of some wood varieties. Combust Flame 2001;124:165e77
31. Scott DS, Piskorz J, Radlein D. Liquid products from the continuous flash pyrolysis of biomass. Ind Eng Chem Process Des Dev 1985;24:581e8.
32. Scott DS, Piskorz J, BergougnouMA, Graham R, Overend RP. The role of temperature in the fast pyrolysis of cellulose and wood. Ind ChemRes 1988;27:8e15.
33. Funazukuri T, Hudgins RR, Silveston PL. Correlation of volatile products from fast cellulose pyrolysis. Ind Eng Chem Process Des Dev 1986;25:172e81
34. Wang X, Kersten SRA, Prins W, van Swaaij WPM. Biomass pyrolysis in fluidized bed reactor. Part 2: experimental validation of model results. Ind Eng Chem Res 2005;44:8786e95.
35. Zanzi R, Sjöström K, Björnbom E. Rapid pyrolysis of agricultural residues at high temperature. Biomass & Bioenergy 2002;23:357e66.
36. Encinar JM, González JF, González J. Fixed-bed pyrolysis of Cynara cardunculus L. Product yields and compositions. Fuel Process Technol 2000;68:209e22.
37. Dupont C, Commandré JM, Gauthier P, Boissonnet G, Salvador S, Schweich D. Biomass pyrolysis experiments in an analytical entrained flow reactor between 1073K and 1273K. Fuel 2008;87:1155e64
38. Fagbemi L, Khezami L, Capart R. Pyrolysis products from different biomasses: application to the thermal cracking of tar. Appl Energy 2001;69:293e306.

39. Di Blasi C, Signorelli G, Di Russo C, Rea G. Product distribution from pyrolysis of wood and agricultural residues. Ind Eng Chem Res 1999;38:2216e24
40. Schmid, J. C., Müller, S., & Hofbauer, H. (2016). First Scientific Results with the Novel Dual Fluidized Bed Gasification Test Facility at TU Wien. *24th European Biomass Conference and Exhibition*, 2–6. doi.org/10.5071/24thEUBCE2016-2CV.3.16
41. Ahrenfeldt, J., Henriksen, U., Gøbel, B., & Fjellerup, J. (2005). Experimental Characterisation of Residual-Tar in Wood Char Lyngby: DTU Mekanik. MEK-ET-2005-06
42. Paviet, F., Chazarenc, F., & Tazerout, M. (2009). Thermo Chemical Equilibrium Modelling of a Biomass Gasifying Process Using ASPEN PLUS. *International Journal of Chemical Reactor Engineering*, *7*(1). doi.org/10.2202/1542-6580.2089
43. Klose, W., & Wölki, M. (2005). On the intrinsic reaction rate of biomass char gasification with carbon dioxide and steam. *Fuel*, *84*(7–8), 885–892. doi.org/10.1016/j.fuel.2004.11.016
44. Kramb, J., Konttinen, J., Gómez-Barea, A., Moilanen, A., & Umeki, K. (2014). Modeling biomass char gasification kinetics for improving prediction of carbon conversion in a fluidized bed gasifier. *Fuel*, *132*, 107–115. doi.org/10.1016/j.fuel.2014.04.014
45. Smith R J, B., Loganathan, M., & Shantha, M. S. (2010). A Review of the Water Gas Shift Reaction Kinetics. *International Journal of Chemical Reactor Engineering*, *8*(1). doi.org/10.2202/1542-6580.2238
46. Wheeler, C., Jhalani, A., Klein, E. J., Tummala, S., & Schmidt, L. D. (2004). The water-gas-shift reaction at short contact times. *Journal of Catalysis*, *223*(1), 191–199. doi.org/10.1016/j.jcat.2004.01.002
47. Lima, D. F. B., Zanella, F. A., Lenzi, M. K., & Ndiaye, P. M. (20012). Modeling and Simulation of Water Gas Shift Reactor: An Industrial Case. *Cdn.Intechopen.Com*. Retrieved from cdn.intechopen.com/pdfs/34193/InTech-Modeling_and_simulation_of_water_gas_shift_reactor_an_industrial_case.pdf
48. Zainal, Z.A.; Ali, R.; Lean, C.H.; Seetharamu, K.N. (2001) Prediction of performance of a downdraft gasifier using equilibrium modeling for different biomass materials. Energy Conversion and Management 42: 1499-515.
49. de Souza-Santos, M. L. (1989) Comprehensive Modelling and Simulation of Fluidized-Bed Boilers and Gasifiers. Fuel, 68: 1507-21.
50. Bentzen, J.D.; Brandt, P.; Gøbel, B.; Hansen, C.H.; Henriksen, U. (1998) 100kW Totrinsforgasningsanlæg på DTU Resultater til og med foråret 1998, ET-ES 98-11, Institut for Energiteknik, Technical University of Denmark, Denmark.

51. Callaghan, C. A. (2006). Kinetics and Catalysis of the Water-Gas-Shift Reaction: A Microkinetic and Graph Theoretic Approach. *Department of Chemical Engineering*, *Ph. D. Thesis* . United States of America, 31 March 2006.

52. Biba, V., Macak, J., Klose, E., and Malecha, J., "Mathematical model for the gasification of coal under pressure," Ind. Eng. Chem. Process, vol. 17, pp. 92-98, 1978.

53. Wheeler, C., Jhalani, A., Klein, E. J., Tummala, S., & Schmidt, L. (2004). The water–gas-shift reaction at short contact times. *Journal of Catalysis*, *223*, 191–199. https://doi.org/10.1016/j.jcat.2004.01.002

54. Gao, J., Wang, Y., Ping, Y., Hu, D., Xu, G., Gu, F., & Su, F. (2012). A thermodynamic analysis of methanation reactions of carbon oxides for the production of synthetic natural gas. *RSC Advances*, *2*(6), 2358. doi.org/10.1039/c2ra00632d

55. Fjellerup, J., Ahrenfeldt, J., Henriksen, U., & Gøbel, B. (2005). *Formation, Decomposition and Cracking of Biomass Tars in Gasification*. *Renewable Energy* (Vol. 30). Retrieved from http://linkinghub.elsevier.com/retrieve/pii/S0960148104002927

56. Donnot, A., Reningovolo, J., Magne, P., & Deglise, X. (1985). Flash pyrolysis of tar from the pyrolysis of pine bark. *Journal of Analytical and Applied Pyrolysis*, *8*, 401–414. https://doi.org/https://doi.org/10.1016/0165-2370(85)80039-5

57. Koppatz, S., Pfeifer, C., & Hofbauer, H. (2011). Comparison of the performance behaviour of silica sand and olivine in a dual fluidised bed reactor system for steam gasification of biomass at pilot plant scale. *Chemical Engineering Journal*, *175*, 468–483. https://doi.org/https://doi.org/10.1016/j.cej.2011.09.071

58. Bustamante, F., Enick, R. M., Cugini, A. V., Killmeyer, R. P., Howard, B. H., Rothenberger, K. S., … Shi, S. (2004). High-Temperature Kinetics of the Homogeneous Reverse Water-Gas Shift Reaction. *AIChE Journal*, *50*(5), 1028–1041. https://doi.org/10.1002/aic.10099

59. Bustamante, F., Enick, R. M., Cugini, A. V., Killmeyer, R. P., Howard, B. H., Rothenberger, K. S., … Shi, S. (2004). High-Temperature Kinetics of the Homogeneous Reverse Water-Gas Shift Reaction. *AIChE Journal*, *50*(5), 1028–1041. https://doi.org/10.1002/aic.10099

60. **Chiester et al., 1984:** Chiester DC, Kornosky RM, Fan LS, Danko JP. Characteristics of fluidization at high pressure. Chem Eng Sci, 39 (1984), p. 253-61

61. **Tannous et al., 1994:** Tannous K, Hemati M, Laguérie C. Caractéristiques de fluidisation et expansion des couches fluidisées de particules de la catégorie D de Geldart. Powder Technol 1994;80:55-72.

62. **Babu et el., 1978:** Babu P, Shah B, Talwalker A. Fluidization correlations for coal gasification materials; minimum fluidization velocity and fluidized bed expansion ratio. AIChE Symp Ser 1978;74:176–86
63. **Nakamura et al., 1985:** Nakamura M, Hamada Y, Toyama S, Fouda AE, Capes CE. An experimental investigation of minimum fluidization velocity at elevated temperatures and pressures. Can. J. Chem. Eng. 1985;63:8-13.
64. **Chyang and Huang 1988:** Chyang CS, Huang WC. Characteristics of large particle fluidization. Chin. IChE 1988;19:91-9.
65. **Hofbauer, H., & Rauch, R. (2002).** Six Years Experience with the FICFB-Gasification Process, (January).
66. **ES Pettyjohn, EB Christiansen:** Effect of particle shape on free-settling rates of isometric particles. Chem Eng Prog 44:157–172, 1948.
67. **Geldart D.** Types of gas fluidization. Powder Technol 7:285– 292, 1973.
68. **Gómez-Barea and Leckner, 2010:** Gómez-Barea A, Leckner B. Modeling of biomass gasification in fluidized bed. Prog Energ Combust 2010;36:444-509.
69. **Noda et al., 1989:** Noda K, Uchida S, Makino T, Kamo H. Minimum fluidization velocity of binary mixture of particles with large size ratio. Powder Technol 1986;46:149–54.
70. **Teplitskii et al., 2009:** Teplitskii YS, Kovenskii VI, Borodulya VA. Velocity of complete fluidization of a polydisperse mixture of various fuels Proceedings of the 20th International Conference on Fluidized Bed Combustion 2009, pp. 298-304
71. **Formisani, 1991:** Formisani B. Packing and fluidization properties of binary mixtures of spherical particles. Powder Technol 1991;66:259-64.
72. **Broadhurst, T. E., & Becker, H. A. (1975).** Onset of Fluidization and Slugging in Beds of Uniform Particles, 21(2), 238–247.
73. **Leva, M.,** “Fluidization”, McGraw Hill, New York 1959
74. **Davidson JF, Harrison D.** Fluidised Particles. London: Cambridge University Press, 1963.
75. **Partridge BA, Rowe PN.** Chemical reaction in a bubbling gas-fluidised bed. Trans Inst Chem Engrs 44:T335–T348, 1966.
76. **Kunii D, Levenspiel O.** Fluidization Engineering. New York: John Wiley, 1969.
77. **Kato K, Wen CY.** Bubble assemblage model for fluidized bed catalytic reactors. Chem Eng Sci 24:1351–1369, 1969.
78. Toomey RD, Johnstone HP. Gaseous fluidization of solid particles. Chem Eng Progress 48:220–226, 1952.

79.**Hepbasli, 1998:** Hepbasli, A. Estimation of bed expansions in a freely-bubbling three-dimensional gas-fluidized bed (1998) International Journal of Energy Research, 22 (15), pp. 1365-1380

80.**Babu et el., 1978:** Babu P, Shah B, Talwalker A. Fluidization correlations for coal gasification materials; minimum fluidization velocity and fluidized bed expansion ratio. AIChE Symp Ser 1978;74:176–86

81.**Darton, R. C. (2014).** Bubble Growth Due To Coalescence in Fluidized Beds, (October 1977).

82.**Fuchs, J., Schmid, J. C., & Benedikt, F. (2018).** A general method for the determination of the entrainment in fluidized beds, 12(4), 359–372.

83.Kunii D, Levenspiel O (1991) Fluidization engineering, 2nd edn. Butterworth-Heinemann, Boston

84.Nguyen, M. T., Sengupta, D., Raspoet, G., & Vanquickenborne, L. G. (1995). Theoretical study of the thermal decomposition of acetic acid: Decarboxylation versus dehydration. *Journal of Physical Chemistry*, *99*(31), 11883–11888. https://doi.org/10.1021/j100031a015

85.Fuentes-Cano, D., Gómez-Barea, A., Nilsson, S., & Ollero, P. (2016). Kinetic Modeling of Tar and Light Hydrocarbons during the Thermal Conversion of Biomass. *Energy and Fuels*, *30*(1), 377–385. https://doi.org/10.1021/acs.energyfuels.5b02131

86.Malek, L. (2016). Technical Report of Scientific Experimental Research, 1–31.

87.Mauerhofer, A. M., Schmid, J. C., Benedikt, F., Fuchs, J., Müller, S., & Hofbauer, H. (2019). Dual FLuidized bed steam gasification: Change of product gas Quality along the reactor height. *Energy*, *173*, 1256–1272. https://doi.org/10.1016/j.energy.2019.02.025

88.Nilsson S, Gomez-Barea A, Fuentes-Cano D, Ollero, P. Gasification reactivity of char from dried sewage sludge in a fluidized bed. Fuel 2012;92:346-53

89.Lundberg, L., Tchoffor, P. A., Pallarès, D., Johansson, R., Thunman, H., & Davidsson, K. (2016). Influence of surrounding conditions and fuel size on the gasification rate of biomass char in a fluidized bed. *Fuel Processing Technology*, *144*, 323–333. https://doi.org/10.1016/j.fuproc.2016.01.002

90.Nilsson S, Claro JG, Gómez-Barea A, Fuentes D, Ollero P. Gasification of char from dried sewage sludge with steam and CO_2 in fluidized bed. Proceedings of 18th European Biomass Conference, May 2010, Lyon (France), pp. 624-7. Oral presentation.

91.Barrio, M., Gøbel, B., Rimes, H., Henriksen, U., Hustad, J. E., & Sørensen, L. H. (2008). Steam Gasification of Wood Char and the Effect of Hydrogen Inhibition on the Chemical Kinetics. *Progress in Thermochemical Biomass Conversion*, 32–46. https://doi.org/10.1002/9780470694954.ch2

92. Prusakov, P. G., & Sergeeva, L. V. (1974). Physical and Thermody-namic Properties of Aliphatic Alcohols. *J. Phys. Chem. Ref. Zubarev*, *47*(5), 1443.

93. J. D. Parent and S. Katz. Equilibrium Compositions and Enthalpy Changes for the Reaction of Carbon, Oxygen and Steam. IGT Research Bulletin, 1948.

94. Jones, W.P., and Lindstedt, R.P. 1988. Global reaction schemes for hydrocarbon combustion. Combust. Flame, 73, 233–249.

95. W. F. Podolski, Y. G. Kim, *Ind. Eng. Chem. Process Des. Dev.* **1974**, *13*, 415.

96. P. Fott, J. Vosolsobe, V. Glaser, *Collect. Czech. Chem. Commun.* **1979**, *44*, 652.